

Abstract

Progress toward Searching for Electron Electric Dipole Moment using PbO

Yong Jiang

2008

Observation of a non-zero electron electric dipole moment (EDM) will be explicit evidence for physics beyond the Standard Model. There is significant interest in developing experiments that can probe beyond the current limits for the electron EDM. An experiment to look for the EDM of the electron using the metastable $a(1)(^3\Sigma^+)$ state of the PbO molecule has been implemented at Yale University. We populate the $a(1) [^3\Sigma^+]$ state of ^{208}PbO using laser-microwave double resonance, and we detect fluorescence, using quantum beat spectroscopy to extract minute frequency changes due to the electron EDM. The experimental method and setup will be described in this thesis. We have demonstrated the ability to manipulate the internal molecular state in such a way as to produce the desired states for our EDM experiment. Efforts were carried out to optimize the state excitation efficiency using an adiabatic following scheme. We performed various experiments to confirm our understanding of molecular state evolution dynamics in a variety of experimental configurations. Our experiment improved the accuracy of previously measured molecular constants of PbO, which cast light on the feasibility of future systematic error checking and reduction. Due to various technical issues, the sensitivity to an electron EDM in this generation of EDM experiment is far less than expected. Two novel proposals for a second generation EDM experiment are considered.

**Progress toward Searching for Electron Electric
Dipole Moment using PbO**

A Dissertation
Presented to the Faculty of the Graduate School
of
Yale University
in Candidacy for the Degree of
Doctor of Philosophy

by
Yong Jiang

Dissertation Director: David DeMille

May 2008

UMI Number: 3317137

INFORMATION TO USERS

The quality of this reproduction is dependent upon the quality of the copy submitted. Broken or indistinct print, colored or poor quality illustrations and photographs, print bleed-through, substandard margins, and improper alignment can adversely affect reproduction.

In the unlikely event that the author did not send a complete manuscript and there are missing pages, these will be noted. Also, if unauthorized copyright material had to be removed, a note will indicate the deletion.

UMI[®]

UMI Microform 3317137

Copyright 2008 by ProQuest LLC.

All rights reserved. This microform edition is protected against unauthorized copying under Title 17, United States Code.

ProQuest LLC
789 E. Eisenhower Parkway
PO Box 1346
Ann Arbor, MI 48106-1346

Copyright © 2008 by Yong Jiang

All rights reserved.

Acknowledgements

It is my pleasure to express my thanks to the many people who made this thesis possible.

In the first place I would like to gratefully and sincerely thank my research advisor, Professor David DeMille, for his advice, guidance, understanding, and patience. With his enthusiasm, his truly scientist intuition, his inspiration, and his great efforts to explain things clearly and simply, he provided me sound advice, great ideas, genuine encouragement and support throughout my PhD life. I could not have imagined having a better advisor and mentor for my PhD. I am greatly indebted to him more than he knows.

I gratefully acknowledge all the members of my thesis committee for their accessibility and valuable advice.

Collective and individual acknowledgments are also owed to my colleagues at Yale. Best regards to all members of Prof. DeMille's research group for their friendship and help. Especially I gratefully acknowledge Sarah Bickman, Paul Hamilton and Amar Vutha who provided me with one of the most comfortable working places I have ever had. I would like to extend my sincerest thanks to my co-workers David Kawall, Richard Paolino, Frederik Bay, Valmiki Prasad, and etc. There are many others who contributed to this work. Sidney Cahn offered advice on technical issues and provided some much needed humor and entertainment in what could have otherwise been a somewhat stressful laboratory environment. Vincent Bernardo and the entire Gibbs Machine Shop did great jobs on metal machining. I am grateful to all of the faculty and staff in Department of Physics at Yale, for assisting me in many different ways and many other issues for their hard work,

expertise and patience.

I am especially indebted to my wife Yi Wang, who has continually offered her ardent love, selfless dedication, and persistent confidence in me. Her staunch support, quiet patience, and unwavering faith have taken the load off my shoulder. And The birth of our beautiful baby boy Leon brings an additional and enjoyable dimension to our life. I thank my parents for their faith in me and allowing me to be as ambitious as I wanted. Also, I thank Yi's parents. They provided Yi and me with unending encouragement and support. I wish to thank my entire extended family for providing a loving environment for me.

Finally, I would like to thank everybody who was important to the successful realization of thesis, as well as expressing my apology that I could not mention personally one by one.

Contents

Acknowledgements	iii
1 Introduction	1
1.1 General Introduction to EDM Experiments	1
1.1.1 Motivation for Searches for EDM	1
1.2 Electron EDM Experiments with Atoms or Molecules	4
1.2.1 Atomic EDM Experiments	5
1.2.2 EDM Enhancement in Diatomic Molecules	7
2 Probing the Electron EDM using PbO	10
2.1 Principal Properties of the PbO $a(1)$ State	10
2.2 Experimental Method	15
2.3 Experimental Setup	19
2.4 Quantum Beat Spectroscopy in Fluorescence	22
2.4.1 Quantum Beats	23
2.4.2 Data Analysis	25
2.5 Statistical Sensitivity of EDM Experiment	33
2.6 Overview of Systematic Effects	34
2.6.1 Applied External Field	35
2.6.2 Leakage Current Effects	39
2.6.3 The Internal Co-Magnetometer	40

3	Experimental Apparatus	43
3.1	Development of the Vapor Cell	44
3.1.1	Electrodes with Guard Rings	46
3.1.2	Leakage Current Suppression	51
3.2	Development of the Oven	54
3.3	Eddy Current Suppression	57
3.4	Plunger	69
3.5	Non-Magnetic BNC Feedthrough	71
3.6	Magnetic Shield and Magnetic Coils	72
3.7	High Voltage Amplifier	76
3.7.1	Circuit Design	77
3.7.2	Performance Measurement	79
3.8	Laser Excitation and Fluorescence Detection	81
3.8.1	Laser Excitation	81
3.8.2	Beam Homogenizer	82
3.8.3	Fluorescence Collection	84
3.8.4	Fluorescence Detection	86
4	Molecular State Preparation	89
4.1	Previous Attempts using RF Excitation	89
4.1.1	RF Coherent Excitation	91
4.1.2	RF Experimental Setup	93
4.1.3	RF Transition Efficiency	97
4.2	State Population Transfer using Microwave Excitation	102
4.2.1	a(1) J=2 Rotational State	102
4.2.2	Microwave Coherent Excitation	105
4.2.3	Population Transfer Path	106
4.2.4	Experimental Setup	110

4.2.5	State Preparation by Rabi Oscillation	113
4.3	Adiabatic Following in Microwave Excitation	120
4.3.1	Adiabatic Following	121
4.3.2	Generalized Landau-Zener Model	123
4.3.3	Adiabatic Following Experiment	130
4.3.4	Double Pulsed Adiabatic Following	133
4.3.5	Technical Concern	137
4.3.6	Conclusion	138
5	Measurement of Molecular Parameters	139
5.1	Zeeman Effect Measurement	139
5.2	Stark Effect Measurement	142
5.3	Quantum Beats in Electric Field	143
5.4	Conclusion	155
6	Current Status and Future Directions	156
6.1	Current Status	156
6.2	Future Direction I: Microwave Absorption	162
6.2.1	General Description	162
6.2.2	Absorption Cross Section	162
6.2.3	Signal to Noise	169
6.3	Future Direction II: Beam EDM	172
6.3.1	Cold Beam Experiment	172
6.3.2	Candidates for Cold Molecular Beam EDM Experiment	173

List of Figures

2.1	a(1) J=1 State in the Electric Field	16
2.2	Schematic Diagram of Energy Levels of $a(1) \ ^3\Sigma_1^+$ PbO	17
2.3	Schematic of PbO EDM Experiment Setup	20
2.4	Energy Level Diagram for Quantum Beat	24
2.5	Typical Waveform of Quantum Beat Fluorescence Signals	26
3.1	Vapor Cell and its Cut View	44
3.2	Electric Field in the Cell	48
3.3	Electric Field Inhomogeneity in the Cell	49
3.4	Optimal Voltage Ratio	50
3.5	Bent Quartz Tube and Corner Bracket	53
3.6	Oven inside the Heat Shield	55
3.7	Heater Currents	58
3.8	Network Model of Eddy Current	60
3.9	Heater Current and Frequency Spectrum	61
3.10	Current Loop above a Metal Sheet	63
3.11	Plunger System	70
3.12	Non-Magnetic BNC Feedthrough	73
3.13	Magnetic Shields and Aluminum Supports	75
3.14	Schematic Diagram of High Voltage Amplifier	77
3.15	Performance Measurement of High Voltage Amplifier	80

3.16	Engineered Diffuser	83
3.17	Winston Cones and Support	84
3.18	Schematic Diagram of a Winston Cone	85
3.19	Simulation and Sample of Winston Cone	86
3.20	Simplified Model for Photodiode Transimpedance Amplifier	87
4.1	RF Excitation Scheme and Mechanism for Systematic Suppression	90
4.2	V-Shape Level Structure and Transition Probability	92
4.3	RF Coil and RF Network Scheme	94
4.4	Transmission Line Model	95
4.5	Beat Disappearance Experiment using RF transition	98
4.6	RF Excitation Experiment Result	100
4.7	RF-Excited Beat with Various Guard Ring Voltage	101
4.8	Schematic Diagram of Energy Levels of PbO	103
4.9	Molecular Polarization in Electric Field	105
4.10	Related Level Structure and Transition Probability	107
4.11	Population Transfer Path via J=2 Level	109
4.12	Microwave Experimental Setup	110
4.13	Calibration of Microwave Amplifier Gain and Insertion Loss of Experimental Apparatus	112
4.14	Transition by Vertical Polarized MW at Zero E Field	114
4.15	Interference of J=1 Beat and J=2 Beat	115
4.16	Transition by Vertical Polarized MW in External E Field	116
4.17	Transition Driven by Horizontally Polarized MW	118
4.18	Parametrization of Generalized Landau-Zener Model	124
4.19	Fourier Transform of Frequency-Modulated Sinusoid Pulse	125
4.20	Generalized Landau-Zener Model	128

4.21	Transition Probability at Different Frequency Deviation and Power using Adiabatic Following	129
4.22	Typical Result using Adiabatic Following	131
4.23	Optimization of Frequency Sweeping Rate	133
4.24	Beat Amplitude at Various Sweeping Rates.	134
4.25	Selective Preparation of EDM States using MW Adiabatic Following	136
5.1	Beat Frequency Change with RF Transition	141
5.2	Resonance Frequency Dependence on Applied Voltage	143
5.3	Beat Lifetime at Level Crossing	145
5.4	J=1 Level Crossing in Electric Field	146
5.5	a(1) J=1 Beat Amplitude in Electric Field	148
5.6	Beat Amplitude Changes as Electric Field Increases	150
5.7	a(1) J=2 Beat Amplitude in Low Electric Field	151
5.8	Calculated Quantum Beat Frequency Change in the Electric Field	152
5.9	Interference between beats at High Electric Field and High Magnetic Field	154
6.1	PbO Spectrum	158
6.2	Level Scheme for Absorption of Horizontally Polarized Microwave	163
6.3	Current Microwave Absorption Setup	166
6.4	Level Scheme for Absorption of Vertically Polarized Microwave	168
6.5	MW Absorption Setup	170
6.6	Electronic States in HfO and ThO	175

List of Tables

1.1	Calculated P,T-odd coefficients of polar diatomic paramagnetic molecules and molecular ions	9
3.1	Signal to Noise Ratio of Detectors	88
4.1	RF Field Strength at Various Frequencies	96
6.1	Expected and Actual Increase of the Signal, Contrast and Backgrounds . .	160
6.2	Frequency Resolution and eEDM Sensitivities in Beam Experiment	174

Chapter 1

Introduction

1.1 General Introduction to EDM Experiments

Although a half-century of devoted efforts have yielded only null results, there is still significant interest in developing experiments that can probe beyond the current limits for the electron electric dipole moment (EDM). Observation of a non-zero electron EDM will be explicit evidence for physics beyond the Standard Model.

1.1.1 Motivation for Searches for EDM

Symmetries are essential to modern physics. They are related to conservation laws and invariants to the dynamics of the world. A broken symmetry will be the key to revealing novel particles or interactions. A non-zero electric dipole moment of a non-degenerate quantum system directly violates both parity and time-reversal symmetries. Further, through the CPT theorem, an EDM implies a breakdown of CP symmetry. A non-degenerate system in its rest frame can be described by the internal angular momentum \mathbf{j} . The non-zero projection \mathbf{d} of an EDM along (or opposite to) \mathbf{j} is of most interest to theorists, because a parity transformation reverses the polar vector \mathbf{d} yet leaves unchanged the axial vector \mathbf{j} , yielding the parity symmetry violation; under time reversal transformation, \mathbf{d} stays intact, and \mathbf{j} changes sign, so that time reversal is also broken.

Through the investigation of CP violation, the Standard Model can be tested by two types of experiments. One is based on the precise measurement of the decay modes of particles containing s, c, b, or t quarks, such as K meson decay [1], and B meson decays at BaBar [2] and Belle [3]. Such CP-violation can be incorporated into the Standard Model as a single complex phase in the quark mixing matrix (CKM matrix); all such observations are consistent with the Standard Model predictions. The other category is based on the precision measurement of matter without flavor changing processes. In particular, CP-violating electric dipole moments of elementary particles have an extraordinary sensitivity to CP-violation models. The single complex phase in the Standard Model can only generate highly suppressed CP-violating phenomena without flavor change. The EDM appears uncanceled only in high-order loop corrections [4] (3-loop diagrams for the neutron and 4-loop diagrams for the electron). The Standard Model prediction for the neutron EDM is $d_n^{(SM)} \approx 10^{-34}$ e · cm and the electron EDM is even smaller, $d_e^{(SM)} \approx 10^{-38}$ e · cm. The prediction of EDMs by the Standard Model is, although non-zero, far too small to be observed by any contemporary technique or in the conceivable future. However, other sources of CP violation, which can contribute much larger effects than the Standard Model's prediction, are called upon to explain the significant abundance of matter over anti-matter in the universe [5].

The search for the EDM of elementary particles is motivated by the fact that the observable value of the EDM will be explicit evidence for the presence of new CP-violating physics beyond the Standard Model, and hence will shed light on the future direction of fundamental physics. The Standard Model is consistent with all available data at low energy scales. Many extensions of the Standard Model introduce hypothetical new particles. Their couplings, which yield additional CP violation phases, can generate an electron EDM at lower-loop correction levels. Such models turn out to favor the prediction that the electron EDM will be within the next 3 orders of the current experimental sensitivity $|d_e| < 1.6 \times 10^{-27}$ e · cm [6]. Already the parameter space of several popular theories, including Supersymmetry (SUSY), are strongly restricted by current measurements of EDMs. SUSY

is a plausible candidate to be the key theory underlying physics beyond the Standard Model. However, the natural scale for the electron EDM given by naive SUSY turns out to be about 100 times larger than the current experimental limit on $|d_e|$. This problem motivated many theoretical attempts to suppress EDMs below their natural scale in SUSY, as well as further experimental attempts to narrow down the parameter space in SUSY. Measurement of an EDM can be the first manifestation of SUSY. If d_e is not seen in the next few orders of magnitude and if SUSY is correct, it becomes necessary to introduce fundamentally new theoretical constructions, as a means of suppressing CP violation in the mechanism of SUSY-breaking.

Any improvements in sensitivity beyond current experimental limits will have a profound impact on the understanding of fundamental physics. The search for EDMs, as a probe to CP-violating physics beyond the Standard Model, is near the top of the priority list for contemporary physics. With such strong theoretical motivations, there have been both searches and proposals for searches for EDMs in many different systems: the electron [7], the neutrino [8], the muon [9], the Λ^0 hyperon [10], the τ lepton [11], and the neutron [12, 13, 14] etc; solid state systems [15, 16]; diamagnetic atoms and molecules [17, 18]; and paramagnetic atoms, molecules and molecular ions [19]. The EDM experiments using atoms or molecules takes advantage of the sophisticated methods of atomic, molecular, and optical physics. Measurements of EDMs in diamagnetic atoms or molecules are most sensitive to P,T-odd mechanisms in the hadronic sector, and measurements of EDM in paramagnetic systems are most sensitive to leptonic sources of P,T-violation, in particular the electron EDM. Our experiment using PbO^* [20] belongs to the latter category and the following discussion will concentrate mostly on electron EDM.

1.2 Electron EDM Experiments with Atoms or Molecules

With the presence of a non-zero electron EDM, the Hamiltonian of the system is

$$\mathcal{H} = -(\mu\vec{\mathcal{B}} + d_e\vec{\mathcal{E}}) \cdot \frac{\vec{J}}{|\mathcal{J}|}, \quad (1.1)$$

where \mathcal{B} and \mathcal{E} are magnetic and electric field, μ is the magnetic moment, d_e is the electron EDM, and J is the angular momentum of the system. Initially the system is spin polarized perpendicular to the electric field. The system will precess due to the torque on d_e in the presence of the electric field \mathcal{E} . The static magnetic field \mathcal{B} is applied to increase the precession frequency prominently enough to be detectable in the laboratory. By alternating the relative direction of the electric field $\vec{\mathcal{E}}$, indicated by the direction of the arrows in Eq. 1.2, respective to the direction of the magnetic field $\vec{\mathcal{B}}$, a non-zero EDM would either increase or decrease the precession frequency.

$$\begin{aligned} \mathcal{B} \uparrow, \mathcal{E} \uparrow: \omega_{\uparrow\uparrow} &= \mu\mathcal{B} + d\mathcal{E}; \\ \mathcal{B} \uparrow, \mathcal{E} \downarrow: \omega_{\uparrow\downarrow} &= \mu\mathcal{B} - d\mathcal{E}; \\ \omega_{\uparrow\uparrow} - \omega_{\uparrow\downarrow} &= 2d\mathcal{E}. \end{aligned} \quad (1.2)$$

The change in precession frequency $2d\mathcal{E}/\hbar$ due to \mathcal{E} reversal with respect to \mathcal{B} is the typical experimental observable. The measurement of this additional linear Stark shift $2d_e\mathcal{E}$ arising from the non-zero electron EDM lies at the heart of all electron EDM experiments.

The best limits on the electron electric dipole moment are derived from measurements using atoms and molecules [19]. There are also several other means to search for electron EDM d_e . One feasible way is to utilize the techniques of electron g-2 experiment [7] to observe the precession angular velocity modified by the presence of EDM. Another way to search for d_e is to apply a large electric field to a suitable paramagnetic solid. In principle, the interaction of the EDM of the unpaired electrons with the electric field at sufficiently low temperature can yield a net magnetization of the sample, which can be detected by a

superconducting quantum interference device (SQUID) magnetometer [15]. Alternatively, application of an external magnetic field to a suitable ferromagnetic solid can yield an EDM-induced electric polarization of the sample, which is detectable in principle by ultra-sensitive charge measurement techniques [16]. Another approach has been proposed, in which a sufficiently large external electric field applied to a gaseous sample of diamagnetic diatomic molecules can generate an observable P,T-odd magnetization [21].

1.2.1 Atomic EDM Experiments

A permanent atomic EDM arises from the intrinsic EDMs of unpaired valence electrons, neutrons, and protons. However, Schiff's theorem [22] states that an atom or molecule cannot exhibit a linear Stark effect to first order in the EDM of any constituent particle, in the limit of non-relativistic quantum mechanics. Since a neutral atom is not accelerated in an external electric field, the average force on each charged particle in the atom must be zero, such that, in the non-relativistic limit only including electrostatic force, the average electric field at each charged particle must vanish. It follows that the externally applied static electric field must be canceled, on average, by the internal polarizing field.

Sanders first pointed out that Schiff's theorem fails when relativistic effects are taken into account [23]. To show this, the relativistic electron EDM Hamiltonian is applied,

$$\mathcal{H}_{\text{EDM}} = -d_e(\gamma^0 \vec{\Sigma} \cdot \vec{\mathcal{E}} + i\vec{\gamma} \cdot \vec{\mathcal{B}}).$$

where $\Sigma = \begin{pmatrix} \sigma & 0 \\ 0 & \sigma \end{pmatrix}$, and γ^0 and γ are the usual 4×4 Dirac matrices.
In the $\mathcal{B} = 0$ case,

$$\mathcal{H}_{\text{EDM}} = -d\gamma^0 \Sigma \cdot \mathcal{E} = -d\Sigma \cdot \mathcal{E} - d(\gamma^0 - 1)\Sigma \cdot \mathcal{E}, \quad (1.3)$$

In the non-relativistic limit, only the first term survives. Yet to first order, this term contributes nothing to the energy shift, as stated in Schiff's theorem. However, the second

term gives rise to the linear Stark effect associated with the EDM as the relativistic effect. Detailed deduction leading to this effect is omitted here (Readers refer to Ref [24]). The breakdown of Schiff's theorem here is due to the Lorentz contraction of the EDM. The linear Stark effect due to an EDM can exist even when the expectation value of the total electric field is actually zero, $\langle \vec{\mathcal{E}} \rangle = 0$. This statement is rather counter-intuitive, and contradicts to the widespread intuitive explanation for the failure of Schiff's theorem which assumed that the presence of relativistic effects upset the condition $\langle \vec{\mathcal{E}} \rangle = 0$.

The effects of P,T-violation increase in atoms with:

(i) close levels of opposite parity. The odd parity of \mathcal{E} in the EDM Hamiltonian \mathcal{H}_{EDM} (see Eq. 1.1) requires the mixing of states with different parities. The atomic wave function of an valence electron $|\psi\rangle$ in the presence of an external electric field \mathcal{E}_{ext} to the first-order is given as:

$$|\psi\rangle = |\psi_0\rangle + \sum \frac{|\psi_n\rangle \langle \psi_n | e\vec{\mathcal{E}}_{\text{ext}} \cdot \vec{r} | \psi_0 \rangle}{E_0 - E_n},$$

where $E_0 - E_n$ is the energy difference between close levels of opposite parity, and $|\psi_0\rangle$, $\{|\psi_n\rangle\}$ are unperturbed atomic wave functions. The smallness of this energy difference will increase the portion of opposite parity mixing, thus enhancing the atomic dipole moment greatly.

(ii) a high nuclear charge Z . The enhancement factor of the effective electric field \mathcal{E}_{eff} experienced by d_e over \mathcal{E}_{ext} is usually defined as $R = \mathcal{E}_{\text{eff}}/\mathcal{E}_{\text{ext}} = d_a/d_e$, where d_a is the atomic dipole moment. The linear Stark energy shift ΔE due to the EDM d_e can be written as $\Delta E = d_e \cdot \mathcal{E}_{\text{eff}}$. The size of the enhancement factor R is determined by the relativistic effects, the details of atomic structure, and the corresponding degree of polarization P of the atom by the external field. R is proportional to the matrix element $\langle \psi | \mathcal{H}_{\text{EDM}} | \psi \rangle$, which receives a dominant contribution from $(\gamma^0 - 1)$ of order $Z^2\alpha^2$ around the region very close to the nucleus where $\mathcal{E} \sim Ze/r^2$. Hence, R grows rapidly with Z as $R \propto Z^3$ approximately. For thallium ($Z=81$), $R=-585$ [25], and \mathcal{E}_{eff} is significantly enhanced over \mathcal{E}_{ext} .

The linear Stark shift is measured by observing the change in frequency when the

electric field is reversed with respect to the magnetic field. To date, measurement of permanent EDMs in neutrons, atoms, and molecules only provide null results. The most precise measurement of an atomic EDM in a paramagnetic system has been obtained for ^{205}Tl , giving the current limit on d_e [6].

1.2.2 EDM Enhancement in Diatomic Molecules

Paramagnetic polar diatomic molecules are attractive for use in the search for an electron EDM. The strategy is to polarize the molecules along an external electric field, thereby aligning the enormous intra-molecular field, leading to an effective enhancement of the external field by several orders of magnitude compared to the case using atoms. This enhancement is due to the presence of close spin-rotational levels of opposite parity.

As shown in previous section, the EDM sensitivity in the atoms is enhanced by close levels of opposite parity and a high nuclear charge Z . Polar diatomic molecules containing a heavy nucleus are chosen in EDM experiments, such as YbF in the ground $^2\Sigma_{1/2}$ state [26], or PbO in the metastable $a(1) \ ^3\Sigma_1$ state [20]. The approximate relation for the enhancement factor $R \propto Z^3$ also applies for the polar diatomic paramagnetic molecules with unpaired valence electrons (see Section 1.2.1). However, nearly complete polarization $P \approx 1$ for the polar diatomic molecules can be achieved with only a modest applied electric field. Hence, the intrinsic sensitivity of heavy polar molecules to an eEDM can be 100~1000 times greater than for atoms.

In a polar diatomic molecule, adjacent spin-rotational states, usually separated by some small Ω -doublet splittings, or at most by energies at the order of the rotational constant B_r , are ideal candidates for the close levels of opposite parity. In the rest frame of the diatomic molecule, the molecule possesses the axial symmetry and the electron state can be characterized by the projection Ω of electrons' total angular momentum \mathbf{j} on the molecular axis $\hat{\mathbf{n}}$ (if the spin-orbit interaction is quite large). If ignoring the rotation of molecule, the molecular energy does not change upon reflection of the molecular wavefunction in a plane passing through the internuclear axis $\hat{\mathbf{n}}$, while the sign of $\Omega = \mathbf{j} \cdot \hat{\mathbf{n}}$ reverses. This indicates

that the states $|\Omega\rangle$ and $|\Omega\rangle$ are degenerate, and states of definite parity constructed as linear combinations of $|\Omega\rangle$ and $|\Omega\rangle$ are naturally degenerate also. However, the interaction of the electrons with the rotation of the molecule can lift the degeneracy of the opposite parity levels. The rotational energy of the nuclei is

$$H_{rot} = BN^2, \quad \mathbf{N} = \mathbf{J} - \mathbf{j},$$

where \mathbf{N} , \mathbf{J} , and \mathbf{j} are the molecular rotational angular momentum, total angular momentum, and electron spin, respectively. The effective spin-rotational interaction is

$$V_{spin-rot} = -2BJ \cdot \mathbf{j}.$$

This gives rise to the Ω -doublet splitting of levels of opposite parity for the same $|\Omega|$ at the magnitude $\Delta E \sim BJ \sim \frac{m}{M}JR_y$ (m and M are the mass of the electron and the molecule respectively), which is typically $10^3 \sim 10^4$ times smaller than the normal atomic energy interval $E \sim R_y$, where R_y is Rydberg constant. Hence, relatively modest external fields ($\approx 10^2 \sim 10^4$ V/cm) can cause nearly complete polarization of $\hat{\mathbf{n}}$ along $\vec{\mathcal{E}}_{ext}$. The application of the external electric field is necessary, because otherwise, the internuclear axis $\hat{\mathbf{n}}$ will just precess about the molecular angular momentum \mathbf{J} , leaving the internal electric field $\vec{\mathcal{E}}_{int}$ oriented randomly in space, causing no net molecular EDM.

The contribution of d_e is included by adding the following effective EDM Hamiltonian H' to $V_{spin-rot}$:

$$H' = W_d d_e \mathbf{j} \cdot \hat{\mathbf{n}}.$$

Here, $W_d = \frac{1}{d_e \Omega} \langle \Psi | H_{EDM} | \Psi \rangle$ where Ψ is the relativistic molecular electronic wave function and $H_{EDM} = 2d_e \begin{pmatrix} 0 & 0 \\ 0 & \vec{\sigma} \cdot \vec{\mathcal{E}}_{int} \end{pmatrix}$ ($\gamma^0 - 1$ term in Eq. 1.3). The effective molecular field is defined as $\mathcal{E}_{eff} = W_d \Omega$. Certain paramagnetic polar diatomic molecules, listed in Table 1.1, have been identified as attractive candidates for experimental electron EDM searches.

Molecule	Electronic state	W_d $10^{24} \text{ Hz e}^{-1} \text{ cm}^{-1}$	\mathcal{E}_{eff} GV/cm
BaF [27]	$X^2\Sigma_{1/2}^+$	-3.6	7.5
YbF [28, 29]	$X^2\Sigma_{1/2}^+$	-12.1	26
HgF [30]	$X^2\Sigma_{1/2}^+$	-48	99
PbF [30]	$X^2\Pi_{1/2}^+$	14	-29
PbO [31]	$a(1)^3\Sigma_1^+$	$-6.1^{+1.8}_{-6}$	26
	$B(1)^3\Pi_1$	$-(8.0 \pm 1.6)$	34
HI ⁺ [32]	$X^2\Pi_{3/2}$.22	-1.3
PtH ⁺ [33]	$X^3\Delta_3$		73
HfH ⁺ [33]	$(X?)^3\Delta_1$		-17
HfF ⁺ [33]	$(X?)^3\Delta_1$		-18

Table 1.1: Calculated P,T-odd coefficients of polar diatomic paramagnetic molecules and molecular ions [19]

Our proposal takes advantage of the unique properties of PbO, which we argued should make it possible to work in the high-density environment of a closed vapor cell. This in turn will allow high counting rates and signal-to-noise (S/N), along with reasonable spin coherence times.

Chapter 2

Probing the Electron EDM using PbO

In this chapter, I will describe the principles of the EDM experiment carried out at Yale. We populate and detect fluorescence from the metastable excited state $a(1) [^3\Sigma^+]$ of ^{208}PbO to search for an electron EDM. The principal properties of the $a(1)$ state will be described in Section 2.1. The experimental method and setup will be described in Section 2.2 and 2.3. Quantum beat spectroscopy used to extract minute frequency change and the associated data analysis methods will be discussed in Section 2.4. Statistical sensitivity and systematic errors of the PbO experiment will be discussed in Section 2.5 and 2.6.

2.1 Principal Properties of the PbO $a(1)$ State

Lead monoxide, PbO, is thermodynamically stable, and it is easy to obtain an isotopically pure sample in fair amounts for research purposes at relatively low cost. The metastable excited electronic state $a(1) [^3\Sigma_1^+]$ has the electron configuration $\sigma_1^2\sigma_2^2\pi_1^3\pi_2$ [34, 35] with σ_1 and π_1 centered on O, and σ_2 predominantly of the Pb 6s-type. Spin-orbit interaction mixes the nominal configuration $\sigma_1^2\sigma_2^2\pi_1^3\pi_2$ with configurations $\sigma_1^2\sigma_2\pi_1^3\pi_2^2$ and $\sigma_1^2\sigma_2\pi_1^4\pi_2$, which contain an unpaired σ orbital. The unpaired electron in the molecular orbital of

σ symmetry has no orbital angular momentum about the molecular axis. Thus it can penetrate close to the nucleus of heavy atom Pb, yielding a significant EDM enhancement factor [35]. This makes PbO a great candidate for eEDM experiment. The $a(1) v' = 5$ state can be accessed via laser excitation with laser wavelength 570 nm from the ground electronic state $X(0) [^1\Sigma_0^+]$ $v = 1$ vibrational level, or 548 nm from $v'' = 0$ level, without resort to high temperature chemistry. This wavelength range is within the range of a tunable dye laser using rhodamine 6G (Rh6G). The $a(1)$ state has a relatively long natural lifetime $\tau[a(1)] = 82(2) \mu\text{s}$ [20]. Thus PbO can be used in a vapor cell at quite a high density, generating very large signals. Another appealing characteristic of $a(1) ^3\Sigma_1^+$ state is the existence of a very small parity-doublet splitting due to spin-rotation coupling, as mentioned in the previous chapter. The PbO molecules can be completely polarized with small external fields (> 15 V/cm). Even this small polarizing field yields the effective internal electric field $\mathcal{E}_{\text{eff}} > 10^7$ V/cm. All the above properties make the $a(1) ^3\Sigma_1^+$ state of PbO a very good candidate for an EDM search¹.

The $a(1)$ state can be categorized in molecular spectroscopy as Hund's case (c)[36]. The i 'th molecular electron total angular momentum \mathbf{j}_i is formed from its coupled orbital and spin angular momenta, \mathbf{l}_i and \mathbf{s}_i respectively. The \mathbf{j}_i couple together to form the total electronic angular momentum \mathbf{J}_e . In a diatomic molecule, the internuclear axis $\hat{\mathbf{n}}$ is an axis of rotational symmetry. \mathbf{J}_e precesses about $\hat{\mathbf{n}}$, forming the projection Ω on the axis $\hat{\mathbf{n}}$. A state with $J_e = 1$ can have projections Ω along or against the internuclear axis $\hat{\mathbf{n}}$: $\Omega = \mathbf{J}_e \cdot \hat{\mathbf{n}} = \pm 1$ or 0. Ω couples with the rotational angular momentum \mathbf{N} to form the total molecular angular momentum \mathbf{J} . Possible values of J are $|\Omega|$, $|\Omega| + 1$, $|\Omega| + 2$, ... In the case of the $a(1)$ state, the states of interest have $|\Omega| = 1$ [36] and $J=1$ or 2. $J=1$ states are the eEDM state and $J=2$ states are involved as intermediate states for laser-microwave double resonance to populate $J=1$ states. Two states with $\Omega = \pm 1$ and all other quantum numbers identical are degenerate in the lowest approximation due to rotational symmetry

¹The $B(1)[^3\Pi_1] (\sigma_1^2\sigma_2\pi_1^4\pi_2)$ state has also been considered as an EDM candidate, and the enhancement factor is shown in Tab. 1.1, but it has a much shorter lifetime than $a(1)$.

argument. However, Coriolis coupling of the electron spin to rotational motion breaks this degeneracy, and causes a splitting (“ Ω -doublet splitting”) into two states of opposite parity, called e and f [37], with parity $(-1)^J$ and $(-1)^{J+1}$ respectively. These are separated by the fairly small interval $\Delta_\Omega(J) = qJ(J+1)$, where $q=5.6(1)$ MHz is the field-free Ω -doublet splitting for the $a(1)$ ($v' = 5$) [38, 39].

We can denote $a(1)$ [$^3\Sigma^+$] using the semi-empirical description of molecular states in the basis $|\gamma, J, M, \Omega\rangle$, where γ denotes all the quantum numbers except for angular momenta, as $a(1)$ states are of Hund’s case (c), and γ, J, M, Ω are of complete set of good quantum numbers. The parity of $|\gamma, J, M, \Omega\rangle$ is characterized by the property $\sigma_v|\gamma, J, M, \Omega\rangle = (-1)^{J-\Omega}|\gamma, J, M, -\Omega\rangle$ [40], where σ_v is the symmetry operator reflecting through a plane passing through the internuclear axis. Without the perturbation from the external electromagnetic fields, e and f components are represented in the basis $|\gamma, J, M, \Omega\rangle$,

$$\begin{aligned} |\gamma, J, M, e, |\Omega| = 1\rangle &= (|\gamma, J, M, \Omega = 1\rangle - |\gamma, J, M, \Omega = -1\rangle)/\sqrt{2}; \\ |\gamma, J, M, f, |\Omega| = 1\rangle &= (|\gamma, J, M, \Omega = 1\rangle + |\gamma, J, M, \Omega = -1\rangle)/\sqrt{2}, \end{aligned} \quad (2.1)$$

with parity $(-1)^J$ and $(-1)^{J+1}$ respectively.

Using the Wigner-Eckart theorem, we can transform any operator’s matrix elements between the lab frame and molecule-fixed frame. Such a transformation is necessary because many useful operators are defined in the frame co-rotating with the molecule. The relevant transformations are

$$\langle \gamma, J, M, \Omega | T_q^{(k)} | \gamma', J', M', \Omega' \rangle = (-1)^{J-M} \begin{pmatrix} J & k & J' \\ -M & q & M' \end{pmatrix} \langle \gamma, J, \Omega | \mathbf{T}^{(k)} | \gamma', J', \Omega' \rangle, \quad (2.2)$$

and

$$\langle \gamma, J, \Omega | \mathbf{T}^{(k)} | \gamma', J', \Omega' \rangle = \sum_{q=-k}^{+k} (-1)^{J-\Omega} \sqrt{(2J'+1)(2J+1)} \begin{pmatrix} J & k & J' \\ -\Omega & q & \Omega' \end{pmatrix} \langle \gamma, \Omega | T_q^{(k)} | \gamma', \Omega' \rangle. \quad (2.3)$$

For example, the matrix element of electric dipole moment $\mu_{e,z}^{JM}$ to connect e and f components is defined as $\langle \gamma, J, M, e | \mu_{e,z} | \gamma, J, M, f \rangle$. Since μ_e is defined in molecule-fixed frame, we need to apply Eq. 2.1, 2.2, 2.3 to evaluate μ_e . Because μ_e is a vector operator with rank $k = 1$, only terms with $|\Delta\Omega| \leq 1$ will survive for $\langle \gamma, \Omega | \mu_e | \gamma', \Omega' \rangle$. For the a(1) state, $|\Omega| = 1$, hence only $\Omega = \Omega' = \pm 1$ contribute. Omitting the redundant yet straight-forward derivation, we can have

$$\begin{aligned}
\mu_{e,z}^{JM} &= \langle \gamma, J, M, e | \mu_{e,z} | \gamma, J, M, f \rangle \\
&= \frac{1}{2} \langle \gamma, J, M, \Omega = 1 | \mu_{e,z} | \gamma, J, M, \Omega' = 1 \rangle - \frac{1}{2} \langle \gamma, J, M, \Omega = -1 | \mu_{e,z} | \gamma, J, M, \Omega' = -1 \rangle \\
&= \frac{(-1)^{2J-M-\Omega}}{2} \begin{pmatrix} J & 1 & J \\ -M & 0 & M \end{pmatrix} \begin{pmatrix} J & 1 & J \\ -1 & 0 & 1 \end{pmatrix} \\
&\quad \times (\langle \gamma, \Omega = 1 | \mu_e | \gamma', \Omega = 1 \rangle + \langle \gamma, \Omega = -1 | \mu_e | \gamma', \Omega = -1 \rangle) \\
&= \frac{M\mu_a}{J(J+1)},
\end{aligned} \tag{2.4}$$

where $\mu_a = \langle \gamma, \Omega = 1 | \mu_e | \gamma', \Omega = 1 \rangle = \langle \gamma, \Omega = -1 | \mu_e | \gamma', \Omega = -1 \rangle = 1.64(3) \text{ MHzV}^{-1}\text{cm}$ is the molecular electric dipole moment in the a(1) state [41].

Similarly, we can calculate the matrix elements of $\vec{\mu}_e \cdot \vec{\mathcal{E}}$, as well as $\vec{\mu}_B \cdot \vec{\mathcal{B}}$, in the lab-frame basis $|\gamma, J, M, \Omega\rangle$, where μ_e and μ are electric dipole operator and magnetic dipole operator respectively. They are all of the form $\vec{U} \cdot \vec{V}$.

$$\begin{aligned}
&\langle \gamma, J, M, \Omega | \vec{U} \cdot \vec{V} | \gamma', J', M', \Omega' \rangle \\
&= \langle \gamma, J, M, \Omega | \sum_{p=-1}^{+1} (-1)^p U_p V_{-p} | \gamma', J', M', \Omega' \rangle \\
&= (-1)^{2J-M-\Omega} \sqrt{(2J+1)(2J'+1)} \times \\
&\quad \sum_{p=-1}^{+1} (-1)^p V_{-p} \begin{pmatrix} J & 1 & J' \\ -M & p & M' \end{pmatrix} \sum_{q=-1}^{+1} \begin{pmatrix} J & 1 & J' \\ -\Omega & q & \Omega' \end{pmatrix} \langle \gamma, \Omega | U_q | \gamma', \Omega' \rangle,
\end{aligned}$$

where p and q are the index of spherical vectors \vec{U} and \vec{V} .

Equipped with such a useful computational tool, we can study analytically the quantum dynamics of molecular states under the effect of external electromagnetic fields. For simplicity, here we just study the state evolution in static vertical electric field $\vec{\mathcal{E}} = \mathcal{E}\hat{z}$ and $\vec{\mathcal{B}} = \mathcal{B}\hat{z}$, and write out the Hamiltonian in the basis of $|J = 1, M, e(f)\rangle$. For now, we do not include the T,P-odd EDM term, and ignore the difference of g-factors between e and f states. Then the Hamiltonian matrix is given by

$$\mathcal{H} = \begin{pmatrix} g\mu_B\mathcal{B}/2 + \Delta_\Omega & 0 & 0 & -\mu_a\mathcal{E}/2 & 0 & 0 \\ 0 & \Delta_\Omega & 0 & 0 & 0 & 0 \\ 0 & 0 & -g\mu_B\mathcal{B}/2 + \Delta_\Omega & 0 & 0 & \mu_a\mathcal{E}/2 \\ -\mu_a\mathcal{E}/2 & 0 & 0 & g\mu_B\mathcal{B}/2 & 0 & 0 \\ 0 & 0 & 0 & 0 & 0 & 0 \\ 0 & 0 & \mu_a\mathcal{E}/2 & 0 & 0 & -g\mu_B\mathcal{B}/2 \end{pmatrix},$$

where the rows (and columns) are labeled by $\{|M = +1, e\rangle, |M = 0, e\rangle, |M = -1, e\rangle, |M = +1, f\rangle, |M = 0, f\rangle, |M = -1, f\rangle\}$, respectively.

After diagonalizing the Hamiltonian \mathcal{H} , we obtain the eigenenergies $\{E_i\}$:

$$\left\{ \frac{1}{2}(g\mu_B\mathcal{B} + \Delta_\Omega + \delta_E), \Delta_\Omega, \frac{1}{2}(-g\mu_B\mathcal{B} + \Delta_\Omega + \delta_E), \frac{1}{2}(g\mu_B\mathcal{B} + \Delta_\Omega - \delta_E), 0, \frac{1}{2}(-g\mu_B\mathcal{B} + \Delta_\Omega - \delta_E) \right\}, \quad (2.5)$$

where quadratic Stark splitting $\delta_E = \sqrt{(\mu_a \cdot \mathcal{E})^2 + \Delta_\Omega^2}$. The vertical electric field $\vec{\mathcal{E}}$ mixes the e and f parity eigenstates to a new set of eigenstates $\{|\Psi_i\rangle = |J = 1, M, \tilde{e}(\tilde{f})\rangle\}$, where the tilde is used to denote the mixed states in the presence of the external electric field in

this literature. For example,

$$\begin{aligned}
|J = 1, M = 1, \tilde{e}\rangle &= \frac{(\Delta_\Omega + \delta_E)|J = 1, M = 1, e\rangle - (\mu_a \cdot \mathcal{E})|J = 1, M = 1, f\rangle}{\sqrt{(\Delta_\Omega + \delta_E)^2 + (\mu_a \cdot \mathcal{E})^2}} \\
&\stackrel{\mu_e \cdot \mathcal{E} \gg \Delta_\Omega}{\Rightarrow} -|J = 1, M = 1, \Omega = -1\rangle; \\
|J = 1, M = -1, \tilde{e}\rangle &= \frac{(\Delta_\Omega + \delta_E)|J = 1, M = -1, e\rangle + (\mu_a \cdot \mathcal{E})|J = 1, M = -1, f\rangle}{\sqrt{(\Delta_\Omega + \delta_E)^2 + (\mu_a \cdot \mathcal{E})^2}} \\
&\stackrel{\mu_e \cdot \mathcal{E} \gg \Delta_\Omega}{\Rightarrow} |J = 1, M = -1, \Omega = 1\rangle.
\end{aligned} \tag{2.6}$$

The asymptotic convergence of the $M \neq 0$ energy eigenstates to the molecular states with definite Ω quantum number is the result of molecular polarization in the presence of external electric field. We can use the molecular polarization P , the ratio of Rabi frequency $\mu_a \mathcal{E}$ over the Stark splitting δ_E , as a measure of the Stark mixing of e and f states.

$$P = \frac{\mu_a \mathcal{E}}{\sqrt{(\mu_a \cdot \mathcal{E})^2 + \Delta_\Omega^2}}. \tag{2.7}$$

The smallness of the Ω -doublet splitting $\Delta_\Omega = 11.2$ MHz enhances the ease of polarization with respect to the external electric field. It is easy to check that only mild electric field strength is enough to fully polarize $a(1)$ [$^3\Sigma^+$] states. $|P|$ rapidly increases toward unity as \mathcal{E} approaches 100 V/cm, already reaching 0.975 at 30 V/cm, 0.99 at 50 V/cm, and 0.997 at 90 V/cm. Fig. 2.1 shows the lowest $J=1$ Ω -doublet of $a(1)$ with vibrational quantum number $v'=5$, in the external electric field.

2.2 Experimental Method

The general idea of the PbO EDM experiment is as follows. In an external electric field $\vec{\mathcal{E}}_{\text{ext}} = \mathcal{E}_{\text{ext}} \hat{z}$, opposite parity states e and f with the same values of M in the $a(1)$ [$J=1$, $v'=5$] Ω -doublet will mix together and give rise to quadratic Stark splitting, by $\delta_E = \sqrt{\Delta_\Omega^2 + (\mu_a \mathcal{E}_{\text{ext}})^2}$ (see Eq. 2.5). $|P|$ is approaching unity as \mathcal{E}_{ext} increases according to Eq. 2.7, the parity eigenstates of e and f components will fully mix. Hence, the $M \neq 0$

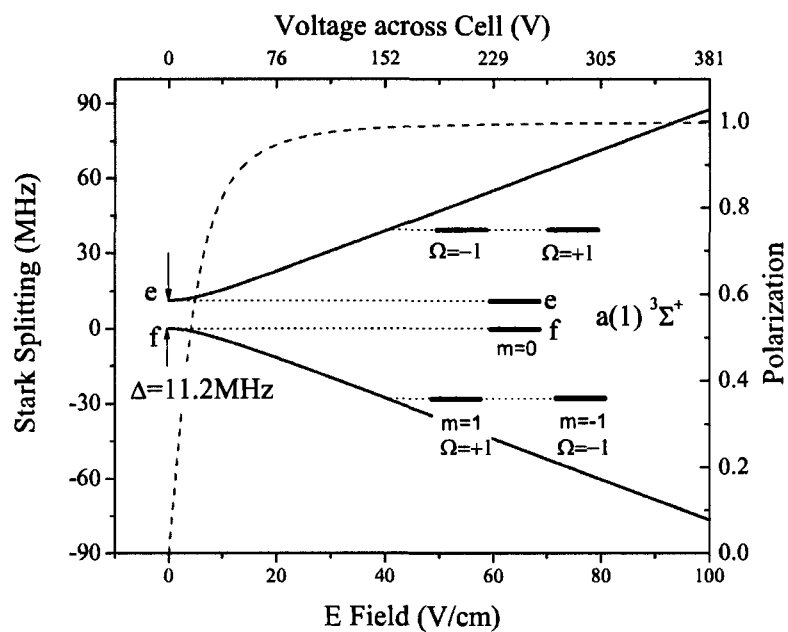


Figure 2.1: $a(1) [^3\Sigma_1^+]$ Ω -Doublet in the Electric Field. The dash line shows the polarization reaches 0.975 at 30 V/cm, 0.986 at 40 V/cm, and 0.99 at 50 V/cm. The energy level diagram shows the Stark splitting at 40 V/cm with 152 V across the electrodes with 1.5" spacing.

energy eigenstates correspond to definite Ω rather than definite parity. The energy of the molecule can be written as

$$B_r J(J+1) + W_d d_e \Omega - \mu_e \mathcal{E}_{\text{ext}} \Omega M / J(J+1), \quad (2.8)$$

where B_r is the rotational constant and $W_d = \Omega \mathcal{E}_{\text{eff}}$ is the EDM enhancement factor for the PbO a(1) state [35]. The semi-empirical estimate of Ref. [35] is $|W_d| \geq 1.2 \times 10^{25}$ Hz/(e·cm). A separate theoretical effort using a configuration interaction calculation concludes $W_d = -(6.1_{-0.6}^{+1.8}) \times 10^{24}$ Hz/(e·cm) [31], agreeing within a factor of 2. As the a(1) $^3\Sigma_1^+$ state of PbO is the excited states with two unpaired valence electrons, it is difficult to do the electronic structure calculations on such a molecular system, so the discrepancy within a factor of 2 is acceptable and further theoretical investigation will be motivated by the progress of experiment.

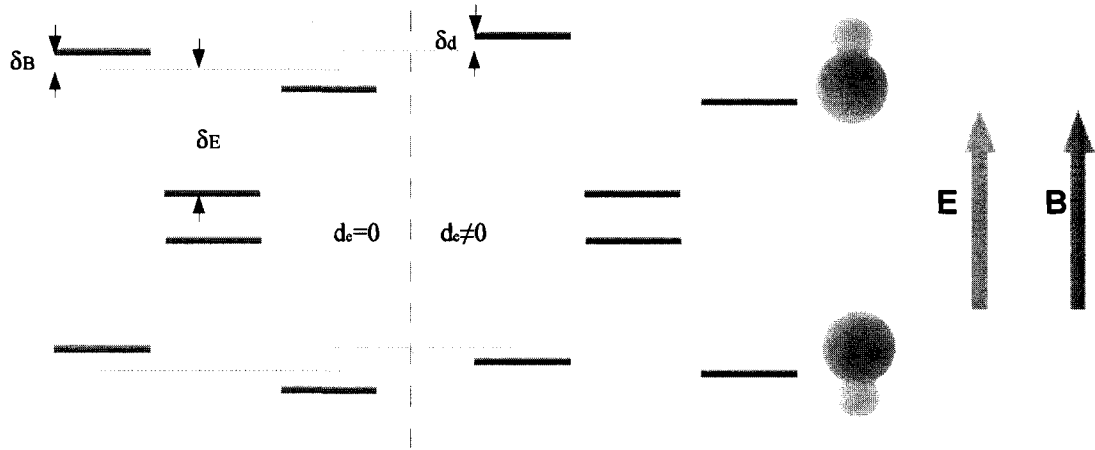


Figure 2.2: Schematic Diagram of Energy Levels of a(1) $^3\Sigma_1^+$ PbO. The shifts in $M=\pm 1$ levels of the upper and lower Ω -doublet components of the a(1)[$J=1, \nu'=5$] state of PbO in the external fields. In left panel, dotted lines: level positions in the absence of external magnetic field and assuming $d_e=0$; solid lines: Zeeman shifts in presence of $B_z \neq 0$ but $d_e = 0$ still assumed. In right panel, additional shift in solid lines, $B_z \neq 0$ and $d_e \neq 0$ assumed.

Hence, there is an additional contribution δ_d in the situation $d_e \neq 0$, $\delta_d = d_e \mathcal{E}_{\text{eff}}$ with $\mathcal{E}_{\text{eff}} = W_d \Omega$, different sign for the $\Omega = 1$ and $\Omega = -1$ components of the Ω -doublet in the

polarized state. Such a difference in sign is very significant because it provides an excellent opportunity for effective diagnostics and suppression of systematic errors. We will discuss this point further in Section 2.6.3.

To detect this shift δ_d in the EDM search, we apply a static magnetic field $\vec{B} = B\hat{z}$ which shifts the a(1) levels further by $g_p\mu_B BM/J(J+1)$, where μ_B is the Bohr magneton, and g_p is the effective g -factor of the polarized state taking into account of g -factor intrinsic difference from different Ω -doublet components $\delta g = g_e - g_f$ and perturbed difference due to the Stark mixing of $J=2$ rotational level (such effect will be discussed later in Section 2.6.1 and Section 5.2). $g_e(g_f)$ is the Landé g -factor in the molecule-fixed frame of the $e(f)$ member of the Ω -doublet and $g_p \approx 1.86$ for the a(1) state. The coherent state precesses around the external field direction \hat{z} and accumulates the relative phase between the $M=\pm 1$ components with time due to the different Zeeman δ_B and EDM shifts δ_d . The effects of applied electric and magnetic fields on the a(1) $J=1$, $v'=5$ Ω -doublet is summarized in Fig. 2.2.

The spontaneous decay from the a(1) ($v'=5$) to X(0) ($v''=0$) has a Franck-Condon factor as large as 50% and emits the fluorescence at 548nm. The Franck-Condon factor between a(1) ($v'=5$) and X(0) ($v''=1$) is also $\sim 50\%$, but due to the technical difficulty in suppressing scattered laser light and induced transient in detectors, the wavelength range of detection is chosen to differ from the excitation. The coherent interference between $M = 1$ and $M = -1$ Zeeman sub-levels yields quantum beats in fluorescence signal with beat frequency $2(g_p\mu_B B \pm d_e \mathcal{E}_{\text{eff}})/\hbar$, including the EDM contribution, where the sign is determined by the relative alignment between magnetic field and internal effective electric field. We detect this precession as Zeeman quantum beats, which modulate the exponential decay in the unpolarized fluorescence intensity at the beat frequency.

The EDM effect can be distinguished by the dependence of the beat frequency on the relative alignment of $\vec{\mathcal{E}}$ and \vec{B} and the choice of Ω -doublet pair. Since populating the different Ω -doublet components is equivalent to flipping the internal electric field with the external electromagnetic field configuration left intact, this additional degree of freedom

provides the appealing co-magnetometer mechanism to suppress systematic effects.

2.3 Experimental Setup

The PbO EDM experiment at Yale is carried out in a vapor cell containing PbO at the operating temperature 700°C, shown in Fig. 2.3. A barrier to molecule-based searches for d_e has been the production of suitable molecules and the effective detection at high counting rates. The natural lifetime of the PbO a(1) state $\tau [a(1)] = 82(2) \mu\text{s}$ [20] is too short to be useful in a beam experiment. Other candidates potentially suitable to beam experiment will be discussed later in Section 6.3. At the time of the startup of our experiment, there were no mature methods to produce cold molecule beams with high density. The vapor density of PbO in the vapor cell can be substantially high, so our experiment adopts the cell scheme to measure the electron EDM.

The vapor cell for PbO consists of an hollow alumina frame with top and bottom end caps supporting flat gold foil electrodes 6 cm in diameter, surrounding guard ring electrodes used to improve electric field homogeneity, and large flat sapphire windows on all four sides that are sealed to the frame with gold foil as a bonding agent. The electric field $\vec{\mathcal{E}}_{\text{ext}} = \mathcal{E}_{\text{ext}} \hat{z}$ is quite uniform over a cylindrical volume of diameter 5 cm and height 3.8 cm, and is chosen in the range 30~100 V/cm. The cell is enclosed in an quartz oven which sits inside opaque quartz heat shields in a vacuum chamber. One pair of Helmholtz coils carries DC current to control the vertical magnetic field B_z in the range 50~200 mG. Four sets of mutually perpendicular coils made of cosine-distributed rods, two in Helmholtz configuration, two in anti-Helmholtz configuration, generate the homogeneous magnetic fields and the gradient fields along \hat{x} and \hat{y} , respectively, providing systematic diagnostics on magnetic fields. The chamber and magnetic foils are enclosed by up to four layers of magnetic shields to screen out the spurious magnetic field.

The relevant EDM states for the experiment are the a(1) ($\nu'=5$) $^3\Sigma^+$ $J=1$, $M=\pm 1$ levels of either the upper or lower a(1) Ω -doublet. The state preparation to populate the

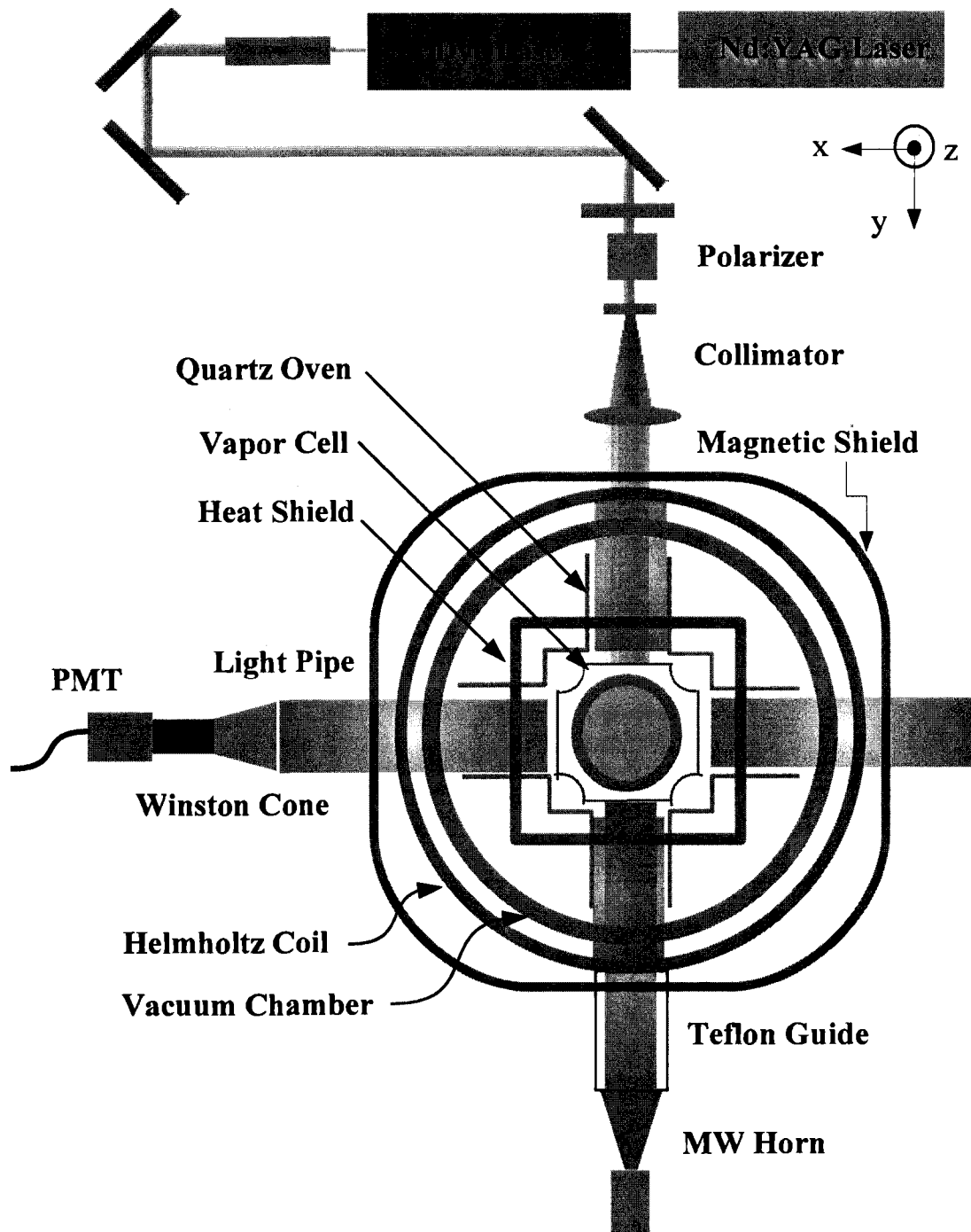


Figure 2.3: Schematic of PbO EDM Experiment Setup

coherent superposition of states of interest is via laser-microwave double resonance. We populate the $J=1$ $M=0$ state of PbO by laser excitation from the ground electronic state $X(0)$ ($v = 1$) and microwave population transfer to $J=1$, $M = \pm 1$ states is accomplished via an intermediate state (the $a(1)$ $J=2$ state).

A pulsed laser beam with vertical \hat{z} linear polarization and wavelength ~ 571 nm propagates along \hat{y} direction and excites the following transition:

$$X[J = 0^+, v = 1] \rightarrow a(1) [J = 1^-, M = 0, v' = 5].$$

The dye laser used here is pumped by the second harmonic of a Nd:YAG (yttrium aluminum garnet) laser at a repetition rate of 100 Hz and delivers 10~20 mJ/pulse of light at wavelength ~ 571 nm propagating in the \hat{y} direction to the vapor cell. The pulses are 8 ns long with a line width of ~ 1 GHz, comparable to the Doppler width of the transition. The laser light traverses the vacuum chamber and oven in a 5 cm diameter light pipe to the cell, then exits through another light pipe.

Following the laser pulse, a Raman transition is driven by two microwave beams propagating in the $-\hat{y}$ direction. The first, with \hat{z} linear polarization, excites the upward 28.2 GHz transition:

$$a(1)[J = 1^-, M = 0, v' = 5] \rightarrow a(1) [J = 2^+, M = 0, v' = 5].$$

The second, with \hat{x} linear polarization and detuned to the red or blue with respect to the first by 20~70 MHz, drives the downward transition:

$$a(1)[J = 2^+, M = 0, v' = 5] \rightarrow a(1) [J = 1, M = \pm 1, v' = 5].$$

As the result, nearly 50% of the $J=1^-$ $M=0$ molecules are transferred to a coherent superposition of $M = \pm 1$ levels in the desired Ω -doublet component. The fluorescence from the

decay:

$$a(1)[J = 1, M = \pm 1, v' = 5] \rightarrow X(0) [v'' = 0],$$

is captured by a light pipe along the \hat{x} direction and orthogonal to the laser beam. The fluorescence passes through an infrared-blocking filter and one interference filter, which blocks scattered laser light and most blackbody radiation from the ovens while passing the signal of interest to a photomultiplier tube (PMT). The quantum beat frequency is extracted from the Fourier transform and least square fitting of the data.

2.4 Quantum Beat Spectroscopy in Fluorescence

The essential part of the PbO EDM experiment is to detect minute changes $\delta\nu$ in the spin precession frequency of the PbO molecules. This change should be correlated with the relative orientation of the applied electric field $\vec{\mathcal{E}}$ with respect to the applied magnetic field $\vec{\mathcal{B}}$. In addition, the Ω -doublet structure of PbO means that $\delta\nu$ should reverse as the internal electric field changes orientation with respect to the magnetic field via Ω -doublet reversal; this can be accomplished through microwave selective excitation without changing external electric or magnetic fields. The details will be discussed in Chapter 4.

Quantum-beat spectroscopy [42, 43] provides a robust way to extract the spin precession frequency ν_b precisely and accurately, by measuring the modulated intensity due to coherent interference between fluorescent decay channels. This signal is almost immune to Doppler effects and pulse to pulse laser power fluctuations. The states in coherent interference will experience the same Doppler shift and hence cancel out the Doppler effect by beating at the frequency difference between them.

Here I will give a brief overview on the quantum beat spectroscopy with its application to the $a(1) [^3\Sigma^+]$ state of PbO, and the data analysis process to interpret the quantum beat signal.

2.4.1 Quantum Beats

After we populate the excited levels $a(1) J=1 v' = 5$ at time $t = 0$, each component of the excited state represented in the energy eigenbasis $\{|\Psi_i\rangle\}$ will evolve at the frequencies corresponding to its energy $\{E_i\}$ derived in Eq. 2.5. Hence at later times t , the wavefunction can be written as $|\Psi_e(t)\rangle = \sum_i e^{-iE_i t} |\Psi_i\rangle \langle \Psi_i | \Psi_e(0)\rangle$, where $\Psi_e(0)$ is the initial excited state. The $a(1) J=1$ state can spontaneously decay down to various sub-levels of the ground state $X(0)$, with the selection rules $\Delta J = 0, \pm 1$ and a change in parity for this E1 transition. The fluorescence intensity will be sinusoidally modulated due to interference between the Zeeman sub-levels in $a(1)$ states in each decay channel. In quantum mechanics, it is assumed that there are no coherent interferences between multiple final states [44], therefore we just sum over all possible final states with different J_f and M_f , incoherently. Then the total fluorescence intensity I satisfies

$$\begin{aligned}
 I &\propto \sum_{J_f} \sum_{M_f} \left| \sum_{M_e} \langle J_f, M_f, \Omega = 0 | \vec{r} \cdot \hat{\epsilon} | \Psi_e(t) \rangle \right|^2 \\
 &= \sum_{J_f} \sum_{M_f} \left| \sum_{M_e} \sum_i e^{-iE_i t} \langle J_f, M_f, \Omega = 0 | \vec{r} \cdot \hat{\epsilon} | \Psi_i \rangle \langle \Psi_i | \Psi_e(0) \rangle \right|^2,
 \end{aligned} \tag{2.9}$$

where $\hat{\epsilon}$ is the light polarization detected and $M_{e(f)}$ is the magnetic quantum number of the initial(final) state. Due to the breaking of the degeneracy of each level and the resulting state precession at frequencies corresponding to the energy differences, the fluorescence intensity oscillates with time. This oscillation is detectable within few MHz bandwidth as the Zeeman splitting of $J=1$ level (100 ~ 400 KHz under our nominal experimental condition).

After the arrival of the pump laser pulse, the molecules will be excited to some superposition of the M sub-levels of the $J=1$ state. For example, suppose $|\Psi_e(0)\rangle = (|M = 1, e\rangle + e^{i\phi} |M = -1, e\rangle) / \sqrt{2}$. This can be prepared by the direct excitation from the $X(0) J=0$ ground state by a horizontally polarized laser pulse tuned to the R0 line (in the absence of the external electric field). Due to the energy splitting between these sub-levels, the ex-

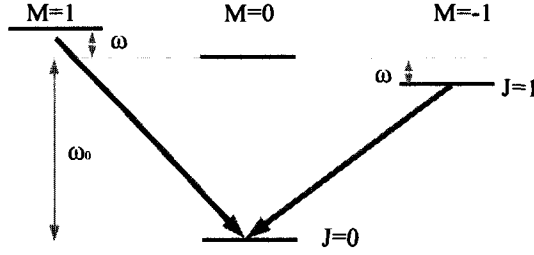


Figure 2.4: Energy Level Diagram for Quantum Beats. ω_0 is the energy splitting without Zeeman effect. In the presence of the external magnetic field, the $M = \pm 1$ sub-levels are shifted by $\pm\omega$ with respect to the $M = 0$ sub-level.

cited state evolves with time into $|\Psi_e(t)\rangle = (e^{-i\omega t}|M = 1, e\rangle + e^{i(\phi+\omega t)}|M = -1, e\rangle)/\sqrt{2}$. Assume the detector is located along the \hat{x} axis, and only $\hat{\epsilon} = \hat{y}$ polarization will be detected here. The matrix element \mathcal{M} for decay into the common level X(0) $J=0$, satisfies $\mathcal{M} = \langle J = 0, M = 0 | \vec{r} \cdot \hat{\epsilon} | J = 1, M = 1 \rangle = \langle J = 0, M = 0 | \vec{r} \cdot \hat{z} | J = 1, M = -1 \rangle$, where $\vec{r} \cdot \hat{\epsilon} = y$. Using Eq. 2.9, we find the fluorescence intensity

$$I \propto \left| \sum_{M_e} \langle J_f = 0, M_f = 0 | \vec{\mu}_e \cdot \hat{\epsilon} | \Psi_e(t) \rangle \right|^2 \propto \left| \mathcal{M} e^{-i\omega t} + \mathcal{M} e^{i(\phi+\omega t)} \right|^2 \propto |\mathcal{M}|^2 (1 + \cos(2\omega t + \phi)).$$

Here in this simple energy level structure, the intensity varies in the pattern $1 + C \cos(2\omega t + \phi)$, with contrast $C = 100\%$ as the intensity modulation factor, at the beat frequency ν_b equal to the splitting $2\omega/2\pi$ between the excited states. However, for the a(1) $J=1$ state, multiple decay channels are allowed by the E1 selection rule $\Delta J = 0, \pm 1$. By applying Eq. 2.9, the expected contrast can be estimated to be around 50% (yet with large uncertainty, due to the lack of knowledge of the branching ratio of a(1) $J=1$ state decay channels), much bigger than the observed contrast $\approx 12\%$. Recently Paul Hamilton has investigated the relationship between the amplitude of quantum beats and laser frequency detuning. The experimental results showed that the line shape of the beat amplitudes have two components: (1) central peaks at the resonance frequency with the line width around 1 GHz, as expected from the 1 GHz band width of our laser system specification; (2) much broader background extended to several GHz detuning range due to the broad stimulated emission

from the dye laser. This beat amplitude spectrum, convolved with the rotational spectrum of the PbO a(1) state, will introduce the intervention of the adjacent rotational lines (names R6, R5 and R1) to contribute the background which will diminish the contrast of quantum beats. Quantitatively the smallness of the observed contrast appears consistent with measured laser spectrum and the overlap with these rotational lines.

By extracting the minute changes $\Delta\nu_b$ in the spin precession frequency of the PbO molecules versus relative orientations of the applied electric field $\vec{\mathcal{E}}$, applied magnetic field $\vec{\mathcal{B}}$, and the internal electric field determined by $M\Omega$ (see Eq. 2.8), we can characterize the size of the EDM signal. The contrast \mathcal{C} is an important measure of the experimental sensitivity [45], since the uncertainty $\delta\nu$ in determining ν is limited by

$$\delta\nu \sim \frac{\sqrt{2}}{2\pi\mathcal{C}\tau\sqrt{N_{\text{tot}}}},$$

where τ is the lifetime of quantum beat signal and N_{tot} is the total number of counted photon events.

2.4.2 Data Analysis

In practice, we must include multiple parameters to explain the signal output from the fluorescence detector. In general, the time-dependent quantum beat fluorescence signals, $I(t)$, can be described the form (shown in Fig. 2.5):

$$I(t) = S(t)[1 + \mathcal{C}e^{-t/\tau} \cos(\omega_a t + \phi)] + B(t),$$

$$B(t) = d + P(t) + \beta L(t).$$

Here \mathcal{C} is defined as the quantum beat contrast, τ is the quantum beat lifetime, ω_a is the spin precession frequency, and ϕ is the phase of the precession. $S(t)$ describes approximately the exponential decay part in the fluorescence signal in the absence of quantum beats. $B(t)$ is the background term, consisting of $P(t)$, an electronic transient from switching off the

PMT gain during the laser pulse; $L(t)$, the residual signal associated with scattered laser light; β , a scale factor; and d , the DC offset due to blackbody radiation from the hot oven.

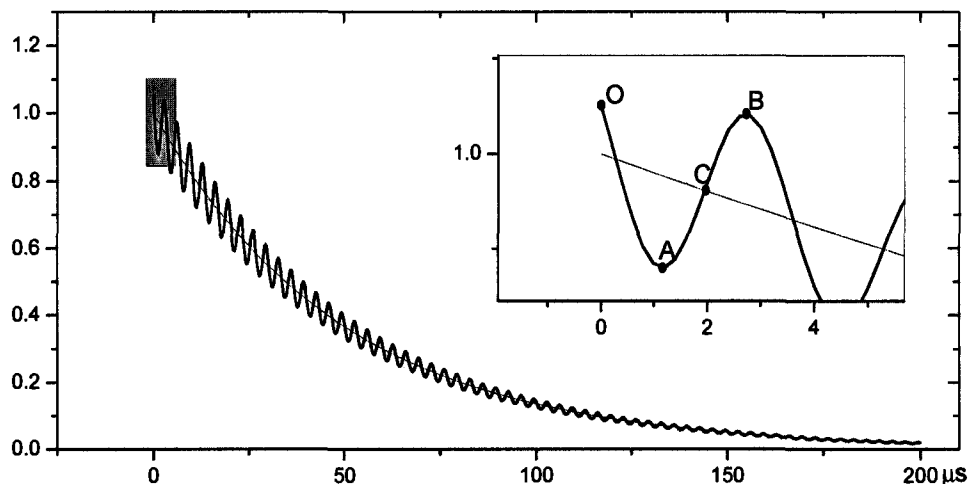


Figure 2.5: Typical waveform of quantum beat fluorescence signals. The top right panel is the zoom-in plot of a period of the data.

Scramble Fit Method

The fluorescence signal in the absence of quantum beats can be determined by applying an inhomogeneous magnetic field $dB_z/dz \sim 0.2$ G/cm, which causes rapid decoherence of the beats, yielding what we refer to as “scrambled” data,

$$I_s(t) = S(t) + B(t).$$

$I_s(t)$ is usually recorded at the end of every sequence of measurement, by switching on the gradient field and averaging data for several hundred laser pulses. The background $B(t)$ is generally stable and can be recorded off-line. The fits start $10 \sim 15 \mu\text{s}$ after the laser pulse ($t=0$) to lessen the impact of the scattered light transient, leading to $B(t) \sim d$, a constant.

The fluorescence decay envelope $S(t) \approx N_0 \exp(-t/T_1)$, where the effective state lifetime $T_1 \sim 50 \mu s$ and N_0 the initial amplitude of fluorescence decay.

Fitting is carried out in two steps. The first step is to fit $I_s(t)$ using the approximate form

$$I_s(t) \approx I_{s0}(t) = Ae^{-t/T} + B$$

to extract the background constant term B and the lifetime T . However, $S(t)$ deviates from an exact exponential form, due to wall quenching and time-dependent acceptance changes resulting from diffusion of the excited molecules. This makes it hard to describe the shape of $S(t)$ by a simple exponential decay. The constant term B affects the quality of the approximation of the exponential decay, so it's worthwhile to fit it instead of just averaging the end of the data sequence. We define the difference function $\tilde{S}(t) = I_s(t) - B$, and use the approximation $\tilde{S}(t) \approx S(t)$ for further fitting.

The second step of fitting is to fit the beat fluorescence signal

$$I(t) = \tilde{A}\tilde{S}(t)[1 + Ce^{-t/\tau} \cos(\omega_a t + \phi)] + \tilde{B}.$$

Initial guesses for the parameters \tilde{A} , ω_a , C , τ , ϕ and \tilde{B} are important for the success of the fit. $\tilde{A} \sim 1$ is the scale factor to account for the laser intensity fluctuation between data and scrambled signal. The quantum beat frequency $\nu_a = \omega_a/2\pi \approx 125 \sim 400$ kHz, corresponding to the magnetic field $B \approx 50 \sim 160$ mG, can be estimated with reasonable accuracy from the power spectrum of the data using the Fast Fourier Transform (FFT). The beat contrast $C \approx 0.1$ can be estimated using the extrema in the first period $T_a = 2\pi/\omega_a$, shown in Fig. 2.5: $C = (I_A - I_B)/I_C$, where the point **A** is the maximum, **B** minimum, and **C** the mid-point of **A** and **B**. The beat phase ϕ can be estimated from the interval between point **O** and point **C**, and the period T_a . Finally the beat lifetime $\tau \sim 100 \mu s$, in addition to the state lifetime T , accounts for shortening of the beat coherence time by collisions and broadening.

The Levenberg-Marquardt method [46] is used for the multiple-parameter fitting. It combines the steepest descent method with Newton's method in the determination of the minimum of χ^2 :

$$\chi^2 = \sum_{i=0}^n \left(\frac{I_i - I(t_i)}{\sigma(I_i)} \right)^2,$$

where $\{I_i\}$ are the time-resolved measurement of fluorescence at the sampling time $\{t_i\}$, and $\sigma(I_i)$ is the uncertainty, or noise, associated with I_i at t_i . In the shot noise limit, we can write $\sigma(I_i) = \alpha\sqrt{|I_i|}$, where α is a proportionality factor. α is estimated from the standard deviation of the data in last several tens of microseconds, typically from 170 μs to 200 μs , where the quantum beat pattern has died out since the lifetime is only $\sim 50 \mu\text{s}$ and the tail of data series is approximately equal to the background B . B is mainly from the blackbody radiation and its statistical uncertainty is characterized by the shot noise. Hence, $\alpha \approx \sigma(B)/\sqrt{|B|}$. In the case where the noise on the background is dominant, the noise $\sigma(I) \approx \sigma(B)$ is independent of time and the statistical uncertainty on the frequency determination is

$$\delta\omega = \frac{4\sigma(B)}{S_0 C \tau^{3/2} \sqrt{2B_d}} \propto \frac{1}{S_0 C \tau^{3/2}}, \quad (2.10)$$

where $S_0 \equiv I_0 - B$ is the initial signal size and B_d is the bandwidth of our detection system; $B_d = \frac{1}{\Delta t}$ with the sampling interval Δt ; and $\sigma(B)/\sqrt{B_d}$ is a constant independent of Δt , which is determined by the experiment setup and the detection scheme. This formula can be derived from the error matrix associated with the χ^2 [45].

Although this fitting method using the direct measurement of scrambled signals gives rather satisfying results, the procedure requires a separate step to record the scrambled and background signals. This method relies greatly on the stability of the experimental configuration, such as ambient magnetic field, oven temperature, and laser intensity, etc, to reach a consistent cancellation of the backgrounds. This procedure was used with no magnetic shields in place previously. However, the application of the magnetic gradient field will change the magnetization of the magnetic shields and perturb the nominal magnetic field distribution as well. The degaussing process required to correct the residual magnetization

would severely limit the duty cycle of the data collection. So after the development of a new data fitting method discussed in the next section, this procedure is obsolete.

Improved “Scrambled” Data Generation Method

An improved method is to use a forward and backward difference operation on the fluorescence data to get a self-contained “scrambled” signal [47, 48], instead of taking extra time to record scrambled data. This technique was generalized to arbitrary order corrections and adapted to our experiment by Paul Hamilton. One quarter of the data is shifted forward in time by half a precession cycle, another quarter of the data is shifted backward in time by half a precession cycle, and the one-half of the data remains untouched. The sum gives the scrambled data:

$$I'_s(t) = [2I(t) + I(t - T_a/2) + I(t + T_a/2)] / 4.$$

Here the period of a precession cycle is $T_a = 2\pi/\omega_a$. This self-contained “scrambled” signal can be used in place of the directly-measured scrambled signal, to feed into the fitting procedure described above.

To get a better understanding of this method, let’s take a look at the scrambled data first. The deviation of the signal decay pattern $S(t)$ from a simple exponential function can be explained by a geometric factor $G(t)$, which takes into account various source of geometry-dependent factors: the finite acceptance angle of the light pipe, the angle-dependent transmission of the interference filter, the wall-collision de-excitation of the excited state, and solid angle change due to the molecules diffusion in the vapor cell. Here $S(t) = G(t) \exp(-t/T)$. We can model molecules initially randomly distributed inside the vapor cell and diffusing with a Maxwell velocity distribution using Monte-Carlo simulation. If the trajectory of the molecule intersects the cell walls, it is assumed that the molecule is de-excited. Otherwise, the excited molecules will decay with the natural lifetime of the $a(1) [^3\Sigma^+]$ state. We can determine the total number of the excited molecules at any

given time by counting any surviving molecules. This Monte-Carlo result yields reasonable agreement with experimental data for the observed decay pattern. In particular, it explains clearly why the signal appears to decay with a apparent lifetime of $40 \sim 50 \mu s$ although the natural lifetime of the $a(1) [^3\Sigma^+]$ state is known to be $T \approx 80 \mu s$. Further light tracing algorithm can be applied to include the other geometric factors. Emitted rays from molecular spontaneous emission are traced to determine if they intersect the light-pipe aperture. If they do, the ray will be collected by the detector, with their intensity modified by a factor proportional to the transmission of the interference filters at the angle of incidence. In general, we can phenomenologically approximate the scramble data by $I_s(t) = [D + A \exp(-t/T)] \exp(-t/T_g)$, where $D \ll A$. For demonstration purposes, I will further simplify the analysis by using $S(t) = A \exp(-t/T_e)$, with the effective lifetime $T_e = 1/(1/T_g + 1/T)$. This leads to

$$I(t) = Ae^{-t/T_e} [1 + Ce^{-t/\tau} \cos(\omega_a t + \phi)] + B. \quad (2.11)$$

Define

$$I_{\pm}(t) \equiv I(t \pm T_a/2) = Ae^{-t/T_e} e^{\mp T_a/2T_e} [1 - Ce^{-t/\tau} e^{\mp T_a/2\tau} \cos(\omega_a t + \phi)] + B,$$

where $T_a = 2\pi/\omega_a$.

Expanding $e^{\pm T_a/2T_e}$ and $e^{\pm T_a/2\tau}$ with the condition $T_a \ll T_e$ and $T_a \ll \tau$, we find

$$I_{\pm}(t) = Ae^{-t/T_e} \left(1 \mp \frac{T_a}{2T_e} + \frac{1}{2} \left(\frac{T_a}{2T_e} \right)^2 \mp \dots \right) \times \left[1 - Ce^{-t/\tau} \left(1 \mp \frac{T_a}{2\tau} + \frac{1}{2} \left(\frac{T_a}{2\tau} \right)^2 \mp \dots \right) \cos(\omega_a t + \phi) \right] + B, \quad (2.12)$$

and so,

$$\begin{aligned}
I'_s(t) &\approx Ae^{-t/T_e} \left(1 + \frac{T_a^2}{16T_e^2} \right) - ACe^{-t/T_e} e^{-t/\tau} \cos(\omega_a t + \phi) \frac{T_a^2(\tau + T_e)^2}{16\tau^2 T_e^2} + B \\
&\approx Ae^{-t/T_e} + B.
\end{aligned} \tag{2.13}$$

Compared with Eq. 2.11, the oscillating term $\cos(\omega_a t + \phi)$ is suppressed by the factor $T_a^2(\tau + T_e)^2/(16\tau^2 T_e^2) \sim 10^{-3}$ in amplitude. Such a suppression is also applied to the higher harmonic term $\cos(N\omega_a t + \phi)$ at frequency $N\omega_a$, $N = 1, 2, \dots$. This leads to a good approximation of the scrambled signal in the absence of quantum beats. In practice, this method gives a satisfying result in data analysis and has been implemented in LabviewTM by Paul Hamilton to fit the data on the fly.

Due to the discrete sampling of the signals, the incomplete cancellation of oscillation might arise from the error δt originating from rounding $T_a/2\Delta t$ to the closest integer number, where Δt is the sampling interval in time and $\delta t \sim \Delta t/2$. From Eq. 2.12, the error will lead to additional terms

$$\begin{aligned}
&Ae^{-t/T_e} \frac{\delta t (\delta t T_a^2 + 8T_e^2 T_a + 8T_e^2 \delta t)}{32T_e^4} - ACe^{-t/T_e} e^{-t/\tau} \frac{\pi \delta t (T_e + \tau)}{2T_e \tau} \sin(\omega_a t + \phi) \\
&+ ACe^{-t/T_e} e^{-t/\tau} \frac{\delta t^2 [8\pi^2 T_e^2 \tau^2 + (\pi^2 - 2) T_a^2 (T_e + \tau)^2]}{8T_a^2 T_e^2 \tau^2} \cos(\omega_a t + \phi).
\end{aligned}$$

Our data collecting system has the maximum sampling rate of 5 MHz, or $\Delta t = 0.2 \mu\text{s}$, with an effective lifetime $T_e \sim 50 \mu\text{s}$ and $\tau \sim 100 \mu\text{s}$. These error terms, especially the term with $\cos(\omega_a t + \phi)$, are pronounced. The suppression on the oscillating term will be only the factor of about 10^{-2} in amplitude, if $\delta t \sim \Delta t/2$ is assumed. However, we are free to choose a beat precession period that is a multiple of the sampling period, if needed, to make δt as small as possible. In practice, the self-contained “scrambled” signal gives rather satisfying results.

Ratio Fit Method

Another fitting method under investigation is the Ratio Fit Method, as an extension of the improved scramble fit method. The basic idea of Ratio Fit method is to divide out the exponential decay in the time spectrum. We define the ratio as

$$R(t) = \frac{[2I(t) - I(t - T_a/2) - I(t + T_a/2)] / 4}{[2I(t) + I(t - T_a/2) + I(t + T_a/2)] / 4}.$$

The denominator is just the scrambled data we discussed before. Following the derivation in the previous section, The numerator can be approximated by

$$-\frac{Ae^{-\frac{t}{T_e}} T_a^2}{16T_e^2} + ACe^{-t/T_e} e^{-t/\tau} \cos(\omega_a t + \phi) \left[1 + \frac{T_a^2 (T_e + \tau)^2}{16T_e^2 \tau^2} \right]$$

The ratio function can be written as

$$\begin{aligned} R(t) &\approx -\frac{AT_a^2}{16(A + Be^{t/T_e})T_e^2} + \frac{Ce^{-\frac{t}{\tau}} \cos(\phi + t\omega_a)}{1 + e^{t/T_e} B/A} \left\{ 1 + \frac{T_a^2}{16T_e^2} \left[\frac{(T_e + \tau)^2}{\tau^2} - \frac{A}{A + Be^{t/T_e}} \right] \right. \\ &\quad \left. + \frac{ACe^{-\frac{t}{\tau}} (T_e + \tau)^2 \cos(\phi + t\omega_a) T_a^2}{16(A + Be^{t/T_e}) T_e^2 \tau^2} \right\} \\ &\approx \frac{Ce^{-t/\tau} \cos(\omega_a t + \phi)}{1 + e^{t/T_e} B/A}. \end{aligned}$$

If the blackbody background is low enough or a background subtraction is applied, so that $B \ll A$, the further approximation can be made:

$$R(t) \approx Ce^{-t/\tau} \cos(\omega_a t + \phi).$$

In this form, only four parameters C , τ , ω_a and ϕ need to be fitted.

The advantages in using the ratio fit method to extract ω_a lies in the reduction of the number of fit parameters, from six to four, and the decreased sensitivity to the fluctuation of the experimental parameters such as the laser intensity, the oven temperature, the blackbody radiation, and the geometric effect. Therefore, some background terms, such

as the scale factor A and the blackbody background B , may be neglected when fitting the data. Such a fitting method is used in Muon $g-2$ experiments [47, 48] and is under investigation for the applicability to our experiment.

2.5 Statistical Sensitivity of EDM Experiment

In quantum optics, the evolution of two distinct states can be represented by time-dependent Bloch vector, exactly analogous to a spin-1/2 possessing in the magnetic field. Here I will adopt such a description in a discussion of statistical sensitivity of EDM experiment. The spin precesses at the frequency f in the external magnetic field along axis \hat{y} for time T , the unit observation time. The uncertainty in determining the precession frequency f in a single measurement is $\delta f = \frac{1}{2\pi T}$. The uncertainty in f will be reduced by the factor of \sqrt{N} by repeating such measurement N times, such that,

$$\delta f = \frac{1}{2\pi T\sqrt{N}}.$$

For an EDM d_e in the electric field $\vec{\mathcal{E}}_{\text{eff}}$, the associated frequency shift is $\Delta E/2\pi\hbar$, with $\Delta E = d_e \cdot \mathcal{E}_{\text{eff}}$. For shot-noise limited detection of a signal with coherence time τ , counting rate dN/dt and unit observation time T , the energy resolution can be parameterized as following:

$$\delta(\Delta E) = \frac{\hbar}{\tau\sqrt{T \cdot dN/dt}}.$$

In PbO EDM experiment, the useful signal is the amplitude modulation of the fluorescence. The beat frequency uncertainty is determined by the quantum beat contrast \mathcal{C} , the effective lifetime τ , the counting rate dN/dt , and the integration time T [45],

$$\delta\nu \sim \frac{1}{\pi\sqrt{2}\mathcal{C}\tau\sqrt{T \cdot dN/dt}}. \quad (2.14)$$

The counting rate dN/dt can be estimated from the number of the available molecules

\mathcal{N} in the useful rovibrational level for the laser excitation to start with, the excitation efficiency ϵ_e , detection efficiency ϵ_d , decay branching to $X(0) v'' = 0$ level f_{FC} , and the laser repetition rate r ,

$$dN/dt \sim \mathcal{N}r\epsilon_e\epsilon_d f_{\text{FC}}.$$

Our experiment aims at achieving improvements on the excitation efficiency, detection efficiency, and the beat contrast to increase the sensitivity to the electron EDM. This thesis is devoted to discuss the current progress of this experiment. The experimental setup and preliminary experiment result will be described in Chapter 3, 4 and 5 in this thesis. The status of this experiment with improvements on the excitation efficiency and detection efficiency will be described in Chapter 6. Readers please refer to Section 6.1 for the estimation of the excitation efficiency, detection efficiency, and the beat contrast.

2.6 Overview of Systematic Effects

Great concern has been taken in examining the systematic effects since EDM searches, as precision experiments are quite susceptible to systematic effects. Due to the smallness of the electron EDM compared to the magnetic moment, all of the EDM experiments are especially sensitive to the spurious magnetic fields. If a change of the magnetic field \mathcal{B} is associated with the application of the external electric field \mathcal{E} and dependent on the field strength, the frequency difference derived from the field reversal could yield a false EDM signal which will be hard to distinguish from the authentic EDM signal. Such systematic effects can be shown as follows. The Larmor frequency in the external fields, following the notation in Eq. 1.1, is

$$\begin{aligned} \mathcal{B} \uparrow, \mathcal{E} \uparrow: \quad \omega_{\uparrow\uparrow} &= \mu(\mathcal{B} + \alpha\mathcal{E} + \beta\mathcal{E}^2) + d\mathcal{E}, \\ \mathcal{B} \uparrow, \mathcal{E} \downarrow: \quad \omega_{\uparrow\downarrow} &= \mu(\mathcal{B} - \alpha\mathcal{E} + \beta\mathcal{E}^2) - d\mathcal{E}, \\ \omega_{\uparrow\uparrow} - \omega_{\uparrow\downarrow} &= 2(d + \mu\alpha)\mathcal{E}. \end{aligned}$$

Here α and β are the linear and quadratic coefficients of a stray magnetic field dependent on the electric field. These stray fields are the result of imperfections that are related to the details of the experimental apparatus, such as inhomogeneity of electric fields, inhomogeneity of magnetic fields, etc. To most EDM experiments, two types of systematic effects are of special concern: transverse magnetic fields associated with the molecules' motion in the electric field and the geometric phase, and vertical magnetic fields associated with leakage currents. Both can generate stray \mathcal{E} -dependent magnetic fields. These types of effects must be diagnosed by systematic variation of experimental configurations.

2.6.1 Applied External Field

The molecules moving in an electric field $\vec{\mathcal{E}}$ and magnetic field $\vec{\mathcal{B}}_0$ will experience a magnetic field in their rest frame $\vec{\mathcal{B}}_m = \vec{v} \times \vec{\mathcal{E}}/c$, where $\vec{\mathcal{E}}$ and $\vec{\mathcal{B}}_0$ are nearly parallel with angle θ . The motional magnetic field is prominent in the atomic beam experiment where the atoms propagate along the definite direction perpendicular to the applied electric field and large electric field is required to induce the polarization of atomic states. For the Berkeley Tl EDM experiment [49], the beam velocity is $v \approx 3.9 \times 10^4 \text{ cm s}^{-1}$, and the applied electric field is $\mathcal{E} \approx 107 \text{ kV/cm}$, so the motional magnetic field is $\mathcal{B}_0 \approx 0.5 \text{ mG}$ compared to the nominal applied magnetic field 0.42 G. Two counter-propagating atomic beams were used to cancel the systematic effect due to the motional magnetic field. In experiments using vapor cells, the atoms or molecules are moving randomly inside the cell and have the average $\langle \vec{v} \rangle = 0$ without any preferential direction. Imperfect excitation caused by laser or microwave detuning and/or wavefront curvature, will cause the preferential selection of a certain velocity class due to the Doppler effect and hence may introduce a certain level of preferential direction.

However, in our EDM experiment using molecules, this systematic effect is highly suppressed, because the close-lying parity states in molecules will induce a large Stark tensor effect. This suppresses the level shift due to the transverse magnetic field, as shown in the following discussion. Under the typical experimental condition where the electric field

is strong enough that the molecules are almost completely polarized, the applied electric field $\vec{\mathcal{E}}$ will define the quantization axis \hat{z}' locally. A static magnetic field is applied to lift the degeneracy of $M = \pm 1$ Zeeman sub-levels. In our experiment, the magnetic field is about several hundred milli-gauss, which induces a Zeeman beat frequency of several hundred kilohertz. Large Helmholtz coils around the vacuum chamber are used to generate the static magnetic field $\vec{\mathcal{B}} = \mathcal{B}\hat{z}$ along the vertical \hat{z} direction in the lab frame, and the whole system is shielded with magnetic shields to screen out the ambient magnetic field. Hence, it is believed that the static magnetic field has a sufficiently homogeneous direction and magnitude distribution over the whole volume of cell. Thus, if the electric field is locally along the non-vertical direction in the lab frame, there will be a misalignment of angle θ between electric field and magnetic field, which would lead to the beat frequency broadening. The axial projection of the magnetic field in the local molecule-fixed frame defined by the electric field, $\mathcal{B}_{z'} = \mathcal{B} \cos \theta$, determines the Zeeman beat frequency $2g\mu\mathcal{B}_{z'}$. The effective g -factor is approximately 1.86 for the a(1) EDM state of PbO. The dependency on the alignment θ will inhomogeneously broaden the beat frequency.. The radial projection of magnetic field, $\mathcal{B}_0 \sin \theta$, together with the motional magnetic field gives the transverse magnetic field $\mathcal{B}_{y'}$. With the vertical component $\mathcal{B}_{z'} = \mathcal{B}_0 \cos \theta$ and the total magnetic field can be expressed as $\vec{\mathcal{B}} = \mathcal{B}_{y'}\hat{y}' + \mathcal{B}_{z'}\hat{z}'$.

For simplicity, consider the $J=1$ case. Let \mathcal{B}_0 be sufficiently weak such that the Zeeman shifts of the $J=1$, $M_J = \pm 1$, $E_{\pm} = \pm g\mu_B\mathcal{B}_{z'}$ are small compared to the quadratic Stark effect $\Delta = a\mathcal{E}^2$. Denote the energy difference between $M_j = 0$ and the average of $M_j = \pm 1$ by Δ . The Hamiltonian matrix is

$$H = \begin{pmatrix} k_1 & -ik_2 & 0 \\ ik_2 & k_3 & -ik_2 \\ 0 & ik_2 & -k_1 \end{pmatrix},$$

where the rows (and columns) are labeled by $M_J = +1, 0, -1$, respectively, while $k_1 =$

$g\mu_B\mathcal{B}_{z'}$, $k_2 = g\mu_B\mathcal{B}_{y'}/\sqrt{2}$, and $k_3 = -\Delta$.

Assuming $|k_2| \ll |k_1|$ (i.e. $\theta \ll 1$) we diagonalize the matrix to obtain the energy eigenvalues:

$$\begin{aligned}\lambda_+ &= k_1 + \frac{k_2^2}{k_1 - k_3} + \text{higher order terms,} \\ \lambda_- &= -k_1 - \frac{k_2^2}{k_1 + k_3} + \dots, \\ \lambda_0 &= k_3 + \frac{k_2^2 k_3}{k_3^2 - k_1^2} + \dots\end{aligned}$$

The energy difference $\lambda_+ - \lambda_-$ is of interest, because the change of this energy difference under the field reversal is the EDM signal we looking for. In our experiment, it gives the frequency of the quantum beats:

$$\begin{aligned}\omega_b &= \lambda_+ - \lambda_- = 2k_1 + 2\frac{k_2^2 k_1}{k_1^2 - k_3^2} \\ &\cong 2k_1 \left(1 - \frac{k_2^2}{k_3^2}\right) \\ &= 2g\mu_B\mathcal{B}_{z'} \left[1 - \frac{1}{2} \left(\frac{g\mu_B\mathcal{B}_{y'}}{\Delta}\right)^2\right] \\ &= 2g\mu_B\mathcal{B}_{z'} \left[1 - \frac{(g\mu_B)^2 (\mathcal{B}_0 \sin \theta)^2 + 2\mathcal{B}_m\mathcal{B}_0 \sin \theta + \mathcal{B}_m^2}{\Delta^2}\right].\end{aligned}\tag{2.15}$$

The frequency shift due to the transverse magnetic field $-g\mu_B\mathcal{B}_{z'} \left(\frac{g\mu_B\mathcal{B}_{y'}}{\Delta}\right)^2$ is highly suppressed due to the smallness of $g\mu_B\mathcal{B}_{y'}$ compared to the Stark effect Δ . In the perfect alignment case $\theta = 0$, the motional field $\mathcal{B}_{y'} \sim \mathcal{B}_m = \vec{v} \times \vec{\mathcal{E}}/c$. For our experiment, only a moderate electric field (~ 50 V/cm) is needed to polarize the PbO molecules in $a(1) \ ^3\Sigma^+$ states and induces significant Stark shift ($\Delta \sim 40$ MHz). The molecules' typical velocity is about $v \sim 3 \times 10^4$ cm/s in the vapor cell at 700°C. The motional field is only about 0.2 μ G, leading a negligible shift of ~ 40 pHz due to the Stark tensor effect, and this shift does not reverse with respect to the electric field reversion, hence the motional field alone will not contribute to the systematic error. The term $(\mathcal{B}_0 \sin \theta)^2$ does not reverse with respect to the electric field as well. If we include the misalignment due to the electric field directional inhomogeneity, although the cross term $\mathcal{B}_m\mathcal{B}_0 \sin \theta$ has the P,T-odd $\vec{\mathcal{B}} \cdot \vec{\mathcal{E}}$

dependence, the Stark tensor effect will suppress this systematic effect to 10^{-30} e·cm level. With the co-magnetometer mechanism which will be introduced later, the systematic effect related to the motional field can be further suppressed.

Another type of systematic effect related to the motion of the molecules and the configuration of the electromagnetic field is the geometric phase. If the quantization axis varies slowly as the molecules moves around, the molecules will accumulate a geometric phase proportional to the solid angle traced out by the tip of the quantization axis. The geometric phase will shift the precession phase, hence generating a false EDM signal if the geometric phase has the P,T-odd $\vec{B} \cdot \vec{E}$ dependence. The variation of the quantization axis can originate from the velocity-related transverse component of magnetic field, in the presence of electromagnetic field gradients. The effect of geometric phase has been discussed in details for linear motion in beam experiments [50] and the specular motion inside a trap [51, 52] (not applicable to our experiment). As discussed above, the systematic effect due to the transverse component of magnetic field has been highly suppressed due to the Stark tensor effect in our experiment, and the Ω -doublet co-magnetometer suppresses it even further. It is believed that the systematic effect due to geometric phases will not be problematic at our current sensitivity level. The false EDM due to geometric phases depends on velocity, the magnitude and gradient of the magnetic field, the alignment between electric field and magnetic field, collisions, etc, yet the real EDM does not. Systematics can be examined by making these conditions deliberately larger or smaller. Amar Vutha in our lab has been working on the details of geometric phase shifts.

The magnitude inhomogeneity of the electric field will cause variation of the polarization P of the molecules (see Eq 2.7), hence inducing different g -factors at different electric field strength. This is in addition to the intrinsic small difference of the Landé factors g_e and g_f of the unpolarized levels. Ignoring mixing with higher levels, the change of g -factor in the electric field is $\Delta g \sim \delta g \Delta \Omega / (4\mu_a \mathcal{E})$, where $\delta g = g_e - g_f \sim -31(9) \times 10^{-4}$ and $\mu_a \sim 1.64$ MHzV $^{-1}$ cm [39]. The strength of the electric field can also vary the portion of the mixing of the next rotational level J=2 into J=1 level (see Section 5.2). The associated change of

g -factor is $\Delta g \sim 3\mu_a \mathcal{E} g / (10B_r)$, where $B_r \sim 14.1$ GHz is the rotational constant of the $a(1)$ state. In conclusion, the dependence of the effective g -factor g_{eff} on the magnitude of the electric field is $g_{\text{eff}} \sim g(1 + \alpha/\mathcal{E} + \beta\mathcal{E})$, where $|\alpha| \sim 2.8 \times 10^{-3}$ V/cm, $|\beta| \sim 3.5 \times 10^{-5}$ V⁻¹cm, and the signs of α and β depend on which component of the Ω -doublet is populated. In our nominal experimental configuration, $\mathcal{E} \sim 40$ V/cm, and $\beta\mathcal{E} \sim 10^{-3}$ is the dominant contribution to the beat frequency broadening due to the magnitude inhomogeneity. So, including the effect from the directional inhomogeneity and magnitude inhomogeneity of the electric field, the beat frequency is

$$\omega_b \cong 2g\mu_B \mathcal{B} \cos \theta (1 + \beta\mathcal{E}). \quad (2.16)$$

This formula reveals the correlation between the quantum beat frequency and the inhomogeneous electric field. An additional systematic effect will arise if electric field or magnetic field reversal is not perfect, as the additional shift due to stray field is not canceled. Again the Ω -doublet provides a great mechanism to suppress the systematics due to the imperfection of the electromagnetic field control.

2.6.2 Leakage Current Effects

The EDM will manifest itself as a linear Stark shift in the presence of the electric field. High voltage is needed to polarize the molecules completely to increase the internal effective electric field. Leakage currents will inevitably flow through the insulators between the high voltage electrodes. These currents will generate stray magnetic fields and induce an additional frequency shift which is correlated with the electric field direction and mimicking an EDM. This leakage current effects is one of the primary systematic effects in cell-based EDM experiments. This effect can be described by the Hamiltonian of the system,

$$H = - \left\{ \mu \left[\vec{\mathcal{B}} + \hat{z}(\vec{\beta} \cdot \vec{\mathcal{E}}) \right] + d\vec{\mathcal{E}} \right\} \cdot \frac{\vec{J}}{|J|},$$

where \mathcal{B} and \mathcal{E} are static magnetic and electric fields, μ is the magnetic moment, \vec{J} is the total angular momentum, and $\vec{\beta}$ characterizes the effective helicity of the current density \vec{j} flowing around the cell body. To first order, the leakage currents are expected to follow the electric field lines and hence should be parallel with the applied external electric field. This current can not produce a component of \mathcal{B} parallel to \hat{z} so it will not produce a first order frequency shift. However, leakage currents caused by high voltage are often difficult to measure and control due to imperfections in the cell walls together with the high temperature vapor cell environment.

To estimate the largest acceptable leakage current, we assume a worst-case scenario, where the leakage current I_l makes a full loop around the cell. This is, of course, unlikely. Our cell has dimensions on the order of 8 cm. The field at the center of such a loop is $\mathcal{B} \sim 0.16I_l$ G/A, so that a leakage current of 10 μ A will generate a field of $\mathcal{B}_z \sim 1.6 \times 10^{-6}$ G. For the a(1) $^3\Sigma_1^+$ J=1 states of PbO, with the averaged g -factor $g \sim 1.86$, this corresponds to a beat frequency shift of $\delta\nu = 2g\mu_B\mathcal{B} \approx 0.8$ Hz, which would lead to an apparent EDM $d_e \approx 6.7 \times 10^{-26}$ e · cm. Such a shift will be a worrisome problem even for short-term projected sensitivity level. However, thanks to the appealing feature of the a(1) [$^3\Sigma^+$] Ω -doublet pair, we can utilize it as an internal co-magnetometer to suppress the effect of leakage currents, as shown in the next section.

2.6.3 The Internal Co-Magnetometer

A new generation of EDM experiments will use the co-magnetometer mechanism, in addition to \mathcal{E} and \mathcal{B} field reversals, to suppress systematic effects at unprecedented sensitivities. For example, a second type of atoms which is not sensitive to the electric dipole moment can co-exist in the same volume to measure the magnetic field [6, 53].

Our experiment use a new type of internal co-magnetometer using the Ω -doublet states to reject systematics associated with magnetic fields. We can excite the other $M = \pm 1$ pair of nearly-degenerate doublet levels, simply by changing the microwave frequency in the population downward transfer stage from J=2 level to J=1 level (see Section 2.2).

Switching between these two pairs of states changes the polarization alignment of the molecules, and thus reverses the direction of the internal electric field without any change in the external magnetic or electric fields. This operation changes the sign of the energy shift due to an EDM (δ_d in Fig 2.2), yet leaves the sign of most terms caused by systematic effects intact. Since the response of the two pairs of states to a spurious magnetic field remains the same, the systematic effects are canceled.

However, such systematic effects are not completely canceled, because there are some residuals due to the small difference of the Landé factors of the unpolarized levels, g_e and g_f , and the mixing of the next rotational level with $J = 2$, plus the incomplete polarization of the molecule, as we have discussed in Section 2.6. The suppression of magnetic systematic effects is determined by the uncertainty of the effective g -factors, the Stark shift Δ , and the Ω -doublet splitting Δ_Ω . By comparison of the data associated with the two sets of levels and application of our knowledge on the molecular structure and the magnitude of the applied electric field, the spurious magnetic effects are suppressed by a factor f

$$f = \frac{\sigma(g_m)}{g_m} \sim \frac{\sigma(\delta g)}{g} \cdot \frac{\Delta_\Omega}{4\Delta},$$

where $\sigma(g_m) \sim 10^{-3}$ is the uncertainty on the effective g -factors and approximated by the uncertainty on $\delta g = g_e - g_f$. The experimental limit on the intrinsic g -factor difference in the absence of an external electric field \mathcal{E} is $\delta g = g_e - g_f = -31(9) \times 10^{-4}$ [39]. The g -factor change due to the mixing of $J=2$ level can be predicted well and is believed to contribute the uncertainty of g -factor in higher order. Based on the typical values $\Delta \sim 40$ MHz and $\Delta_\Omega = 11.2$ MHz, this additional reversal using Ω -doublet will provide a dramatic reductions of systematic errors due to the stray magnetic field, by a factor of about $f \sim 7 \times 10^{-5}$.

In particular, the Ω -doublet co-magnetometer leads to a great suppression of the insidious effect due to the leakage current I_l associated with the electric field, which is the primary concern in the PbO EDM experiment. The residual frequency shift due to the leakage current after the Ω -doublet subtraction will be $f\Delta\nu_{b,e} \approx 2$ mHz, yielding the sys-

tematic effect $d_{\text{leakage}} \sim 3 \times 10^{-28} \text{ e}\cdot\text{cm}$. In current status of experiment, it will be sufficient suppression on the leakage current to reach the projected sensitivity of $d_e = 1 \times 10^{-25} \text{ e}\cdot\text{cm}$ with the leakage current kept below $I_l < 10 \mu\text{A}$.

Chapter 3

Experimental Apparatus

The key to reaching the projected high statistical sensitivity of the PbO eEDM experiment is the high density obtained when hot molecules are contained in a vapor cell. Great efforts have been taken on material selection and engineering construction, since usually commercially available parts can't meet the strict requirements of our experiment. We have constructed a new generation of the vapor cell (Section 3.1) and the oven (Section 3.2) used to heat the cell, which allows easy optical access and the application of homogeneous electric and magnetic fields. This ensures that we can use laser excitation and fluorescence detection of the PbO molecules. Magnetic shields have been set up to provide a quiet magnetic environment for the experiment (Section 3.6). All the coaxial electrical feedthroughs (Section 3.5) and thermocouples have been replaced by home-made components using nonmagnetic materials. A lot of work has been done to measure and minimize the leakage current flowing around the cell body (Section 3.1.2), including various spacer material tests, terminal blocks, and electrode lead suspending components to isolate the current path. Three types of photodetectors were constructed and their respective signal to noise characteristics have been measured, aiming to improve the detection efficiency (Section 3.8). The schematic of the PbO EDM experiment setup is shown in Fig. 2.3. In this chapter, I will describe most of the apparatus used in our experiment. The apparatus for the microwave excitation will be described in next chapter.

3.1 Development of the Vapor Cell

As our PbO EDM experiment must be carried out in a vapor cell, the construction of the cell is crucial to meet the experimental requirement to provide a clean and robust structural framework for holding a high density of PbO vapor.

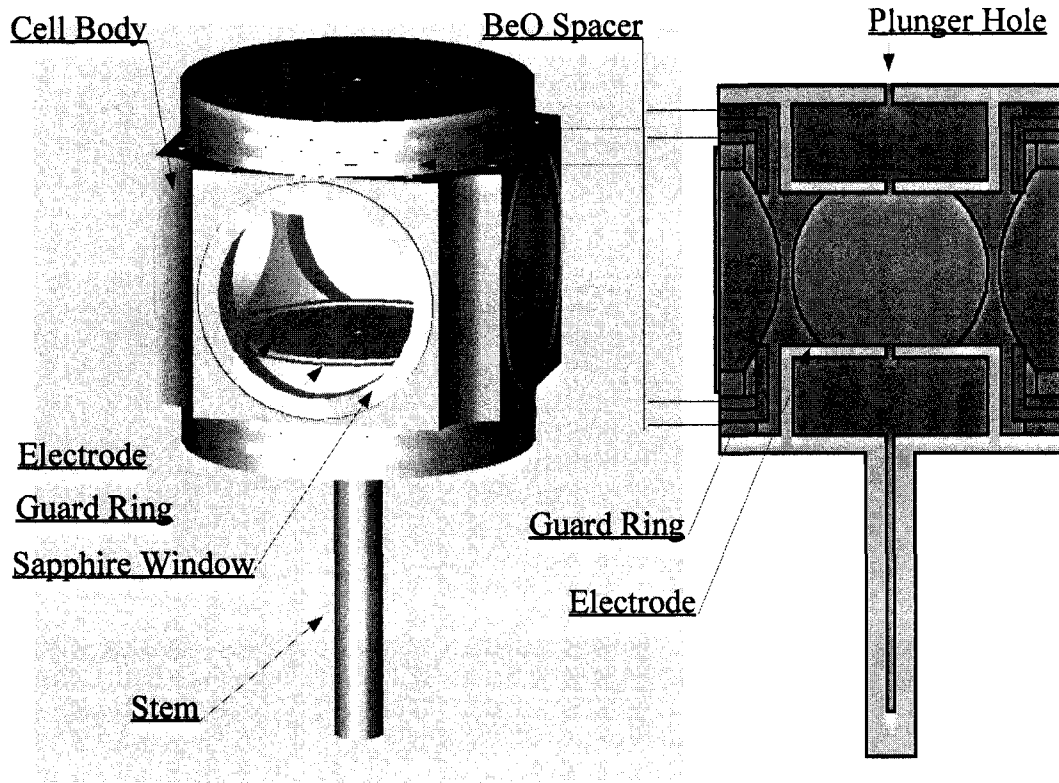


Figure 3.1: Vapor Cell and its Cut View. The vapor cell consists of an hollow alumina frame with top and bottom end caps supporting flat gold foil electrodes, plus surrounding guard ring electrodes, and large flat sapphire windows on all 4 sides.

The cell body is an alumina block, $3.5'' \times 3.5'' \times 2.5''$, with holes bored through the centers of each face to form a frame structure. The cell is made large enough to reduce the rate of wall quenching of the EDM state, ensuring that the coherence time is not limited by collisions with the wall. Reentrant gold electrodes and guard rings are inserted through the vertical holes with 3'' diameter in the top and bottom of the cell. The reentrant design of the electrodes improves the aspect ratio of the electric field region to minimize the fringe

effect of electric fields due to the finite size of the electrodes, and also provides a metallic boundary for the molecules, reducing stray fields due to surface charges on the dielectric parts of the cell. The horizontal holes through the sides are 2" diameter and covered with sapphire windows using a gold foil bonding technique. A large solid angle of optical access is necessary to convey a significant fraction of the fluorescence out of the cell, improving the detection efficiency. Beryllium oxide (BeO) or sapphire electrical insulating spacers are inserted in the interval between the cell body and the guard ring support, and between the guard ring and the electrode to diminish leakage currents. The surface of the cell body is kept clean to avoid contamination which could lead to surface leakage currents. The stem serves as the PbO reservoir, incorporated with the cell. The depletion of the PbO is slow enough that we can run our experiments for weeks with no need to refill PbO. In nominal operation, the temperature of the stem is typically kept tens of degrees below the rest of the oven in order to remain as a reservoir of PbO and vapor condensation point. The cell structure is shown in Fig 3.1.

Given the experimental environment of high temperature ($T \sim 700^\circ\text{C}$) and frequent thermal cycling, the alumina cell body and flat sapphire windows are chosen to satisfy the material constraints. There are several components that must be bonded with the cell body, including: sapphire windows, with c-axis normal to the window plane to eliminate birefringence; re-entrant electrodes; and separate guard-ring electrodes designed to improve field homogeneity. We have developed a bonding method based on a surface-oxide bond using gold foil as bonding agent. Such bonds can withstand the high temperature and aggressive PbO vapor environment and remain mechanically strong, while maintaining vacuum integrity during frequent thermal cycling. The contact surfaces of the cell body, electrode support, guard ring support and spacer have been polished to improve the solidity of the bonding. As discussed in the previous chapter, leakage currents associated with the applied field should be kept below $10 \mu\text{A}$ under operating conditions to take advantage of current statistical sensitivity to the electron EDM (see Section 2.6.3). Gold foils are chosen due to their low vapor pressure at the operating temperatures, preventing formation of

conducting surface layers on the cell. Beryllium oxide or sapphire are used as insulating spacers due to their high resistivity under our operating conditions.

3.1.1 Electrodes with Guard Rings

The vapor cell is designed with re-entrant electrodes and guard rings, with separately controlled voltages for better electric field homogeneity.

As shown in Eq. 2.16, the quantum beat frequency of a(1) J=1 levels in an inhomogeneous electric field is

$$\omega_b \cong 2g\mu_B\mathcal{B} \cos \theta (1 + \beta\mathcal{E}), \quad (3.1)$$

where θ is the misalignment angle between the electric field $\vec{\mathcal{E}}$ and magnetic field $\vec{\mathcal{B}}$, and β is the proportionality factor denoting the perturbation due to the mixing of the J=2 and J=1 rotational levels.

To minimize the spread of θ , the electric field lines should be as parallel as possible to the vertical magnetic field. However, it is a challenge to meet this requirement in the limited space inside the vapor cell. The diameter of the electrodes is constrained by the cell volume and oven space. The space between the electrodes is chosen to be comparable to the free path of PbO flying within the a(1) state life time. As a result, the aspect ratio of the electric field is quite limited and can not be simply enlarged by moving the electrodes closer. The capacitor-like electrodes will have significant fringe fields. The cell body is made out of ceramic and the resistivity drops exponentially with increasing temperature. The cell windows are bonded to the cell body with gold foil rings which are grounded deliberately to conduct away any charge accumulated on the window. Fringe fields will be worse as the electric field lines must be normal to the conductor surface.

One thought was to design curved electrodes with a smaller spacing at the edge to reduce the fringing fields. However, such a complicated geometry would impose great challenges on machining the shape and maintaining the curvature in the experimental environment.

Instead we chose to insert guard rings around the electrodes to modulate the electric

field lines and suppress the fringe fields. By applying higher voltage on the guard rings, the electric field lines starting from the electrodes' edge will be "pushed" toward the center, making them more perpendicular to the main electrode surface. The ability to apply various voltages on the guard rings enables us to adjust the electric field homogeneity. Hence it is a good diagnostic of the systematic effect due to the electric field homogeneity (see Section 2.6.1). This additional freedom and relatively simple structure makes the guard ring scheme win over the curved surface scheme. Unfortunately, there is no straight-forward analytic solution to such a geometry. We use the commercial electromagnetic design software Maxwell[®] 3D from *Ansoft Corporation* to simulate the electric field distribution in the cell. The simulation results are presented in Fig. 3.2, plotted together with the cell model in wire frame.

In the simulation, voltages on the main electrode are set to ± 200 V. The volume of interest is a cylindrical region 2" diameter and 1.4" high. The simulation result provides the value of electric field $\vec{\mathcal{E}}$ at the sampling points. The local direction of the electric field is given by $\cos \theta = \frac{\vec{\mathcal{E}} \cdot \hat{z}}{|\vec{\mathcal{E}}|}$. The beat frequency spread is calculated using Eq 2.16 with $2g\mu_B B \sim 300$ KHz, shown in Fig. 3.3A. The histogram is given by counting the beat frequency distribution over equally spaced sampling points inside the vapor cell. As laser illumination is within a 2" diameter cylindrical region and the fringe effect is only prominent at the corners of the electric field region, the collection efficiency of fluorescence emitted by the molecules excited in these regions is low and the time for these molecules to enter the center region is comparable to the lifetime of the $a(1) \ ^3\Sigma^+$ state. Hence, the effect of the inhomogeneous broadening will be suppressed if the geometric factor is taken in account. The magnitude deviation $\delta = \frac{||\vec{\mathcal{E}}| - |\vec{\mathcal{E}}_0||}{|\vec{\mathcal{E}}_0|}$ is also calculated, where $|\vec{\mathcal{E}}_0|$ is the field magnitude at the center, shown in Fig. 3.3B. The simulation shows that if main electrodes are set at ± 200 V, the optimal voltage for guard rings is ± 360 V, as the optimal ratio is 1.8:1 for our dimension of the electrodes and guard rings.

The experimental verification of the optimal voltage ratio is shown in Fig. 3.4A, where the beat signal is monitored as the laser populates the $M = \pm 1$ states in the presence of

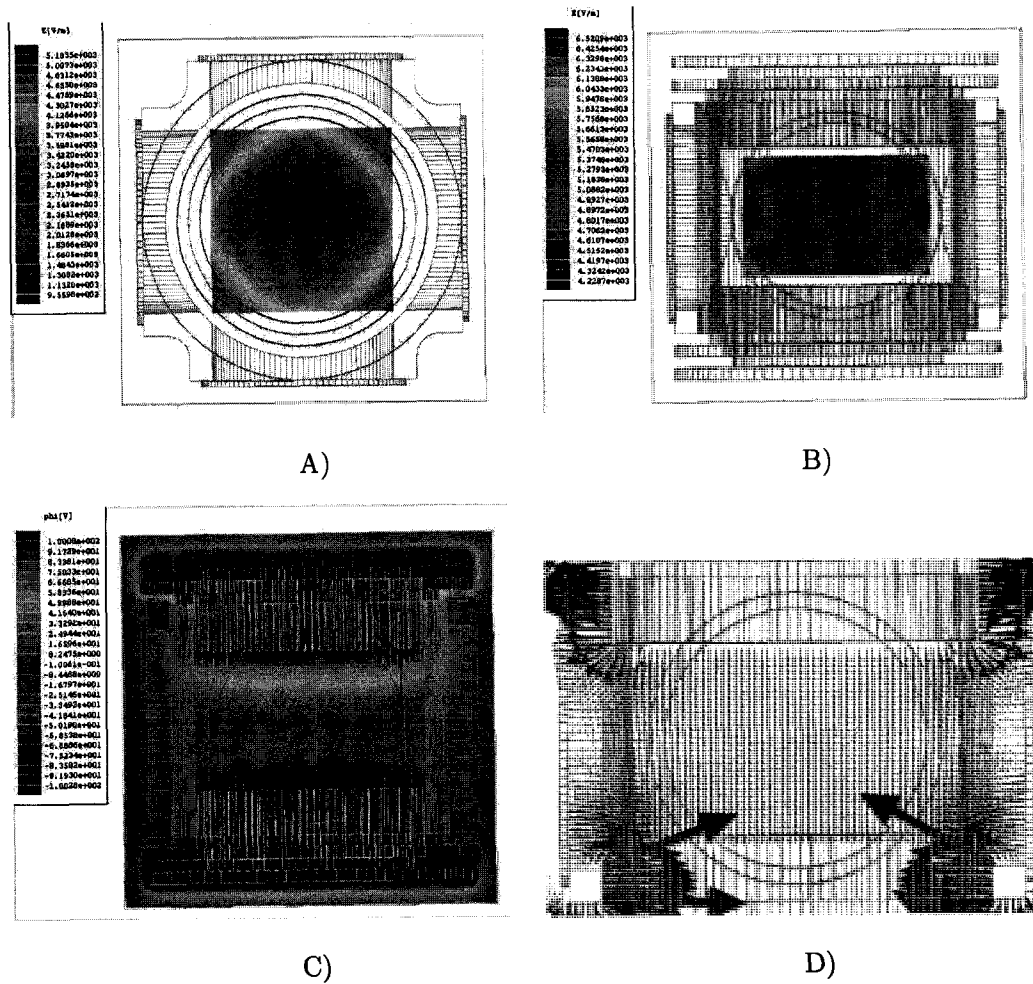


Figure 3.2: Electric Field in the Cell. The voltage of the guard ring is 375V and main electrode is 200V. A) Top View of E Field Magnitude; B) Side View of E Field Magnitude; C) Side View of Potential; D) Side View of E Field Line.

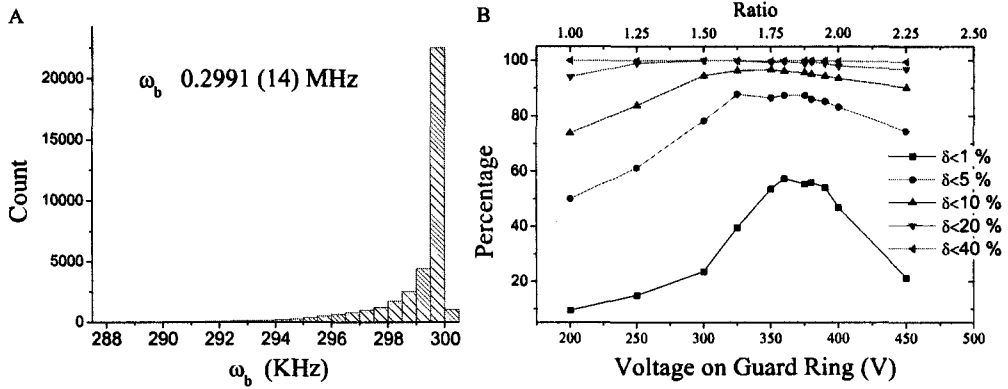


Figure 3.3: Electric Field Inhomogeneity in the Cell. Voltages on the main electrode are set to ± 200 V. A) Beat frequency spread in the electric field from the simulation result, with nominal beat frequency 300 KHz and guard ring voltage ± 360 V. B) Magnitude inhomogeneity is characterized by the magnitude deviation $\delta = \frac{|\vec{\mathcal{E}}| - |\vec{\mathcal{E}}_0|}{|\vec{\mathcal{E}}_0|}$. Simulation indicates that over $\approx 90\%$ of the cell volume, the magnitude inhomogeneity δ is less than 5% in the optimal situation.

various electric fields and the guard rings are fixed at ± 135 V. The beat amplitude reaches maximum when the voltages applied on the main electrodes are around ± 75 V respectively, or 150 V across the electrodes, yielding the optimal voltage ratio of 1.8 as expected.

Furthermore, the beat lifetimes are extracted from the beat signal using the fitting routine (see Section 2.4.2). The beat lifetime can be interpreted as the coherence time, directly related to the line width broadening due to the field inhomogeneity. Fig. 3.4B shows the longest beat lifetime appears around 150 V across the electrodes, coincident with the result of beat amplitude.

An additional experiment using microwaves to resolve the $M = \pm 1$ level carried out by Paul Hamilton shows the upper limit of broadening due to the electric field inhomogeneity is less than 1.2%, consistent with the design specification of the electrodes. Vertically polarized microwaves with low power are used to drive the population of a(1) $J=1$ level to the $J=2$ level. As the microwave frequency scans through the resonance condition for $M = \pm 1$ respectively, the disappearance of beats in the $J=1$ state is observed as the

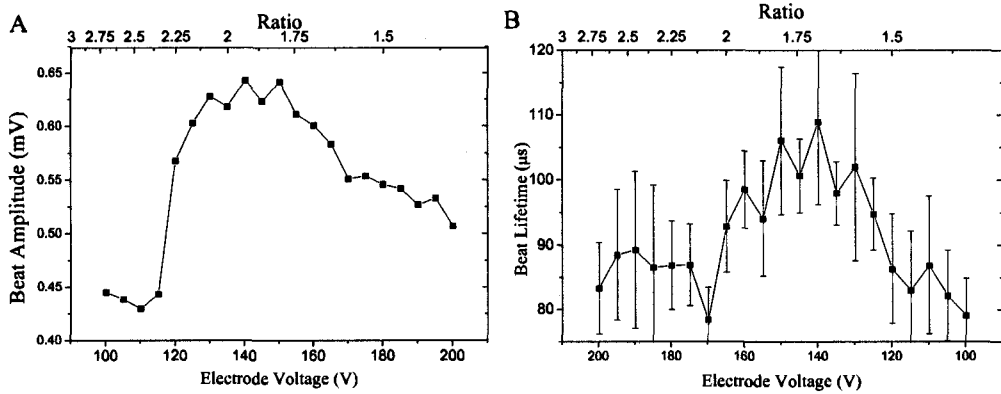


Figure 3.4: Optimal Voltage Ratio. Simulation result indicates that optimal voltage across the electrodes should be around 150 V when guard rings fixed at ± 135 V. A) Beat amplitude peaks around 150 V across the electrodes. B) Beat lifetime peaks around 150V across the electrodes.

microwave depletes the population in either $M = 1$ or $M = -1$ level. The resonance peaks for $M = \pm 1$ level are resolved, imposing an upper limit on the electric field inhomogeneity. The inhomogeneous broadening due to the electric field must be less than the Zeeman splitting in order to resolve the lines.

Finally, we can also diagnose the electric field distribution by tilting the magnetic field using the cage coils (See Section 3.6) to exaggerate the misalignment between the electric field and magnetic field. This has not yet been attempted, however.

Inhomogeneous electric fields might induce possible systematic effects (see Section 2.6.1), and it can affect the microwave excitation efficiency. To get a brief idea, let us assume 1% homogeneity of the electric field over the cell volume. For a nominal Stark shift of 60 MHz, a 1% inhomogeneity induces a 600 kHz linewidth of $M = \pm 1$ sublevels. For comparison, the 28.2 GHz microwave resonance has 24 kHz Doppler width for the $J=1 \rightarrow J=2$ transition. Microwave pulses must be less than a microsecond to cover the Zeeman splitting (~ 300 kHz) between $M = \pm 1$ sublevels and the inhomogeneous broadening. Because we must use short pulses, higher microwave power is demanded to drive a π -pulse between the rotational levels. To improve the transfer efficiency, an adiabatic passage method is adopted

which will be discussed in Section 4.3. Nevertheless, we will prefer to control the electric field inhomogeneity less than 1% over the cell volume. The electric field inhomogeneity casts technical questions on testing the microwave absorption scheme (see Section 6.2) in the current cell as well. In this case, the microwaves are in continuous-wave mode and broadened only due to the Doppler effect. Electric field inhomogeneity will diminish the absorption cross section. When a new generation of long vapor cell is constructed, it will have rod electrode arrays to apply a cosine-distributed voltage and thus have better electric field homogeneity.

3.1.2 Leakage Current Suppression

We have taken great caution to minimize the leakage current I_L associated with the electric field in our cell. The resistivity of alumina, which is used as the cell body and electrode support material, is not high enough at high temperatures to keep the leakage currents below the nominal requirement $I_L < 10\mu\text{A}$. Therefore, electrical insulation with higher resistivity and chemical stability in the presence of PbO vapor is needed between the electrodes and the cell body. These requirements eliminate most insulating materials. In testing insulating materials, efforts were taken to electrically isolate the vapor cell from the potential external electrical leakage paths so that we could measure the realistic leakage current flowing through the cell body. The measured apparent leakage currents are much higher than the expectation from reported literature of volume resistivity. The resistivity test conducted in the absence of PbO vapor showed a resistivity of $\rho > 10^{13} \sim 10^{14} \Omega \cdot \text{cm}$ at 700°C for BeO. The BeO spacer used in the actual EDM cell has OD 3.5", ID 2.76" and thickness 1/8", leading to a volume resistance at $1.3 \times 10^{10} \Omega$. The closest leakage path is between the top and bottom guard rings. Two BeO spacers will be sandwiched between guard rings and the cell body. In the nominal condition with 300 V across the electrodes, ± 270 V will be applied on the top and bottom guard rings. The leakage current should be ~ 20 nA, inducing a false EDM of $d_{e,\text{leakage}} \sim 4.3 \times 10^{-27} \text{e} \cdot \text{cm}$. Such a systematic error is higher than our original proposed sensitivity on eEDM and further suppression relies

on the Ω -doublet reversal (see Section 2.6.3). This level of leakage current is considered acceptable but not really satisfying. Even worse, in the presence of PbO vapor in the actual EDM cell, with BeO spacers inserted in place, we have been unable to obtain consistent results for I_L . Encouragingly, BeO does not show any signs of reaction with the PbO. Surface currents might be to blame.

To prevent formation of conducting surface layers on the cell surface, the gold foils are used as the electrode material. Gold has a low vapor pressure at the operating temperatures $\sim 700^\circ\text{C}$. The cell body surface is kept clean to avoid contamination. Bent quartz tubes provide structural support for the electrode leads, shown in Fig. 3.5, enabling the leads to connect from the vapor cell to the outside without touching any high temperature parts of the oven and without straining the electrode leads. An alumina corner bracket, used to support the bent tubes, is attached to the outer heat shield, which is supposed to be much colder than the cell and hence should be a very good insulator. The holes the tubes go through have a slot to match teeth on the quartz tubes which fix their orientation. A fork-shaped stop is mounted on the bracket to keep the tubes from sliding in and out. The assembly with heat shield in place is shown in Fig. 3.6. The cell is supported by four ceramic poles to minimize the surface of contact to the rest of the apparatus and eliminate the leakage paths to the chamber body. Ceramic terminal blocks are used to isolate the out-going leads and connect to the custom nonmagnetic coaxial feedthroughs (see in Fig. 3.6 and Fig. 3.12). Four channels of trans-impedance amplifiers with isolated ground, low noise and high sensitivity are used to monitor the leakage current. So far, the material tests have found the suitable insulating materials are high purity alumina, high purity sapphire, and Beryllium oxide.

Paul Hamilton has taken leakage current measurements under the typical experimental conditions in the presence of PbO vapor. High voltage is applied to a single electrode or guard ring while the rest of the electrodes and guard rings are bundled together and tied to ground. By monitoring the currents flowing in all electrodes and guard rings, it is possible to determine the leakage path among the cell, electrodes and guard rings. Currently there

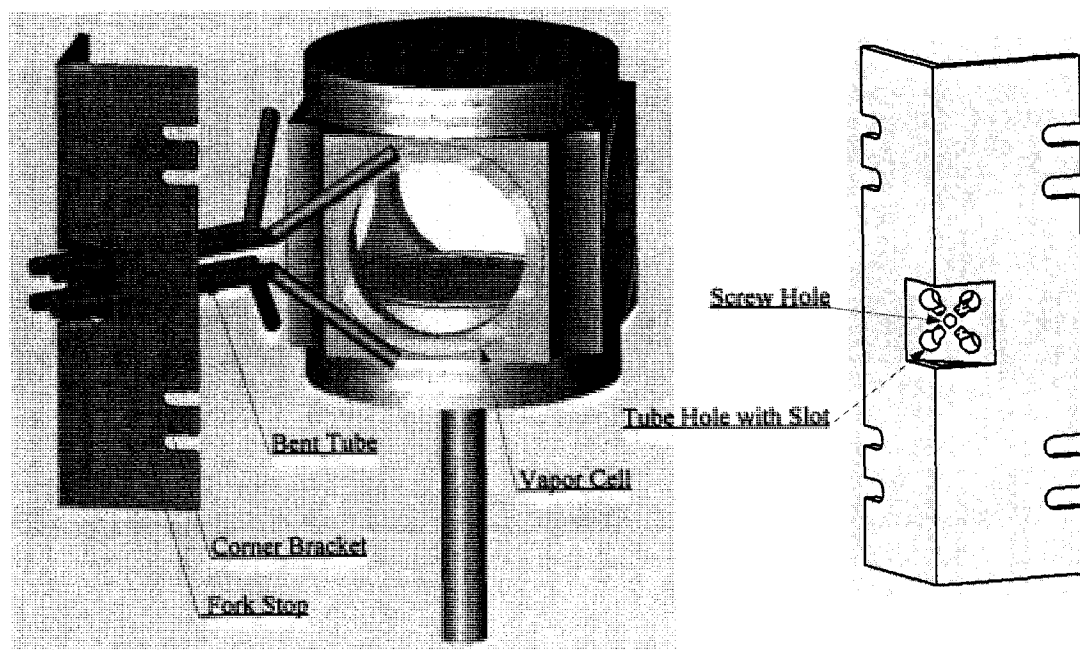


Figure 3.5: Bent Quartz Tube and Corner Bracket. Bent quartz tubes are fixed by the corner bracket to span right angles between adjacent pairs. Gold wires beaded in high purity alumina beads go through quartz tube and reach the fixtures on the terminal blocks outside the oven.

is a discrepancy between the sum of all incoming currents and outgoing currents. It's believed that there must be a current leakage path directly to ground. The incomplete insulating of stem with the stem thermocouple might be one additional leakage path.

So far, we have observed leakage-currents around $10\ \mu\text{A}$ with $150 \sim 300\ \text{V}$ across the cell. It's sufficient to meet the requirement for the short-term targeted sensitivity of $10^{-25}\ \text{e} \cdot \text{cm}$ before Ω -doublet comparison (see in Section 2.6.3). Further improvement on leakage current suppression will be necessary in order to improve sensitivity to eEDM.

3.2 Development of the Oven

We have successfully constructed an oven capable of meeting our requirements for this generation of the EDM experiment. The oven can uniformly heat the cell above 700°C , without cold spots that could cause PbO to condense. It can tolerate and sustain these high temperatures continually for hours without inducing thermal stress on the vapor cells, and still provide large openings for optical access via light pipes. The oven is resistant to thermal shocks, and it is relatively free of chemical reactions.

The oven consists of a cube, with the sides, top and bottom made from stacks of three quartz plates sandwiching resistive heater foils. The prototype of the oven was constructed in an earlier phase of our experiment, and has been described in detail in Frederik Bay's thesis [45]. The quartz plates have grooves cut to hold tantalum heating foils in place. The foils are cut in a zigzag pattern and mounted in pairs of two, one on each side of the central grooved plate, with currents running in opposite directions to minimize spurious magnetic fields. Quartz cylinders are fused on the side plates to serve as window heaters; these prevent cold spots from developing on the cell windows due to the insertion of the light pipes. Additional cylinders are fused on the bottom plate to serve as a stem heater (to vaporize the deposit of PbO), and on the top as a plunger heater (to avoid thermal gradients). Each heater foil set is connected through twisted pairs of wire, which are in turn connected to the home-designed coaxial vacuum feedthroughs to a power supply. With one

supply for each heater element, we have independent control of the temperature of each heating component. The thermocouples are inserted in the space between the stem heater and the stem, and between the vapor cell and the side heaters, to measure the temperature distribution inside the oven. These thermocouples are custom made using one gold wire and one 60/40 gold-palladium alloy wire. The whole oven rests on four ceramic posts to adjust its vertical position and to electrically isolate it from the rest of the chamber. The oven, heat shield and the supports are shown in Fig. 3.6.

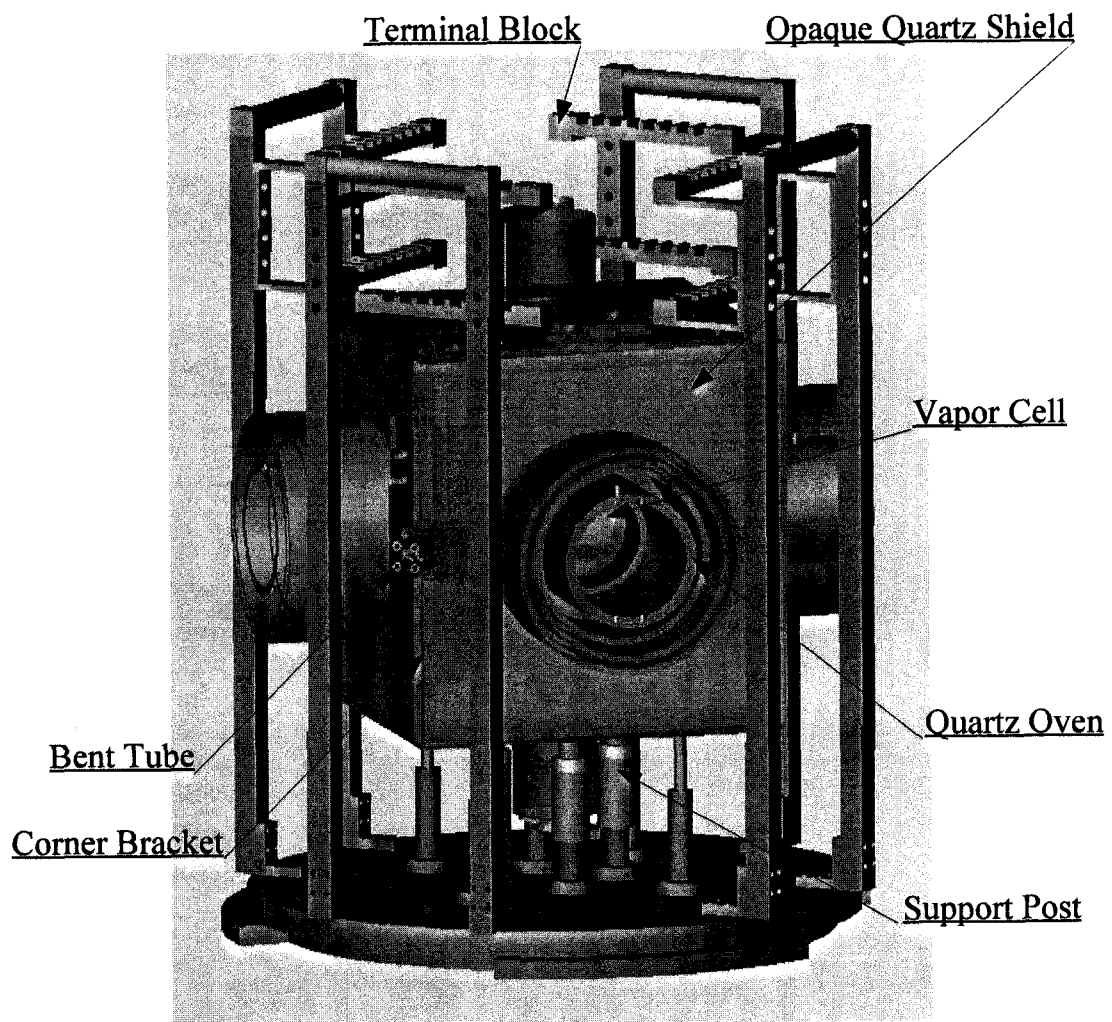


Figure 3.6: Oven inside the Heat Shield. Three layers of opaque quartz heat shields are held together with ceramic bolts and nuts. The whole oven rests on four ceramic posts. The terminal blocks are mounted on the aluminum bars.

Several modifications were applied to the current oven. Ceramic glues and high emissivity paints are avoided in the current oven, as there are concerns that the outgassing from these materials might contaminate the cell surfaces and cause severe leakage current problems. Opaque quartz is chosen as the oven plate material, instead of the transparent quartz coated with a high-emissivity paint, to make the temperature of the heater elements appear more uniform to the cell and detectors.

The heat shields for the current oven are also made out of opaque quartz rather than thick-metal shields to avoid eddy currents as we switch the heater current on and off. The oven is enclosed in a heat shield which consists of three layers of opaque quartz plates, plus reflective metal foils. It is suspected that the low reflectivity of opaque quartz, together with the enlarged separation of the heater components, causes additional power consumption, compared with a previous setup using transparent quartz oven plates and metallic heat shields. The net fraction of radiant energy that escapes a single-layer radiation shield [54] is given by

$$T = \frac{(1 - r_1)(1 + t)(1 - r_2t)}{2(1 - r_1r_2t^2)},$$

where r_1 is the reflectivity of interior surface, r_2 is the reflectivity of exterior surface, and t is the transmissivity of the solid material. The net transmittance through a set of n solid layers is given by

$$T_n = \frac{1}{1 + n(\frac{1}{T} - 1)}$$

The inner surface of the inner heat shield is covered with thin tantalum foils, and the inner surfaces of two outer shields are covered by copper foils, to increase the surface reflectivity. Further attempts are being made to investigate the heating efficiency and blackbody backgrounds.

The entire oven assembly is held together with opaque quartz brackets and ceramic nuts and bolts. However, there is concern that outgassing of the micro bubbles in the opaque quartz oxidize the tantalum heating foils and cause them to become brittle and break after a couple months of heating cycling.

Maintaining the temperature stability is important since temperature changes can also affect the state lifetime T and beat lifetime τ (see Section 2.4.2) through changes in the wall collision or diffusion rate of PbO. In an early era of this experiment, the heaters had to be turned off during measurements to avoid spurious magnetic field generated by the heater current flowing around the cell. The new heating scheme, which will be discussed in the next section, has been used routinely to avoid shutting down the oven and measurements can be taken at the full duty cycle of laser operation.

3.3 Eddy Current Suppression

Resistive heating turns out to be the only feasible heating scheme in our system to achieve high temperatures with a homogeneous distribution over the large volume of the oven. Because of the extreme sensitivity of our experiment to magnetic fields, it is necessary for the heater currents to be turned off completely during data taking periods, to avoid generating stray magnetic fields. To maintain the necessary temperature requires high power, 1000~1500 W, and the heater currents are substantially high (3~5 A). As our laser system operates at 100 Hz, the heaters must be turned on and off at the same frequency to achieve a significant duty cycle. To meet these requirements, the heater foils were designed in a zigzag shape and set together in pairs in close layers, with currents running in opposite directions, as shown in Fig. 3.3. This keeps the inductance of the heaters very low, and allows rapid switching while avoiding large eddy-currents being induced in the vacuum can (see Section 3.2). Previous attempts to switch the heaters involved MOSFET-based circuit switching linear power supplies. The square shape of the DC current pulses, however, presented serious problems with persistent eddy currents in the vacuum can.

We implemented a new heating scheme to take data continuously without shutting down the oven heaters. We drive the heaters with specially-shaped audio frequency pulses $I_h(t)$ (see Eq. 3.2), generated with low-noise stereo amplifiers (Hafler P3000, P4000, and QSC units). The input to the amplifier is generated with an arbitrary waveform generator

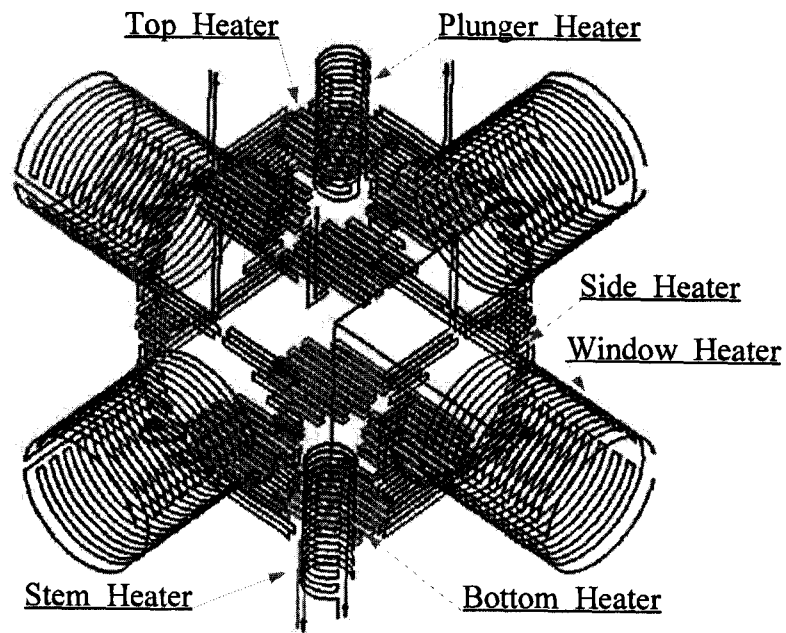


Figure 3.7: Heater Currents. The heater foils were designed in zigzag shape, set together in pairs in close layers, with heater currents running in opposite directions to keep the inductance of the heaters very low.

(Agilent 33120A). The pulse period is $T = 10$ ms. The pulse contains a high frequency component $\sin(2\pi ft)$ at frequency $f \sim 15$ KHz with an envelope, which consists of an adiabatically rising ramp, a flat top, and a lowering ramp, shown in Fig. 3.3C. The mathematical expression of the waveform is shown in Eq. 3.2. This waveform maximizes duty cycle and minimizes eddy-current residuals simultaneously. The envelope and its first derivative are continuous everywhere in order to ensure smooth turn-on and turn-off, and to avoid low-frequency components. The high-frequency components of the heater current limits the skin depth for the induced electromagnetic field, leading to a high resistive dissipation rate for induced eddy currents.

$$I_h(t) \propto \begin{cases} \sin(2f\pi t) \cos^2\left(\pi\left(\frac{5t}{T} - \frac{3}{4}\right)\right) & T/20 < t < 3T/20 \\ \sin(2f\pi t) & 3T/20 < t < 17T/20 \\ \sin(2f\pi t) \cos^2\left(\pi\left(\frac{5t}{T} - \frac{17}{4}\right)\right) & 17T/20 < t < 19T/20 \\ 0 & \text{anywhere else} \end{cases} \quad (3.2)$$

To justify the validity of this heating scheme, Fig. 3.3 shows an intuitive picture of how the waveform of input was chosen and analyzed in the frequency domain. This picture is based on a model of eddy currents using inductive couplings to the vacuum chamber. The time-varying current from the heater $I_h(t)$ can be decomposed into each frequency component $I_h(\omega)$ by Fourier transform, $I_h(t) = \int I_h(\omega)e^{i\omega t}d\omega$. The resistance and self-inductance of the tantalum foils are represented by R_h and L_h respectively, the self inductance of the chamber is denoted as L_c , and the resistance of the chamber can where the eddy currents flow around is denoted as R_c . In return, the eddy current will generate the spurious magnetic field \mathcal{B}_e persisting even after the heater is turned off.

The eddy current generation mechanism is modeled as the mutual inductance M between the can and current loops that heater currents form from unbalanced compensation of heater foils and leads. The induced voltage component at angular frequency ω is given

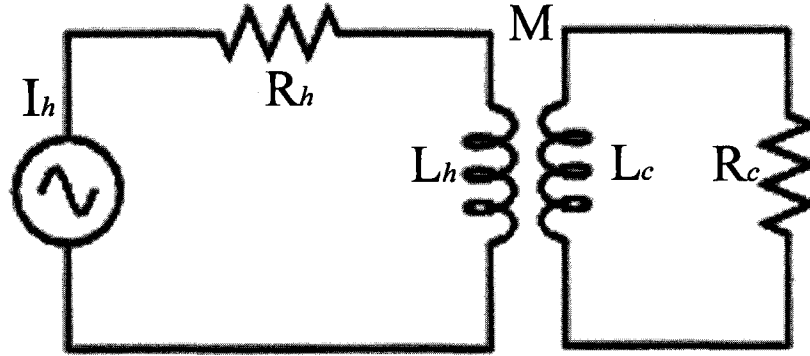


Figure 3.8: Network Model of Eddy Current. The mutual inductance M between the can and stray current loops that heater currents form induces the eddy current.

by $V_e(\omega) = -i\omega M I_h(\omega)$, and the resulting eddy current $I_e(\omega)$ is

$$I_e(\omega) = \frac{V_e(\omega)}{Z_c} = \frac{-i\omega M}{R_c + i\omega L_c} I_h(\omega), \quad (3.3)$$

where $Z_c = R_c + i\omega L_c$ is the impedance of the vacuum chamber can at angular frequency ω . We use the inverse Fourier Transform to find $I_e(t)$ in the time domain for a given input $I_h(t)$. $K(\omega) \equiv -i\omega M / (R_c + i\omega L_c)$ is a transfer function that behaves as a high-pass filter. At high frequency $|\omega| \gg \tau^{-1} = R_c/L_c$ where τ is the typical RL time constant, the induced current $I_e(\omega) \approx -M I_h(\omega)/L_c$, directly proportional to the driving current $I_h(\omega)$ up to a real constant (approximately). Hence, $I_e(\omega)$ has approximately the same temporal characteristic as the driving current so that it will diminish as quickly as the driving current turns off. However at low frequency $|\omega| \ll \tau^{-1}$, $I_e(\omega) \approx -\frac{i\omega M}{R_c} I_h(\omega)$, which behaves like a current response in a parallel RC circuit with $R = R_c$ and $C = 1/M$. As we learned from elementary circuit theory, the induced current will persist with time constant $\tau' = M/R_c$ if we turn off the driving current suddenly. The waveform of the driving current should thus contain only high frequency components.

The frequency spectra of a square pulse, a sinusoidal wave with square envelope, and a sinusoidal wave with ramped envelope are shown in Fig. 3.3. The DC square pulse $I(t) \propto h(t - \frac{T}{20}) - h(t - \frac{19T}{20})$ where $h(\cdot)$ is the step function and $t \in [0, T]$ with 90%

duty cycle, has dominant zero and low frequency components, shown in Fig. 3.3A. The square-envelope sinusoidal wave $I(t) \propto \sin(2f\pi t) [h(t - \frac{T}{20}) - h(t - \frac{19T}{20})]$, has only high frequency components. Intuitively, every half periods of sinusoidal wave will generate eddy currents in one direction. The other halves will generate eddy currents in the reverse direction and mostly cancel the eddy currents generated in the previous half periods. The higher frequency the driving current oscillates at, the more complete such cancellation will be. The square envelope in time domain will lead to a *sinc* envelope in frequency domain which will spread out rather broadly. The ramp-envelope sinusoidal wave (see Eq. 3.2) has a narrower spread in frequency due to the continuity of its envelope and first derivative. Thus the ramp-envelope sinusoidal wave is expected to give the smallest eddy currents persisting after the pulse is off.

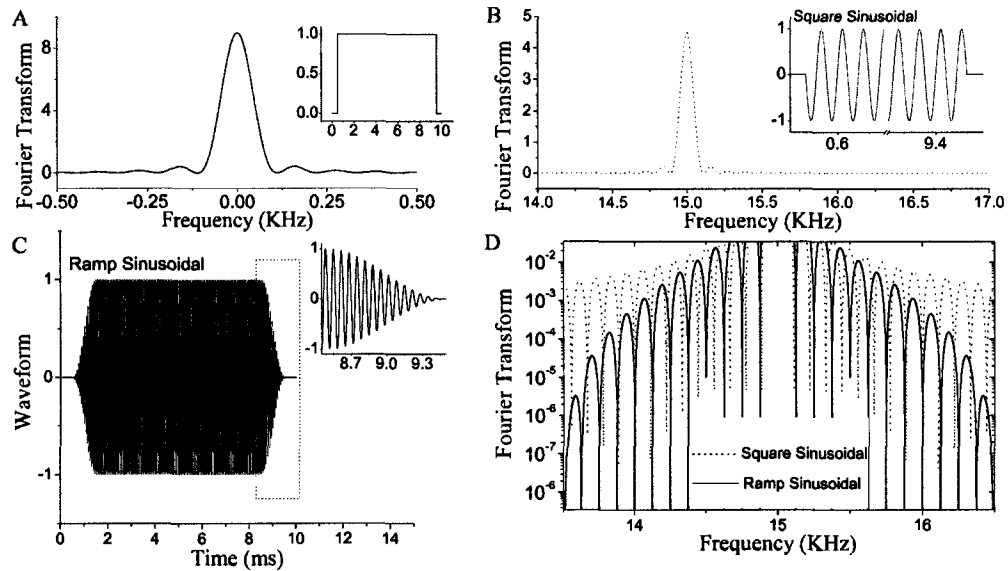


Figure 3.9: Heater Current and Frequency Spectrum. A) DC square pulse has dominant zero and low frequency components. B) Sinusoidal wave with square envelope has only high frequency components. C) Waveform of sinusoidal wave with ramp envelope used in our experiment. D) Compare of frequency spectrum between square-envelope sinusoidal wave and ramp-envelope sinusoidal wave. The latter one has narrower spread in frequency.

To apply this network model to our experiment, we estimate the parameters in Eq. 3.3 based on the geometry of the chamber and oven (see Section 3.2). The typical dimension of eddy current loop is about 2" in diameter; the skin depth, $\delta = 1/\sqrt{\pi f \mu \sigma}$, for the aluminum chamber at frequency 15 KHz is about 0.8", comparable to the thickness of the chamber; the resistance of chamber R_c is therefore about $1 \mu\Omega$; the self-inductance of the chamber can L_c is about $1 \mu\text{H}$; the mutual inductance M between the vacuum can and the heater foil loop is about 0.2 nH, and that between the can and the lead loop is about 0.4 nH. Hence, the eddy current persisting after the heater is turned off is about 3 mA and the corresponding residue magnetic field B_e at the chamber center is around 10^{-2} mG, when using the square pulse drive currents. If there is metallic heat shield set close by the heat foil, the mutual inductance can be as high as 3 nH and induced magnetic field around 2 mG. By contrast, we estimated the magnetic field will be around $B_e \sim 10$ nG in the case of square-envelope sinusoidal current, and $B_e \leq 1$ nG using the ramp-envelope sinusoidal wave now in use.

To study the transient phenomena due to eddy current analytically, we follow a similar approach as that in Ref [55]. There are also several other approaches to study eddy current effect [56, 57, 58]. Ref. [55] concerns the mutual-inductance between the drive coil and pick-up coil in the presence of a conductor with application to flaw detection in conductors. Here we study the relationship between the persistence of the eddy current and the drive current waveform, and provide the optimization of the waveform to suppress the eddy current.

We use the assumption of a good conductor, make the quasi-static approximation (appropriate to the low frequency domain), and apply a Laplace transform on Maxwell's equations to obtain the vector potential $\bar{A}(\vec{r}, s)$, which satisfies

$$\nabla^2 \bar{A}(s) = s\mu\sigma \bar{A}(s),$$

where μ is magnetic permeability of the medium, and σ is electrical conductivity of the medium.

We only consider a simplified model where a current loop is parallel with an infinite large metal sheet with thickness d , as shown in Fig. 3.3. We write $\bar{A}(r, \phi, z; s) = \int_0^\infty \bar{A}(\bar{r}, t) e^{-st} dt$ in cylindrical coordinates (r, ϕ, z) , and assume that the components of \bar{A} are independent of ϕ (due to the axial symmetry of the problem) and also that \bar{A} has only a $\hat{\phi}$ component, so that $\bar{A}(r, \phi, z) = A_\phi(r, z)\hat{\phi}$.

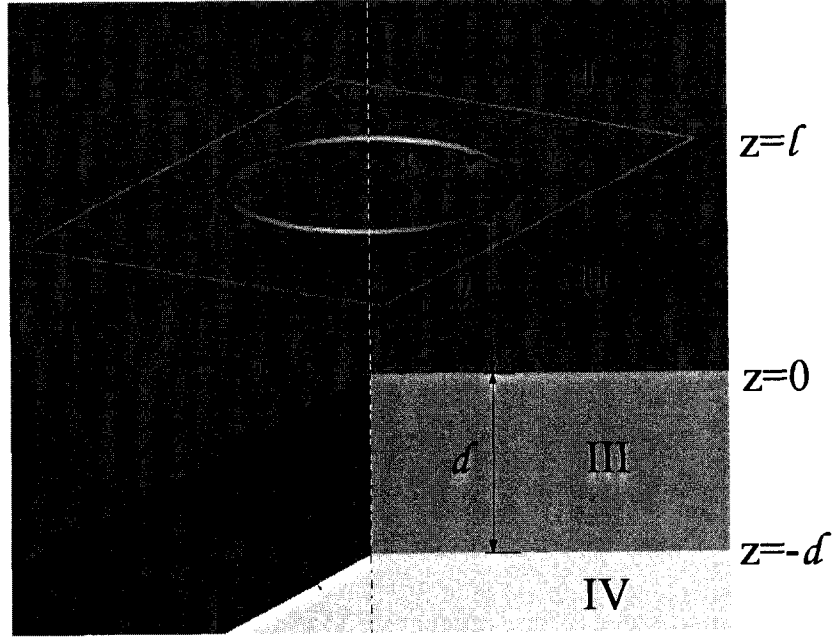


Figure 3.10: Current Loop above the Metal Sheet. Here a current loop is parallel with an infinite large metal sheet with thickness d . The distance between the loop and the sheet is l . Denote the space above the loop as region I, between loop and sheet as region II, inside the sheet as region III, and below the sheet as region IV.

From $\vec{B} = \nabla \times \vec{A}$, we have

$$\vec{B} = \nabla \times (A_\phi \hat{\phi}) = -\frac{\partial A_\phi}{\partial z} \hat{r} + \frac{1}{r} \frac{\partial}{\partial r} (r A_\phi) \hat{z}.$$

We divide the space into regions I, II, III, IV, the space above the loop as region I, between loop and sheet as region II, inside the sheet as region III, and below the sheet as region IV, shown in Fig. 3.3. In the region I, II, and IV, which is outside of the metal sheet,

$$\partial^2 A_\phi / \partial r^2 + \partial^2 A_\phi / \partial z^2 + \frac{1}{r} \partial A_\phi / \partial r - \frac{A_\phi}{r^2} = 0.$$

In the region III, where the metal presents a finite conductivity,

$$\partial^2 A_\phi / \partial r^2 + \partial^2 A_\phi / \partial z^2 + \frac{1}{r} \partial A_\phi / \partial r - \frac{A_\phi}{r^2} - s\mu\sigma A_\phi = 0.$$

The boundary conditions require that the the vector potential is continuous on the boundary, and the discontinuity of the divergence of the vector potential on the boundary is only due to the existence of the current loop between region I and region II.

$$\begin{aligned} A_\phi^{(I)}(r, l) &= A_\phi^{(II)}(r, l), \\ \frac{\partial}{\partial z} A_\phi^{(I)}(r, l)|_{z=l} &= \frac{\partial}{\partial z} A_\phi^{(II)}(r, l)|_{z=l} - \mu I \delta(r - r_0), \\ A_\phi^{(II)}(r, 0) &= A_\phi^{(III)}(r, 0), \\ \frac{\partial}{\partial z} A_\phi^{(II)}(r, l)|_{z=0} &= \frac{\partial}{\partial z} A_\phi^{(III)}(r, l)|_{z=0}, \\ A_\phi^{(III)}(r, -d) &= A_\phi^{(IV)}(r, -d), \\ \frac{\partial}{\partial z} A_\phi^{(III)}(r, l)|_{z=-d} &= \frac{\partial}{\partial z} A_\phi^{(IV)}(r, l)|_{z=-d}. \end{aligned}$$

In the region III, separation of variables $A_\phi(r, z) = R(r)Z(z)$ gives:

$$\begin{aligned} r^2 d^2 R / dr^2 + rdR/dr - R - \alpha^2 R &= 0, \\ d^2 Z / dz^2 + \alpha_1^2 Z &= 0, \end{aligned}$$

where $\alpha_1^2 = \alpha^2 + s\mu\sigma$, and α is the “constant” from separation of functions.

The radial equation has the solution $R(r) = aJ_1(\alpha r) + bY_1(\alpha r)$, where $J_1(\cdot)$ and $Y_1(\cdot)$ are Bessel functions of the first and second kind, respectively, with order 1. For $R(r)$ to be finite at $r = 0$, b must be zero. The equation for $Z(z)$ has solution $Z(z) = Ae^{-\alpha_1 z} + Be^{\alpha_1 z}$.

The general solution for each region is thus

$$A_\phi(r, z) = \int_0^\infty [B(\alpha)e^{-\alpha z} + C(\alpha)e^{\alpha z}] J_1(\alpha r) d\alpha.$$

In each region,

$$\begin{aligned}
A_{\phi}^{(I)}(r, z) &= \int_0^{\infty} B_1(\alpha) e^{-\alpha z} J_1(\alpha r) d\alpha, \\
A_{\phi}^{(II)}(r, z) &= \int_0^{\infty} [B_2(\alpha) e^{-\alpha z} + C_2(\alpha) e^{\alpha z}] J_1(\alpha r) d\alpha, \\
A_{\phi}^{(III)}(r, z) &= \int_0^{\infty} [B_3(\alpha) e^{-\alpha z} + C_3(\alpha) e^{\alpha z}] J_1(\alpha r) d\alpha, \\
A_{\phi}^{(IV)}(r, z) &= \int_0^{\infty} C_4(\alpha) e^{\alpha z} J_1(\alpha r) d\alpha.
\end{aligned}$$

Applying the boundary conditions:

$$\begin{aligned}
B_1 e^{-\alpha l} &= B_2 e^{-\alpha l} + C_2 e^{\alpha l}, \\
-B_1 e^{-\alpha l} &= -B_2 e^{-\alpha l} + C_2 e^{\alpha l} - \mu I r_0 J_1(\alpha r), \\
B_2 + C_2 &= B_3 + C_3, \\
-B_2 + C_2 &= \frac{\alpha_1}{\alpha} (-B_3 + C_3), \\
B_3 e^{\alpha_1 d} + C_3 e^{-\alpha_1 d} &= C_4 e^{-\alpha d}, \\
-\alpha_1 B_3 e^{\alpha_1 d} + \alpha_1 C_3 e^{-\alpha_1 d} &= \alpha C_4 e^{-\alpha d},
\end{aligned}$$

and solving the above equations, we obtain

$$B_1(\alpha) = \frac{1}{2} \mu I r_0 J_1(\alpha r_0) \left[e^{\alpha l} + \frac{(\alpha_1^2 - \alpha^2) + (\alpha^2 - \alpha_1^2) e^{2\alpha_1 d}}{-(\alpha_1 - \alpha)^2 + (\alpha_1 + \alpha)^2 e^{2\alpha_1 d}} e^{-\alpha l} \right].$$

The first term in this expression is simply, the static magnetic field generated by the current loop without the perturbation from the existence of the metal sheet. The effect of the metal sheet is characterized by the second term which gives rise to the vector potential $\Delta \bar{A}_{\phi}^{(I)}$ due to the eddy currents:

$$\Delta \bar{A}_{\phi} = \frac{\mu I(s) r_0}{2} \int_0^{\infty} J_1(\alpha r_0) J_1(\alpha r) e^{-\alpha(z+l)} \frac{(\alpha_1^2 - \alpha^2) + (\alpha^2 - \alpha_1^2) e^{2\alpha_1 d}}{-(\alpha_1 - \alpha)^2 + (\alpha_1 + \alpha)^2 e^{2\alpha_1 d}} d\alpha.$$

We define the kernel function $K(s)$ as

$$K(s) = \frac{(\alpha_1^2 - \alpha^2) + (\alpha^2 - \alpha_1^2)e^{2\alpha_1 d}}{(\alpha_1 - \alpha)^2 - (\alpha_1 + \alpha)^2 e^{2\alpha_1 d}}.$$

In the time domain, the transient eddy current can be expressed as

$$\Delta A_\phi(t) = -\frac{1}{2}\mu r_0 \int_0^\infty J_1(\alpha r_0) J_1(\alpha r) e^{-\alpha(z+l)} \mathcal{L}^{-1}[I(s) * K(s)] d\alpha, \quad (3.4)$$

where the “*” indicates a convolution between heater current and the kernel function, and we exchanged the order of integration without strict justification. The above results are exact up to the quasi-static approximation, yet it is hard to get an intuitive idea how to optimize the current pulse from this expression. We make the rough approximation of a good conductor, equivalent to the assumption $|\alpha_1| \gg \alpha$, such that

$$K(s) = \frac{(\alpha_1^2 - \alpha^2)(1 - e^{-2\alpha_1 d})}{\alpha_1^2(1 - \frac{\alpha}{\alpha_1})^2[1 - (\frac{\alpha_1 - \alpha}{\alpha_1 + \alpha})^2 e^{-2\alpha_1 d}]} \approx \frac{s\mu\sigma}{\alpha^2 + s\mu\sigma}. \quad (3.5)$$

This shows the familiar result of Eq. 3.3, where $i\omega$ is replaced by s . The inverse Laplace transform of $K(s)$ yields the result

$$K(t) = \delta(t) - \frac{\alpha^2}{\mu\sigma} e^{-\frac{\alpha^2}{\mu\sigma} t}.$$

The convolution of the Dirac delta function with the driving current simply gives the component proportional to the driving current, which will vanish together with the turn-off of driving current. The second term in $K(t)$ produces a lasting decay component. Over the interesting spatial scale, we can ignore the contribution from $\alpha \gg l^{-1}$ due to the factor of $e^{-\alpha l}$ in Eq. 3.4, so that the condition $|\alpha_1| \gg \alpha$ will always hold as we recall that $\alpha_1^2 = \alpha^2 + s\mu\sigma$. α^{-1} can be treated as the characteristic scale of the system. From the equation above, we observe that the time scale over which eddy currents persist is $\tau_e \sim \mu\sigma/\alpha^2$, which will be substantially long for small α .

To further investigate the situation, we make the approximation

$$K(s) \approx 1 - \frac{\alpha^2}{s\mu\sigma}, \quad (3.6)$$

appropriate for $\frac{\alpha^2}{s\mu\sigma} \ll 1$, and simplify the problem by only considering the magnetic field along the symmetry axis $r = 0$. In this case

$$\begin{aligned} \Delta \vec{B}(t, r = 0) &= \mathcal{L}^{-1}[\vec{B}(s)], \\ \Delta \vec{B}(s, r = 0) &= -\frac{1}{2}\mu r_0 \int_0^\infty \alpha e^{-\alpha(z+l)} J_1(\alpha r_0) I(s) K(s) d\alpha \hat{z} \\ &\approx \frac{1}{2}\mu r_0 \int_0^\infty \alpha e^{-\alpha(z+l)} J_1(\alpha r_0) I(s) \left(-1 + \frac{\alpha^2}{s\mu\sigma}\right) d\alpha \hat{z} \\ &= \vec{B}_1(s, r = 0) + \vec{B}_2(s, r = 0). \end{aligned}$$

Here

$$\begin{aligned} \vec{B}_1(s, r = 0) &= -\frac{I(s)}{2}\mu r_0 \int_0^\infty \alpha e^{-\alpha(z+l)} J_1(\alpha r_0) d\alpha \hat{z}; \\ \vec{B}_2(s, r = 0) &= \frac{r_0 I(s)}{2\sigma s} \int_0^\infty \alpha^3 e^{-\alpha(z+l)} J_1(\alpha r_0) d\alpha \hat{z} \\ &= \frac{I(s)}{s} \frac{3r_0^2}{2\sigma} \frac{[(l+z)^2 - r_0^2]}{[r_0^2 + (l+z)^2]^{7/2}} \hat{z}. \end{aligned}$$

Notice that the upper bounds of the integration have been extended to the infinity approximately as $e^{\alpha(z+l)}$ term makes the contribution from large α negligible.

$\vec{B}_1(s)$ gives rise to the same temporal character as the driven pulse $I(s)$, reflecting the damping effect due to the adjacent metal sheet. However, we are more interested in the second term $\vec{B}_2(s)$, which governs the residual magnetic field during the times that the driving pulse is off. The *temporal* characteristic of the residual magnetic field $B_2(t)$ due to eddy current is

$$B_2(t) = \mathcal{L}^{-1}[B_2(s)] \propto \mathcal{L}^{-1}\left[\frac{I(s)}{s}\right] = \int_0^t I(t') dt'. \quad (3.7)$$

We wish minimize $|\int_0^T I(\tau)d\tau|$ in the period of pulse T under the constraint of

$$\int_0^T I^2(t')dt' = P \cdot T/R_h,$$

where R_h is the resistance of the heater, and P is the total power the heater consumes.

It is easy to see that only an oscillatory waveform without a DC component can make

$$\int_0^T I(t')dt' = 0.$$

A DC square pulse $I(t) \propto h(t - \frac{T}{20}) - h(t - \frac{19T}{20})$, will result in a non-zero temporal integral of the current, which in turn induce a long-persisting eddy current. Yet if we apply a sinusoidal wave with a square pulse envelope, $I(t) \propto \sin(2f\pi t) [h(t - \frac{T}{20}) - h(t - \frac{19T}{20})]$, the integral of Eq. 3.7 will give $\sim \sin(\frac{9f\pi T}{10}) \sin(f\pi T)/f\pi$, suppressed by using a high frequency, which justifies our original thoughts. If we introduce a ramp in the pulse's rising and falling edges using one quarter period of sine function as the envelope, to make overall waveform have the envelope and its first derivative continuous everywhere (see Eq. 3.2 and Fig. 3.3), the integral of Eq. 3.7 will give

$$-\frac{25}{4f\pi(f^2T^2 - 25)} \left[\cos\left(\frac{f\pi T}{10}\right) + \cos\left(\frac{3f\pi T}{10}\right) - \cos\left(\frac{17f\pi T}{10}\right) - \cos\left(\frac{19f\pi T}{10}\right) \right],$$

with higher order of suppression as $\frac{1}{f(f^2T^2 - 25)}$.

However, Eq. 3.7 is rather a simplified model to measure the eddy current persistence and can not justify the superior performance of ramp-envelope sinusoidal wave over the square-envelope sinusoidal wave as both can give the zero result of the integral of Eq. 3.7 with appropriate choice of the frequency. We need to consider the transient phenomena due to the discontinuity during switch-on and switch-off. The square pulse case is studied in Ref. [59]. Let us examine the approximation on Eq. 3.5 again. Contrary to the condition leading to Eq. 3.6, for large α ,

$$K(s) \approx \frac{s\mu\sigma}{\alpha^2} - \left(\frac{s\mu\sigma}{\alpha^2}\right)^2.$$

Although the integral in Eq. 3.4 is suppressed by $e^{-\alpha t}$ for large α , according to the property of the Laplace transform,

$$\mathcal{L}^{-1} \left[s^n F(s) - s^{n-1} f(0^-) - \dots - f^{(n-1)}(0^-) \right] = f^{(n)}(t)$$

with $F(s) = \mathcal{L}[f(t)]$. In our case, the waveform is flat initially, so $I(0^-) = 0$ and $I^{(i)}(0^-) = 0$ for all $i \in \mathcal{N}$. The discontinuity of the differentiation of the waveform in time will contribute significantly to the behavior of eddy current as the next order differentiation will be a delta function. It is hard to get an analytical solution to complete the rest of integration in Eq. 3.4 and we have to resort to the numerical method. A numerical calculation based on the exact solution Eq. 3.4 confirms a significant suppression of residual eddy currents using ramp-envelope waveform. The magnetic field due to the residual eddy current is smaller than 0.1nG in the same geometry we used in the previous estimation. The conclusion we draw from above analysis justifies our original thoughts.

The ramp-envelope waveform has been applied to the heating scheme. The waveform with 16000 sample points is generated by *Mathematica* program and saved in spread sheet format. Agilent software *IntuiLink* loads the spread sheet and sends the waveform to Agilent arbitrary waveform generator 33120A. The output of Agilent 33120A is fed through a low-pass filter box to smooth away the digitized steps in the waveform, then goes into the input ports of audio amplifiers to drive the heaters.

3.4 Plunger

The vapor cell is held together firmly by gravity and by the force from the plunger. The cell is assembled in the open air environment so it is necessary to evacuate the vapor cell through a small hole opened on the top electrodes (see Fig. 3.1) at low temperature before PbO vaporizes. It has been observed that gaseous contaminants such as water vapor and carbon dioxide, quench the a(1) PbO state and shorten the state life time. The plunger

system is designed to enable us to open the cell to evacuate it during pumping yet maintain a vacuum seal inside the vapor cell when lowered.

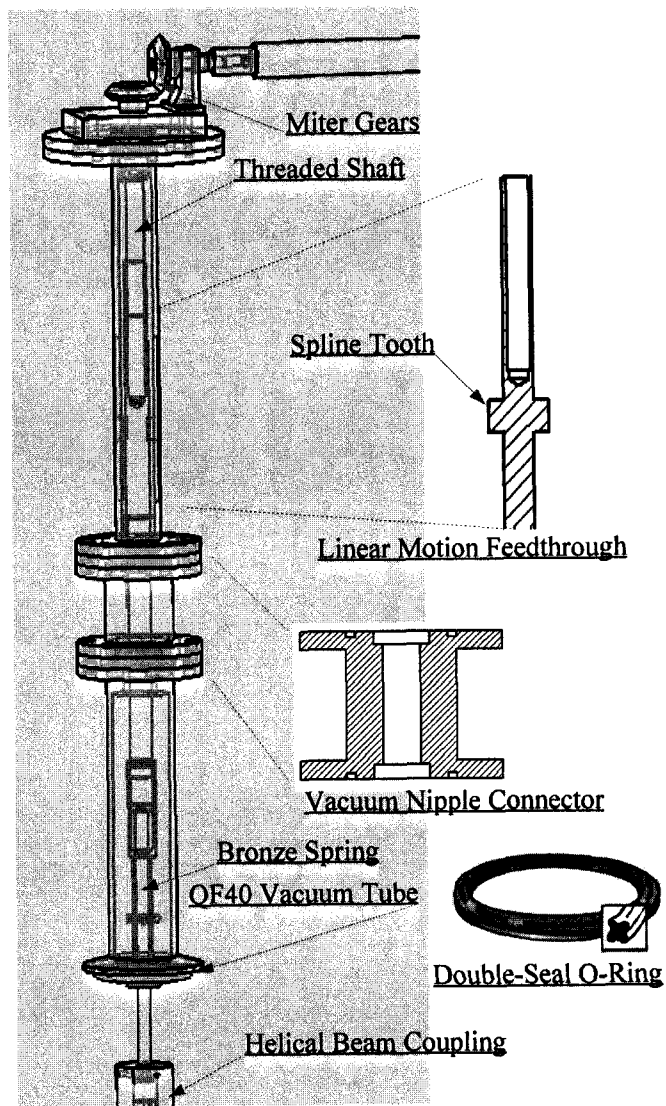


Figure 3.11: Plunger System. The cross sections of linear motion feedthrough, vacuum nipple connector, and double-seal O ring are shown together.

Commercial plungers typically contain ferromagnetic material such as stainless steel for spring and shaft. We have designed and constructed our own plunger excluding the usage of magnetic materials. Shown in Fig. 3.11, from top to bottom, a pair of brass miter gears are put together with rotational axes at right angles. Miter gears are used for their efficient

transmission of motion between intersecting shafts at a right angle. The horizontal shaft extends outside of the magnetic shields and is turned by hand. A threaded vertical shaft driven by the miter gear is coupled to a linear motion feedthrough to convert the rotation to linear translation in the up or down direction. A spline tooth extruded sideways from the linear motion feedthrough is constrained in a slot to limit the displacement range. The axial seal and radial seal are provided by the O-rings sitting inside the vacuum nipple connector as the mid-part of the plunger system, provide good vacuum seal and allow the translation feed into the vacuum chamber by shaft. Double-seal O rings with X-shape cross section are used for the axial seal around the movable shaft. An aluminum QF-40 vacuum tube is used to mount the plunger system to the top plate of vacuum chamber. Inside the tube, a flexible coupling is used to allow some compression on the cell. Phosphor bronze spring (alloy ASTM B 159, contain $\text{Fe} \leq 0.1\%$) and aluminum helical beam couplings are used in place of steel counterparts used in commercial products. An alumina rod with a polished end is coupled to the shaft and provides the seal to the hole on the top electrode plate. The plunger heater around the rod prevents the thermal gradients to the rest of the oven when the oven is heated up.

3.5 Non-Magnetic BNC Feedthrough

Commercial vacuum co-axial feedthroughs typically contain some ferromagnetic components or plating material, thus custom co-axial feedthroughs were designed to replace them. The co-axial feedthrough consists of an outer brass ground tube and center pin to conduct the electrical signal through the vacuum chamber, as shown in Fig. 3.12. One end of the ground tube is open to the air with an inner thread to mate with a BNC plug, and the other half has outer threads such that hex nuts can be used to fasten the tube as it goes through the holes on an alumina QF-40 flange. A brass rod serving as the ground lead is attached to a hex nut mounted on the vacuum end of the tube. Additional nuts are used to lock down the BNC plug and ground lead nut. The center pin is made out of 2-56

threaded rods with a nut and a smooth sleeve tube weld close to one end. The center pin goes through Delrin spacer and bushing with a small O-ring sandwiched between the spacer and bushing to provide axial sealing. Some spacers and bushings were made out of Teflon. Either material works well. The bushing is pushed against the shoulder inside the ground tube with another O-ring sandwiched in between to provide radial sealing. In a symmetric way, there are similar sealing components on the other side of the shoulder. Then a hex nut is mounted along the center pin to fasten the bushings together. Further in the very end, an alumina washer fixed with two 2-56 nuts serves as a centering spacer. Barrel connectors are mounted to the center pin and the ground pin to connect the leads coming out from the oven. Quartz sleeves are sometimes inserted around the barrel connectors as insulation.

Each QF-40 flange contains three BNC feedthroughs to save space. Alumina is chosen as the flange material to insulate the feedthroughs. The outer surface of the alumina QF-40 flange is well polished to provide good contact surface for the O-ring which is embedded in the groove located at the outer shoulder of the ground tube. The flat part of flange is made thicker to strengthen the flange and has a tilt edge to adapt easily with the standard vacuum fastening components. The groove is compatible to the standard centering O-ring. Aluminum supporting rings are used to hold the flange onto the vacuum chamber wall. A small cross-section O-ring with diameter slightly smaller than the flange is placed between the flange and the aluminum supporting ring to even out the pressure and avoid cracking the flange. All BNC plugs and coaxial cables connected to the feedthroughs inside the shield are free from ferromagnetic materials.

3.6 Magnetic Shield and Magnetic Coils

Magnetic shields eliminate problems due to ambient magnetic field fluctuations and field gradients. Mu-metal is a high permeability ferromagnetic material commercially available for magnetic shielding. Multilayer Mu-metal shields are used in our experiment to improve the shielding effect. Considerable engineering and construction efforts were taken to

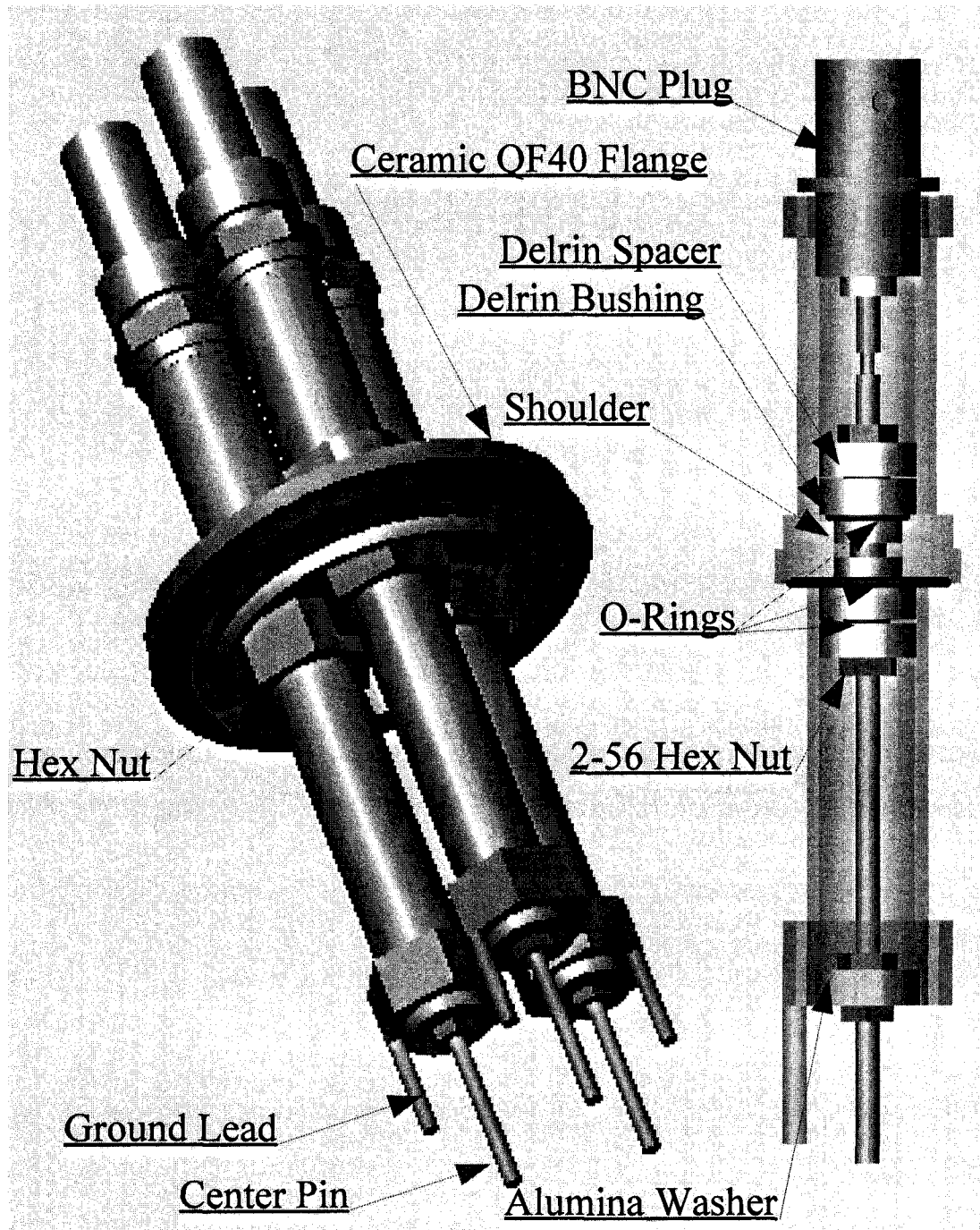


Figure 3.12: Non-Magnetic BNC Feedthrough.

ensure good mechanical overlap between rims of the lids, and coverage of end caps and holes needed for optical access and electrical feedthroughs. Normal experimental usage involves the flipping of magnetic field during runs, or, the disassembling and reassembling of shields to access the chamber. Both of these can cause the significant change of internal magnetic field distribution inside the shields. In these cases, the shield assembly must be degaussed by inducing an alternating magnetization in the shields. This degaussing process is accomplished with several current loops around each layer of the shields and the end caps, carrying gradually reducing alternating currents which drive the magnetization of these shields from the initial condition of saturation to zero. The rate of current decrease is much less than the frequency of current reversal to make sure the magnetization after saturation is approximately symmetric on reversal, such that no net magnetization remains when the current amplitude reduces to zero.

Care must be taken with magnetic field noise from the shields themselves. Johnson noise currents in the magnetic shields produce magnetic fields and magnetic field gradients that are flat in frequency space. Slow variations of the temperature cause small mechanical stresses, leading to $1/f$ noise. Magnetic noise can also come from Johnson noise in hot conducting materials such as the cell electrodes or oven heaters, from eddy currents resulting from changes in the magnetic field, or from switching off the currents through the heaters (see Section 3.3). These effects must be measured carefully in the future.

The magnetic shield setup is shown in Fig 3.13. There are four layers of shields. Each layer of magnetic shield consists of two half-cylinders and two end caps. An aluminum support structure is constructed to fix the top and bottom end caps in place. The magnetic shields are bolted together firmly to ensure a tight contact with the edges of the top and bottom end caps. The center hole of the bottom end cap is left for the aluminum vacuum system and the top hole is left for the cable and water connections feeding into the shields.

A set of Helmholtz coil used to generate vertical homogeneous magnetic field is wrapped on a circular plastic frame around the vacuum chamber inside the magnetic shield, with minor modification of the coil pair spacing to account for the homogenizing effects of the

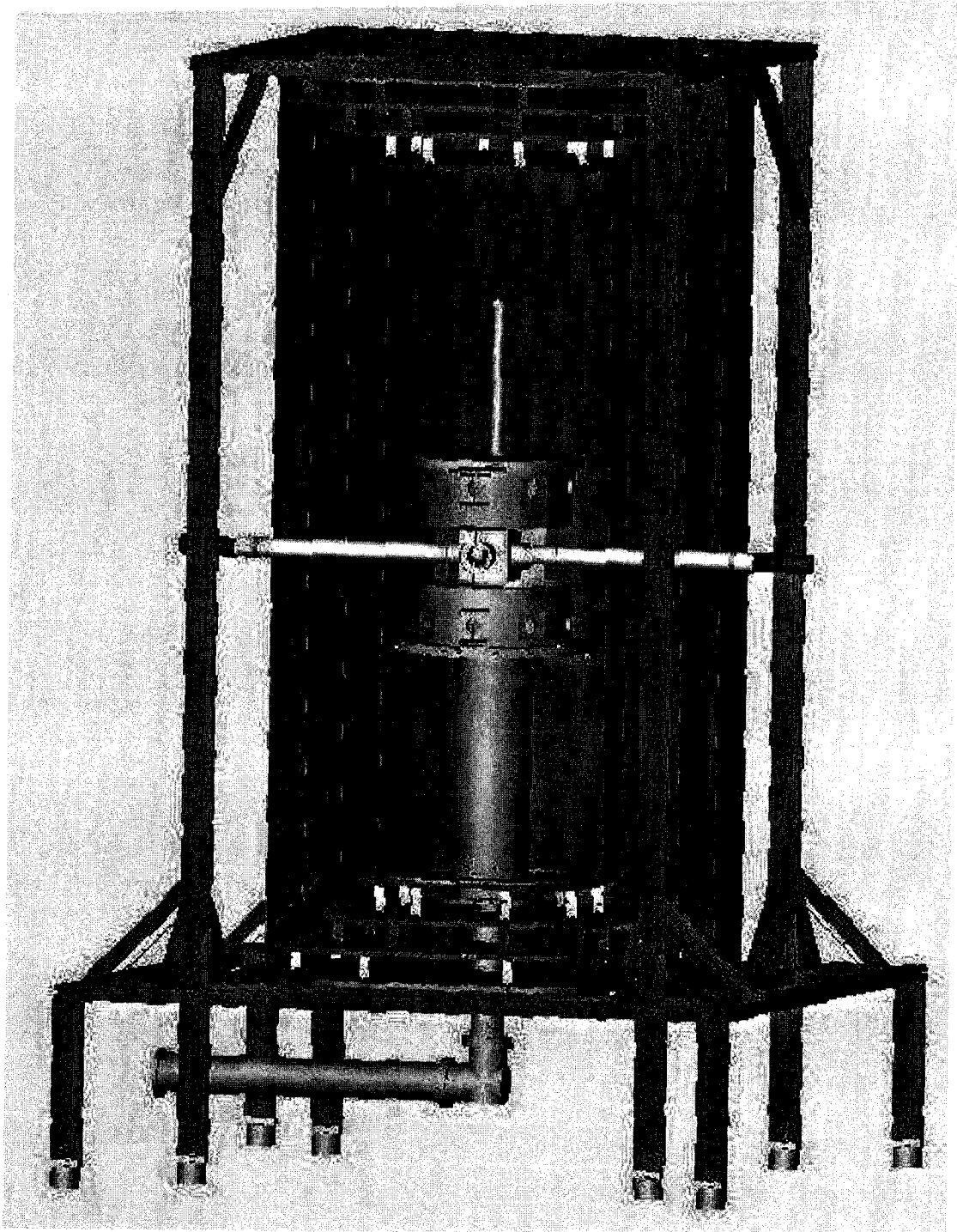


Figure 3.13: Magnetic Shields and Aluminum Supports

magnetic shielding. Additional anti-Helmholtz coils are used to generate the magnetic gradient in the \hat{z} direction. Two pairs of auxiliary coils in anti-Helmholtz configuration, with a "cosine" distribution winding to form a current cage around the chamber, are used to generate magnetic gradients in the \hat{x} and \hat{y} directions. Two similar cage coils, in Helmholtz configuration, are used to generate the magnetic field along the \hat{x} and \hat{y} direction, in order to tip the magnetic field when adjusting the alignment of the magnetic field and the electric field. All of these auxiliary coils are also used as diagnostics for systematics.

3.7 High Voltage Amplifier

The Ω -doublet feature provides excellent diagnostics for systematics related to the electric field flipping, as we can simply change the microwave frequency to address the different Ω -doublet pairs and flip the intra-molecular electric field without any change to the external electric field. The near equality of the g-factors of the polarized levels in PbO a(1) state indicates the possibility to suppress systematic effects substantially (see Section 2.6.3). Thus, it will be helpful to provide nearly perfect electric field reversal. We targeted a goal of $\bar{E}/\delta E \ll 10^{-5}$, to take full advantage of the systematic suppression mechanism. With a nominal value of 300 V applied to the field electrodes, the voltage discrepancy in reversal should be kept much smaller than 30 mV, say below tens of millivolt, to achieve this condition.

We require a linear amplifier capable of providing an output in excess of ± 400 V, across a predominantly capacitive load, with changes on the time scale of milliseconds. In order to meet the experimental requirement of flipping the high voltage to high accuracy in a time scale shorter than the ambient magnetic field drift, the challenge is to build a high voltage amplifier that can boost the output of a voltage standard with excellent reversibility and stability. Previous attempts using commercial HV amplifier chips provided unsatisfactory results, due to the high cost and fragility of these chips. Here a simple circuit, described

below, has been implemented with high-voltage capability, low power consumption, and excellent linearity and reversibility, employing voltage feedback via photovoltaic coupling around a high-voltage MOSFET ladder.

3.7.1 Circuit Design

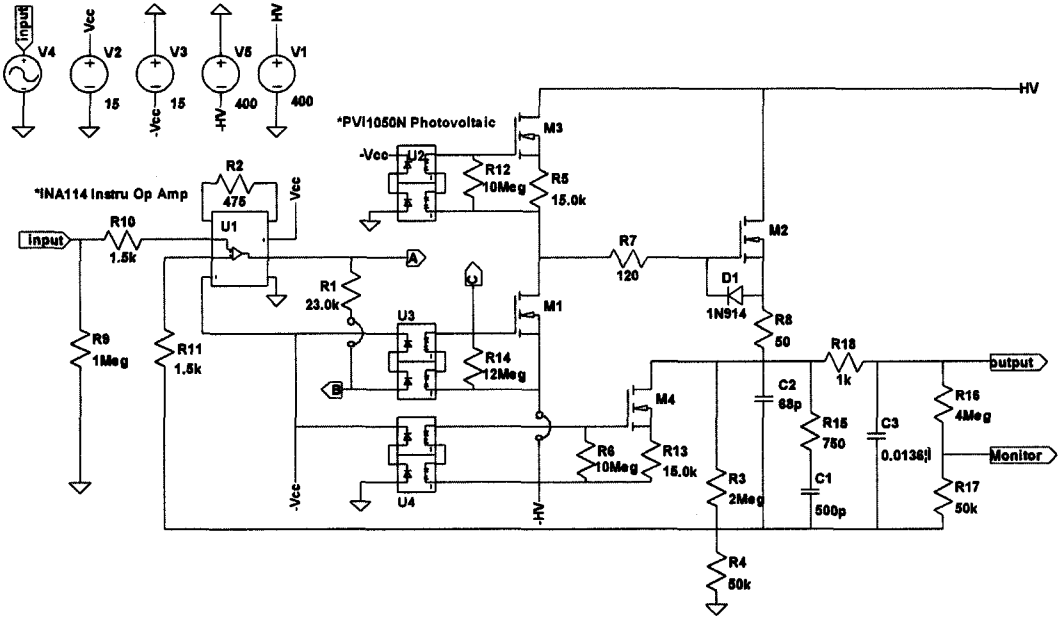


Figure 3.14: Schematic Diagram of High Voltage Amplifier. U1 is INA114, an instrumentation amp; U2 through U4 are PVI1050N photovoltaic driver; M1 through M4 are high-voltage n-channel MOSFETs TP3N120.

A resistive pull-up amplifier is constructed using complementary NMOS transistors. Negative feedback is applied to control nonlinearity in the optical DC isolation between the low voltage input driver stage and the high voltage output stage. The charging resistors are replaced by a constant-current source. The output of the high-voltage amplifier is symmetrically bipolar.

Bias and Feedback Network

The bias-voltage and feedback circuits comprise a resistive potential divider and optovoltaic coupler, shown in Fig 3.14. A constant fraction of the output voltage is obtained via the potential divider R3 and R4, and applied to the non-inverting input of the operational amplifier INA114, which achieves the feedback control capability together with the inverting cascaded MOSFET amplifier stage. The inverting input of the INA114 is connected to the external input voltage to compare with the feedback voltage, and R2 determines the output gain of the operational amplifier. The output of the INA114 adds with the $-V_{cc}$ bias voltage to drive a photovoltaic coupler PVI1050N from *International Rectifier*, and the resistor R1 determines the operating point of the photovoltaic coupler. The photovoltaic driver is biased to operate with bipolar input, maintain the quiescent output, and maximize the linear output voltage range,

The choice and adjustment of these bias and feedback components is critical in obtaining optimal amplifier performance. R1, R3 and R4 must be high-quality components and have low thermoresistance coefficients to minimize variation in their values which will affect the circuit's linearity, stability and reversibility. The INA114 instrumentation amplifier is preferred due to its low input-offset voltage and low input-bias current. In addition, the INA114 features excellent stability of offsets and gain over time and temperature. The PVI1050N photovoltaic drivers have been chosen for their low cost, low capacitance, good linearity, high-frequency response, relatively low dark current, and sufficiently high responsivity.

Output Stage

M1 through M4 are high-voltage n-channel MOSFETs, which have maximum drain-to-source and gate-to-drain voltage ratings of 1200 V. These FETs are well-suited for high-voltage push-pull circuits. M1 and M2 form a push-pull high-voltage amplifier [60]. M3, M4 and the associated biasing resistors R5 and R13, respectively, form constant-current

sources. Two resistors, R5 and R13, control the current in the MOSFET ladder. The voltage drop across them depends upon the sink current, and apply V_{ds} on the MOSFET to make it behave as the current source. Here we use photovoltaic drivers as a voltage source of V_{gs} on all MOSFETs to eliminate the necessity of battery operation otherwise. Complementary NMOS transistors TP3N120 were used for good linearity performance, without increasing complexity or using expensive components. The low load capacitance, determined by the parallel combination of the electrode capacitance and the coaxial cable capacitance, allows the use of relatively high-value feedback resistors. The purpose of C1 through C3, R15 and R18 in the network is to filter out high frequency oscillation, and dominate the stray capacitance distributed along the output channel. These high value capacitors cancel the ripple of frequencies over 10 Hz from the high voltage supply.

3.7.2 Performance Measurement

Measurements of the stability, gain linearity, and reversibility of the high voltage amplifier were taken over nearly three days. In each step, a random input voltage V_{in} ranging from -8 V to +8 V was generated by a computer-controlled voltage standard 501J from *Electronic Development Corp.*, fed into the input port and held for 5 seconds before taking a measurement; then, the sign was flipped to generate $-V_{in}$ and held for another 5 seconds before taking another measurement. The settling time with load attached is much shorter than one second, and square-pulse-distortion with 1 Hz repetitive rate and full range of output is negligible. Output voltages V_{out}^{\pm} with respect to each input value were recorded using *Hewlett Packard 3455A Digital Voltmeter* (with greater than 1 part per million resolution) and used to check the reversibility $V_{out}^+ + V_{out}^-$. Also, stability and gain linearity were checked by repeating the above steps for a long period of time.

Gain Linearity

By plotting V_{out} vs V_{in} , a measurement of output linearity is accomplished. Residual imperfections cause an offset voltage of the order of a millivolt, as shown in Fig. 3.7.2A.

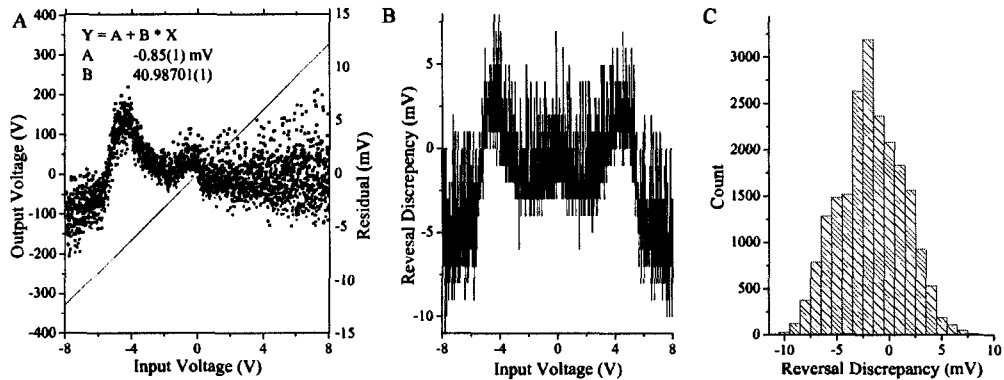


Figure 3.15: Performance Measurement of High Voltage Amplifier. (A) Gain linearity in full range, with an offset voltage of the order of a millivolt. (B) Reversibility $V_{out}^+ + V_{out}^-$ in full range, with maximum discrepancy 10mV. (C) Histogram of the reversal discrepancy.

Reversibility and Stability

In Fig. 3.7.2B, the output voltage reversibility, $V_{out}^+ + V_{out}^-$, is plotted against V_{in} ranging from -8 V to +8 V. Only small discrepancies between output voltages after sign flipping were observed. The histogram of deviations is shown in Fig. 3.7.2C, with standard deviation 3 mV and maximum ± 10 mV. The high-quality feedback and biasing components were chosen to govern the temperature stability of gain and reversibility. A small voltage drift (< 10 mV) was observed by deliberate heating-up of the circuit by about 10°C , but it would be unlikely to suffer such temperature variation under ordinary laboratory conditions. In this respect, the performance is much better than previous high-voltage amplifier schemes attempted in our lab.

In conclusion, the high-voltage linear amplifier described here can provide a single-ended output voltage of up to ± 400 V across a capacitive load with excellent reversibility. It has been demonstrated that this amplifier performs superior to the previous setup. This system has the following features:

1. Its simplicity, low cost and easily replaceable components,

2. Optical coupling allows a high degree of adjustability and utilization of contemporary cheap MOSFET components,
3. Improved linearity and reversibility performance due to high-quality feedback and deep internal gain stages.

Currently, we still work with the unit using the commercial amplifier chip as the commercial chips have much faster frequency response and can be used for high frequency Stark modulation. For final EDM data, we will swap in the new high-voltage linear amplifier.

3.8 Laser Excitation and Fluorescence Detection

3.8.1 Laser Excitation

A pulsed dye laser is used to drive the weakly-allowed transition $X(0) \rightarrow a(1)$ in the first step of the laser-microwave double resonance. A SCANmate 2E dye laser from *Lambda Physik* is equipped with components to suppress the amplified spontaneous emission (ASE) and the output bandwidth of the laser is limited to ~ 1 GHz, which is comparable to the Doppler width experienced by PbO molecules at 700°C . An Nd:YAG laser from *Spectra Physics* serves as the pump laser generating pulses at 532 nm wavelength as the second harmonics of 1064 nm, with 7~10 ns pulse width, 100 mJ per pulse, and a repetition rate of 100 Hz (custom design using two pairs of flash lamps firing alternately, with repetition rate of 50 Hz). The Q-switch triggering TTL pulse of the Nd:YAG laser serves as the timing reference for the rest of the experiment.

Shown in Fig. 2.3, the laser beam coming out of the dye laser is first expanded by a collimating telescope. As the original laser beam is vertically polarized, a $\lambda/2$ waveplate is used to rotate the polarization direction and a Glan-Laser prism inserted to ensure the transmitted beam is linearly polarized along the desired direction. The laser beam is expanded further by another collimating telescope to $\sim 2''$ diameter before going through the $2''$ diameter quartz light pipe.

3.8.2 Beam Homogenizer

It has been observed that the laser beam profile contains an interference pattern of vertical stripe lines, and produces some locally intense spots, leading to the suspicion that PbO in certain regions of the vapor cell is completely saturated by the laser regions. To achieve better excitation efficiency, we tried using an optical diffuser to smooth out the interference pattern. The diffuser will scatter the incident illumination in random directions so that the amplitude and phase of the output light are scrambled into a more uniform distribution. Randomization of the distribution of the scatter centers and modulation of the wavefront play important roles. The intensity homogenization capability and light transmission efficiency are of particular importance.

Volume diffusers, such as opal glass, transmit about 20% of visible light, and even worse, depolarize the incident illumination. As the laser polarization must be preserved to pump the molecules into the desired Zeeman sub-levels, a volume diffuser can not be used as a beam homogenizer.

Surface diffusers [61] preserve polarization and are usually more efficient in the range 70% ~ 90%, depending on the scatter angles, without anti-reflection coatings. Common surface diffusers, such as ground glass and holographic diffusers, scatter light with a Gaussian intensity profile. We tried Engineered DiffusersTM developed at RPC Photonics, shown in Fig. 3.16, which provide a homogeneous distribution of energy with high efficiency within the specified diffusing angles. The engineered distributions of microlens array control the resulting pattern [62]. The microlens are made of injection molded ZEONOR. The diffuser without anti-reflection coating has the transmission efficiency ~ 90%, and is achromatic within wavelength 400 ~ 700 nm, which covers our laser operation wavelength.

The laser beam has ~ 0.5 cm diameter after the first stage of expanding telescope and is polarized by the polarization cube which then illuminates the diffuser. The diffuser is placed at the front focal plane of a lens system with focal length 26 cm. The lens collimates the output of the diffuser and delivers laser light to the back focal plane with all the ray

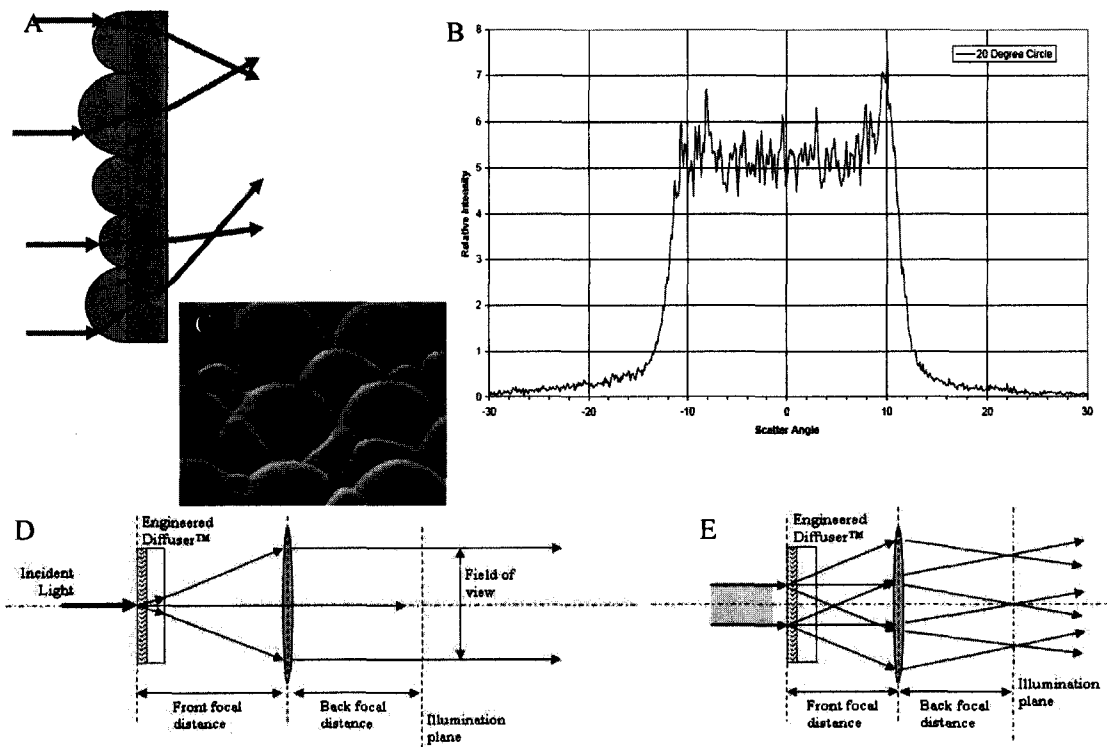


Figure 3.16: Engineered Diffuser. Figure courtesy of RPC Photonics. A) Refractive surface diffuser. B) Illuminating intensity in the diffusing angle. C) Zoom-in image of microlens. D) Homogenizer of small collimated beam. E) Illumination system with finite collimated beam.

bundles parallel to the optical axis. Due to the limited damage threshold of the diffuser, the incident laser beam can't be made too small by focusing it down and collimating. However the finite collimated illumination case, as shown in Fig. 3.16E, will regenerate the initial interference pattern at some position. The homogenizing effect looks good at certain distances. Careful positioning of the optics should avoid the interference pattern reforming in the cell volume and should provide good homogeneous laser illumination.

3.8.3 Fluorescence Collection

To increase the collecting solid angle, the cell window and light pipe are made about two inches in diameter. Light concentrators are needed to adapt the aperture between the light pipe and the photomultiplier with a smaller diameter. Winston cones [63] are used to meet the purpose, which maximize the collection of incoming rays passing through the entrance aperture by allowing off-axis rays to bounce inside several times before passing out the exit aperture, shown in Fig. 3.17. The first Winston cone is inserted between the light pipe extension and the interference filter, and second one matches the aperture of the photomultiplier.

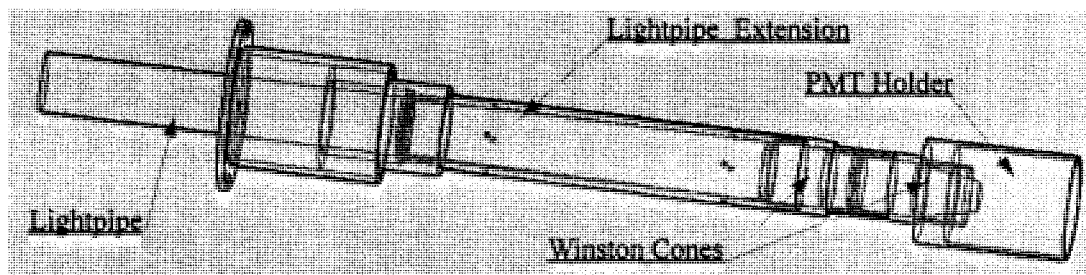


Figure 3.17: Winston Cones and Support.

A Winston cone is an off-axis parabola of revolution, which is governed by the equation of the surface in (r', z') coordinates (shown in Fig 3.18), $r'^2 = 4f(z' + f)$. By rotating the axes,

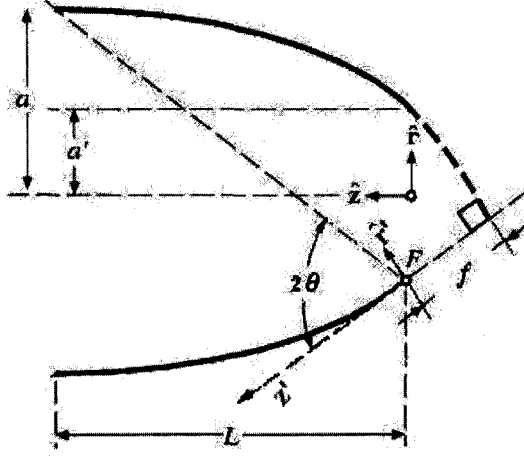


Figure 3.18: Schematic diagram of a Winston cone light concentrator. The entrance and exit apertures are of radius a and a' , respectively. F is the focus of the upper parabola segments, and f is its focal length. The length of the cone is L . The origins and orientations of the focus-centered and symmetry axis-centered coordinate systems are shown also.

$$\begin{bmatrix} r \\ z \end{bmatrix} = \begin{bmatrix} \cos \theta & -\sin \theta \\ \sin \theta & \cos \theta \end{bmatrix} \begin{bmatrix} r' \\ z' \end{bmatrix} - \begin{bmatrix} a' \\ 0 \end{bmatrix},$$

the equation is expressed in (r, z) coordinates with $r = \sqrt{x^2 + z^2}$, a and a' the radius of entrance and exit apertures respectively,

$$(r \cos \theta + z \sin \theta)^2 + a'r(1 + \sin \theta)^2 - 2a'z \cos \theta(1 + \sin \theta) - a'^2(3 + \sin \theta)(1 + \sin \theta) = 0.$$

where θ is the half of opening angle Θ_G . a and a' will completely specify the geometry of Winston cone by

$$\Theta_G \equiv 2\theta = 2 \sin^{-1} \left(\frac{a'}{a} \right).$$

with the relation $L = (a + a') \cot \theta$ and $f = a'(1 + \sin \theta)$.

In our case, the first cone has the radius of entrance aperture $a = 2''$ and exit aperture $a' = 1.8''$, leading to a curve length of $L = 0.92''$; the second Winston cone has $a = 1.8''$ and $a' = 1''$, leading to a curve length of $L = 2.095''$, shown in Fig. 3.19. Both are made

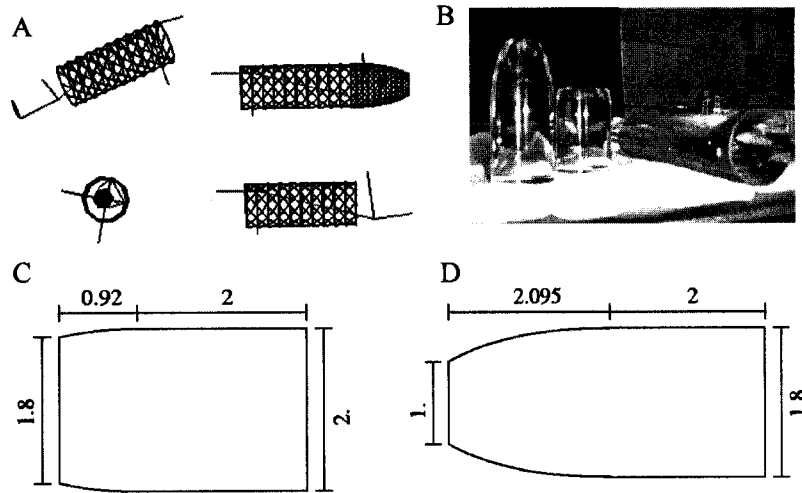


Figure 3.19: Simulation and Sample of Winston Cone. A) Ray-tracing applied to Winston cone geometry. B) Sample of Winston cones. C) and D) Dimension of Winston Cones. The first Winston cone is inserted between the light pipe extension and the interference filter, and second one matches the aperture of the photomultiplier, shown in Fig. 3.17.

out of transparent plastic Lexan. Ray tracing and Monte Carlo simulations have been implemented to verify the optics property of the Winston cone setup and determine the optimal filter design for blocking as much blackbody radiation from the oven as possible [64].

3.8.4 Fluorescence Detection

To achieve high sensitivity to the eEDM, a high counting rate and signal-to-noise ratio are desired. Detection efficiency is of essential importance. The EDM experiment's features of minute signal and high precision impose tough requirements on the fluorescence detector and the associated amplifiers. To approach the shot noise limit of our system and explore the full capability of the proposed scheme, the intrinsic noise in the amplifier must be less than the anticipated shot noise. The bandwidth of the detection circuit must set broad enough not to attenuate the oscillatory quantum beats signal, which is nominally at 300 kHz, yielding the 3 dB point above 900 kHz. Even worse, the large pulse of scattered light from the laser can easily saturate the detection circuit if not handled properly. The

amplifiers need to recover from the scattered light in a short time, comparable to several cycles of the quantum beat signal in order to not lose too much useful signal. The effective a(1) state life time in the vapor is only around $50 \mu\text{s}$.

Great efforts have been taken to optimize the detection efficiency. Three different types of detectors have been built and tested: PMT, APD and PIN photodiodes. PMTs have a large intrinsic gain stage, and can create a voltage across a small resistor with large photoelectric current. The PIN photodiode does not have any internal gain and the APD only has a modest gain. Both the PIN photodiode and the APD require a transimpedance amplifier as a front-end gain stage. The simplified model, shown in Fig. 3.20, for the transimpedance amplifier is used to investigate the noise characteristics.

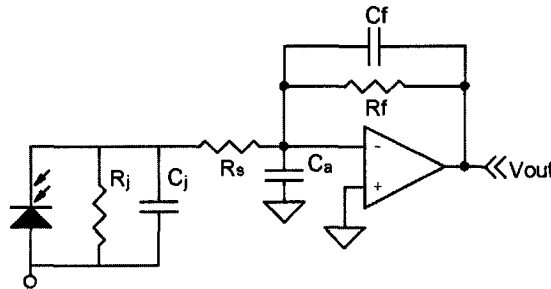


Figure 3.20: Simplified Model for Photodiode Transimpedance Amplifier. A photodiode is modelled as an ideal photodiode in parallel with a junction capacitance C_j , a shunt resistance R_j and a series resistor R_s . C_a is the input capacitance of the amplifier. R_f is a feedback resistance, and C_f is a feedback capacitance.

The details about the detection system have been discussed in Sarah Bickman's thesis [64]. Eventually, based on the noise feature of each detectors and current signal level, shown in Tab. 3.1, PMTs were chosen as our detectors to measure the EDM signal in the current phase.

	Parameter	PMT	PIN	APD	Unit
η_{qe}	quantum efficiency	15%	100%	85%	
η_{col}	collection efficiency	100%	100%	25%	
N_{sig}	available signal	3×10^6	3×10^6	3×10^6	photons/shot
N_{ds}	detected signal	5×10^5	3×10^6	7×10^5	electrons/shot
I_{sig}	signal current	2×10^{-9}	1×10^{-8}	2×10^{-9}	A
G	intrinsic gain	$\sim 10^5$	1	200	
R_f	feedback resistor	100	600	2	$k\Omega$
C_f	feedback capacitor		0.26	62	pf
V_{sig}	signal voltage	2×10^{-2}	6×10^{-3}	8×10^{-4}	V
N_b	total blackbody	1.5×10^7	1.5×10^7	1.5×10^7	photons/shot
N_{db}	detected blackbody	5×10^5	3×10^6	7×10^5	electrons/shot
F	noise factor	1	1	2	
I_{sn}	peak shot noise current	2×10^{-14}	6×10^{-14}	4×10^{-14}	A/\sqrt{Hz}
V_{sn}	shot noise voltage	200	30	20	nV/\sqrt{Hz}
V_{det}	amplifier noise	9	220	8	nV/\sqrt{Hz}
SNR	signal to noise	2×10^5	1×10^5	1×10^5	per pulse

Table 3.1: Signal to Noise Ratio of Detectors [64]. The laser fires at the rate 100 shots per second and the nominal beat frequency is ~ 300 KHz. In this table, the following definition and relations have been applied. η_{col} is the collection efficiency of the detector, determined by the cell geometry, filter transmission, detector aperture, and etc. Detected signal $N_{ds} = N_{sig}\eta_{qe}\eta_{col}$. Signal current $I_{sig} = eN_{ds}/\tau$, where e is the electron charge and τ is the effective life time of the a(1) state. Shot noise of the photoelectric currents is $I_{sn} = \sqrt{2eI_{sig}}\sqrt{FG}$. The output voltage is converted from I_{sig} by the feedback impedance $Z_f = R_f/(1 + i\omega R_f C_f)$, $V_{sig} = Z_f I_{sig}$, and the corresponding shot noise on V_{sig} is $V_{sn} = Z_f \sqrt{2eI_{sig}}\sqrt{FG}$. The additional amplifier noise is Johnson noise and the voltage noise density across a resistor R is $V_J = \sqrt{4k_B T R}$. For PIN and APD, $SNR = V_{sig}/\sqrt{V_{sn}^2 + V_{det}^2}$

Chapter 4

Molecular State Preparation

We have demonstrated the ability to manipulate the internal molecular state to produce the desired states for our EDM experiment, using microwave excitation. Efforts were carried out to optimize the state excitation efficiency. We performed various experiments to confirm our understanding of molecular state evolution dynamics in a variety of experimental configurations.

In this chapter, the details of molecular state preparation scheme using microwaves will be discussed. Although our previous attempt using RF excitation were unsuccessful (see Section 4.1), the microwave excitation scheme provides a convincing demonstration of our ability to populate the desired molecular states (see Section 4.2). An adiabatic following scheme has been implemented to optimize the efficiency of population transfer (see Section 4.3). The experimental results from various configurations and parameter regimes will be compared and discussed.

4.1 Previous Attempts using RF Excitation

The spectral width of pulsed laser and optical Doppler width are too broad to resolve the Ω -doublet levels. Moreover, in the presence of the external electric field $\vec{\mathcal{E}}$, the e and f components of the Ω -doublet levels with $M \neq 0$ are mixed. Both components will

be excited by a laser pulse with horizontal polarization as needed to create the desired $M = \pm 1$ superposition. Thus, a simple laser excitation scheme will prepare the molecule in a superposition of electrical polarizations, instead of a pure EDM state with defined $M\Omega$ value. This will average the EDM signal to zero. Hence, the ability to populate individual Ω -doublet component is necessary to resolve the EDM signal.

In the original proposal of this experiment, we planned to use laser-RF double-resonance excitation to populate $a(1) J=1 v' = 5 e$ and f components separately. Although this method ultimately did not succeed, we describe our efforts in this direction here for completeness.

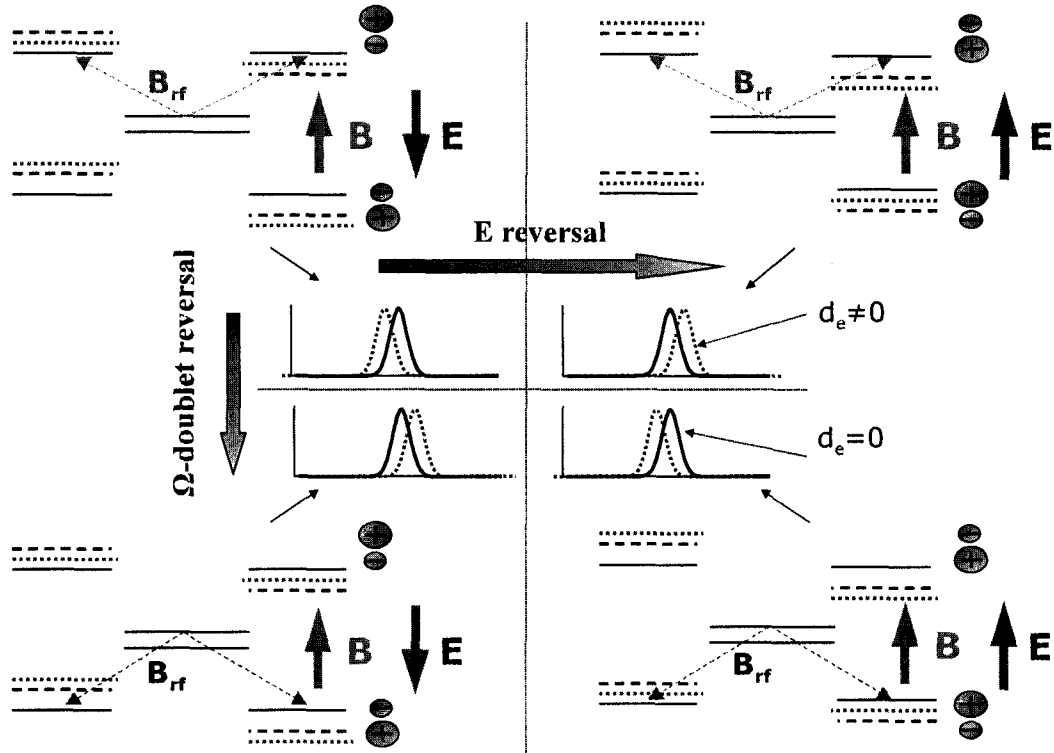


Figure 4.1: RF Excitation Scheme and Mechanism for Systematic Effects Suppression. The signature of an eEDM can be revealed by reversing the applied \mathcal{E} field relative to \mathcal{B} field or tuning the RF frequency to selectively populate one or the other Ω -doublet pair. Solid-line energy levels show Stark shifts; dashed-line show Zeeman shifts; and dotted-dashed-line show the additional linear Stark shift which would arise from a non-zero eEDM.

Laser-RF double-resonance excitation could, in principle, selectively prepare the molecules in a single state of electrical polarization, as shown in Fig. 4.1. By choosing the correct resonant frequency the molecule can be either aligned or anti-aligned to the external electric field $\vec{\mathcal{E}}$. The RF pulse width must be sufficiently short to avoid resolving the Zeeman splitting between $M = \pm 1$ in either \tilde{e} and \tilde{f} components, so that the molecules can be prepared in the spin superposition to generate the quantum beat signal. Short pulse width implies that RF excitation must be sufficiently strong to drive a π -pulse to transfer the population from $M = 0$ to the $M = \pm 1$ superposition. In our case, the time required for a π -pulse $T_\pi \ll \nu_{\text{beat}}^{-1}$, yielding pulse duration $T_\pi \lesssim 1 \mu\text{s}$ and RF field strength $\mathcal{M}_1 \gtrsim 1$ Gauss.

4.1.1 RF Coherent Excitation

In the RF excitation scheme, the relevant states will form a V-shape or Λ -shape energy level diagram, shown in Fig. 4.1. The coherent excitation in such a V-shape system will be studied, shown in Fig. 4.2, and the Λ -shape case is identical. Define Δ as the Stark splitting between lower and upper two levels without Zeeman splitting, $\vec{\mathcal{B}}_1 = \mathcal{B}_1 \cos$ as the RF field, Ω_r as the Rabi frequency, 2ω as the Zeeman splitting between the upper two levels, and ω_0 as the frequency of the external radiation source. We describe the system in the basis $\{|a\rangle, |b\rangle, |c\rangle\}$.

$$i\hbar \frac{\partial}{\partial t} \Psi(t) = H(t) \Psi(t),$$

$$H(t) = \hbar \begin{pmatrix} \Delta + \omega & 0 & -\Omega_r \cos(\omega_0 t) \\ 0 & \Delta - \omega & \Omega_r \cos(\omega_0 t) \\ -\Omega_r \cos(\omega_0 t) & \Omega_r \cos(\omega_0 t) & 0 \end{pmatrix}, \quad \Psi(t) = \begin{pmatrix} a(t) \\ b(t) \\ c(t) \end{pmatrix},$$

where $\Omega_r = |\langle a | \vec{\mu}_B \cdot \vec{\mathcal{B}}_1 | c \rangle| = |\langle b | \vec{\mu}_B \cdot \vec{\mathcal{B}}_1 | c \rangle|$.

We study the resonance case $\Delta \approx \omega_0$ and apply rotating-wave approximation (RWA)

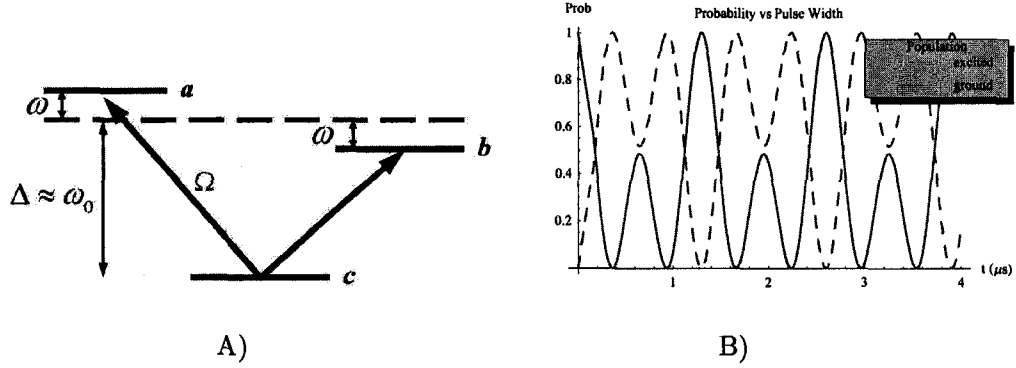


Figure 4.2: V-Shape Level Structure and Transition Probability. A) 2ω is Zeeman splitting between level a and b, Ω_r is the Rabi frequency, and radiation pulse is near resonance with the energy splitting $\Delta \approx \omega_0$. B) The red(blue) line shows the ground(excited) population varies with the pulse width in the coherent excitation.

so the three-level-system Hamiltonian in the rotating frame reads

$$H = \hbar \begin{pmatrix} \omega & 0 & -\Omega_r/2 \\ 0 & -\omega & \Omega_r/2 \\ -\Omega_r/2 & \Omega_r/2 & 0 \end{pmatrix}.$$

Here, the eigenenergies are $\{E_i\} = \{-\Omega_1, \Omega_1, 0\}$, where $\Omega_1 = \sqrt{\omega^2 + \Omega_r^2/2}$, corresponding to eigenvectors $\{|\Psi_i\rangle\}$. Assume the initial state is $|\Phi_0\rangle = \{0, 0, 1\}$. The final state is

$$|\Phi_1\rangle = \sum_i e^{-iE_i t} |\Psi_i\rangle \langle \Psi_i | \Phi_0 \rangle = \frac{1}{2\Omega_1^2} \begin{pmatrix} \omega\Omega_r(1 - \cos \Omega_1 t) + i\Omega_r \sin \Omega_1 t \\ \omega\Omega_r(1 - \cos \Omega_1 t) - i\Omega_r \sin \Omega_1 t \\ 2\omega^2 + \Omega_r^2 \cos \Omega_1 t \end{pmatrix}.$$

The population of each state is shown in Fig. 4.2, where the upper levels' population are the same and equal to $\frac{1}{2} \left[1 - \left(\frac{\omega^2}{\Omega_1^2} + \frac{\Omega_r^2}{2\Omega_1^2} \cos \Omega_1 t \right) \right]$. To transfer completely from the initial state, we need to satisfy $2\omega^2 + \Omega_r^2 \cos \Omega_1 t = 0$, yielding the requirement $\Omega_r \geq \sqrt{2}\omega$. The

complete population transfer occurs at

$$\frac{1}{\Omega_1} \left[2k\pi \pm \arccos \left(-\frac{2\omega^2}{\Omega_r^2} \right) \right],$$

where $k = 0, 1, 2, \dots$. Evidently, this reduces to the ordinary π pulse condition, π/Ω_1 , for the degenerate case when $\omega = 0$. If the π pulse condition holds, the final state ends in $\left\{ \frac{2\omega + i\sqrt{2(\Omega_r^2 - 2\omega^2)}}{2\Omega_r}, \frac{2\omega - i\sqrt{2(\Omega_r^2 - 2\omega^2)}}{2\Omega_r}, 0 \right\} = \left\{ \frac{e^{i\phi}}{\sqrt{2}}, \frac{e^{-i\phi}}{\sqrt{2}}, 0 \right\}$, where $\phi = \arccos \frac{\sqrt{2}\omega}{\Omega_r}$. If the size of Ω_r is comparable to $\sqrt{2}\omega$, the final state will end up in $\{1/\sqrt{2}, 1/\sqrt{2}, 0\}$.

In this RF excitation scheme, the RF pulse drives the M1 transition between $M=0$ and $M = \pm 1$ states. The typical values in our experimental conditions are $\Omega_r \sim 1$ MHz and $\omega \sim 0.15$ MHz, leading to the corresponding pulse width $0.36 \mu\text{s}$, $1.03 \mu\text{s}$, $1.74 \mu\text{s} \dots$. The typical RF pulse width is chosen to be around $1 \mu\text{s}$, so that it is shorter than the beat period to avoid inducing different initial beat phases during excitation and washing out the beat contrast.

4.1.2 RF Experimental Setup

The requirement on a RF experimental setup is that we should drive a RF transition, with pulse with width $\leq 3 \mu\text{s}$, and a frequency ranging from 20 MHz to 70 MHz, and switching between two frequencies 11.2 MHz apart every other laser shot. The setup should sustain 700°C temperature and fit inside the limited space between the oven and vapor cell, without putting any magnetic components close to the vacuum chamber.

We constructed a RF system that could deliver RF pulses with sufficient magnetic field to drive the M1 transition, and switch between frequencies separated by $\Delta_\Omega = 11.2$ MHz to access both Ω -doublet levels of PbO a(1) $^3\Sigma^+$. The fast switching feature, enabled by electromechanical relays, helps to eliminate various sources of systematic error by using the Ω -doublet as an internal co-magnetometer.

Dimensional constraints in the current experimental setup forced us to implement the system using single Helmholtz coils around the vapor cell braced by ceramic supports, and

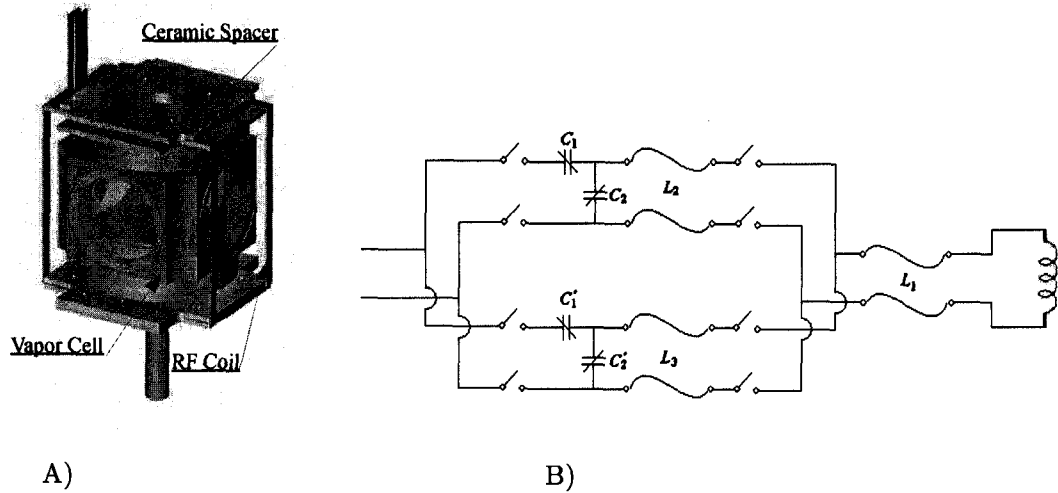


Figure 4.3: RF Coil and RF Network Scheme. A) Square Helmholtz coils made of copper strips are connected in parallel to generate RF pulse; B) High power RF switches are used to swap two separate impedance matching networks into the transmission line connected to the RF coils. Transmission lines L_2 and L_3 with different lengths, satisfy the resonance condition in Eq. 4.2 and are inserted to minimize the reflected power.

a single high power RF amplifier as the source with a long transmission line in between, shown in Fig. 4.3. The square Helmholtz coils are made of copper strips with width 0.25", side length 4.25", and separation 2.08". The RF amplifier is located several meters away from the chamber to avoid generating the spurious magnetic fields during operation. Note that a transmission line of certain length will have a series of resonance frequencies, explained below in Eq. 4.1, at which the existence of the transmission line can be ignored and is equivalent to bring the load directly to the source.

We use impedance matching techniques and a switching circuit to choose different impedance matching networks and lossless coaxial cables of different lengths to drive the rf coils at the chosen resonance frequency, shown in Fig. 4.3. The basic structure is that

1. Each impedance matching network consists of a serial capacitor C_1 and parallel capacitor C_2 , a certain length of cable (L_2 or L_3), and relays to connect or disconnect the output line.
2. A common extension cable (L_1) shared to connect to the Helmholtz coil.

3. The electromechanical relays.

A single-turn square Helmholtz coil is connected parallel to reduce inductance, yielding a self inductance $0.25 \mu\text{H}$ and capacitance 24.7 pF . Low-loss semi-rigid coaxial cables are from *Tim-Co* (Catalog No. L14C), impedance $50 \pm 0.5 \Omega$, outer diameter $0.141''$. Electromechanical relays switch between the two impedance-matched networks, with each network working with typical values of $C_1 \sim 15 \text{ pF}$, $C_2 \sim 60 \text{ pF}$ for 33.6 MHz , or $C_1 \sim 8 \text{ pF}$, $C_2 \sim 25 \text{ pF}$ for 44.8 MHz , etc. These capacitors are variable mica compression trimmers from *Arco Electronics*. The electromechanical relays are *Radiall* RF Coaxial SPDT switch R570313100, with insertion Loss $< 0.20 \text{ dB}$. The switches and impedance matching networks are mounted on double-sided copper clad and enclosed in a $5'' \times 6'' \times 9''$ aluminum box. The enclosure and the copper clad are grounded to the RF cable ground for better shielding.

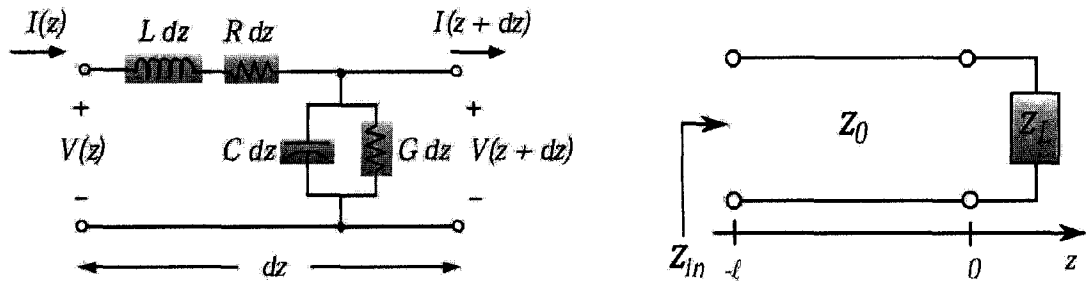


Figure 4.4: Transmission Line Model. Left: Network model is used to derive the telegraph equation for transmission line. Here R is a series resistance per unit length, L series inductance per unit length, G shunt conductance per unit length, and C shunt capacitance per unit length. Right: Load Z_l is connected to the transmission line with characteristic impedance Z_0 , length l .

To explain how this system works, I will give a brief description of transmission line theory. The transmission line, capable of guiding TEM waves, can be modeled as small cascaded circuit elements, shown in Fig. 4.4, where R is a series resistance per unit length, L series inductance per unit length, G shunt conductance per unit length, and C shunt capacitance per unit length. The voltage and current in the transmission line satisfy the

telegraph equation:

$$\frac{\partial V(z)}{\partial z} = \gamma^2 V(z), \quad \frac{\partial I(z)}{\partial z} = \gamma^2 I(z), \quad \gamma = \alpha + j\beta = \sqrt{(R + j\omega)(G + j\omega C)}.$$

In the lossless case, $R = G = 0$, $\beta = \omega\sqrt{LC}$. The general solutions are the superpositions of forward and reverse waves in voltage and current, $V(z) = V_0^+ e^{-\gamma z} + V_0^- e^{\gamma z}$, and $I(z) = I_0^+ e^{-\gamma z} + I_0^- e^{\gamma z}$. The ratio of forward voltage to current is the characteristic impedance $Z_0 = V_0^+ / I_0^+ = -V_0^- / I_0^-$. Denote the load impedance Z_L , the impedance of rf coil. The input impedance $Z_{in} = V(-l) / I(-l)$ is

$$Z_{in} = \begin{cases} Z_0 \frac{Z_L + Z_0 \tanh \gamma l}{Z_0 + Z_L \tanh \gamma l}, & \text{(general)} \\ Z_0 \frac{Z_L + jZ_0 \tan \beta l}{Z_0 + jZ_L \tan \beta l}. & \text{(lossless)} \end{cases} \quad (4.1)$$

Note that in the lossless case, the input impedance is exactly equal to the load impedance and the existence of the transmission line can be ignored, if the length l satisfies the resonance condition,

$$\beta l = \omega l \sqrt{LC} = n\pi, \quad n = 0, \pm 1, \pm 2, \dots \quad (4.2)$$

So we can choose a pair of frequencies, attach the additional cables L_2 or L_3 together with cable L_1 , shown in Fig. 4.3 to compensate for the frequency difference and satisfy the resonance condition Eq. 4.2, and use independent impedance matching network for each frequency. In a simplified version of the RF network setup, around $L_1 = 30'$ long extension cable is used. Such cable will have resonance condition at the multiple frequencies with 11.2 MHz apart, then L_2 and L_3 can be omitted.

f_{rf} (MHz)	P_f (W)	P_r (W)	B_{rf} (Gauss)	T_π (μ s)
33.6	603	44	1.27	0.87
44.8	614	44	1.37	0.8
56.0	647	81	1.03	1.07

Table 4.1: RF Field Strength at Various Frequencies. f_{rf} is the RF frequency, P_f is the forward power, P_r is the reflected power, B_{rf} is the magnetic field strength, and T_π is the π pulse width.

We constructed a system capable of generating a RF field sufficiently strong to drive the RF transition in around $1 \mu\text{s}$, at two frequencies separated by $\Delta_{\Omega} = 11.2 \text{ MHz}$. The results are listed in Tab. 4.1. The RF field is measured using a calibrated pickup coil. The pickup coil is 1/8" diameter pickup loop using 32-gauge magnet wire, with 50Ω SMT resistor in serial and extended using semi-rigid cable. The pickup coil's intrinsic resonance frequency is 206MHz, far beyond our working frequency, hence has flat frequency response at RF frequency range. The forward power P_f and the reflected power P_r are read from the panel of the RF amplifier. The reflected powers are due to the imperfect tuning of the impedance matching networks. The reflected power is small enough that we can still deliver a sufficiently high power RF pulse.

4.1.3 RF Transition Efficiency

We encountered great difficulty to achieving high RF-transition efficiency in exciting the desired a(1) $J = 1$, $M = \pm 1$ spin superpositions. The reason for this difficulty remains elusive and possible explanations will be discussed later. In the meantime, we demonstrated de-excitation of the $M = \pm 1$ superposition states efficiently. We applied a static electric field and drove laser excitation with horizontal polarization to prepare the molecules in the $M = \pm 1$ superposition states, subsequently applied the horizontal RF pulse, and monitored the Zeeman quantum beats. The experimental result was in qualitatively reasonable agreement with the expectation: nearly-complete disappearance of beats with the transition to an $M = 0$ state at the correct frequencies and pulse width T_{π} .

The typical method to carry out the experiment was to fix the RF frequency, and vary the voltage applied on the electrodes, thus changing the Stark energy splitting, to cross through the resonance frequency. Fig. 4.5 shows the beat dips as the electrode voltage scans. As the molecules populate both $M = \pm 1$ states of \tilde{e} and \tilde{f} components by the horizontal polarized laser in the presence of the electric field, the first beat amplitude dip will occur when the energy splitting between $M = \pm 1 \tilde{e}$ and $M = 0 f$ components matches the RF frequency, and second dip occurs when the energy splitting between $M = \pm 1 \tilde{e}$ and

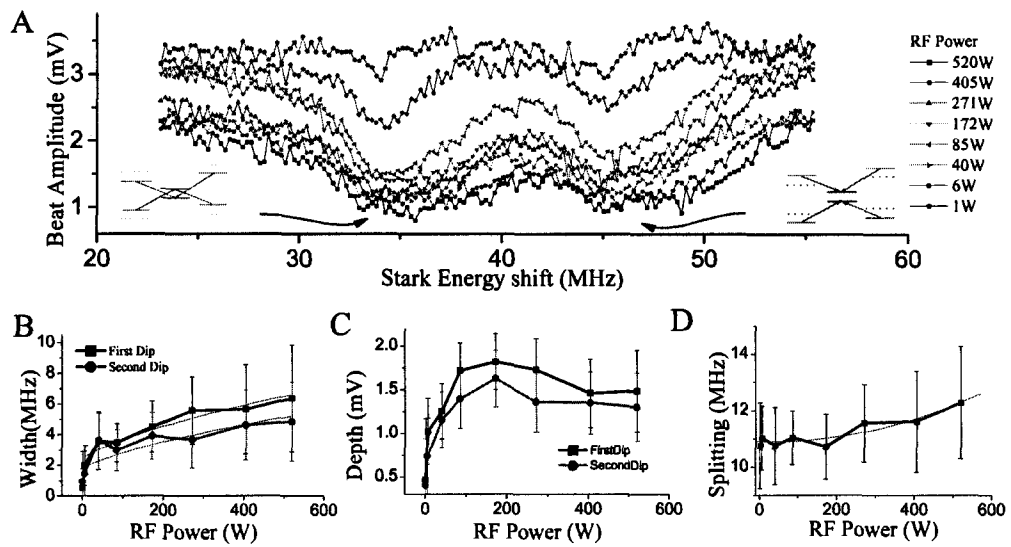


Figure 4.5: Beat Disappearance Experiment using RF transition. A) Experimental data are taken with various RF powers. The x -axis is the stark splitting due to the electric field; B) Beat disappearance dip width broadens due to the power broadening effect. C) Beat disappearance dip depth shows saturation as RF power increases; D) Separation between two dips is as expected, around 11 MHz, however, shows increasing trend as RF power increases.

$M = 0$ e components matches the RF frequency. The frequency difference between these two dips will be the Ω -doublet splitting, which is 11.2 MHz. The related energy diagrams are shown in Fig. 4.5A.

The beat disappearance dip width and depth are extracted from fitting the voltage-scan data with two Lorentzians. The dip width change is due to the power broadening, described by

$$\gamma' = \gamma\sqrt{1 + sP},$$

where γ' is the actual line width, γ is the natural line width, P is RF power and s is a scale factor. As RF power increases, the beat disappearance effect reaches saturation as the depth reaches a plateau. There is a line width difference between these two dips, as well as the asymmetric shape. Such phenomena may be due to the molecular polarization difference at the different electric fields. Different molecular polarization will induce different portion of Ω -doublet mixing, leading to slightly different Rabi frequencies and thus the different saturation parameters. As expected, the dips are separated by the Ω -doublet splitting 11 MHz. The increasing trend as the RF power increases, might be explained by the AC Stark effect. AC Stark effect induced by the oscillatory electric field will cause the shift of energy levels, which may increase the line width and degrade the population transfer efficiency as well.

The beat disappearance experiments provide reasonable results and the precise voltage condition to meet the resonance where the beat amplitude dips. After the resonance position is located, the laser polarization is rotated to vertical, in order to pump the molecules from the ground state $X(0)$ to the $a(1)$ $J=1$ $M = 0$ \tilde{e} component. Beat appearance was expected, as the laser-RF double resonance occurs and population should transfer to the beat-generating $M = \pm 1$ states. However, the efficiency of such transfer turns out to be quite poor.

Shown in Fig. 4.6, the optimal beat appearance amplitudes are typically around 0.5 mV, compared to the original $M = \pm 1$ beat, which is around 2.5 mV. The original beat

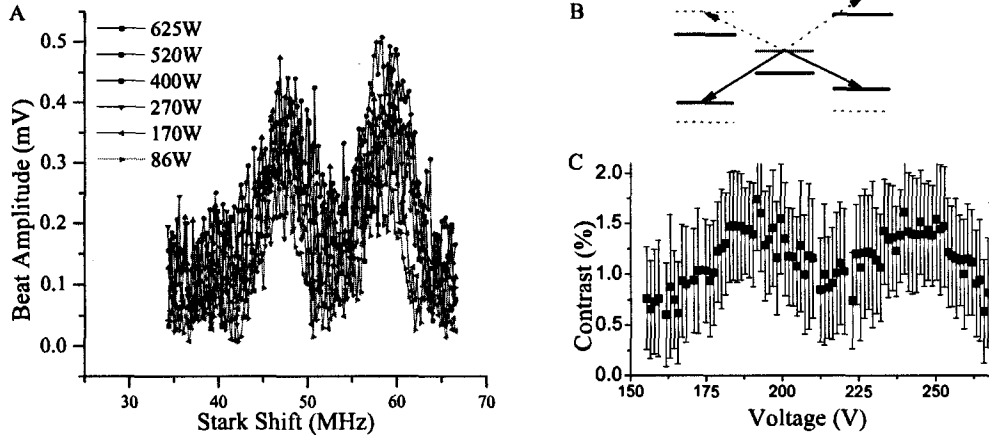


Figure 4.6: RF Excitation Experiment Result. A) Experiments are carried out with various RF powers, yet only reach 20% transition efficiency; B) As the voltage is scanned, due to Stark effect, the different Ω -doublet pairs match the resonance conditions with the RF pulse at fixed RF frequency. The solid(dashed) arrow indicates the scenario that the first(second) dip occurs; C) Small contrast of RF-excited beats, compared to the contrast of 5% ~ 8% induced by horizontally polarized laser, reflects the poor effective transition efficiency.

amplitude is measured a few minutes before rotating the laser polarization, with the $M = \pm 1$ states prepared directly by horizontally polarized laser beam without the RF beam. The beat appearance is generally less than 20% of the original size, indicating the transfer efficiency is less than 20% using RF scheme. Contrast of the beats, an important factor in the figure of merit for the EDM experiment, is quite small as a result.

The effect of the inhomogeneity of static vertical electric field was also investigated. The excitation efficiency is affected by the line width broadening due to the inhomogeneity of the external electric field. The homogeneity is artificially degraded by varying the voltage ratio between the guard rings and the main electrodes. The beat appearance amplitude is generally better, although not significantly, around the optimal voltage ratio setup, shown in Fig. 4.7. The experimental result is listed here for the completeness of our efforts of optimization. As we tried to optimize the electric field homogeneity as well as other experimental parameters, we still could not attain better efficiency of RF transition.

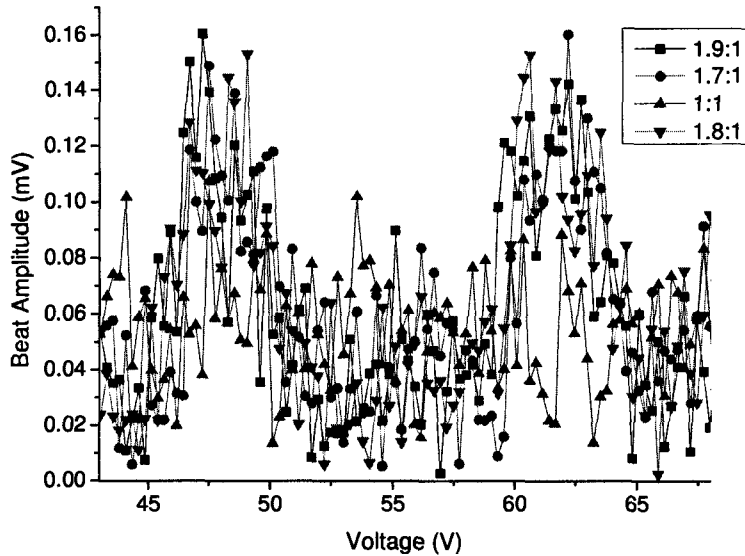


Figure 4.7: RF-Excited Beat with Various Guard Ring Voltage. Guard ring voltages are varied in hopes of improving the RF transition efficiency. The ratios of the Guard ring voltage versus the main electrode voltage are listed in the legend for the corresponding curves.

One possible explanation for such low efficiency is the RF field inhomogeneity. The inhomogeneity comes from the variation of magnitude, direction, and phase of the oscillating magnetic field. As the cell volume is comparable to the Helmholtz dimension, the direction varies greatly in the near field close to the coils. The RF excitation prepares the molecules with different initial phases between the $M = \pm 1$ Zeeman sub-levels as the effective Rabi frequencies vary due to the RF field inhomogeneity. Hence the beat signal in fluorescence will have different phases and the beat contrast will be washed out. The magnitude inhomogeneity leads to different Rabi frequencies to drive the π pulse, hence diminishing the excitation efficiency. Another explanation is related to the mixed electric/magnetic dipole (E1/M1) nature of the $M = 0 \rightarrow M = \pm 1$ transitions. The Ω -doublet levels are mixed under external electric field $\vec{\mathcal{E}}$ so that E1/M1 transitions are essentially fully allowed. The E1 amplitude can be comparable to the desired M1 amplitude even though the induced RF electric fields ($\vec{\mathcal{E}}_1$) are small for the $\vec{\mathcal{M}}_1$ pulse in the RF frequency range. Numerical

simulation of induced $\vec{\mathcal{E}}_1$ shows it will mostly be along the vertical direction \hat{z} due to the metallic surface of the electrodes embedded in the cell. The E1 process will induce line broadening mainly in higher order (AC Stark shifts from the component $\vec{\mathcal{E}}_1 \parallel \vec{\mathcal{M}}_1$).

In conclusion, we achieved little progress to improve the efficiency of the RF excitation scheme after taking a lot of efforts. Eventually we gave up this direction and resorted to new excitation scheme which will be discussed in the next section.

4.2 State Population Transfer using Microwave Excitation

Although tremendous work has been done trying to improve the efficiency of the RF excitation scheme, we achieved little progress and eventually gave up this direction. However, the microwave excitation scheme was proposed and implemented in the mean time. The first trial was so appealing and convincing that we chose this scheme as the primary excitation method.

The general description of microwave excitation is as following, shown in Fig. 4.8. A pulsed laser at 571 nm excites PbO molecules from the $X[J = 0^+, v=1]$ state to the $a(1)[J = 1^-, M=0, v'=5]$ state. These are transferred to a coherent superposition of $M = \pm 1$ levels in either the \tilde{e} or \tilde{f} component of the Ω -doublet by a sequential Raman transition at ~ 28.2 GHz using the $a(1)[J=2, v'=5]$ intermediate state. The $a(1)[J=1, M = \pm 1, v'=5]$ molecules are detected by fluorescence at 548 nm that accompanies their decay to $X[v''=0]$.

4.2.1 $a(1)$ J=2 Rotational State

In order to explain the whole excitation procedure, it's necessary to give a complete description of the relevant states. First we will study the level structure of $a(1)$ J=2 under the external static electromagnetic field, $\vec{\mathcal{E}} = \mathcal{E}\hat{z}$ and $\vec{\mathcal{B}} = \mathcal{B}\hat{z}$. The Ω -doublet splitting is $\propto J(J+1)\Delta_\Omega$ for each J level respectively, so that Ω -doublet splitting for J=2 will be three times that of J=1 level, equal to $3\Delta_\Omega$. The Landé factor depends on angular momentum

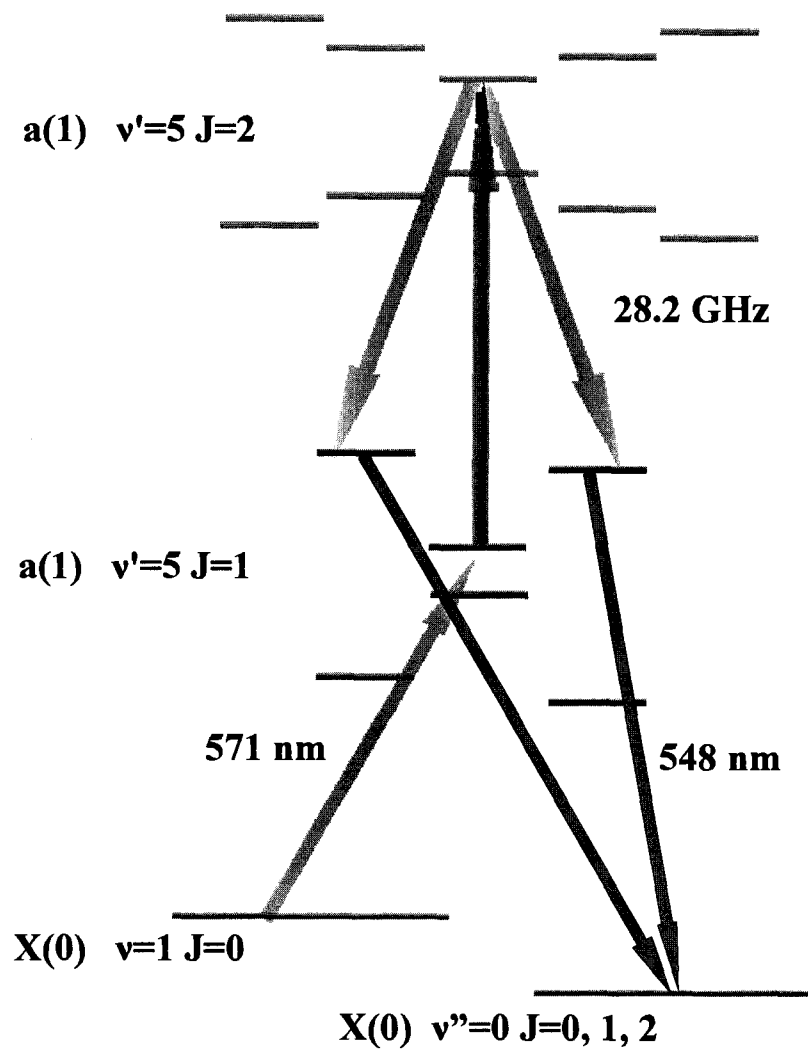


Figure 4.8: Schematic diagram of energy levels of PbO. Pulsed laser at 571 nm excites PbO molecules to the $a(1)$ state. Raman transition at 28.2 GHz using microwaves transfers the population to a coherent superposition of $J=1 M = \pm 1$ levels in either \tilde{e} or \tilde{f} components of the Ω -doublet.

J by the factor $1/J(J+1)$, yielding a g-factor in J=2 level that is one third of J=1 level g-factor. We can write out the Hamiltonian under the basis of $|J=2, M, e(f)\rangle$. Without the T,P-odd EDM term, and ignoring the intrinsic difference in g-factors between e and f states, we can diagonalize the Hamiltonian (omitted here to save space), and get the energy splitting as

$$\left\{ \frac{1}{6}(2g\mu_B\mathcal{B} + 9\Delta_\Omega + \Omega_2), \frac{1}{6}(g\mu_B\mathcal{B} + 9\Delta_\Omega + \Omega_1), 3\Delta_\Omega, \frac{1}{6}(-g\mu_B\mathcal{B} + 9\Delta_\Omega + \Omega_1), \right. \\ \left. \frac{1}{6}(-2g\mu_B\mathcal{B} + 9\Delta_\Omega + \Omega_2), \frac{1}{6}(2g\mu_B\mathcal{B} + 9\Delta_\Omega - \Omega_2), \frac{1}{6}(g\mu_B\mathcal{B} + 9\Delta_\Omega - \Omega_1), 0, \right. \\ \left. \frac{1}{6}(-g\mu_B\mathcal{B} + 9\Delta_\Omega - \Omega_1), \frac{1}{6}(-2g\mu_B\mathcal{B} + 9\Delta_\Omega - \Omega_2) \right\},$$

where $\Omega_1 = \sqrt{(\mu_a \cdot \mathcal{E})^2 + 81\Delta_\Omega^2}$, and $\Omega_2 = \sqrt{4(\mu_a \cdot \mathcal{E})^2 + 81\Delta_\Omega^2}$, $\mu_a = 3.27$ Debye and $\Delta_\Omega = 11.2$ MHz [41]. The electric field will mix the e, f parity eigenstates to a new set of eigenstates $|J=2, M, \tilde{e}(\tilde{f})\rangle$.

We can take the molecular polarization $P = \langle M\Omega \rangle$, the expectation value of the multiplication of quantum numbers M and Ω , as the measure of the Stark mixing of e and f states.

$$P = 2 \frac{9\Delta + \Omega_1}{\sqrt{2}\sqrt{\Omega_1^2 + 9\Delta \cdot \Omega_1}} \frac{M\mu_a\mathcal{E}}{\sqrt{2}\sqrt{\Omega_1^2 + 9\Delta \cdot \Omega_1}} = \frac{M\mu_a\mathcal{E}}{\sqrt{(\mu_a \cdot \mathcal{E})^2 + 81\Delta^2}},$$

compared to J=1 case $P = \frac{\mu_a\mathcal{E}}{\sqrt{(\mu_a \cdot \mathcal{E})^2 + \Delta^2}}$.

The relation between the molecular polarization and the static electric field is shown in Fig. 4.9. Due to the large Ω -doublet splitting of the J=2 level, it will take higher electric field strength to completely polarize J=2 level. It will manifest interesting features in the moderate electric field strength, where J=1 states have been fully polarized yet J=2 e and f components are only partially mixed.

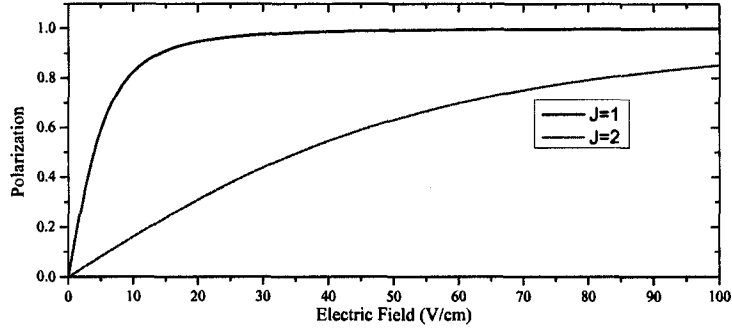


Figure 4.9: Molecular Polarization in Electric Field. As the Ω -doublet splitting of $J=1$ levels is three times smaller than $J=2$ level, $J=1$ level is much easier to be polarized by the external electric field.

4.2.2 Microwave Coherent Excitation

Similar to the RF excitation scheme, the microwave excitation scheme associates with various energy level configurations. The V-shape and Λ -shape studied in RF excitation scheme can be applied here directly. The only difference is that microwave will drive the E1 transition instead of M1 transition for RF excitation. Furthermore, the vertically polarized microwave pulse can associate together four levels, the intermediate $a(1)$ $J=2$ $M = \pm 1$ states and the desired $J=1$ $M = \pm 1$ state, if either pair is populated initially, as shown in Fig. 4.10.

Here we study the coherent excitation in such a level system. Using the similar notation to RF case, we describe the system under the basis $\{|a\rangle, |b\rangle, |c\rangle, |d\rangle\}$.

$$i\hbar \frac{\partial}{\partial t} \Psi(t) = H(t) \Psi(t),$$

$$H(t) = \hbar \begin{pmatrix} \Delta + \omega/3 & 0 & \Omega \cos(\omega_0 t) & 0 \\ 0 & \Delta - \omega/3 & 0 & \Omega \cos(\omega_0 t) \\ \Omega \cos(\omega_0 t) & 0 & \omega & 0 \\ 0 & \Omega \cos(\omega_0 t) & 0 & -\omega \end{pmatrix}, \quad \Psi(t) = \begin{pmatrix} a(t) \\ b(t) \\ c(t) \\ d(t) \end{pmatrix}.$$

We study the resonance case $\Delta \approx \omega_0$ and apply rotating-wave approximation (RWA); in the rotating frame, the three-level-system Hamiltonian reads

$$H = \hbar \begin{pmatrix} \omega/3 & 0 & \Omega/2 & 0 \\ 0 & -\omega/3 & 0 & \Omega/2 \\ \Omega/2 & 0 & \omega & 0 \\ 0 & \Omega/2 & 0 & -\omega \end{pmatrix}.$$

Eigenenergies $\{E_i\}$ are $\{-(3\nu + 4\omega)/6, (-3\nu + 4\omega)/6, (3\nu - 4\omega)/6, (3\nu + 4\omega)/6\}$, where $\nu = \sqrt{4\omega^2/9 + \Omega^2}$, corresponding to eigenvectors $\{|\Psi_i\rangle\}$. Here we consider the case that the upper levels are equally populated, so the initial state is $|\Phi_0\rangle = \{1/\sqrt{2}, e^{i\phi}/\sqrt{2}, 0, 0\}$, where ϕ denotes the initial phase difference between two sub-levels of the upper states. The final state is

$$|\Phi_1\rangle = \sum_i e^{-iE_i t} |\Psi_i\rangle \langle \Psi_i | \Phi_0 \rangle = \frac{1}{\sqrt{2}} \begin{pmatrix} e^{-\frac{2}{3}i\omega t} (\cos \frac{\nu t}{2} + \frac{2i\omega}{3\nu} \sin \frac{\nu t}{2}) \\ e^{i(\phi + \frac{2}{3}\omega t)} (\cos \frac{\nu t}{2} - \frac{2i\omega}{3\nu} \sin \frac{\nu t}{2}) \\ -\frac{i\Omega}{\nu} e^{-\frac{2}{3}i\omega t} \sin \frac{\nu t}{2} \\ -\frac{i\Omega}{\nu} e^{i(\phi + \frac{2}{3}\omega t)} \sin \frac{\nu t}{2} \end{pmatrix}. \quad (4.3)$$

To optimize the population transfer, requires $\Omega/\nu \rightarrow 1$, yielding $\Omega \gg 2\omega/3$. The maximum population transfer occurs when $\sin \frac{\nu t}{2} = 1$, yielding the π -pulse condition $T_\pi = \pi/\nu \approx \pi/\Omega$. The residual population in the upper levels will be $1 - (\Omega/\nu)^2$, which indicates that this transfer scheme cannot be 100% efficient.

4.2.3 Population Transfer Path

Now that we have studied the generalized individual excitation steps, we can apply these results sequentially to give the complete picture of the population transfer. We introduce the notation $|J, M, \tilde{e}(\tilde{f})\rangle$ to describe the relevant a(1) levels shown in Fig. 4.8, and for simplicity, we only consider high electric field limit $P \approx 1$, where the molecules are fully

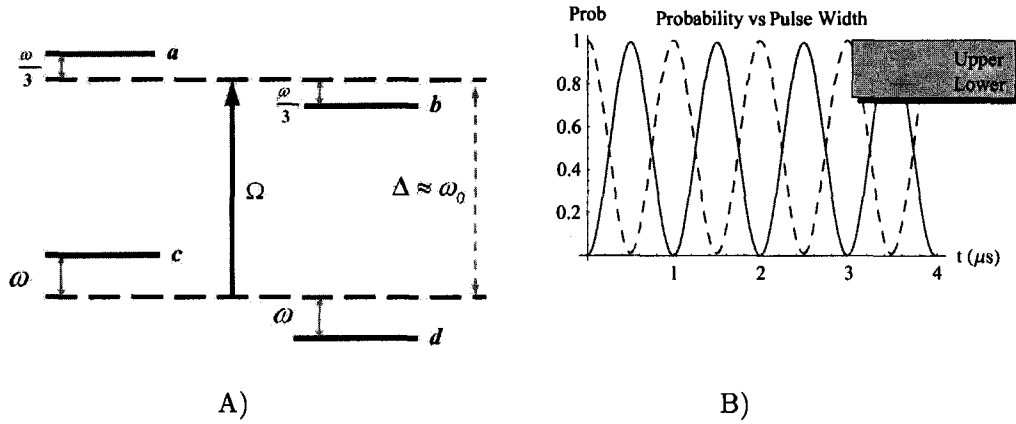


Figure 4.10: Related Level Structure and Transition Probability. A) Zeeman splitting for $J=1$ $M = \pm 1$ level is three times bigger than $J=2$ $M = \pm 1$ level, leading to the $J=1$ beat frequency is three times faster than $J=2$ beat. B) The solid(dash) line shows the ground(excited) population varies with the pulse width in the coherent excitation.

polarized.

$$\begin{aligned}
 |1, 0, \tilde{e}\rangle &= |J = 1, M = 0, e, |\Omega| = 1\rangle = \frac{1}{\sqrt{2}}(|J = 1, M = 0, \Omega = 1\rangle - |J = 1, M = 0, \Omega = -1\rangle), \\
 |2, 1, \tilde{e}\rangle &= \frac{1}{\sqrt{2}}(|J = 2, M = 1, e, |\Omega| = 1\rangle - |J = 2, M = 1, f, |\Omega| = 1\rangle) \\
 &= -|J = 2, M = 1, \Omega = -1\rangle, \\
 |2, -1, \tilde{e}\rangle &= \frac{1}{\sqrt{2}}(|J = 2, M = -1, e, |\Omega| = 1\rangle + |J = 2, M = 1, f, |\Omega| = 1\rangle) \\
 &= |J = 2, M = -1, \Omega = 1\rangle.
 \end{aligned}$$

Similarly,

$$\begin{aligned}
 |2, 1, \tilde{f}\rangle &= |J = 2, M = 1, \Omega = 1\rangle, & |2, -1, \tilde{f}\rangle &= |J = 2, M = -1, \Omega = -1\rangle, \\
 |1, 1, \tilde{e}\rangle &= -|J = 1, M = 1, \Omega = -1\rangle, & |1, -1, \tilde{e}\rangle &= |J = 1, M = -1, \Omega = 1\rangle, \\
 |1, 1, \tilde{f}\rangle &= |J = 1, M = 1, \Omega = 1\rangle, & |1, -1, \tilde{f}\rangle &= |J = 1, M = -1, \Omega = -1\rangle.
 \end{aligned}$$

Let's first consider the situation where the molecules are prepared in the state $|\Psi_0\rangle = |1, 0, \tilde{e}\rangle$, and transferred to $|\Psi_1\rangle$, the superposition of $|2, 1, \tilde{e}\rangle$ and $|2, -1, \tilde{e}\rangle$, by the microwave beam which is horizontally polarized and resonant with the splitting between $|\Psi_0\rangle$ and $|\Psi_1\rangle$. For \hat{x} polarization, we calculate the matrix element, yielding

$$\begin{aligned}\Omega_x &= \mathcal{E}_x \langle 2, 1, \tilde{e} | \mu_{e,x} | 1, 0, \tilde{e} \rangle = \frac{\mathcal{E}_x}{\sqrt{2}} \langle 2, 1, \Omega = 1 | \mu_{e,x} (|1, 0, \Omega = 1\rangle - |1, 0, \Omega = -1\rangle) \\ &= \frac{\mathcal{E}_x}{\sqrt{2}} \langle 2, 1, \Omega = 1 | \mu_{e,x} | 1, 0, \Omega = 1 \rangle = -\frac{1}{2} \sqrt{\frac{3}{20}} \mu_a \mathcal{E}.\end{aligned}$$

$$\text{Similarly, } \Omega'_x = \mathcal{E}_x \langle 2, -1, \tilde{e} | \mu_{e,x} | 1, 0, \tilde{e} \rangle = \frac{1}{2} \sqrt{\frac{3}{20}} \mu_a \mathcal{E}.$$

For the current experiment setup, the microwave pulse is propagating anti-parallel to the laser beam (in \hat{y}) direction with the pulse width shorter than the period of the Zeeman beat. The \hat{x} polarized microwave pulse is applied to transfer the molecules from $|\Psi_0\rangle$ to $|\Psi_1\rangle$. To achieve 1 MHz Rabi frequency Ω , recall $\mu_a = 3.27$ Debye, and $\Omega = \frac{1}{2} \sqrt{\frac{3}{20}} \mu_a \mathcal{E} = 2\pi \cdot 1\text{MHz}$. Thus we require $\mathcal{E} = 5.2 \times 10^{-3}$ sV/cm. The Poynting vector $S = \frac{c}{8\pi} \mathcal{E}^2 = 3.2 \times 10^4$ erg/cm² · s = 3.2 mW/cm², and with a beam area $A \approx 25$ cm². We need the microwave power

$$P = S \cdot A \approx 75 \text{ mW} = 18.75 \text{ dBm}.$$

For the population transfer using vertical microwaves to drive from J=2 state to J=1 state, the matrix element Ω_z reads

$$\begin{aligned}\Omega_z &= \mathcal{E}_z \langle 2, 1, \tilde{e} | \mu_{e,z} | 1, 1, \tilde{e} \rangle = \mathcal{E}_z \langle 2, 1, \Omega = 1 | \mu_{e,z} | 1, 1, \Omega = 1 \rangle = \frac{1}{2} \sqrt{\frac{3}{5}} \mu_a \mathcal{E}, \\ \Omega'_z &= \mathcal{E}_z \langle 2, -1, \tilde{e} | \mu_{e,z} | 1, -1, \tilde{e} \rangle = \frac{1}{2} \sqrt{\frac{3}{5}} \mu_a \mathcal{E}.\end{aligned}$$

$$\text{However, } \Omega''_z = \mathcal{E}_z \langle 2, 1, \tilde{e} | \mu_{e,z} | 1, 1, \tilde{f} \rangle = \frac{\mathcal{E}_z}{\sqrt{2}} \langle 2, 1, \Omega = 1 | \mu_{e,z} | 1, 1, \Omega = -1 \rangle = 0.$$

For an E1 vertical transition, selection rules forbid either $\Delta M = 2$ or $\Delta \Omega = 2$ between the initial state and final state. The same argument applies to the matrix element between

$|2, -1, \tilde{e}\rangle$ and $|1, -1, \tilde{f}\rangle$. We also need to consider the transition from $|2, \pm 1, \tilde{f}\rangle$ to $|1, \pm 1, \tilde{f}\rangle$,

$$\Omega_z'' = \mathcal{E}_z \langle 2, 1, \tilde{f} | \mu_z | 1, 1, \tilde{f} \rangle = \frac{\mathcal{E}_z}{\sqrt{2}} \langle 2, 1, \Omega = -1 | \mu_z | 1, 1, \Omega = -1 \rangle = \frac{1}{2} \sqrt{\frac{3}{5}} \mu_a \mathcal{E}.$$

To access the anti-aligned state, we choose the path of population transfer as $|J = 1, M = 0, e\rangle \xrightarrow{\hat{x} \text{ pulse}} |J = 2, M = \pm 1, \tilde{e}\rangle \xrightarrow{\hat{z} \text{ pulse}} |J = 1, M = \pm 1, \tilde{e}\rangle$. To access the aligned state, we use the path $|J = 1, M = 0, e\rangle \xrightarrow{\hat{x} \text{ pulse}} |J = 2, M = \pm 1, \tilde{f}\rangle \xrightarrow{\hat{z} \text{ pulse}} |J = 1, M = \pm 1, \tilde{f}\rangle$. We take the advantage that $|J = 1, M = 0, e\rangle$, not mixed with $|J = 1, M = 0, f\rangle$, has both $\Omega = 1$ and $\Omega = -1$ components, which allows it to access both \tilde{e} and \tilde{f} states. This transfer path is shown in Fig. 4.11A. Another path of population transfer is $|J = 1, M = 0, e\rangle \xrightarrow{\hat{z} \text{ pulse}} |J = 2, M = 0, e\rangle \xrightarrow{\hat{x} \text{ pulse}} |J = 1, M = \pm 1, \tilde{e}(\tilde{f})\rangle$, where population transfer to \tilde{e} or \tilde{f} is determined by the microwave frequency of the second pulse, shown in Fig. 4.11B. To achieve 1 MHz Rabi frequency requires microwave power $P \approx 20 \text{ mW} = 13 \text{ dBm}$ for \hat{z} linear-polarized microwave. The π -pulse condition is $T_\pi \approx \pi/\Omega_z'' \approx 0.5 \mu\text{s}$.

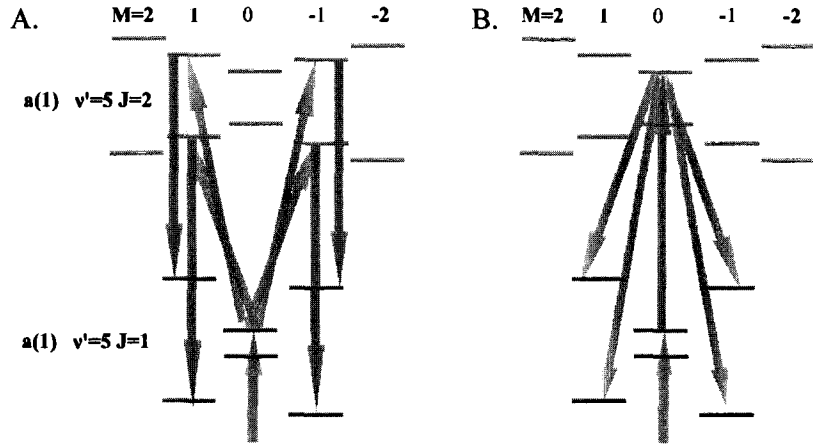


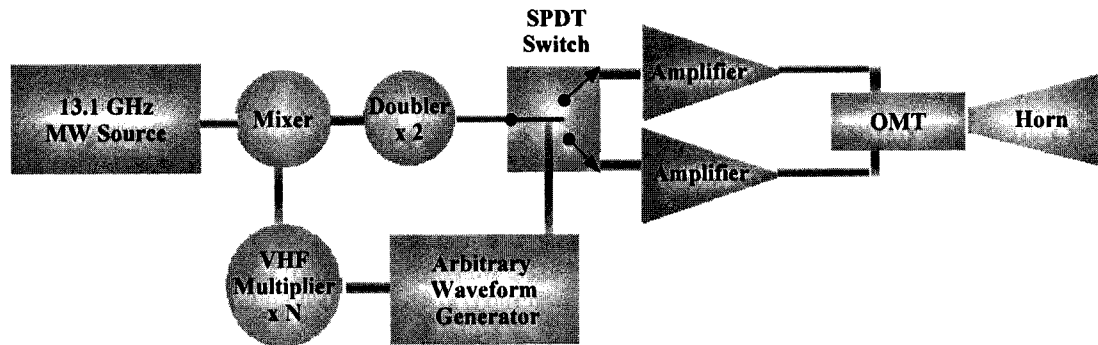
Figure 4.11: Population Transfer Path via J=2 Level.

However in the nominal experimental environment, the moderate voltage across the electrodes can only fully polarize the J=1 levels and not the J=2 levels, leading to partial mixing of e and f components in J=2 levels (see Section 4.2.1). Thus the transition between $|J = 2, M = \pm 1, \tilde{f}(\tilde{e})\rangle$ to $|J = 1, M = \pm 1, \tilde{e}(\tilde{f})\rangle$ will be much weaker than for $\tilde{e}(\tilde{f}) \mapsto \tilde{e}(\tilde{f})$.

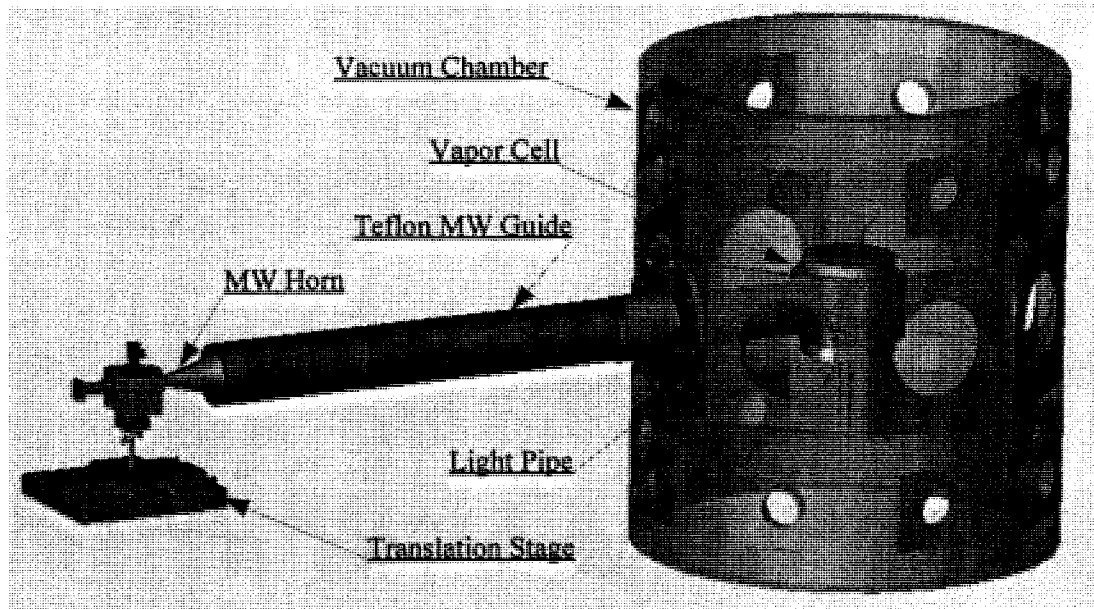
At 400 V across the electrodes, the Rabi frequency for the former transition is four times smaller than the latter with the same microwave power.

4.2.4 Experimental Setup

Our microwave setup consists of microwave source, microwave horn, orthomode transducer, microwave amplifier, microwave switch, microwave guide, etc, shown in Fig. 4.12.



(A)



(B)

Figure 4.12: Microwave Experimental Setup. (A) Microwave source. (B) Experimental Setup.

We use an arbitrary waveform generator to provide the desired RF frequency around 31 MHz, followed by several VHF multipliers giving 32 times that frequency to reach 1 GHz. The set of VHF multipliers consists of

1. one low noise quadrupler, featuring ultra low phase noise and low conversion loss, quadrupling from $31.25 \text{ MHz} \pm 7.5\%$ to $125 \text{ MHz} \pm 7.5\%$ with output power at 12 dBm, suppressed harmonics -25 dBc, sub-harmonics -30 dBc;
2. second quadrupler converting from $125 \text{ MHz} \pm 7.5\%$ to $500 \text{ MHz} \pm 7.5\%$ with similar output features;
3. and one connectorized diode doubler converting from $500 \text{ MHz} \pm 7.5\%$ to $1 \text{ GHz} \pm 7.5\%$ with output power at 0 dBm and suppressed harmonics -25 dBc.

This 1 GHz output is mixed with 13.1 GHz microwaves by a mixer to obtain microwaves around 14.1 GHz with power of 10 ~ 15 dBm. The 13.1 GHz microwaves are generated by a phase locked oscillator with output power 16.2 dBm, power flatness $\pm 0.25 \text{ dB}$, harmonics -40 dBc, and phase noise -104 dBc/Hz at 10 kHz. An Agilent E8257C microwave generator is used together with our self-constructed microwave source to calibrate the microwave power and to utilize some features, such as external triggering, CW/pulsed modes, and AM/FM/PM modes, to cross check the performance of our source.

In practice, our home-made microwave source is stable and easy to control, providing ample freedom to generate microwaves with various pulse widths, envelopes, and pulse sequences with arbitrary intervals by programming the input arbitrary waveform.

After the output of the mixer, a frequency doubler is used to obtain the desired 28.2 GHz microwaves. Microwave amplifiers are used to boost the power, and variable attenuators are to control the actual output power. During the proof-of-principle phase, a microwave amplifier from *MK Milliwave Technologies* with small signal gain amplification 29 dB was used, corresponding to 0.5 Watts microwave output. The calibration of the MK microwave amplifier is shown in Fig. 4.13A. The discussion in the following sections are based on

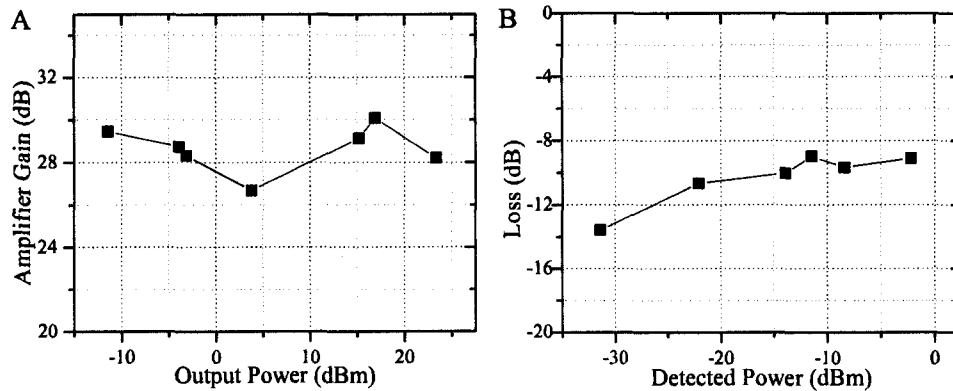


Figure 4.13: Calibration of Microwave Amplifier Gain and Insertion Loss of Experimental Apparatus. These calibration works were done by Paul Hamilton. (A) The gain of the *MK Milliwave* microwave amplifier is around 29 dB. (B) The insertion loss in the presence of the vapor cell is around -10 dB.

the experimental results using this amplifier. Recently, a new microwave amplifier from *QuinStar Technology, Inc.* with a gain of 37 dB is used in one branch, corresponding to 5 Watts microwave output. A microwave switch is inserted to steer the microwaves to the correct port of the orthomode transducer to generate the desired polarization, either vertical or horizontal, then fed into the conical microwave horn. Microwaves emitted from the microwave horn have small angular spread and propagate along the teflon microwave pipe and quartz light guide into the vapor cell. The insertion loss in the presence of the vapor cell, including the interface reflections and angular spreading, is around -10 dB, shown in Fig. 4.13B. After the installation of the magnetic shields, the microwave components are brought far away from the chamber. The teflon microwave guide serves as a guide adapting the microwave horn to the quartz light pipe to guide the microwaves from outside the shield into the vapor cell. It is a solid cylinder made out of Teflon. Teflon's absorption at our working frequency is low and the microwave guide maintains the solid angle spread as the microwaves propagate inside the guide and experience the total internal reflection when reaching the inner surface of the teflon guide. The microwave beam propagates anti-parallel

to the laser beam along the \hat{y} axis (See Fig. 4.12). We can trigger the microwave pulse at various times with respect to the laser pulse. The fluorescence detectors are located along the \hat{x} axis orthogonal to the laser beam path.

4.2.5 State Preparation by Rabi Oscillation

In the early attempts to test the feasibility of microwave excitation, ordinary Rabi oscillations using monochromatic microwave pulses were studied for population transfer. We carried out various experiments to check our understanding of the excitation dynamics and optimize the experimental parameters to enhance the excitation efficiency. We demonstrated the ability to drive several transitions between the Zeeman sub-levels of the rotational states under various external electric field strengths. In particular we demonstrated the ability to populate the desired EDM states at proper electric fields. Here I will discuss the evidence of population transfer through various transitions. However, most of experimental results shown here were taken before the installation of magnetic shields and the finalization of the detection scheme. These results served as a demonstration and have not been repeated during this thesis. Further investigations are being carried out and will provide new results soon.

Transition Driven by Vertically Polarized MW

Evidence for the transition from $|J = 1, M = \pm 1, e\rangle$ to $|J = 2, M = \pm 1, e\rangle$ with no electric field is shown in Fig. 4.14. Here a horizontally polarized laser pulse pumps the molecules to the $J=1$, $M=\pm 1$ state. The parity eigenstates of each rotational level remain unmixed, so the E1 transition driven by a vertically polarized microwave square pulse couples only to $|J = 2, M = \pm 1, e\rangle$. The microwave pulse is 200 ns in width. We scanned the microwave frequency around 28.2 GHz. In the power spectrum of the fluorescence signal, the bins at $J=1$ and $J=2$ beat frequency are monitored. When the microwave frequency is on resonance with the rotational splitting, 28.217 GHz, the initial population in the $J=1$ state is transferred to the $J=2$ state, and the $J=1$ beat signal decreases as the $J=2$ beat signal

shows up.

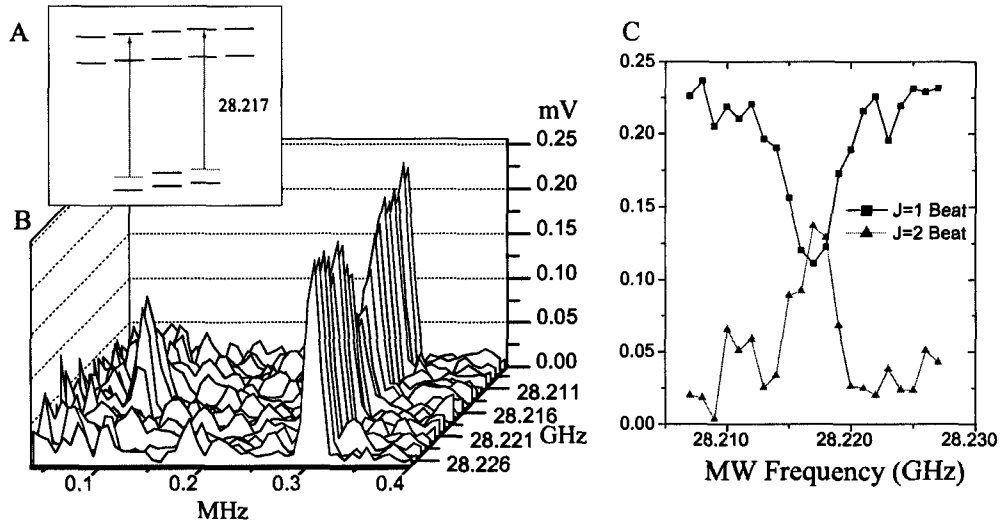


Figure 4.14: Transition by Vertical Polarized MW at Zero E Field. A) Related energy diagram; B) Fourier transform of the data shown in waterfall plot; C) The J=1 beat amplitude drops and J=2 beat amplitude peaks as microwave frequency is in resonance with the transition.

After the MW pulse, the J=2⁺ state, and the residual of the J=1⁻ state as well due to incomplete transfer, precess in the same magnetic field according to their own Zeeman frequencies. J=1 beat and J=2 beat signals might be co-existing simultaneously, hence it can be used to reveal the relationship of g-factors in both levels, shown in Fig. 4.15.

The beat amplitudes in Fig. 4.15C are obtained by subtracting the data by the self-contained “scrambled” signal, using the method described in Section 2.4.2. It is fit to the following function:

$$\exp(-t/\tau) [A_0 + A_1 \cos(\omega_1 t + \phi_1) + A_2 \cos(\omega_2 t + \phi_2)] + B,$$

where τ is beat lifetime, $A_{1,2}$, $\omega_{1,2}$ and $\phi_{1,2}$ are beat amplitude, frequency and phase of J=1 and J=2 levels respectively. A_0 and B are introduced to account for the residual of

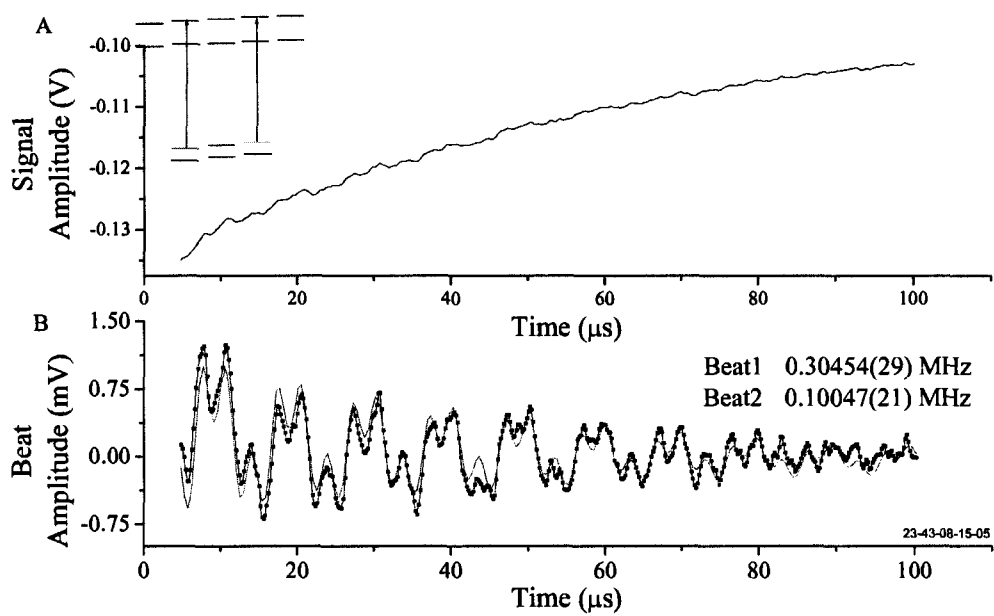


Figure 4.15: Interference of J=1 Beat and J=2 Beat. (A) The interference of J=1 beat and J=2 beat shown in time domain. (B) Beat amplitudes and the fitting result.

the imperfect “scrambled” signal. We expect $\omega_1 \propto g_{1-}$ and $\omega_2 \propto g_{2+}$, following the relation $g_{J\Omega} \propto 1/J(J+1)$. The interference will diminish the beat amplitudes and introduce an apparent shortening of beat lifetime, as shown in Fig. 4.15. The fitting result shows the approximated relation of $g_{1-} : g_{2+} = 3 : 1$ as expected. This set of data was taken before the installation of magnetic shield. Relatively high noise background was as expected, yielding low amplitudes of beat signal and imperfect data fitting. The experimental result listed here is for the completeness of demonstration of our experimental efforts.

Similarly, the transition from the $a(1) |J = 1, M = \pm 1, f\rangle$ state to $|J = 2, M = \pm 1, f\rangle$ in the absence of an external electric field, has been observed clearly. The initial state is prepared by driving the Q1 transition, from the ground state $X(0) J=1^-$ to $a(1) J=1^+$ as the f component of the Ω -doublet. Yet, no prominent signal can be observed at the parity-forbidden E1 transitions from $|J = 1, M = \pm 1, e\rangle$ state to $|J = 2, M = \pm 1, f\rangle$, or from $|J = 1, M = \pm 1, f\rangle$ state to $|J = 2, M = \pm 1, e\rangle$.

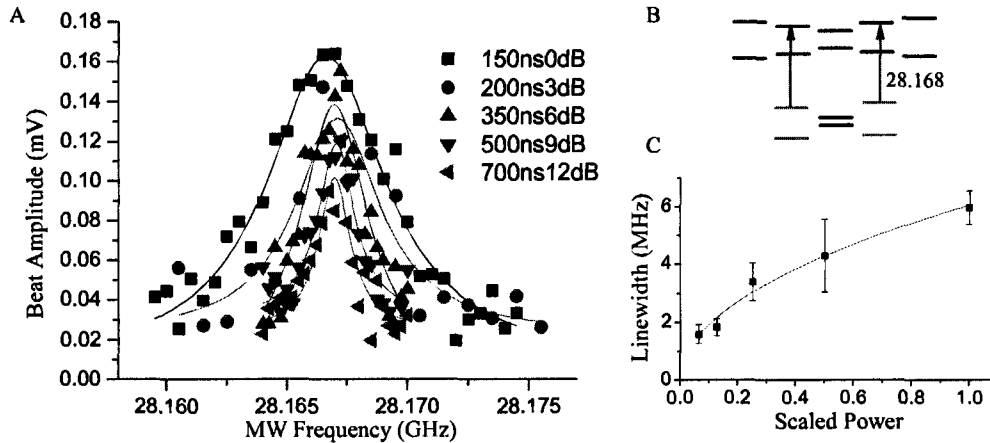


Figure 4.16: Transition by Vertical Polarized MW in External E Field. (A) Beat amplitude at different MW power level. The pulse widths are changed to ensure the π -pulse condition. 150 ns pulse width will correspond to MW power at 19 ~ 23 dBm with insertion loss. (B) Related energy diagram; (C) Line width of the transition versus the power. The x-axis is scaled down to unity at the maximum power.

Evidence for the transition from $|J = 1, M = \pm 1, \tilde{e}\rangle$ to $|J = 2, M = \pm 1, \tilde{e}\rangle$ in the

presence of an external electric field is shown in Fig. 4.16A. The voltage across the electrodes is 300 V. We varied the microwave power and scanned the pulse width to make the beats most prominent to obtain the optimal pulse width. Then the microwave frequency is scanned to check the resonance width. As we turned down the power, a longer pulse was expected to meet the π -pulse condition and the resonance width was expected to be narrower, as shown in Fig. 4.16C. The effect of power broadening and saturation can be described by the power-broadened line-width

$$\gamma' = \gamma\sqrt{1 + s_0}, \quad (4.4)$$

where $s_0 = 2|\Omega|^2/\gamma^2$ is the saturation parameter, γ is the decay rate of the excited state, Ω is the Rabi frequency, and the MW power $P \propto |\Omega|^2$. The resonance line-width is fit to Eq. 4.4 in Fig. 4.16.

In conclusion, we have demonstrated the transition between the $J=1$ and $J=2$ rotational levels driven by vertically polarized microwave pulse. The resonance frequency, resonance line shape and width, and pulse width for Rabi flopping are consistent with the reported molecular constants [65, 66, 41] and theoretical calculation.

Transition Driven by Horizontal Polarized MW

Evidence for the transition from $|J = 1, m = 0, e\rangle$ to $|J = 2, M = \pm 1, \tilde{e}\rangle$ is shown in Fig. 4.17A. A vertically polarized laser pulse pumps the molecules from the ground state $X(0) \ ^1\Sigma^+ \ J=0$ to the $a(1) \ ^3\Sigma^+ \ v' = 5, J=1^-, M=0$ state, which is the e component of $J=1$ Ω -doublet. A horizontally polarized microwave square pulse drives it to $|J = 2, M = \pm 1, \tilde{e}\rangle$ in the presence of the external electric field with strength $\mathcal{E}_0 = 78.7$ V/cm (300 V applied across the electrodes). The microwave pulse is 250 ns in width and attenuated by 3 dB, yielding the estimated microwave power around 16 ~ 21 dBm propagating through the vapor cell. The uncertainty in the microwave power is due to the lack of knowledge in the microwave angular spread in the cell and reflections between multiple interfaces.

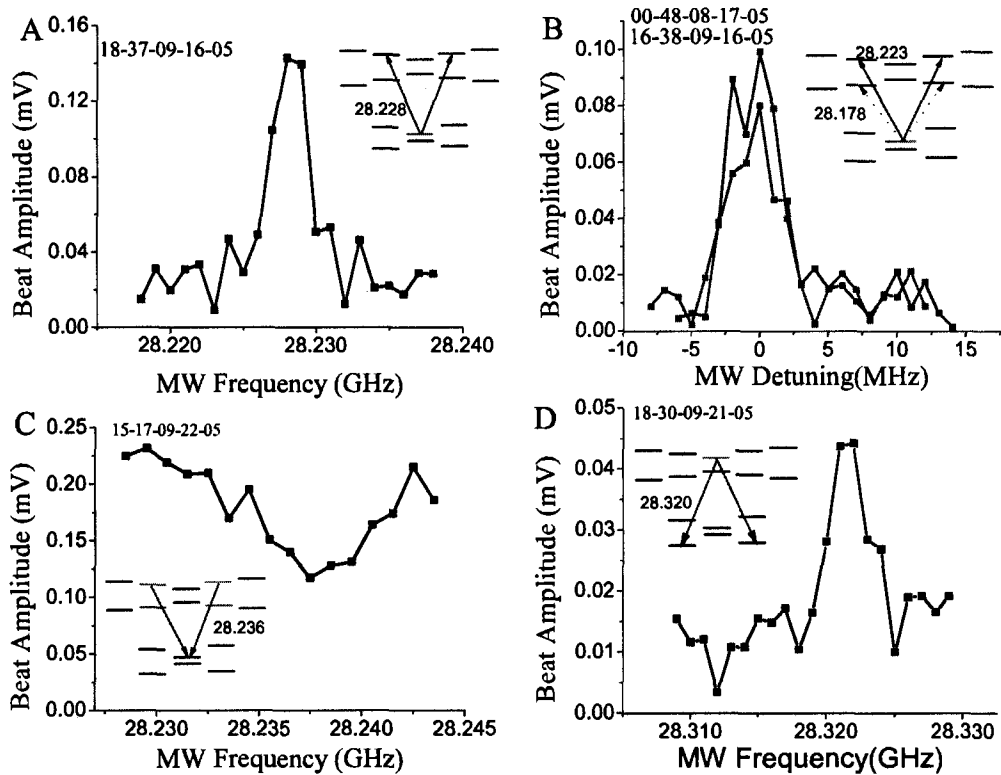


Figure 4.17: Transition Driven by Horizontally Polarized MW. The energy diagrams for related transitions are plotted together with the experimental data. The number sequences at the corners of each figure are the dates of each experiment in the format of hour-minute-month-day-year. A) Typical experimental result; B) Selectively transfer the population to certain Ω -doublet components; C) Beat disappearance. Laser is tuned to the R1 line; D) Evidence for the transition from $|J = 2, M = 0, e\rangle$ to $|J = 1, M = \pm 1, \tilde{f}\rangle$.

We scanned the microwave frequency around 28.2 GHz. In the power spectrum of the fluorescence signal, the bin at the $J=2$ level beat frequency is monitored and compared to the background floor in the frequency domain. As the g -factor in $J=2$ level will be three times smaller than the g -factor in $J=1$ level for the same $|M| = 1$, the molecules will have one third of the precessing frequency. Hence it is quite easy to locate the bin position precisely. Clearly, there is a peak around the expected resonance frequency in the frequency domain which means there is a coherent population building up at $|J = 2, M = \pm 1, e\rangle$.

Evidence for the transition from $|J = 1, M = 0, e\rangle$ to $|J = 2, M = \pm 1, \tilde{f}\rangle$, is shown in Fig. 4.17B. Here we demonstrate that by varying the microwave frequency, we can address the upper level \tilde{e} component and the lower level \tilde{f} component respectively. For this data, the external electric field was 52.5 V/cm or 200 V applied across the electrodes; the microwave pulse was 200 ns in width. As we scanned the microwave frequency, resonance peaks indicating the presence of quantum beats appear at 28.178 GHz and 28.223 GHz, as expected for the \tilde{e} and \tilde{f} components respectively.

If we tune the laser to drive the R1 transition with horizontal polarization in the presence of external field, we will reach the superposition of $|J = 2, M = \pm 1, \tilde{e}\rangle$, and $|J = 2, M = \pm 1, \tilde{f}\rangle$. The microwaves are used to drive the transition from $J=2$ $M=\pm 1$ \tilde{e} to $J=1$ $M=0$ e states. Both $J=2$ \tilde{e} and \tilde{f} components will contribute the amplitude of $J=2$ beat. In this case, we applied 444.4 V applied across the electrodes with horizontal polarized microwave at frequency 28.236 GHz, pulse width 900 ns, with microwave attenuator inserted. The pulse width is chosen to make sure the frequency spread of the microwaves is smaller than the Stark splitting which requires the microwave power to be turned down to avoid power saturation. As this microwave pulse is only resonant with the transition between $J=2$ $M=\pm 1$ \tilde{e} components and $J=1$ $M=0$ e components, the effect of the pulse is to transfer population from the former to the latter, eliminating the contribution to the beat amplitude from $J=2$ \tilde{e} components and decreasing it to half, as shown in Fig. 4.17C.

Evidence for the transition from $|J = 2, M = 0, e\rangle$ to $|J = 1, M = \pm 1, \tilde{f}\rangle$, is shown in Fig. 4.17D. A vertically polarized laser pulse is tuned to drive the R1 transition from

the ground state $X(0) J=1^- v = 1$ to the $a(1) J=2^+, M=0 v' = 5$ state. A horizontally polarized microwave square pulse drives it down to $|J = 1, M = \pm 1, \bar{e}\rangle$ in the presence of the external electric field of 116.54 V/cm or 444 V applied across the electrodes. The microwave pulse is 350 ns in width. We scanned the microwave frequency around 28.322 GHz. In the power spectrum of the fluorescence signal, the bin at $J=1$ beat frequency is monitored. It is clear that a peak shows up in frequency domain right at the expected $J=1$ quantum beat frequency.

In conclusion, we have demonstrated the transition between the $J=1$ and $J=2$ rotational levels for the EDM experiment using microwave pulse. Efforts were extended to carry out the experiments in various experimental configuration and level schemes to confirm our understanding of the molecular structure and state evolution dynamics. The preliminary results from the microwave excitation scheme were quite appealing and convincing. So we chose this microwave excitation scheme as the primary excitation method.

4.3 Adiabatic Following in Microwave Excitation

Although in the previous section we have demonstrated the ability to populate the desired states using π -pulses oscillation, several experimental imperfections hampered the efficiency of excitation. The Doppler effect and electric field inhomogeneity are of major concern. In the vapor cell, the molecules move with a Maxwellian distribution of velocities. Molecules moving along the direction of the pumping radiation beam experience a Doppler shift. The electric field inhomogeneity spatially varies the energy splitting of each Ω -doublet level due to the Stark effect. Thus the excitation of molecules of certain velocity classes or spatial distributions and locations, is not exactly resonant. Hence their population transfer will not be in phase with the transfer of resonant molecules. These velocity-dependent interactions and the inhomogeneity of electromagnetic field diminish the excitation probabilities. One can overcome such experimental imperfection by adiabatic time evolution induced by properly crafted microwave pulses to optimize the population transfer in molecules.

In the following sections, I will go over briefly the related theory and present the experimental results using adiabatic following technique.

4.3.1 Adiabatic Following

First, we look at a two level system coherently driven by laser or microwaves, following the standard procedure [67]. We start with the time-dependent Schrödinger equation:

$$i\hbar \frac{\partial}{\partial t} \Psi(t) = H(t) \Psi(t),$$

$$H(t) = \hbar \begin{pmatrix} \omega_b & \mathbf{d} \cdot \mathcal{E} \cos(\omega t + \phi) \\ \mathbf{d} \cdot \mathcal{E} \cos(\omega t + \phi) & \omega_a \end{pmatrix}, \Psi(t) = \begin{pmatrix} b(t) \\ a(t) \end{pmatrix}.$$

where $\Psi(t)$ is a column vector whose elements are the probability amplitudes of the excited state b and the ground state a.

We apply the rotating-wave approximation (RWA) and the two-level-system Hamiltonian in the rotating frame reads

$$H = \frac{\hbar}{2} \begin{pmatrix} \Delta & \Omega \\ \Omega & -\Delta \end{pmatrix},$$

where the detuning $\Delta = \omega_{ba} - \omega$, and $\Omega = \mathbf{d} \cdot \mathcal{E}$. Next the radiation field is described as a sinusoidally oscillating electric field, with constant amplitude ($d\Omega/dt = 0$), and instantaneous frequency sweeping from large negative detuning through resonance frequency to large positive detuning, $\Delta(t) = \alpha t$, where $t \in (-\infty, +\infty)$ and α is the frequency sweeping rate. The boundary conditions are $b(-\infty) = 0$ and $|a(-\infty)| = 1$. The time-dependent eigenenergies are $E_{\pm} = \frac{\hbar}{2} \left[\Delta(t) \pm \sqrt{\Delta^2(t) + \Omega^2} \right]$

Making the substitutions, $B(t) = b(t) \exp(-i\frac{\hbar}{2} \int \Delta dt)$ and $A(t) = a(t) \exp(+i\frac{\hbar}{2} \int \Delta dt)$,

yields

$$i \frac{d}{dt} \begin{pmatrix} B(t) \\ A(t) \end{pmatrix} = \begin{bmatrix} 0 & \frac{\Omega}{2} \exp(+i\hbar \int \Delta dt) \\ \frac{\Omega}{2} \exp(-i\hbar \int \Delta dt) & 0 \end{bmatrix} \begin{pmatrix} B(t) \\ A(t) \end{pmatrix}.$$

By eliminating $A(t)$, we get $\frac{d^2}{dt^2} B(t) - i\Delta \frac{d}{dt} B(t) + \frac{\Omega^2}{4} B(t) = 0$. The substitution $U(t) = B(t) \exp(-i \int \Delta dt)$ reduces this to the Weber equation $\frac{d^2}{dt^2} U(t) + (\frac{\Omega^2}{4} + \frac{i\alpha}{2} + \frac{\alpha^2}{4} t^2) U(t) = 0$. With the further substitutions, $z = \alpha^{1/2} e^{i\pi/4} t$, $n = \Omega^2/4i\alpha$, this finally reduces to the standard form $\frac{d^2}{dz^2} U(z) + (n + \frac{1}{2} - \frac{1}{4} z^2) U(z) = 0$. The solution is the Weber function $U(z) = A_{\pm} D_{-n-1}(\mp iz)$, $\alpha \gtrless 0$, where $A_{+(-)}$ is a constant to be determined by the boundary condition. The Weber function, also called the parabolic cylinder function, is related to Hermite polynomials by $D_n(x) = 2^{-n/2} e^{-\frac{x^2}{4}} H_n(x/\sqrt{2})$. In particular, the asymptotic behavior of Weber function $D_{\nu}(z)$ [68] is

$$D_{\nu}(z) \approx \exp(-\frac{z^2}{4}) z^{\nu} \left(1 + O\left(\frac{\nu^2}{z^2}\right) \right)$$

By applying the boundary conditions, we find $|A_{\pm}| = \gamma^{1/2} e^{-\pi\gamma/4}$, $\gamma = \Omega^2/|4\alpha|$. Using the asymptotic property of Weber function, we obtain the well-known **Landau-Zener formula** for transition probability as

$$P = |B(+\infty)|^2 = 1 - e^{-2\pi\gamma}, \quad p = 1 - P = e^{-2\pi\gamma} = \exp\left[-\frac{\pi\Omega^2}{2|\dot{\Delta}|}\right]. \quad (4.5)$$

Although this formula is exact only for a constant Rabi frequency Ω and a linearly varying detuning $\Delta(t)$ over an infinite time interval, it demonstrates that the ratio of Ω^2 to $\dot{\Delta}$ provides a measure of the probability of population transfer. If the Hamiltonian evolution is adiabatic, there will be a nearly complete population transfer from the ground state to the excited state. From Eq. 4.5, it's easy to see the condition for adiabatic evolution is that the frequency sweeping rate is negligible compared with the square of Rabi frequency,

explicitly,

$$|\dot{\Delta}| \ll \Omega^2.$$

The radiation pulse, with the detuning $\Delta(t)$ sweeping slowly from some very large negative value to some very large positive value (or vice versa), will produce complete population transfer, known as **adiabatic following**. Compared to Rabi cycling, adiabatic following provides a robust means to produce complete population transfer and suppress the variation of population transfer efficiency against moderate variations in various experimental environments, e.g., the laser intensity, frequency detuning, electromagnetic field inhomogeneity, and interaction time.

Explicitly, the adiabatic condition requires a smooth pulse, long interaction time, large Rabi frequency, and large detuning. In our experiment, the short microwave pulse is used in order to transfer the population without resolving the Zeeman sub-levels. The quantum beats, with typical values around several hundred kilohertz, limit the microwave coupling time, requiring it to be less than tens of micro-seconds. The available and affordable microwave resource put a stringent limit on the frequency deviation and frequency sweeping rate, although not as much when using the arbitrary waveform generator (see microwave setup in Section 4.2.4). In the following section, the generalized Landau-Zener model will be presented, which gives a better description of the transition probability for a finite coupling period.

4.3.2 Generalized Landau-Zener Model

In the original Landau-Zener model, the coupling is supposed to last from $t \rightarrow -\infty$ to $t \rightarrow +\infty$. Vitanov and Garraway gave the analytic solution for the finite coupling period situation [69],

$$\Omega(t) = \begin{cases} \Omega_0, & t_i \leq t \leq t_f \\ 0, & \text{anywhere else} \end{cases}, \quad \Delta(t) = \beta^2 t,$$

where using the parametrization of β^2 is for the convenience of the following literature.

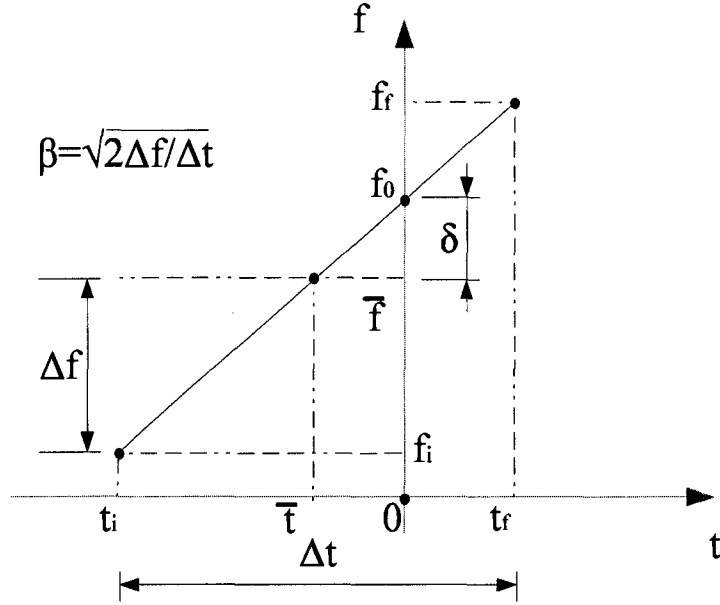


Figure 4.18: Parametrization of Generalized Landau-Zener Model. δ is defined as the the frequency detuning between the center of the sweeping and the resonance, Δf as FM frequency deviation, and $\Delta t = t_f - t_i$ as the pulse width.

They assume the frequency sweeps through the resonance at time $t = 0$ if the time span covers the origin, thus by varying β , t_i and t_f , various situations, including off resonance, can be covered. Define the dimensionless scaled parameters $\omega = \Omega_0/\beta$, $\tau_i = -\beta t_i$, and $\tau_f = \beta t_f$, where the sign choice is for future convenience. The parameters associated with experimental variables are

$$\begin{aligned}
 \tau_f &= [\delta/(2\Delta f/\Delta t) + \Delta t/2] \sqrt{2\Delta f/\Delta t}, \\
 \tau_i &= [\delta/(2\Delta f/\Delta t) - \Delta t/2] \sqrt{2\Delta f/\Delta t}, \\
 \omega &= \Omega_0/\sqrt{2\Delta f/\Delta t},
 \end{aligned}
 \tag{4.6}$$

with δ defined as the the frequency detuning between the center of the sweeping and the resonance, FM frequency deviation Δf and pulse width $\Delta t = t_f - t_i$, shown in Fig. 4.18. The typical values are, Rabi frequency $\Omega \sim 5$ MHz, FM deviation $\Delta f \sim 10$ MHz, pulse width $\Delta t \sim 2 \mu\text{s}$, leading to $\omega \sim 2$ and $\tau \sim 3$.

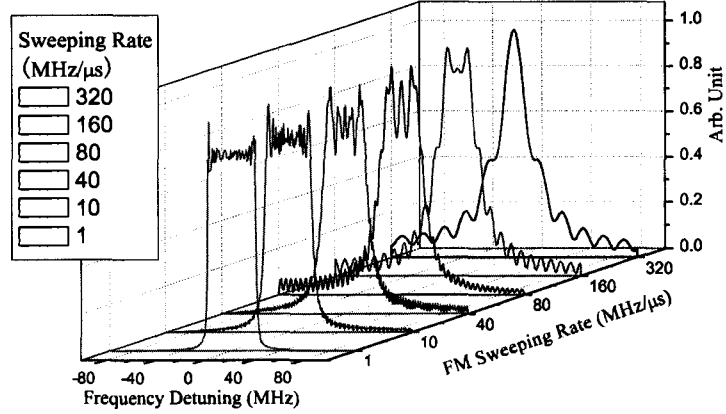


Figure 4.19: Fourier Transform of Frequency-Modulated Sinusoid Pulse. Frequency deviation is fixed at ± 10 MHz. Frequency sweeping rate of $10 \text{ MHz}/\mu\text{s}$ is corresponding to a pulse width of $2 \mu\text{s}$.

The effect of the finite transit time and the finite frequency sweeping range can be studied using the Fourier transform of the frequency-modulated sinusoid pulse, shown in Fig. 4.19. If the inverse of pulse width is much large than the frequency deviation in the fast sweeping case, the Fourier spectrum width will be limited by the inverse of the pulse width. The adiabatic condition corresponds to large Rabi frequency, long transit time and slow frequency sweeping.

Similar to the previous section, the complete analytic solution to the adiabatic following will be related to the Weber equation, expressed in terms of Weber function D_ν , and obtained by applying the proper boundary condition. The transition probability is

$$\begin{aligned}
 P_2(\tau_f, -\tau_i) = & \frac{1}{2 \sinh \frac{\pi\omega^2}{2}} \left| -D_{i\omega^2/2}(\tau_f\sqrt{2}e^{-i\pi/4})D_{i\omega^2/2}(-\tau_i\sqrt{2}e^{i3\pi/4}) \right. \\
 & \left. + D_{i\omega^2/2}(\tau_f\sqrt{2}e^{i3\pi/4})D_{i\omega^2/2}(-\tau_i\sqrt{2}e^{-i\pi/4}) \right|^2.
 \end{aligned} \tag{4.7}$$

The adiabatic solution is obtained in the condition $\omega \gg 1$ is

$$P_2(\tau_f, -\tau_i) \sim \frac{1}{2} + \frac{\tau_i \tau_f}{2\sqrt{(\omega^2 + \tau_f^2)(\omega^2 + \tau_i^2)}} - \frac{\omega^2 \cos[\xi(\tau_f) + \xi(\tau_i)]}{2\sqrt{(\omega^2 + \tau_f^2)(\omega^2 + \tau_i^2)}},$$

where

$$\xi(\tau) = \tau\sqrt{\tau^2 + \omega^2} + \omega^2 \ln\left(\frac{\tau + \sqrt{\tau^2 + \omega^2}}{\omega}\right).$$

The asymptotic expression under the strong-coupling condition $\tau_i^2 + \omega^2 \gg 1$ and $\tau_f^2 + \omega^2 \gg 1$ is

$$\begin{aligned} P_2(\tau_f, -\tau_i) &\sim \frac{1}{2} + \left(\frac{1}{2} - e^{-\pi\omega^2}\right) \frac{\tau_i \tau_f}{\sqrt{(\omega^2 + \tau_f^2)(\omega^2 + \tau_i^2)}} \\ &\quad - e^{-\frac{\pi\omega^2}{2}} \sqrt{1 - e^{-\pi\omega^2}} \frac{\tau_i \tau_f \omega}{\sqrt{(\omega^2 + \tau_f^2)(\omega^2 + \tau_i^2)}} \left[\frac{\cos \xi(\tau_f)}{\tau_f} + \frac{\cos \xi(\tau_i)}{\tau_i} \right] \\ &\quad + \frac{\omega^2 \left\{ e^{-\pi\omega^2} \cos[\xi(\tau_f) - \xi(\tau_i)] - (1 - e^{-\pi\omega^2}) \cos[\xi(\tau_f) + \xi(\tau_i)] \right\}}{2\sqrt{(\omega^2 + \tau_f^2)(\omega^2 + \tau_i^2)}}. \end{aligned}$$

It is readily verified that the strong-coupling asymptotic approximation contains the adiabatic following approximation in the limit $\omega \gg 1$, and it can be used to describe the weak-coupling asymptotic situation in the limit $\tau_i, \tau_f \gg \omega$.

For symmetric crossing, with $\tau_i = \tau_f$, the transition probability is

$$\begin{aligned} P_2(\tau, -\tau) &\sim 1 - e^{-\pi\omega^2} - e^{-\frac{\pi\omega^2}{2}} \sqrt{1 - e^{-\pi\omega^2}} \frac{2\tau\omega}{\omega^2 + \tau^2} \cos \tilde{\xi}(\tau) \\ &\quad + \frac{\omega^2}{\omega^2 + \tau^2} \left[e^{-\pi\omega^2} - (1 - e^{-\pi\omega^2}) \cos^2 \tilde{\xi}(\tau) \right], \end{aligned}$$

where

$$\tilde{\xi}(\tau) = \frac{\pi}{4} - \frac{\omega^2}{2} + \tau\sqrt{\tau^2 + \omega^2} + \omega^2 \ln\left[\frac{1}{\sqrt{2}}(\tau + \sqrt{\tau^2 + \omega^2})\right] + \arg \Gamma\left(1 - \frac{1}{2}i\omega^2\right).$$

Evidently, Eq. 4.3.2 reduces to the well known Landau-Zener formula for infinite coupling

time,

$$P_2(+\infty, -\infty) = 1 - e^{-\pi\Omega_0^2/\beta^2}.$$

To demonstrate the adiabatic following phenomena, the parameters in terms of the experimental variables (see Eq. 4.6), are plugged into the transition probability formula.

The above discussion is valid for two-level system. For the three-level or four-level system, it is rather complicated to work out the analytic solutions. In our V , Λ , and four-level schemes, the Zeeman splitting is small compared with the Stark splitting, so that we can apply the analytic solution as first order approximation to our three-level system. Hence, the following discussion refers to the two-level system.

The density plot Fig. 4.20A indicates an interesting phenomena in that the transition probability for the finite pulse coupling is an oscillating function of the coupling duration 2τ . Furthermore, an increase in ω leads to the increasing adiabatic characteristics of the transition such that the transition probability tends to unity, as shown in the plot, with the brightness representing the almost complete population inversion.

In practice, it is convenient to scan through the frequency detuning δ without resetting the programmed waveform to change the pulse width Δt and FM frequency deviation Δf . After the optimization of other parameters at zero detuning, we can double check the spectral features as we scan through the frequency detuning. So the density plots of transition probability with respect to the frequency detuning and other parameters, such as the pulse width Δt , FM frequency deviation Δf , and Rabi frequency Ω , are shown in Fig. 4.20B, Fig. 4.20C, and Fig. 4.20D.

As shown in Fig. 4.20B, if we fix the microwave power and frequency deviation, increasing the FM pulse width will lead to the complete population transfer as it increases the adiabatic property of such transition.

If we fix the microwave power and the microwave pulse width, increasing the FM frequency deviation, thus increasing the FM frequency sweeping rate, diminishes the transition probability and broadens the resonance line as it decreases the satisfaction of the

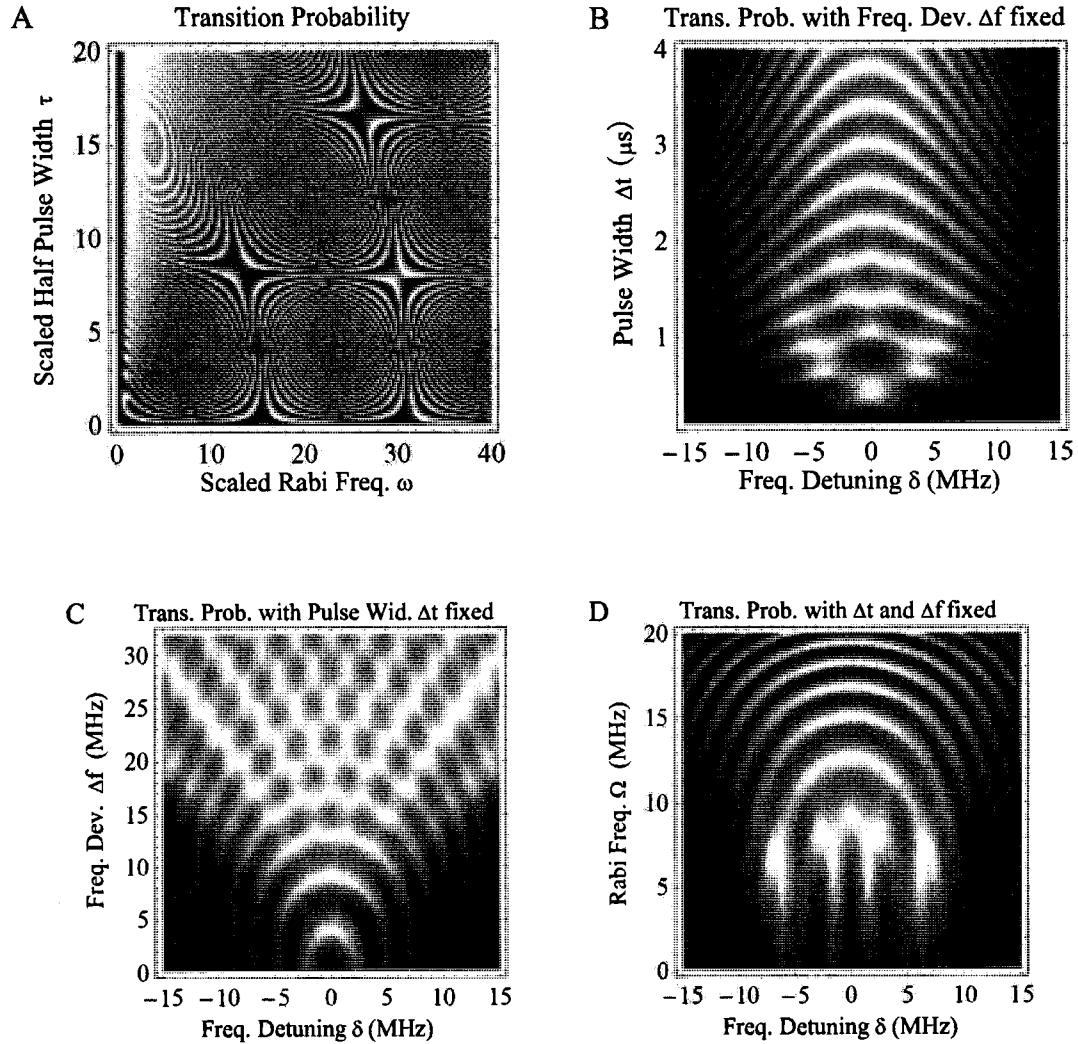
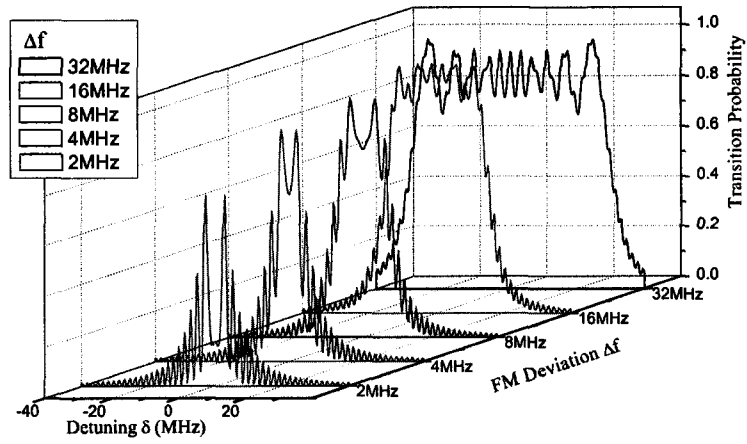
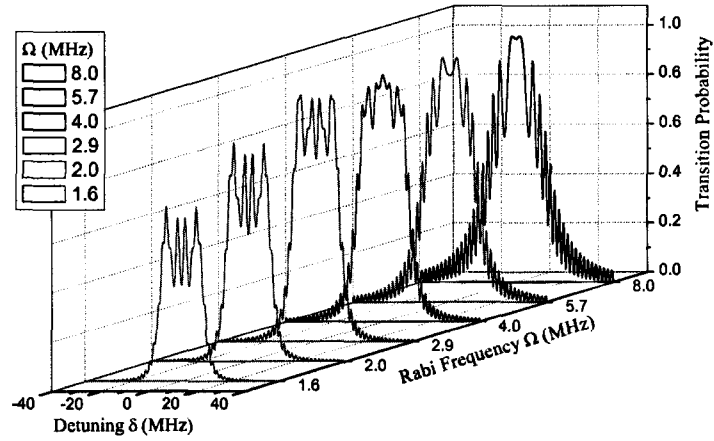


Figure 4.20: Generalized Landau-Zener Model. (A) Density plot of transition probability according to Eq. 4.7, x -axis ω and y -axis τ ; (B) Density plot of transition probability versus initial microwave frequency detuning with various pulse width for fixed frequency deviation, x -axis δ in MHz and y -axis Δt in μs . Here Rabi Frequency $\Omega = 5$ MHz, $\Delta f = 16$ MHz; (C) Density plot of transition probability versus microwave frequency detuning with various frequency deviation for fixed pulse width of $1 \mu s$, Rabi Frequency $\Omega = 5$ MHz, x -axis δ and y -axis Δf . (D) Density plot of transition probability versus microwave power at fixed frequency deviation $\Delta f = 16$ MHz and pulse width $\Delta t = 2 \mu s$, x -axis is δ in MHz and y -axis is Rabi frequency Ω in MHz.



(A)



(B)

Figure 4.21: Transition Probability at Different Frequency Deviation and Power using Adiabatic Following, calculated using Eq. 4.7. (A) Transition probability at different frequency deviations Δf . Here Rabi Frequency Ω is fixed at 4.5 MHz, and pulse width $\Delta t = t_f - t_i = 2 \mu\text{s}$. (B) Transition probability at different Rabi frequencies. Here frequency deviation Δf is fixed at 11 MHz, and pulse width $\Delta t = 2 \mu\text{s}$.

adiabatic condition, shown in Fig. 4.20C. Insufficient FM frequency deviation results in a short coupling time τ (see Eq. 4.6), leading to incomplete population transfer, shown in Fig. 4.21A. If we fix the frequency sweeping rate and span, increasing the microwave power moves the condition of transition into the adiabatic regime with increasing transition probability, shown in Fig. 4.20D. Increasing microwave power broadens the resonance line width, as shown in Fig. 4.21B.

As emphasized previously, the above discussion is valid for two-level system. The application to our three-level or four-level system is just an approximation. But still, the analytic solution serves as a general guidance for the choice of the parameter range of the pulse width, sweeping frequency, and Rabi frequency. The experiments to check the validity of the analytic solution and the modification to our specific level schemes were carried out and will be discussed in the next section.

4.3.3 Adiabatic Following Experiment

The experimental results using the adiabatic following technique are presented here. A carefully engineered control voltage is applied to the external control port of the *Agilent* E8257C for frequency modulation. To avoid spurious effects, we turn on the frequency modulation a few μs before the pulse and hold it at the low(high) voltage, ramp the voltage from low to high (or *vice versa*) during the pulse span, and turn it off at few μs after turning off the microwave switch.

The typical experimental result using the adiabatic following technique is shown in Fig. 4.22.

A vertically polarized laser pulse tuned to the R0 line pumps the molecules from the ground state to the $a(1) \ ^3\Sigma^+ \ J=1^-, \ M=0$ state. A horizontally polarized microwave square pulse then drives them to $|J = 2, M = \pm 1, \tilde{\epsilon}\rangle$ in the presence of the external electric field with strength 78.7 V/cm. The microwave pulse is 2 μs in width and attenuated by 3 dB, with the frequency modulation mode on at 7.5 MHz deviation. The microwave power is estimated to be around 24 dBm inside the cell, corresponding to a Rabi frequency $\Omega_0 \approx$

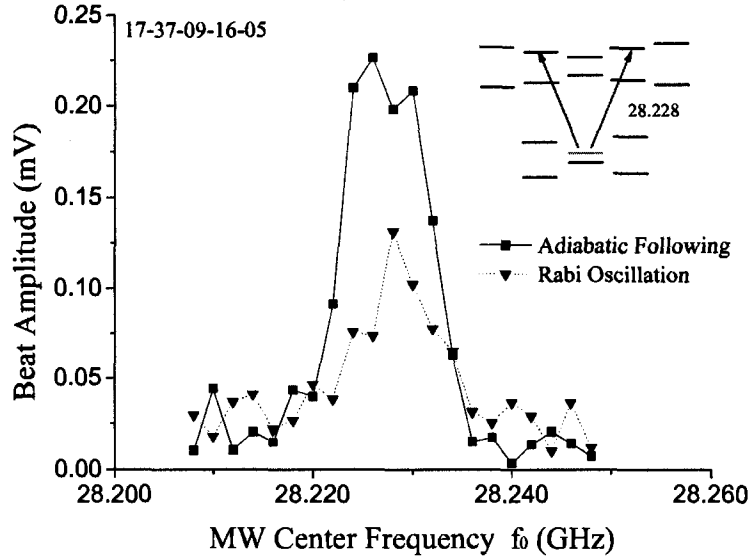


Figure 4.22: Typical Result using Adiabatic Following. Laser vertically polarized, MW horizontally polarized, with electric field strength 78.7 V/cm across the electrodes. Pulse width $\Delta t = 2 \mu\text{s}$, frequency deviation $\Delta f = 7.5 \text{ MHz}$. The initial $J=1$ quantum beat amplitude with laser horizontally polarized is $\sim 0.4 \text{ mV}$.

3.5 MHz. The Rabi oscillation experiment discussed in Section 4.2.5 was carried out to estimate the Rabi frequency as well. An estimate of Ω_0 is obtained by scanning the optimal pulse width with driving a microwave π pulse, as described in the previous section. This gives $\Omega_0 \sim 2 \text{ MHz}$ for the transition between $|J = 2, M = 0, e\rangle$ and $|J = 1, M = \pm 1, \bar{e}\rangle$, as the typical π pulse width is around 500 ns in the ordinary experimental setup. The beat amplitude peaks when the MW square pulse width is around 280 ns, consistent with the result from the estimated Rabi frequency. The FM control voltage is applied to turn on the FM mode 1 μs before switching on the microwave, ramp through $\Delta f = 15 \text{ MHz}$ (frequency deviation $\pm 7.5 \text{ MHz}$ around the resonance frequency f_0) in 2 μs , and turn off 1 μs after switching off the FM switch. This method is used to avoid transient ringing in the FM control voltage.

We scanned the microwave frequency around $f_0 \approx 28.23 \text{ GHz}$ and monitored the amplitude of the $J=2$ level quantum beat in the fluorescence power spectrum. The amplitude

peak indicates coherent population builds up in $|J = 2, m = \pm 1, \bar{e}\rangle$ as the FM center frequency f_0 is scanned through the transition resonance. The initial J=1 quantum beat amplitude with laser horizontally polarized is ~ 0.4 mV. The maximum J=2 quantum beat amplitude using the adiabatic following method is ~ 0.23 mV, shown as the square-solid line in Fig. 4.22. The spectral shape matches the theoretical calculation of transition probability using Eq. 4.7 with parameter $\Delta f = 7.5$ MHz, $\Delta t = 2$ μ s, and Rabi frequency Ω_0 is 3.5 MHz. There is only ~ 0.13 mV J=2 beat amplitude achieved using the Rabi oscillation method (see Section 4.2.5), shown as the triangle-dotted line in Fig. 4.22. The experimental result reflects $\sim 70\%$ improvement in the transfer efficiency by using the adiabatic following.

To ensure the satisfaction of the adiabatic condition $\omega = \Omega_0 / \sqrt{|\dot{\Delta}|} \ll 1$, the Rabi cycling method described in previous section is carried out first to obtain an estimate of the Rabi frequency Ω_0 . Second, various FM deviations and pulse widths are scanned. In Fig. 4.23A, the quantum beat amplitude is plotted against the pulse width Δt with FM deviation Δf fixed at 2 MHz, 5 MHz, 10 MHz, 20 MHz, and 32 MHz respectively, hence various sweeping rate. Fig. 4.23B shows the quantum beat amplitude versus the FM deviation Δf as the pulse width is fixed at 0.75 μ s, 1 μ s, 2 μ s, and 4 μ s respectively.

For the transition between $|J = 1, M = 0, e\rangle$ and $|J = 2, M = \pm 1, \bar{e}\rangle$, the optimal sweeping rate seems to be around 2 \sim 5 MHz/ μ s, which is consistent with $\Omega_0 \sim 5$ MHz, $|\dot{\Delta}| \ll \Omega_0^2$. It suggests that the frequency sweeping rate should be less than 1.5 MHz/ μ s. This requirement is quite consistent with the experimental result. A new amplifier with higher power output will allow larger Rabi frequency and larger frequency deviation. Further experiments will be carried out using the microwave amplifier with higher power output.

We have also explored the parameter space for the optimization of the population transfer. If we plot the transition probability against the FM center frequency, the theoretical prediction of the spectral lines will look like Fig. 4.24A.

However the experimental results, shown in Fig. 4.24B for the transition between $|J =$

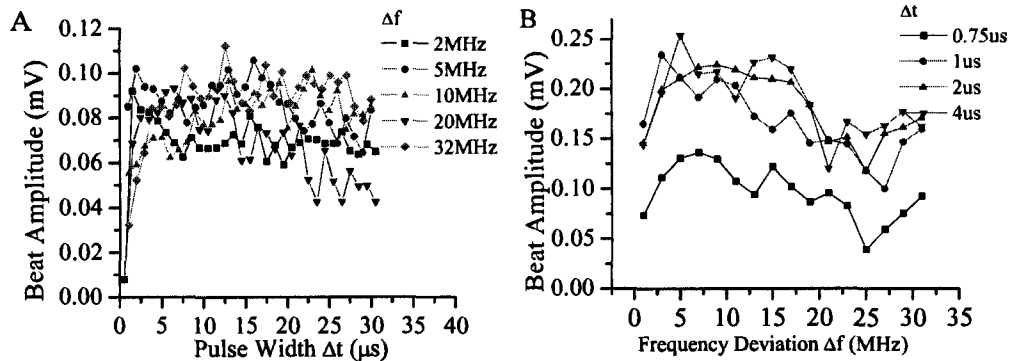


Figure 4.23: Optimization of Frequency Sweeping Rate. (A) Beat amplitude versus pulse width Δt with FM deviation Δf fixed at 2 MHz, 5 MHz, 10 MHz, 20 MHz, and 32 MHz respectively; (B) Beat amplitude versus FM deviation Δf as the pulse width Δt fixed at 0.75 μs , 1 μs , 2 μs , and 4 μs respectively.

$|1, M = 0, e\rangle$ and $|J = 2, M = \pm 1, \tilde{e}\rangle$, indicate asymmetries of the spectral lines and shifts of the line centers. Similar results also occur for the transition from $|J = 2, M = 0, e\rangle$ using the R1 transition down to $|J = 1, M = \pm 1, \tilde{e}\rangle$ with 300 V across the electrodes, shown in Fig. 4.24C; and the transition from $|J = 1, M = \pm 1, e\rangle$ to $|J = 2, M = \pm 1, e\rangle$ in the absence of an external electric field, shown in Fig. 4.24D. These results have not been repeated yet. Further study suggests that it might be related to the sharp turning on at the FM control voltage, causing problems due to control parts' limited bandwidth.

In conclusion, we have reported the experimental results using the adiabatic following technique here. As our experimental results generally reflected a good understanding of the microwave excitation scheme, we did not dwell on the mysteries of the unsuccessful RF excitation scheme and decided to adopt the microwave scheme.

4.3.4 Double Pulsed Adiabatic Following

To prepare the desired EDM states, a sequence of two microwave pulses are used to accomplish the population transfer from the laser-prepared state $|J = 1, M = 0, e\rangle$ to the EDM state $|J = 1, M = \pm 1, \tilde{e}\rangle$ or $|J = 1, M = \pm 1, \tilde{f}\rangle$, using an intermediate $J = 2$ state.

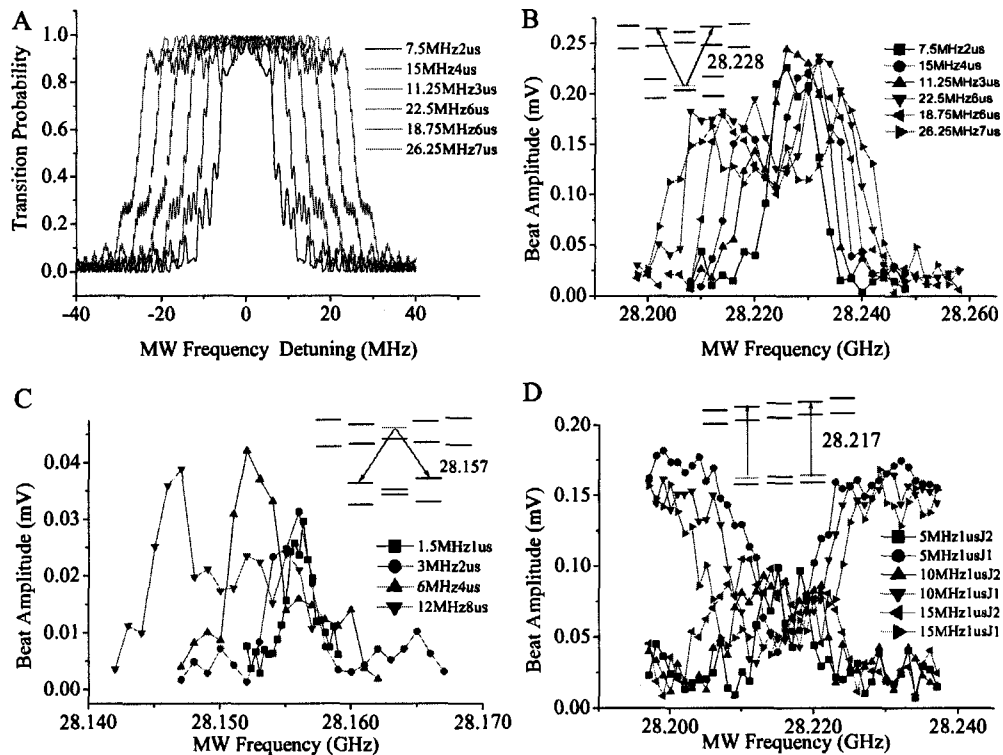


Figure 4.24: Beat Amplitude versus FM Center Frequency at Various Sweeping Rates. (A) Theoretical prediction of spectral line for different sweeping rates; (B) Experimental result for the transition between $|J = 1, M = 0, e\rangle$ and $|J = 2, M = \pm 1, \tilde{e}\rangle$; (C) Transition from $|J = 2, M = 0, e\rangle$ transition down to $|J = 1, M = \pm 1, \tilde{e}\rangle$ at 300V across the electrodes. Laser vertical polarized and tuned to R1 line; (D) Transition from $|J = 1, M = \pm 1, e\rangle$ to $|J = 2, M = \pm 1, e\rangle$ in the absence of the external electric field.

As described in the previous section, we first prepare the molecules in the $|J = 1, M = 0, e\rangle$ state. Two microwave pulses with different polarizations and frequencies are required and made possible by a microwave orthomode transducer (OMT) and conical horn. We apply an adiabatic following technique to both pulses to pursue better population transfer efficiency. For our current setup with a single microwave source, the separated microwave pulses first transfer the population to the a(1) J=2 level, then transfer down to the desired EDM states in separate single-photon steps. For each individual step, we follow experimental procedures similar to those in last section. In addition to the experimental parameter space we explored, the time delay between two consecutive pulses can be optimized as well. The scheme using chirped adiabatic passage with overlapping pulse sequence to populate the desired states selectively [70] is under consideration for future improvements.

The significant achievement in the microwave adiabatic following experiment is to selectively populate the EDM states with a good efficiency. Fig. 4.25A shows the population transfer steps, first applying horizontal microwave to drive from $|J = 1, M = 0, e\rangle$ to $|J = 2, M = \pm 1, \bar{e}\rangle$, then applying vertical microwave to drive down to $|J = 1, M = \pm 1, \bar{e}\rangle$. The laser is vertically polarized and tuned to R0 line, and electric field strength is 39 V/cm. The first MW pulse has $\Delta t = 2 \mu\text{s}$ pulse width, is centered at $f'_0 = 28.220$ GHz, and has a $\Delta f = 11$ MHz frequency deviation; The second pulse has $\Delta t = 2 \mu\text{s}$ pulse width, is centered at $f''_0 = 28.193$ GHz, and has a $\Delta f = 11$ MHz frequency deviation, with $0.5 \mu\text{s}$ delay after the first pulse. The dashed line shows the J=1 beat amplitude when the laser is horizontally polarized, denoting the available molecules in J=1 levels. The dotted line shows the J=2 beat amplitude after the first microwave pulse and the solid line shows the J=1 beat amplitude after the second microwave pulse, compared with the original J=1 beat amplitude, yielding around 43% efficiency and 3% quantum beat contrast.

Fig. 4.25B shows another population transfer path, first applying vertical polarized microwaves to drive from $|J = 1, M = 0, e\rangle$ to $|J = 2, M = 0, e\rangle$, then applying horizontally polarized microwaves to drive down to $|J = 1, M = \pm 1, \bar{e}\rangle$. Here first MW pulse has a $\Delta t = 2 \mu\text{s}$ pulse width, is centered at $f'_0 = 28.217$ GHz, and has an $\Delta f = 11$ MHz frequency

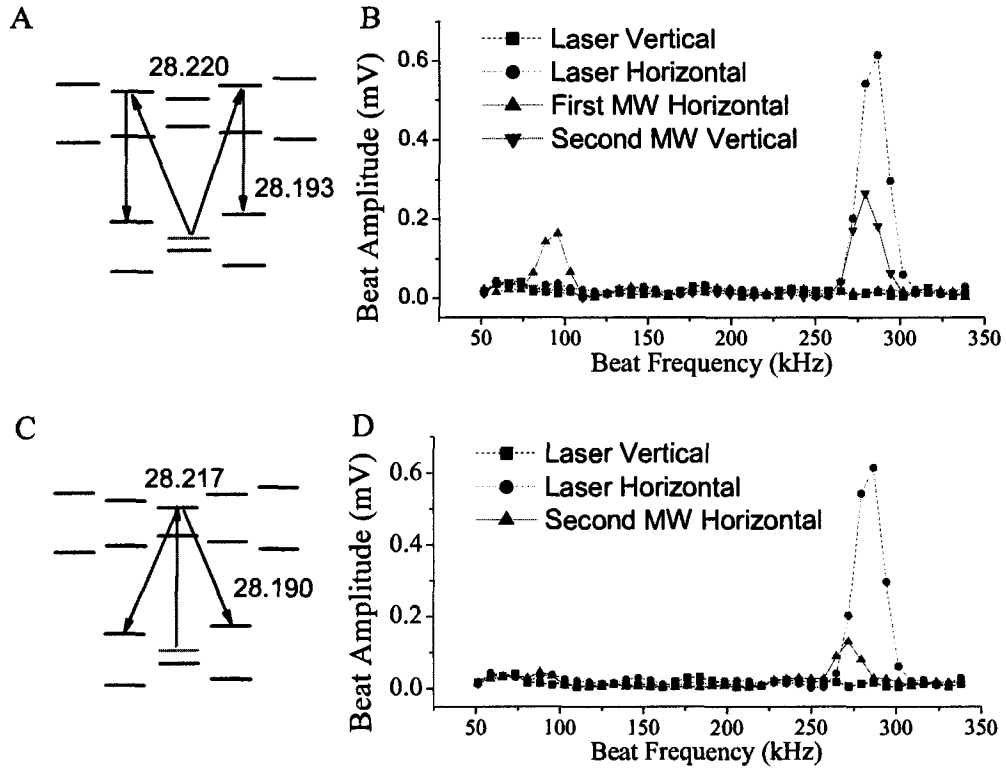


Figure 4.25: Selective Preparation of the EDM States using MW Adiabatic Following. Laser vertically polarized, at 39 V/cm E field strength. (A) and (C) are related energy diagrams for each transfer path; (B) First MW pulse horizontally polarized, $\Delta t = 2 \mu\text{s}$ pulse width, centered at $f'_0 = 28.220$ GHz, $\Delta f = 11$ MHz frequency deviation; Second pulse vertically polarized, $\Delta t = 2 \mu\text{s}$ pulse width, centered at $f''_0 = 28.193$ GHz, $\Delta f = 11$ MHz frequency deviation, and $0.5 \mu\text{s}$ delay after the first pulse; (D) Another transfer path. First MW pulse vertically polarized, $\Delta t = 2 \mu\text{s}$ pulse width, centered at $f'_0 = 28.217$ GHz, $\Delta f = 11$ MHz frequency deviation; Second MW pulse horizontal polarized, $\Delta t = 2 \mu\text{s}$ pulse width, centered at $f''_0 = 28.190$ GHz, $\Delta f = 11$ MHz frequency deviation, and $0.5 \mu\text{s}$ delay after the first pulse.

deviation; the second MW pulse has a $\Delta t = 2 \mu\text{s}$ pulse width, is centered at $f_0'' = 28.190$ GHz, and has an $\Delta f = 11$ MHz frequency deviation, with a $0.5 \mu\text{s}$ delay after the first pulse. The lower efficiency of this transfer path is due to the rather weak transition from $|J = 2, M = 0, e\rangle$ to $|J = 1, M = \pm 1, \bar{e}\rangle$ as the matrix element connecting this transition is one-half of the strong one from $|J = 2, M = \pm 1, \bar{e}\rangle$ to $|J = 1, M = \pm 1, \bar{e}\rangle$. At the time of this data collection, it is thought that the efficiency was limited by the available microwave power.

The results shown above were taken before the installation of a new MW amplifier and the magnetic shields. The results have not been repeated for the new setup yet. Once the efficiency is optimized, we will start the data collection for an EDM measurement.

4.3.5 Technical Concern

To achieve the optimization of the transfer efficiency, there are several technical concerns:

1. Synchronization. As the microwave system consists of several cascaded components. We need to make sure there is no bottleneck component that may have too slow response to the switching pulses due to the limited bandwidth or impedance mismatch. Make sure the switching pulses to control the microwave switch or FM mode have clear rising and falling edge. To avoid such spurious effects, we usually turn on the frequency modulation a few μs before the arriving of the microwave switching pulse and hold it at the low(high) voltage, ramp the voltage from low to high (or vice versa) during the pulse span, and turn it off at few μs after turning off the microwave switch.
2. Interface reflection. The microwave transmits through the microwave guide, quartz light pipe, and the cell window before the interaction with the molecules inside the vapor cell. The gaps between these interfaces may accidentally match the half wavelength condition to cause the microwave standing wave or diminish the transmission of the microwave.

The feature-rich molecular structure distinguishes itself with the simple model of two-level system. In the application of adiabatic following, the frequency sweeping Δf need to be chosen broad enough to satisfy the adiabatic condition (see Section 4.3.2), yet trying to avoid covering the unwanted levels accidentally.

The transfer efficiency will be affected by Zeeman splitting, the microwave pulse delay with respect to the laser pulse, and the pulse interval between two microwave pulses as well. The molecules precess at the beat frequency and hence have accumulate certain phase that will change the transition probability of the second microwave pulse in the double pulsed adiabatic following scheme. Further investigation on the optimization of the transfer efficiency under different magnetic field \mathcal{B} and pulse interval is under consideration.

4.3.6 Conclusion

In conclusion, we have demonstrated the feasibility of EDM state preparation using the microwave technique. With this new approach, it will be possible to measure the electric dipole moment of the electron in the metastable $a(1)[^3\Sigma^+]$ state of PbO.

Chapter 5

Measurement of Molecular Parameters

Our experiment improves the precision on several previously measured molecular constants, which casts light on the feasibility of future systematic error checking and reduction.

5.1 Zeeman Effect Measurement

To demonstrate the power of quantum-beat spectroscopy in the context of our experiment, we have measured the Landé factors, g_e and g_f , of the $a(1)[^3\Sigma^+]$ Ω -doublets for $J=1$. Accurate knowledge of the values of these g -factors is very important: the g -factors enter into semi-empirical estimates of the EDM-enhancement [35] and the uncertainty on the difference $\delta g = |g_e - g_f|$ determines the level at which we can reject systematic magnetic effects by comparing the beat frequencies of the two Ω -doublet states.

In general, we can extract the g -factors by measuring the beat frequency ν_b at different magnitudes of the magnetic field \vec{B} for the e and f levels. These were determined before and after taking data in the volume occupied by the cell with a calibrated 3-axis magnetometer.

One way to access e and f levels is to use direct laser excitation and tune to a certain transition line. This method was used to determine the g -factor difference in previous thesis

work on the PbO EDM experiment [45]. Without the perturbation of the external electric field, electric dipole selection rules allow us to selectively excite either parity state of the $J=1$ Ω -doublet. This is accomplished by tuning the dye laser frequency to either the X(0) $J=0^+$ to a(1) $J=1^-$ transition (R0 line), or the X(0) $J=1^-(e)$ to a(1) $J=1^+(f)$ transition (Q1 line), which are separated by 18 GHz. By driving the Q1 transition and comparing changes in beat frequency with the R0 results for the same changes in \mathcal{B} , the difference in g -factors was determined: $\delta g = -25(13) \times 10^{-4}$. The uncertainty is dominated by the uncertainty in magnetic field calibration and drift. The experiment was carried out prior to the installation of magnetic shields and was susceptible to ambient magnetic field drift, especially as there was several minutes of time delay while changing the laser frequency between R0 and Q1.

We obtained higher accuracy in δg using a more sophisticated method. As before, we drove the R0 transition with \hat{x} polarized light, populating the $J = 1^-(e)$ level. Periodically, we applied a pulse of RF electric field to resonantly drive the $\Delta M = 0$ electric dipole transition between the e and f levels. The time duration $T_{\text{rf}} \sim 5 \mu\text{s}$, frequency $\nu_{\text{rf}} = \Delta\Omega/h$ and amplitude $E_{\text{rf}} \sim 0.12 \text{ V/cm}$ of the rf pulse were adjusted to create a π pulse. This method allowed us to switch more rapidly between the e and f levels than was possible by tuning the laser between the R0 and Q1 transition, thus eliminating much of the noise due to drifts in ambient magnetic field during the measurement.

The observed beat frequency is determined by the relative populations in the e level or f levels and their g -factor difference. As the RF pulse transfers the population from the e level to f level, the beat frequency changes from $\nu_b^e \propto g_e$ to $\nu_b^f \propto g_f$, with $\nu_b^{e(f)} = g_{ef}\mu_B\mathcal{B}/h$. Maximum deviation $\delta\nu_b$ from the beat frequency of the e level ν_b^e , $\delta\nu_b = (g_f - g_e)\mu_B\mathcal{B}/h$, occurs when the population has been completely transferred to the f level by a RF-pulse satisfying the π -condition. The beat frequency change $\Delta\nu_b$ can be described

by the following function:

$$\Delta\nu_b = \delta\nu_b \frac{\Omega_R^2}{\Omega_R^2 + (\omega_{rf} - \Delta_\Omega)^2} \sin^2 \left(\pi t \sqrt{\Omega_R^2 + (\omega_{rf} - \Delta_\Omega)^2} \right), \quad (5.1)$$

where Ω_R is the Rabi frequency, ω_{rf} is the RF frequency, and Δ_Ω is the Ω -doublet splitting.

Measuring the change in beat frequency between data with or without the rf pulse yields $\delta g = -31(9) \times 10^{-4}$, shown in Fig. 5.1. The error is primarily from the uncertainty in the efficiency of the π -pulse transfer. The combined result is $\delta g = -30(8) \times 10^{-4}$ [39].

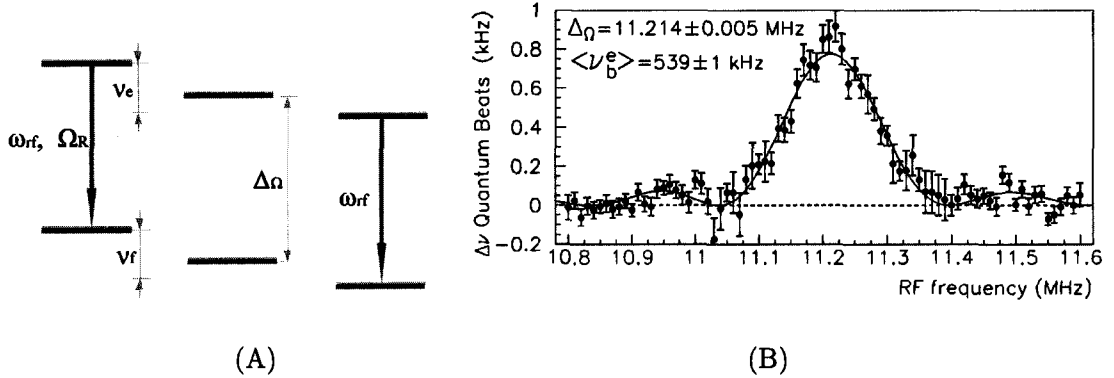


Figure 5.1: Beat Frequency Change with RF Transition. A rf pulse at the frequency of the Ω -doublet splitting transfers population from the e to f levels and changes the beat frequency from $\nu_b^e \propto g_e$ to $\nu_b^f \propto g_f$ [39]. (A) Level diagram. (B) Experimental results and fitting.

This RF-spectroscopic study can also be applied to the measurement of the Ω -doublet splitting, as indicated by Eq. 5.1. We found $\Delta_\Omega = 11.214(5)$ MHz, where the uncertainty is dominated by possible systematic effects due to off-resonant ac Stark shift (Bloch-Siegert shift). This is consistent with the best previous measurement, but 40 times more precise.

Using the microwave excitation method, we can populate the e or f level in $a(1) \ ^3\Sigma^+$ selectively. In principle, we could measure the difference in beat frequency between the e and f levels. Again we can take advantage of quick switching between the e and f level to eliminate ambient magnetic field drift during the measurement. This method is identical to the measurement of eEDM. The difficulty in absolute magnetic field calibration with

the magnetic shields installed might hamper the measurement of the absolute value of the g -factors. However, the g -factor difference δg is more important to the systematic error suppression (see Section 2.6.3). δg can be measured with higher accuracy, based on our knowledge of the absolute value of g -factors ($\sim 2\%$ uncertainty), compared to current result of $\delta g = -30(8) \times 10^{-4}$ [39].

5.2 Stark Effect Measurement

We have successfully demonstrated the ability to apply electric fields in the cell, with the required magnitude to fully polarize the PbO molecules. We have successfully applied ± 222 V on the electrodes (and ± 400 V on the guard rings at 1.8:1 optimal ratio) to produce homogeneous electric fields as large as ~ 120 V/cm with no signs of discharge or other difficulties. The molecular polarization $|P|$ rapidly increases toward unity as the electric field \mathcal{E} increases, already reaching 0.986 at 40 V/cm. The effect of the applied \mathcal{E} -field, has been studied through measurements of the Zeeman beat contrast as a function of electric field strength.

In the early phase of PbO experiment using the first generation cell, we tried driving the $\Delta M = 0$ transition with and without the presence of an electric field by applying an oscillating electric field with a certain DC offset. The detail of the cell structure has been described in earlier thesis work [45]. We used the PbO molecules to sense weak applied electric fields \mathcal{E} ($\mathcal{E} < 2$ V/cm) by measuring the Stark shift in the Ω -doublet splitting. We populated the $J=1^-(e)$ $M = \pm 1$ levels at $\mathcal{E} = 0$ by driving the R0 transition with \hat{x} polarized light. At $t \sim 5 \mu\text{s}$, \mathcal{E} was ramped up adiabatically over $2.5 \mu\text{s}$ ($1/\mathcal{E} \cdot d\mathcal{E}/dt < \Delta\Omega/h$), then a RF π pulse ($T_{\text{rf}} = 5 \mu\text{s}$) was applied to drive the transition to the other state of mixed parity. Next \mathcal{E} was ramped down adiabatically, and the beat frequency ν_b was determined. For ν_{rf} far from resonance, no population was transferred to the f level, so the beats were characterized by g_e , whereas resonant excitation yields beats characterized by g_f . By scanning the RF frequency and measuring the beat frequency, the RF resonance

condition can be determined in the same manner as the RF g -factor measurement described in Section 5.1.

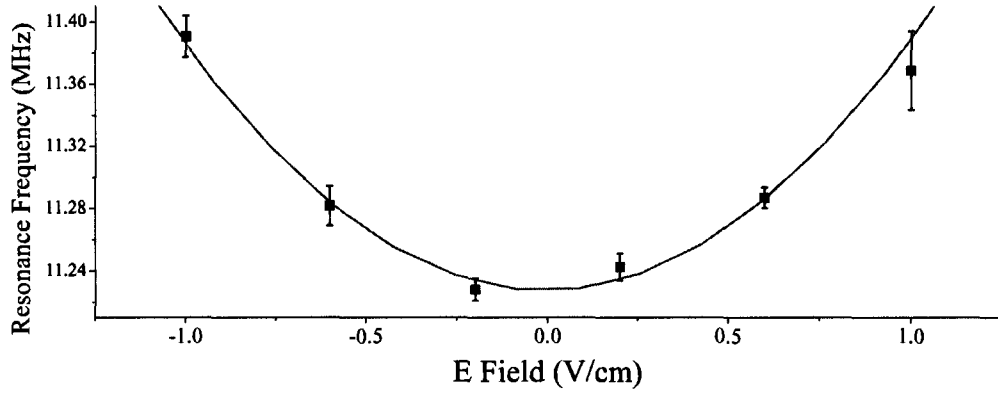


Figure 5.2: Resonance Frequency Dependence on Applied Voltage. The parabolic curve is the fitting result of the resonance frequency as the function of the applied electric field in the cell.

The observed dependence of the splitting on applied voltage gives evidence of an electric field in the cell in qualitative agreement with predictions, shown in Fig. 5.2. However, such a method for determining Stark shifts can not be extended to larger \mathcal{E} fields due to technical limitations in generating the adiabatically ramped-up high voltage.

5.3 Quantum Beats in Electric Field

Strikingly, when we apply a vertical electric field ($\vec{\mathcal{E}}//\vec{B}$), we observed that the beat contrast has a dip at small electric field strength, as shown in Fig. 5.3. If the electric field is parallel to the magnetic field, the contrast dip is due to the level crossing of $M = 0$ and $M = -1$ Zeeman sub-levels¹ at a particular static electromagnetic field, leading to Majorana spin flips that ruin the coherence between $M = \pm 1$ levels, shown in Fig. 5.4. For BEC experiments, Majorana spin flips limit the storage time in an ordinary magnetic

¹ $M = +1$ f level crosses the $M = 0$ f level as well. However, at low electric field, the parity mixing is too small to induce significant population in the f level from the laser excitation from X(0) $J = 0^+$ level at R0 line

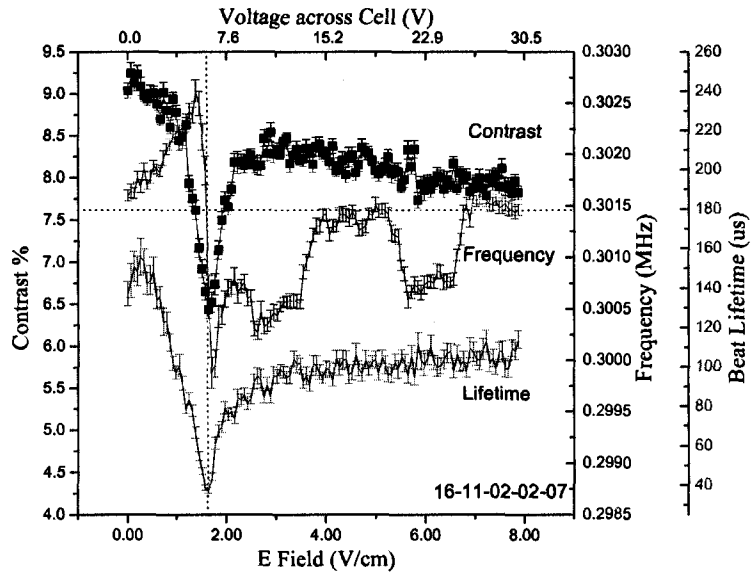
quadrupole trap and the TOP trap is used to suppress the losses due to these spin flips [71]. The Majorana spin flip is related to the transverse magnetic field the molecules experience and can cause the decoherence between $M = \pm 1$ levels, shorten the beat life time, and induce a contrast dip as we scan through the crossing.

Fig. 5.3A shows that the beat lifetime decreases down from $T_{zero} = 160 \mu s$ at zero electric field to $20 \mu s$ when the Majorana spin flip occurs and recovers to $T_{nonzero} = 100 \mu s$ at higher electric field. This might be related to the electric field inhomogeneity in the cell. Before level crossing, the splitting due to the electric field is relatively small compared to the Zeeman splitting. Hence the quantization axis of states is mostly defined by the magnetic field which is believed to be much more homogeneous, and the molecules precess along the external magnetic field. As the electric field strength increases, the contribution of electric field to the energy splitting is comparable to that of magnetic field during level crossing and becomes dominant afterward. Hence the local electric field defines the axis molecules precess around and inhomogeneity introduces decoherence in the quantum beats. The additional decoherence rate γ can be calculated from

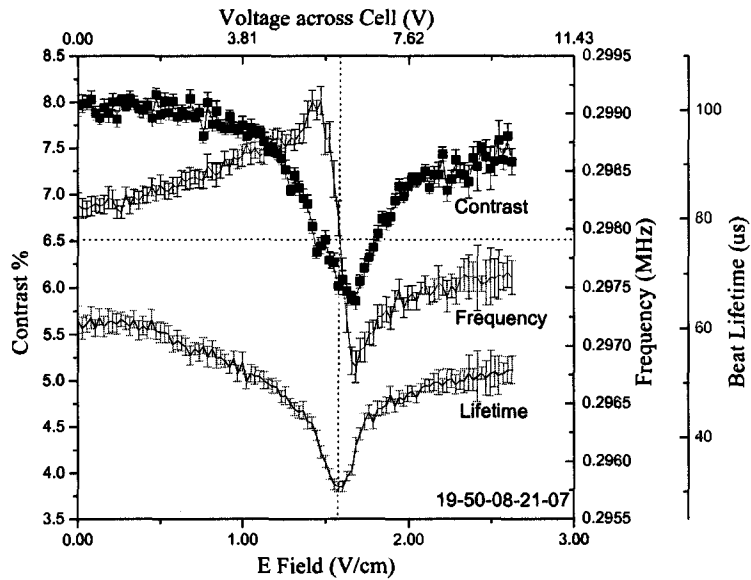
$$\frac{1}{T_{nonzero}} = \frac{1}{T_{zero}} + \gamma,$$

yielding $\gamma = 3.75 \text{ kHz}$. Compared to the beat frequency at 300 kHz, 3.75 kHz will correspond to around 1.3% of electric field inhomogeneity. It is consistent with the result from Fig. 5.3B and the measurement of electric field magnitude inhomogeneity using microwave power broadening. This level of inhomogeneity is as expected from our simulation of electric field distribution inside the vapor cell (see Section 3.1.1).

The beat frequency varies during the level crossing as well. Before the level crossing, the frequency tends to increase, then experiences a jump down to lower frequency as the level is crossed and then tends to recover back. The point at which this frequency jump occurs coincides with the beat lifetime dip. The beat frequency jumps can be explained



(A)



(B)

Figure 5.3: Beat Lifetime at Level Crossing. (A) The beat lifetime decreases from 160 μs to 20 μs when the Majorana spin flip occurs, then recovers back to 100 μs . There are several additional sharp frequency fluctuations; the reason is unclear, possibly due to the ambient magnetic field changing as only one layer of magnetic shield was installed at the time. (B) Another data set. Here the beat lifetime decreases from 60 μs to 30 μs when the Majorana spin flip occurs, then recovers back to 52 μs . Each data point is given by the average of 256 shots.

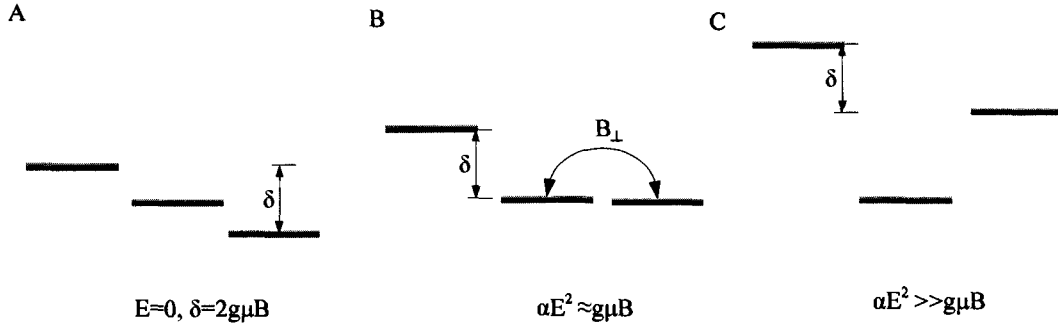


Figure 5.4: $J=1$ Level Crossing in Electric Field. (A) The Zeeman effect in zero electric field, where the quantum beat frequency is $2g\mu_B B$. (B) Level crossing occurs when the Stark shift is equal to the Zeeman shift, $\alpha E^2 \approx g\mu_B B$. B_{\perp} is the transverse magnetic field. (C) Level diagram if the Stark shift is much larger than the Zeeman shift.

by the perturbation from the transverse magnetic field B_{\perp} ,

$$\omega_b \cong g\mu_B B_{\parallel} \left[2 + \frac{(g\mu_B B_{\perp})^2}{(g\mu_B B_{\parallel})^2 - (a\mathcal{E}^2)^2} \right], \quad (5.2)$$

where $a = \mu_a^2 / (4\Delta_{\Omega})$ is the scale factor to describe the quadratic Stark effect. The derivation of Eq. 5.2 is similar to that of Eq. 2.15 in Section 2.6.1. The level crossing occurs at the electric field $\mathcal{E} \cong \sqrt{4g\mu_B B_{\parallel} \Delta_{\Omega}} / \mu_a$. Before level crossing, the denominator of the second term in Eq. 5.2 is positive, so the frequency tends to increase. It experiences a jump down to lower frequency as the level is crossed and tends to recover back at higher fields. Due to the electric field inhomogeneity, the curve of the beat frequency versus electric field is the convolution of Eq. 5.2 and the electric field spread. Notice Eq. 5.2 is only valid asymptotically when $g\mu_B B_{\perp}$ is much less than the level spacing, i.e., before and after the level crossing. In the limiting case, at high electric field, the perturbation from the transverse magnetic field is highly suppressed, as discussed in Section 2.6.1. The experimental results presented here were taken with a single layer of magnetic shield installed, without further trimming of the transverse magnetic field after degaussing of the magnetic shields. The transverse magnetic field here can originate from the static magnetic field inhomogeneity,

the motional magnetic field (see Section 2.6.1), ambient field residual, and the electric field directional inhomogeneity. With the aid of the cosine-distributed magnetic coils and multi-layers magnetic shields (see Section 3.6), we can have better control on the magnetic field distribution and noise, and the interesting phenomena during the level crossing can serve as a nice tool to diagnose the electric field directional inhomogeneity and the systematic effects due to the transverse magnetic field.

As the electric field increases, the beat amplitude changes in rather a complicated pattern, shown in Fig. 5.5. With direct horizontal laser excitation, the mixing of e and f components will lead to population in both. The observed quantum beats will be average fluorescence signals from both components, which have slightly different beat frequencies due to the g -factor difference (discussed later). There are several effects, as discussed below, which will influence the observed beat amplitude.

At zero electric field, the $J = 1^- e$ component can decay to the ground state $X(0)$ $J = 0^+$ and $J = 2^+$, following parity selection rules. These two decay channels have beat contrast of at 100% and 7.7%. Because of the lack of knowledge of the branching ratio between the decay channels, the combined beat contrast can range from 7.7% to 100%. After the level crossing, the beat amplitude does not recover to its initial amplitude at zero electric field. It may be explained by the mixing of different parity levels in $a(1)$ Ω -doublets which will increase the number of decay channels. The induced even-parity $J=1$ f component decays into the ground state $X(0)$ $J = 1^-$ level, as the parity of the $X(0)$ J level is $(-1)^J$. This decay channel has contrast of 33%. Higher electric fields induce more of the $J = 1$ f component, but the effect on the beat amplitude depends on the branching ratio to each decay channel. If the decay to $X(0)$ $J = 0^+$ is the dominant channel, the intrinsic contrast at zero electric field will be larger than 33%, and the introduction of the $J = 1$ f component with lower beat contrast decreases the beat contrast, otherwise, the contrast increases. To see this point, let us consider one situation: the horizontal polarized laser drives the R0 transition and excites the molecules from the ground state $X(0)$ $J = 0$ to the excited state $a(1)$ $^3\Sigma^+$ $J = 1$ in the presence of the external electric field $\vec{\mathcal{E}} = \mathcal{E}\hat{z}$ and

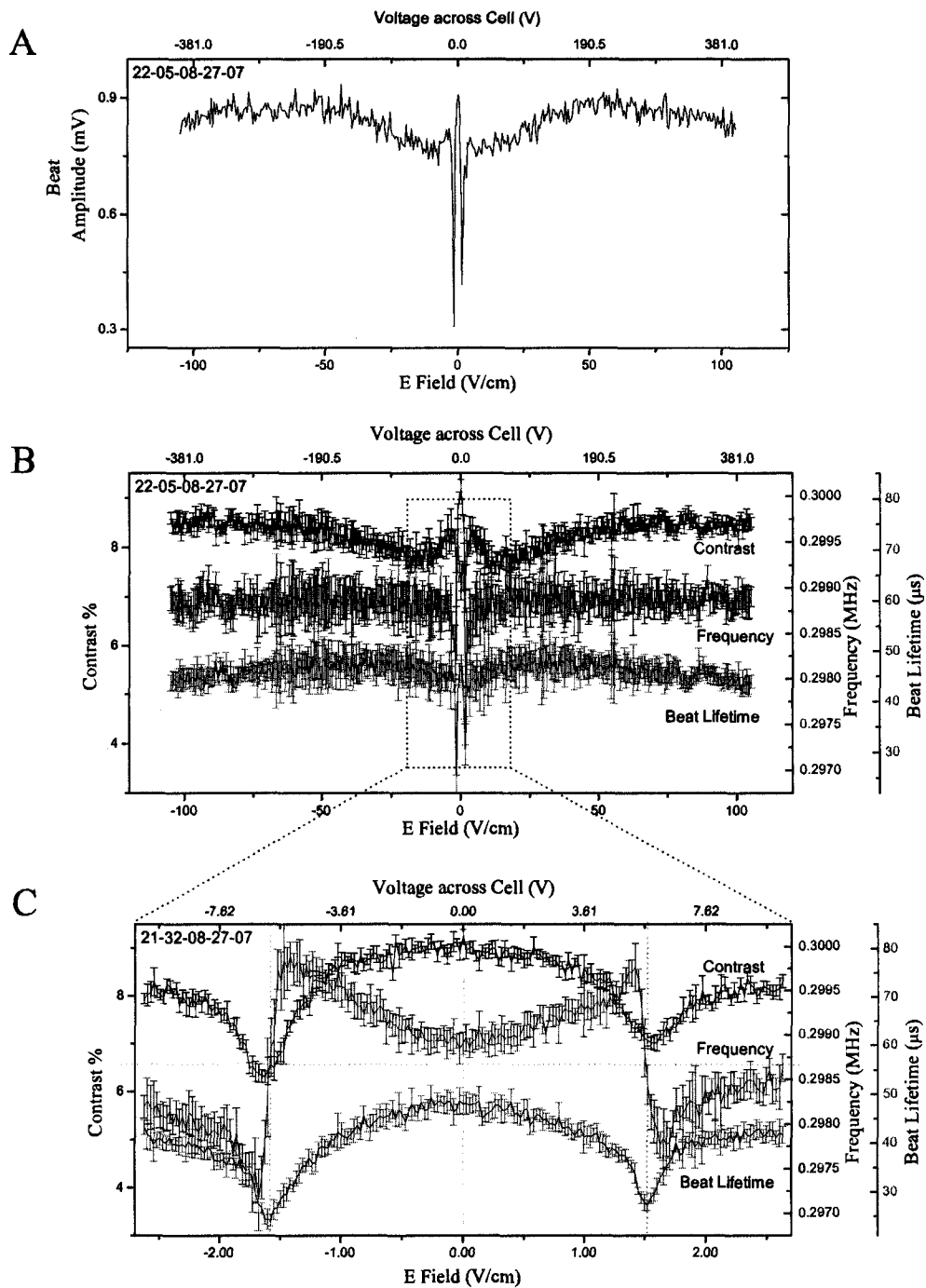


Figure 5.5: a(1) $J=1$ Beat Amplitude in Electric Field. (A) Beat amplitude observed from the Fourier spectrum of fluorescence signal. (B) and (C) Beat contrast, frequency, and beat lifetime.

magnetic field $\vec{B} = B\hat{z}$. Assuming $\mu_a \cdot \mathcal{E} \gg \mu_B \cdot B$, so we can ignore the Zeeman splitting, the initial excited state populates all $J=1$ $M = \pm 1$ sub-levels, represented by the state

$$\left\{ \frac{\Delta_\Omega + \delta_E}{2\sqrt{\delta_E^2 + \Delta_\Omega \cdot \delta_E}}, 0, \frac{\Delta_\Omega + \delta_E}{2\sqrt{\delta_E^2 + \Delta_\Omega \cdot \delta_E}}, \frac{\Delta_\Omega - \delta_E}{2\sqrt{\delta_E^2 + \Delta_\Omega \cdot \delta_E}}, 0, \frac{-\Delta_\Omega + \delta_E}{2\sqrt{\delta_E^2 + \Delta_\Omega \cdot \delta_E}}, \right\},$$

under the basis $\{|J = 1, M = +1, \tilde{e}\rangle, |J = 1, M = 0, e\rangle, |J = 1, M = -1, \tilde{e}\rangle, |J = 1, M = +1, \tilde{f}\rangle, |J = 1, M = 0, f\rangle, |J = 1, M = -1, \tilde{f}\rangle\}$, where Δ_Ω is the Ω -doublet splitting, and δ_E is the quadratic Stark splitting $\delta_E = \sqrt{(\mu_a \cdot \mathcal{E})^2 + \Delta_\Omega^2}$ (see Section 2.1). Denote the radial integral of decay amplitudes through different decay channel as $a = |\langle a(1), J = 1, |\Omega| = 1 || \mu || X(0), J = 0, \Omega = 0 \rangle|^2$, $b = |\langle a(1), J = 1, |\Omega| = 1 || \mu || X(0), J = 1, \Omega = 0 \rangle|^2$, and $c = |\langle a(1), J = 1, |\Omega| = 1 || \mu || X(0), J = 2, \Omega = 0 \rangle|^2$. Currently we lack the spectroscopic data to determine the relative values of a , b , and c . As shown in Fig. 6.1, R0, Q1, and P3 lines are adjacent to nearby strong lines, so that it is hard to estimate the relative ratio from the measurement of the rotational strength. Using Eq. 2.9, the quantum beat signal is

$$\sim \frac{1}{60\delta_E^2} \left\{ [(20a + 45b + 13c)(\mu_a \cdot \mathcal{E})^2 + 2(20a + 13c)\Delta_\Omega^2] - [(20a + c)(\delta_E^2 + \Delta_\Omega^2) + 15b(\mu_a \cdot \mathcal{E})^2] \cos(g\mu B t) \right\},$$

with contrast

$$\frac{(20a + c)(\delta_E^2 + \Delta_\Omega^2) + 15b(\mu_a \cdot \mathcal{E})^2}{2(20a + 13c)\Delta_\Omega^2 + (20a + 45b + 13c)(\mu_a \cdot \mathcal{E})^2}. \quad (5.3)$$

Hence the oscillatory component, which is proportional to the beat amplitude in the Fourier spectrum, varies as electric field changes. The change in beat amplitude saturates at moderate electric field as the molecules can be fully polarized at rather low electric field (See Section. 2.1). The polarization already reaches 0.95 at 20 V/cm.

This effect is less prominent in the $J=2$ beats as it is much harder to polarize the $J=2$ level (see Section 4.2.1). Although the $J=2$ case is not of interest to our EDM experiment, I included the experimental result here for the completeness of our efforts to investigate

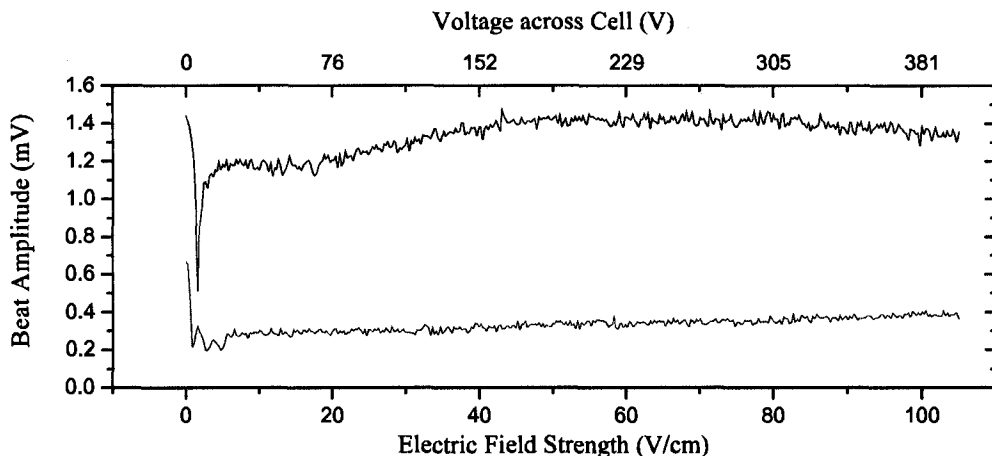


Figure 5.6: Beat Amplitude Changes as Electric Field Increases. The upper trail is J=1 beat amplitude and the lower one is J=2 beat amplitude.

the effects of the electric field to the beat amplitude.

The level crossing at low electric field for J=2 level is quite different with the case for J=1 beat, shown in Fig. 5.7. The J=2 level crossing occurs at the electric field strength three times of that for J=1 level crossing to occur at the same magnetic field \vec{B} .

Let us look at the J=1 case again. As the electric field increases further, the effect due to the g -factor difference in \tilde{e} and \tilde{f} components becomes prominent. Recently Paul Hamilton carried out a close study of the g -factor difference. The experimental result reveals that the mixing of the J=2 level in the presence of an external electric field induces a g -factor dependence on the value of $M\Omega$ and the electric field strength. Here just consider the high electric field situation, where the $M \neq 0$ energy eigenstates will have definite Ω value. If we denote the state with quantum number J, M, and Ω , under the perturbation of external electric field as $|\Psi\rangle$,

$$|\Psi\rangle \equiv |JM\Omega\rangle + \frac{\sqrt{J(J+2)(J+M+1)(J-M+1)}}{(J+1)^2\sqrt{(2J+1)(2J+3)}} \frac{\mu_a \mathcal{E}}{2B_r} |J+1 M\Omega\rangle,$$

where μ_a is the dipole moment in the molecule-fixed frame, B_r is the rotational constant,

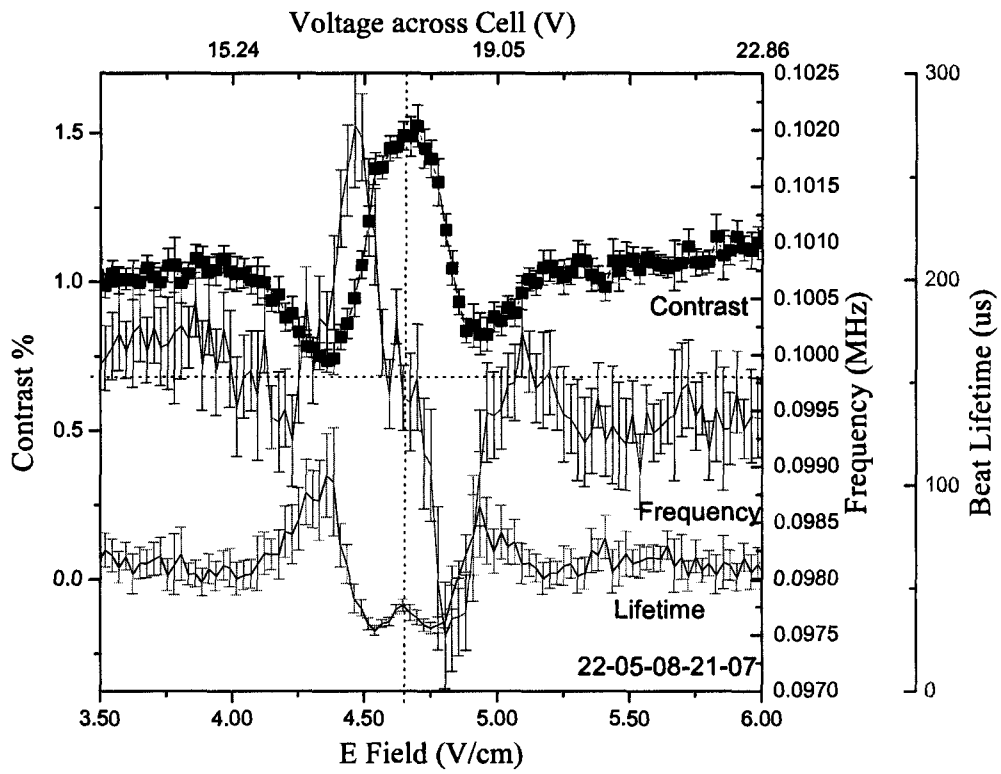


Figure 5.7: a(1) J=2 Beat Amplitude in Low Electric Field.

and \mathcal{E} is the applied electric field. Including the contribution of the next rotational level, the effective g -factor [72] is

$$g_{\text{eff}} = g_{\Omega} \left[1 - \frac{\mu_a \mathcal{E} J^2 (J+2) [(J+1)^2 - M^2]}{B_r M \Omega (J+1)(2J+1)(2J+3)} \right],$$

where g_{Ω} is the g -factor associated with $|JM\Omega\rangle$ state without the electric field perturbation.

In the case of $J = |\Omega| = |M| = 1$, the additional difference due to the electric field is

$$\frac{\delta g}{g} = \frac{g_{\text{eff}} - g_{\Omega}}{g_{\Omega}} = -\frac{3\mu_a \mathcal{E}}{10B_r} M\Omega.$$

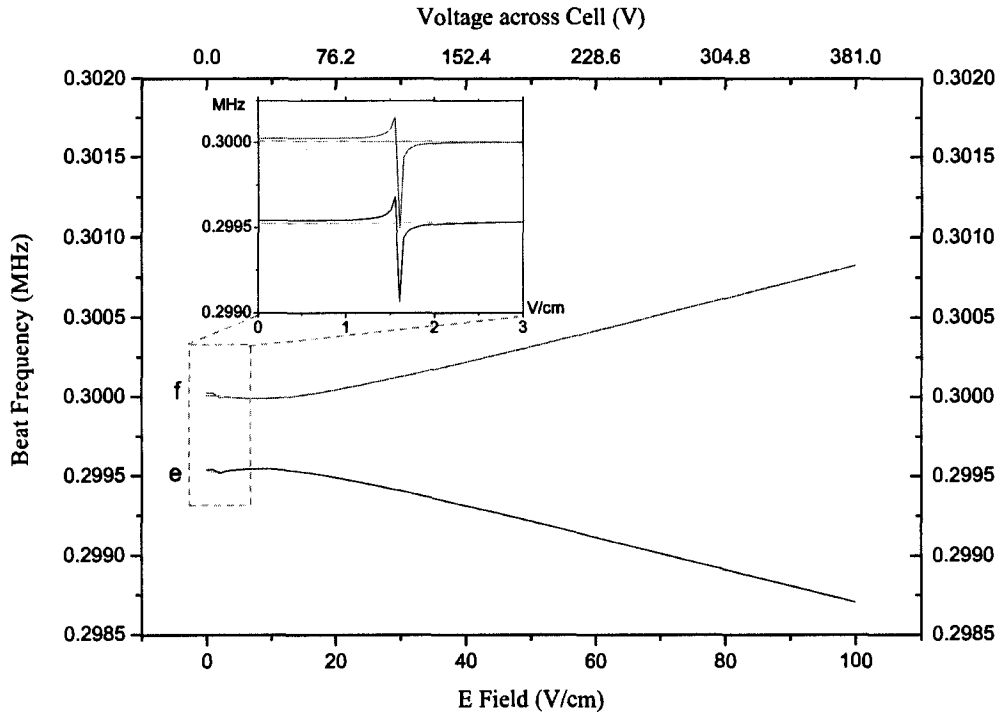


Figure 5.8: Calculated Quantum Beat Frequency Change in the Electric Field. The plot in upper-left panel shows the frequency jump at level crossing. The vertical static magnetic field is ~ 120 mG. The transverse magnetic field is assumed to be 1% of the vertical static magnetic field. The beat frequencies of \tilde{e} and \tilde{f} components get closer at first, then become farther apart nearly linearly in the electric field strength.

This effect, at high electric field, yields an additional g -factor difference between the \tilde{e} and \tilde{f} components, compared to the intrinsic difference in absence of electric field, shown in Fig. 5.8. As nominally $\mu_a \mathcal{E} \sim 50$ MHz at the electric field strength ~ 70 V/cm, $B_r \sim 14$ GHz, the g -factor difference δg between e and f component will be 1% of the average g -factor. In the \tilde{e} component of Ω -doublet states where $M\Omega = 1$, the beat frequency of $M = \pm 1$ Zeeman sublevels decreases by $\frac{3\mu_a \mathcal{E} B}{5B_r}$. In the \tilde{f} component where $M\Omega = -1$, the beat frequency increases by the same amount. Thus the average frequency remain unchanged, as shown in Fig.5.5B. In high magnetic field \mathcal{B} and electric field, the beat frequency splitting due to the different g -factors can be resolved by studying the Fourier spectrum of the quantum beat with the laser horizontally polarized and tuned to the R0 line, populating both of Ω -doublet levels. The interference between these two close frequencies generates apparent lifetime shortening and spectral line broadening, as shown in Fig. 5.9. This effect might be part of the reasons that the observed beat amplitude decreases at high electric fields.

For a large frequency difference, as we increase the electric field, the beat amplitudes will have nodes and anti-nodes during the lifetime period, shown in Fig. 5.9. The frequency difference can be determined by the time span T_n between the laser shot and the node, $\delta\omega = \pi/T_n$. The data analysis by Paul Hamilton has shown that the beat frequency difference dependence on the electric field matches the prediction of theory very well.

Another effect that influences the observed beat amplitude is a technical issue related to the windowing in signal process. As mentioned, we monitor the beat amplitude in the Fourier spectrum. Typically, a *Blackman* window is applied. A simulation by Paul Hamilton demonstrated that the application of a window function in the presence of two closely spaced frequency components modulates the averaged amplitude depending on the frequency difference, with an amplitude peak at a certain frequency difference. The separation of these two peaks in the windowed Fourier transform are not exactly equal to the actual frequency difference. This effect really complicate the dependence of the observed beat amplitude in the electric field. Further quantitative investigation is needed to clarify

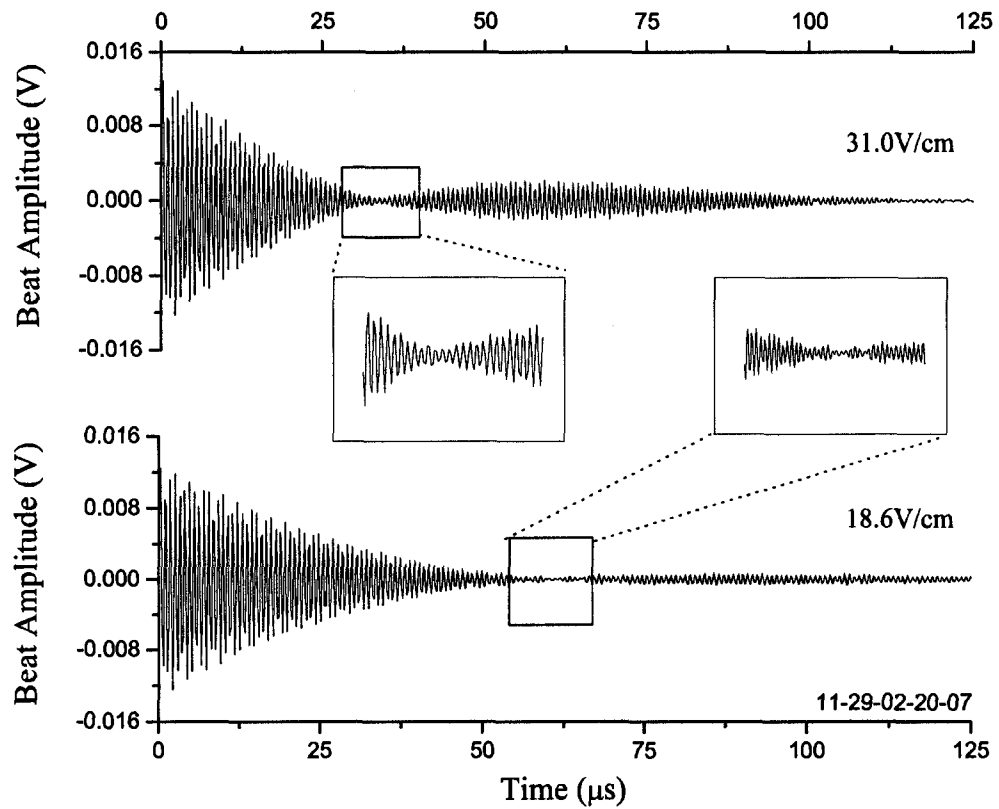


Figure 5.9: Beats Interference at High Electric Field and High Magnetic Field. The beat amplitudes are obtained using the method described in Section 2.4.2. The beat amplitude has a node where two beats are out of phase. These experimental result were taken with the vertical magnetic field ~ 540 mG, corresponding to the quantum beat frequency ~ 1.35 MHz.

this effect.

The above discussion cannot explain the relation between the beat amplitude and the electric field quantitatively. Further experiments and data analysis will be carried out to bring more insight into the effects of the electric field.

5.4 Conclusion

In conclusion, we improve the precision of the g -factors and molecular electric dipole moment of the $a(1)$ $J=1$ states based on the improved experimental setup and data fitting method. Several interesting phenomena of quantum beats in the presence of electric field have been investigated to provide further insight of our feature-rich molecular structures. The revelation of the additional g -factors difference induced by the mixing of $J=2$ level gives better quantitative control on the systematic error suppression using Ω -doublet comparison.

Chapter 6

Current Status and Future Directions

6.1 Current Status

Various attempts have been taken to optimize the excitation efficiency and detection efficiency of PbO EDM experiment. Several results show that our original estimates were over-optimistic and the sensitivity of the current setup will be lower than the original proposed sensitivity by several orders of magnitude.

First, the available signal is much smaller than expected. We have determined that the partial pressure of PbO vapor is much smaller than the number extrapolated from the *CRC Handbook of Chemistry and Physics* [73], which the original proposal is based on. Recently Paul Hamilton carried out an experiment to measure the microwave absorption between the $J=1$ and $J=2$ rotational states of the ground state $X(0)$ of PbO with vibrational number $v = 1$. The experimental results reveal that the observed signal is consistent with a partial pressure of PbO $10 \sim 50$ times smaller than the CRC value. The small fluorescence signal from excitation of the $a(1) [^3\Sigma^+]$ state also places suspicion on the suitability of applying the CRC value to our vapor cell configuration. Other papers in the literatures [74, 75, 76, 77] claim Pb_2O_2 and Pb_4O_4 are created during the vaporization of PbO, and

found the vapor pressure of PbO ranging from 2 ~ 100 times lower than that in the CRC. Hence, we may have overestimated the density of available PbO molecules by a factor of ~ 30 with the nominal amount of PbO source and heater temperature compared to the original proposal. A recent study shows that by using more PbO source to increase the PbO vapor density, the partial pressure of PbO vapor can reach about one tenth of that in the CRC data. Notice that increasing PbO vapor density will lead to higher collision rate and decrease the effective state lifetime. Attempts are being taken to study the optimal vapor pressure and the corresponding heater temperature.

Second, it has been observed that we might be reaching the laser-power saturated region of laser excitation. This is consistent with our observations that increasing laser power does not increase the signal to noise significantly. The manufacture's specification of the spectral width of our pulsed dye laser is about 1 ~ 2 GHz around the lasing frequency, but the spectral profile at a single laser pulse contains narrow spikes spreading under a broad envelope, which average to the 1GHz width over many pulses. Individual shots might have much higher power at certain frequencies, hence the laser excitation will saturate certain velocity groups of the molecules in the vapor cell. Amplified spontaneous emission (ASE) from the dye laser contributes significant fluorescent backgrounds to our detection system, as it causes additional scattered light not resonant with the desired molecular transition and possibly resonant with adjacent rotational lines in ^{208}PbO by accident (see Fig. 6.1). The R6 transition of ^{208}PbO is close to the R0 transition, and the fluorescence that it induces is one of the major backgrounds that reduce the contrast. Recent studies of the laser spectrum were carried out by scanning the laser frequency and monitoring the $J = 1$ quantum beat amplitude. The profile of the fluorescence spectrum can be fitted by a ~1.8 GHz FWHM central Gaussian peak with lower but broad tails fitted to a Gaussian or Lorentzian profile with the FWHM ~12 GHz. The Simulation based on these lineshape fit gave a ratio of 0.36 of fluorescence from R_0 compared to all other lines for the Gaussian tail fit and 0.24 for the Lorentzian tail fit. Correspondingly, the contrast should be reduced by a factor of 3 ~ 4 from the theoretical contrast of R_0 alone. The simulation of the full PbO spectra

including the adjacent rotational lines with these lineshapes also qualitatively agreed with the observation on the fluorescence, shown in Fig. 6.1. We attempted to suppress the ASE by inserting an interference filter at the end of the second beam expanding telescope in the laser path. This filter is from Omega Optical, 2" in diameter, and has a center wavelength of 571.5 ± 1 nm and a full width half maximum of 5 ± 1 nm. Unfortunately, this filter is still insufficient in blocking the ASE and did not improve the contrast of the quantum beats. Further, the spatial pattern of the laser profile is non-Gaussian and contains stripes with local high intensities. It is suspected that such a pattern might saturate the molecules at high intensity regions during the laser shot and not fully excite those at low intensity regions. The Engineered diffuser, discussed in Section 3.8.2, was used to smooth out the spatial pattern to get homogeneous illumination in the vapor cell, but did not appear to increase the signal significantly.

Third, with isotopically enriched ^{208}PbO , we only observed a contrast increase of 1.3 times instead of the expected factor of two improvement. Before the replacement with enriched ^{208}PbO , the natural abundance PbO sample contains 52.4% ^{208}PbO , 22.1% ^{207}PbO , 24.1% ^{206}PbO and 1.4% ^{204}PbO . The amplified spontaneous emission (ASE) from the dye laser contributed to broad background radiation which was accidentally resonant with adjacent rotational lines. The population of these unintended levels leads to an additional decaying background without beats or with beats at different frequencies, which diminishes the beat contrast.

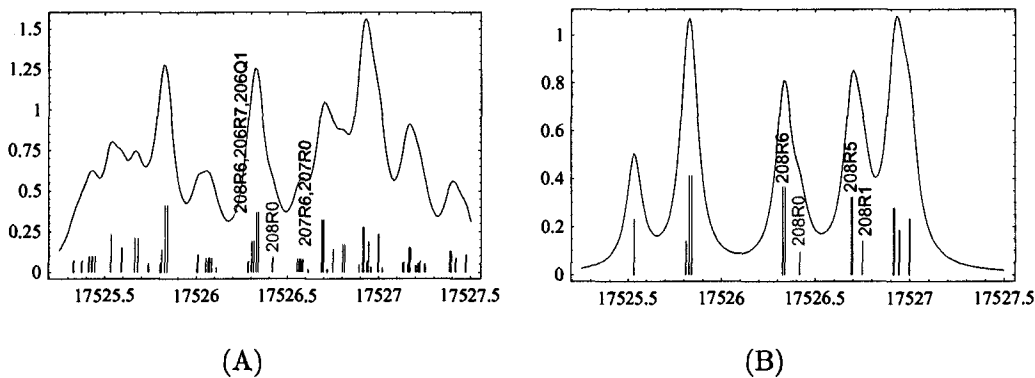


Figure 6.1: PbO Spectrum. A) Natural Abundance. B) Isotopically Pure ^{208}PbO .

Fourth, the excitation efficiency using microwave pulses to transfer the population from the $a(1) J=1 M=0$ states to the desired EDM state is around 30 ~ 40% at the time of this thesis work. The imperfect excitation decreases the contrast of the quantum beats by a factor of 2. With a new microwave amplifier with higher power output, it was expected to improve the excitation efficiency significantly. There are concerns that the boundary conditions set by the metallic electrodes might limit the efficiency on the transition driven by the horizontally polarized microwaves.

Finally, the actual outcome of the detection scheme is less efficient than expected. Currently the fluorescence is collected by a 2" diameter lightpipe, then passing through an IR blocking glass, a sapphire window, and two IF filter before hitting the detector. The first IF filter is a standard IF filter with 50% transmission, 10 nm bandpass, centered at 550 nm. The second filter is an Omega filter with high transmission (~ 90%) and cut on wavelengths of 544 nm and 560 nm. This filter is made using Omega's 3rd Millennium Technology Alpha Gamma technique, which has higher transmission and a steeper cut-off than a standard interference filter. The design and experimental study of the filter properties has been discussed in detail in Ref. [64]. The actual improvement with the Omega filter in place was less than expected. The reason is still under investigation. We choose Hamamatsu R329EGP PMTs with 15% q.e. as detectors for the current experimental stage. Although photodiodes have a much higher quantum efficiency at 550 nm, the current signal size is too small to take advantage of photodiodes; the signal to noise ratio with photodiodes is not better than the PMTs in the current background dominated regime, as discussed in Section 3.8.4. In conclusion, the detection efficiency is estimated to be around 2×10^{-4} , based on fluorescence collection efficiency 4% (from Monte Carlo simulation), IR filter transmission 90%, IF filters' transmission 7%, surface loss 42%, and the detector's quantum efficiency 15%.

Based on the current configuration of the experiment, we can estimate the shot-noise-limited frequency resolution. At the nominal temperature of the PbO vapor $T = 700^\circ\text{C}$, the estimated PbO vapor density is about 1.4×10^{-4} Torr (including the discrepancy from

Improvement	Currently Used?	S_{exp}	C_{exp}	B_{exp}	S_{act}	C_{act}	B_{act}
Increase Laser Power	N	$\times 3$	$\times 1$	$\times 1$	$\times 3$	$\times 0.6$	$\times 1$
Retroreflect Laser	N	$\times 1.5$	$\times 1$	$\times 1$	$\times 1.5$	$\times 0.4$	$\times 1$
2 detectors	N	$\times 2$	$\times 1$	$\times 2$	$\times 2$	$\times 1$	$\times 2$
Pure ^{208}PbO	Y	$\times 2$	$\times 2.5$	$\times 1$	$\times 2$	$\times 1.3$	$\times 1$
Broad IF filter	N	$\times 20$	$\times 1$	$\times 20$?	?	?
Omega IF filter	N	$\times 9$	$\times 1$	$\times 9$	$\times 3.3$	$\times 1$	$\times 5$
Excite from X($v=0$)	N	$\times 3$	$\times 1$	$\times 1$	$\times 3$	$\times 1$	$\times 1$
Photodiode q.e.	N	$\times 9$	$\times 1$	$\times 9$?	$\times 1$?
R329EGP PMT q.e.	Y	$\times 1.6$	$\times 1$	$\times 1.6$?	$\times 1$?

Table 6.1: Expected and Actual Increase of the Signal, Contrast and Backgrounds [64]. S_{exp} , C_{exp} and B_{exp} stand for the expected increase of the signal, contrast and backgrounds. And S_{act} , C_{act} and B_{act} stand for the actual increase of the signal, contrast and backgrounds.

CRC), corresponding to the total number of available PbO molecules 1.4×10^{14} in the whole laser-illuminated volume. This volume is approximated by a cylinder with diameter 1.5" (the electrode spacing), length 3.5" (the vapor cell width), yielding about 100 cm^3 in illuminated volume and $\mathcal{A} = 11 \text{ cm}^2$ in illuminated area. The fraction of molecules in the correct rovibrational state X(0) $v = 1$ $J=0$ is only 1.0×10^{-4} at thermal equilibrium. Assuming the effective dye laser power is about 1 Watt at wavelength 570 nm to drive the transition from X(0) $v = 1$ $J = 0$ level to a(1) $v = 5$ $J' = 1$ level, the total photon number n_{ph} per laser pulse is about 2.9×10^{16} . The laser excitation cross section σ is about $1.3 \times 10^{-16} \text{ cm}^2$, based on

$$\sigma = \frac{1}{2\pi} \lambda^2 \frac{2J' + 1}{2J + 1} \frac{\Gamma_{\text{partial}}}{\Gamma_{\text{Doppler}}}.$$

$\Gamma_{\text{Doppler}} \sim 4.7 \text{ GHz}$ is the FWHM of Doppler broadening at the excitation wavelength 570 nm. $\Gamma_{\text{partial}} \sim 400 \text{ Hz}$ is the decay rate from the a(1) $v = 5$ level to the X(0) $v = 1$ level, based on the state lifetime $\sim 80 \mu\text{s}$ and the branching ratio 0.2. The Franck Condon factor f_{FC} between the a(1) $v' = 5$ level to the X(0) $v = 1$ level is about 0.5. The current microwave excitation efficiency η is about 50%. In conclusion, the excitation efficiency ϵ_e is $f_{\text{FC}}\sigma n_{ph}\eta/\mathcal{A} \sim 0.08$, yielding the total number of excited molecules in the desired EDM state about 1.2×10^9 . The Franck Condon factor f'_{FC} between the a(1) $v' = 5$ level to the X(0) $v'' = 0$ level is also about 0.5. So the emitted photon in fluorescence is about

$n_f = 6 \times 10^8$ per laser shot. The detection efficiency ϵ_d is estimated to be around 2×10^{-4} . The laser fires at $r = 100$ Hz. Hence the counting rate $dN/dt \sim r\epsilon_d n_f$ is 1.2×10^7 /s. The observed contrast is $C \sim 3\%$ using the microwave excitation scheme.

The complete formula of frequency resolution per shot using contrast and signal size is given by Eq. 2.10 (see Section 2.4.2),

$$\delta\nu = \frac{4\alpha\sqrt{S+B}}{2\pi S_0 C \tau^{3/2} \sqrt{2B_d}}.$$

Currently, the observed α is about $1.6 \times 10^{-2} \sqrt{V}$ for a single shot, quantum beat signal size $S \sim 0.1$ V, the blackbody background size $B \sim 0.2$ V, contrast $C \sim 3\%$ using the microwave excitation scheme, the effective lifetime $\sim 50 \mu\text{s}$, and the bandwidth of data acquisition ~ 2.5 MHz. Hence, the current frequency resolution is ~ 240 Hz/ $\sqrt{\text{Hz}}$. The corresponded sensitivity to d_e is only 8×10^{-26} e·cm, assuming that EDM data is collected for 10 days with a 30% duty cycle,.

Although our current sensitivity level is not comparable to the current experimental limit, it is still worthwhile to carry out the EDM data collection as planned. The experimental setup and techniques are ready. Further investigation will help to understand possible systematic effects in EDM measurement using paramagnetic molecules and provide hints on the possibility of sensitivity improvement. There have been already several attempts to improve the sensitivity in the meanwhile. One straight-forward improvement on the current sensitivity level is to use two PMTs set up on both sides of the chamber to improve the counting rate by factor two and sensitivity by $\sqrt{2}$. New heat shield materials are under investigation, aiming to improve the heating efficiency and lower the blackbody radiation background. Studying and engineering the laser profile will help to improve the excitation efficiency. The installation of new microwave amplifier will provide ample adiabatic following parameter space to optimize the population transfer efficiency.

6.2 Future Direction I: Microwave Absorption

The microwave excitation scheme, because of its feature of simplicity and robustness, aroused great interest among us for further exploration. A next generation of the EDM experiment using microwave absorption of PbO vapor as the novel detection scheme was proposed recently. The absorption scheme eliminates the drawbacks of the small solid angle in the fluorescence detection scheme and the signal size scales up linearly with the length of absorption path. For near resonance absorption, 100% contrast is expected in the time-resolved absorption profile. Hence, a promising improvement on the sensitivity of EDM can be achieved in the microwave absorption scheme.

6.2.1 General Description

Once the PbO molecules are prepared in the desired EDM states, it is possible to detect the EDM signal by measuring the absorption on a microwave resonant between these states and a $J=2$ $M=0$ level. By analogy to the discussion of quantum beats in Chapter 2, quantum beats will be seen in time-resolved absorption profile with 100% contrast. The beat frequency can be extracted from the time-resolved absorption profile. The analogy of optical absorption in three levels was studied using density matrix approach in Ref. [78, 79]. By changing the frequencies of the microwave preparation beam and the absorption beam, the beat frequency change between the aligned state and anti-aligned state can be determined to measure the EDM signal.

6.2.2 Absorption Cross Section

Let's consider the absorption cross section for horizontally polarized microwaves first. In the limit of complete polarization of the molecules in the external electric field $\vec{\mathcal{E}}$, we denote $|\Psi_0\rangle$ as one of the EDM states in the external electric field ¹, and $|\Psi_1\rangle$ as the counterpart state in microwave absorption, as shown in Fig. 6.2.

¹ Here the EDM state anti-aligned with $\vec{\mathcal{E}}$ is shown. The absorption cross section for the EDM state aligned with $\vec{\mathcal{E}}$ is identical.

$$\begin{aligned}
|\Psi_0\rangle &= \frac{1}{2} (|J=1, M=1, e, |\Omega|=1\rangle - |J=1, M=1, f, |\Omega|=1\rangle) \\
&+ \frac{1}{2} e^{-i\omega t} (|J=1, M=-1, e, |\Omega|=1\rangle + |J=1, M=-1, f, |\Omega|=1\rangle) \\
&= \frac{1}{\sqrt{2}} (-|J=1, M=1, \Omega=-1\rangle + e^{-i\omega t} |J=1, M=-1, \Omega=1\rangle) \\
|\Psi_1\rangle &= |J=2, M=0, f, |\Omega|=1\rangle \\
&= \frac{1}{\sqrt{2}} (|J=2, M=0, \Omega=1\rangle + |J=2, M=0, \Omega=-1\rangle),
\end{aligned}$$

where ω is the angular frequency of the quantum beat.

A straightforward calculation gives an estimate of the absorption cross-section without Doppler broadening and inhomogeneous broadening,

$$\begin{aligned}
\sigma_{\text{abs}} &= \frac{1}{\Phi} \frac{\mathcal{E}^2}{\gamma \hbar^2} |\langle \Psi_1 | \mu_x | \Psi_0 \rangle|^2 = \frac{8\pi\nu}{c} \frac{1}{\gamma \hbar} \left(\frac{1}{2\sqrt{10}} \mu_a \right)^2 \\
&= 9 \times 10^{-13} (1 + \cos \omega t) \text{ cm}^2.
\end{aligned}$$

where $\Phi = \frac{c\mathcal{E}^2}{8\pi\hbar\nu}$ is the photon flux, ν is the frequency of microwaves, c is the speed of light, γ is the natural line width of a(1) J=1 state $\sim 1/\tau = 2\pi \cdot 3.2$ kHz, τ is the effective lifetime $\sim 50 \mu\text{s}$, and $\mu_a = 3.27 \times 10^{-18}$ esu \cdot cm is the molecular dipole moment in CGS units. The time-resolved absorption depth is modulated at the angular frequency ω with contrast 100%.

Molecules have a Maxwell velocity distribution inside the vapor cell, which will induce Doppler broadening to reduce the absorption cross section. So we must include the effect of Doppler broadening at the temperature $\sim 700^\circ\text{C}$,

$$\Gamma_D = \frac{\nu}{c} \sqrt{\frac{2k_B T}{M}} = 2\pi \cdot 24 \text{ kHz},$$

Moreover, the electric field inhomogeneity in the current cell setup is $\frac{\Delta\mathcal{E}}{\mathcal{E}} \sim 1\%$. With the typical value of the DC Stark shift of $\delta_E \sim 30 \text{ MHz}$, the inhomogeneity-induced broadening

is

$$\Gamma_E \sim \frac{\Delta\mathcal{E}}{\mathcal{E}} \delta_E \sim 2\pi \cdot 300 \text{ kHz},$$

which is the dominant broadening effect. This reduces the absorption cross section according to

$$\sigma \approx \frac{\gamma}{\Gamma_E} \sigma_{\text{abs}} = 10^{-14} (1 + \cos \omega t) \text{ cm}^2.$$

So the total absorption depth will be

$$d = \eta n \sigma l = \eta \cdot 10^{10} \text{ cm}^{-3} \cdot 10^{-14} \text{ cm}^2 \cdot 5 \text{ cm} = 5 \times 10^{-4} \eta. \quad (6.1)$$

where $n \sim 10^{10} \text{ cm}^{-3}$ is the estimated density of molecules in the right rovibrational ground state $X(0) J=0 v=0$ accessible by the laser pumping in the current setup, η is the efficiency of transferring molecules from that ground state to the desired EDM states, which is estimated to be around $1 \sim 5\%$ in the current experiment setup, and l is 5 cm for current vapor cell dimension. In conclusion, the calculation above yields an rough estimate of the expected absorption depth d for the current setup, of the order $\sim 10^{-5}$. It is worthy of notice that the absorption size grows linearly with absorption length if using a longer cell.

To avoid saturation of absorption requires negligible population transfer between the resonance levels. Excluding Doppler and electric field inhomogeneity broadening, this gives a condition on the microwave power

$$\begin{aligned} \frac{1}{\hbar} \langle \mu_x \rangle \mathcal{E}_\mu \tau &\lesssim \frac{\pi}{10} \\ \Rightarrow \mathcal{E}_\mu &\lesssim \frac{\pi}{10} \frac{2\sqrt{10}\hbar}{\mu_a \tau} = 1.28 \times 10^{-5} \text{ sV/cm} \\ \Rightarrow S &= \frac{c}{8\pi} \mathcal{E}_\mu^2 = 2 \times 10^{-8} \text{ W/cm}^2 \\ \Rightarrow P &= AS = 0.5 \text{ } \mu\text{W}, \end{aligned}$$

where $\langle \mu_x \rangle = \frac{1}{2\sqrt{10}} \mu_a$ between $|\Psi_0\rangle$ and $|\Psi_1\rangle$, \mathcal{E}_μ is the electric field strength of the mi-

crowave, S is the Poynting vector of the microwave, A is the illuminating area of the microwave, and P is the desired microwave power. The field strength \mathcal{E}_μ is chosen to be less than the one-tenth of the strength for driving the π -pulse in order to avoid significant population transfer and power broadening. Realistically, the Doppler and electric field inhomogeneity broaden this transition by a factor of $\Gamma_E/\gamma \approx 100$. Hence, the desired microwave power is

$$P = 50 \mu\text{W} \approx -13 \text{ dBm}. \quad (6.2)$$

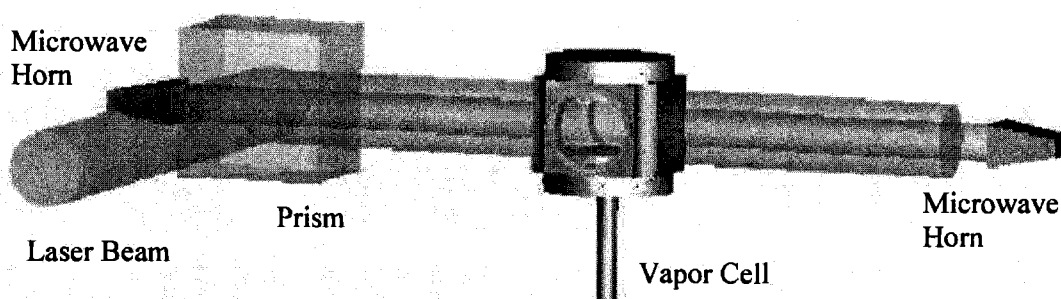


Figure 6.3: Current Microwave Absorption Setup. Two microwave horns are set up on both sides of the cell, one for microwave emission and one for detection. Laser beam is incident from the sideways, and is deflected by the prism to propagate parallel with the microwave.

In current setup, inhomogeneities of the electric field dominate the broadening of the transition and reduce the absorption cross section dramatically. In order to cover the broadening, the spectral width of the microwave needs to be comparable to the absorption line width. One way to achieve that is using random phase modulation on the microwave source. The microwave oscillator is given random “kicks” with time interval t_c , so that the phase experiences a random walk with step size $\delta\phi \ll 1$ radian. Hence, at time t , the phase of the oscillator will have a Gaussian distribution in probability [80]:

$$P(\phi, t) = \frac{1}{\sqrt{2\pi}\sigma} e^{-\frac{\phi^2}{2\sigma^2}},$$

where the standard deviation of the phase $\sigma = \delta\phi\sqrt{t/t_c}$. In average, the amplitude of

microwave is proportional to the quantity:

$$A(t) = \int_{-\infty}^{\infty} P(\phi, t) e^{i\omega_0 t + \phi} d\phi = e^{i\omega_0 t - \frac{\delta\phi^2 t}{2t_c}}.$$

The spectral distribution of the microwave is then given by the Lorentzian function

$$I(\omega) \propto \frac{\gamma^2/4}{(\omega - \omega_0)^2 + \gamma^2/4}$$

where $\gamma = \delta\phi^2/t_c$. A reasonable size of $\delta\phi$ can be chosen as 0.3, and $t_c \sim 200$ ns, yielding the broadening of ~ 450 kHz to cover the electric field inhomogeneity-broadened line. In practice, we can sample a noise source at a 20 ns time interval to give a control voltage to the phase modulation port of the microwave source with phase modulation amplitude around 0.1 radian.

Notice that the coupling between $|\Psi_1\rangle$ and $|\Psi_2\rangle = |J = 2, M = 0, f, |\Omega| = 1\rangle$ is stronger. Moreover, the mixing between the $M = 0$ f and $M = 0$ e is forbidden, and the mixing between $|\Psi_1\rangle$ and $|\Psi_2\rangle$ is suppressed by the rotational level splitting 28.2 GHz. Hence this coupling is not broadened by the electric field inhomogeneity.

$$\begin{aligned} \sigma'_{\text{abs}} &= \frac{1}{\Phi} \frac{\mathcal{E}^2}{\gamma\hbar^2} |\langle\Psi_2|\mu_z|\Psi_1\rangle|^2 = \frac{8\pi\nu}{c} \frac{1}{\gamma\hbar} \left(\frac{1}{\sqrt{5}}\mu_a\right)^2 \\ &= 1.4 \times 10^{-11} \text{ cm}^2. \end{aligned}$$

The corresponding absorption depth d is $\sim 4 \times 10^{-3}$, assuming the vapor cell length is 5" as current setup. We have carried out a microwave absorption experiment probing the vertical transition from $|\Psi_2\rangle$ to $|\Psi_1\rangle$ using the vertically polarized microwave and the current vapor cell setup. The experimental result confirmed the calculation. We could monitor the microwave emission from $|\Psi_1\rangle$ to $|\Psi_2\rangle$ while another microwave beam drives the population from the EDM states to $|\Psi_1\rangle$, as shown in Fig. 6.4.

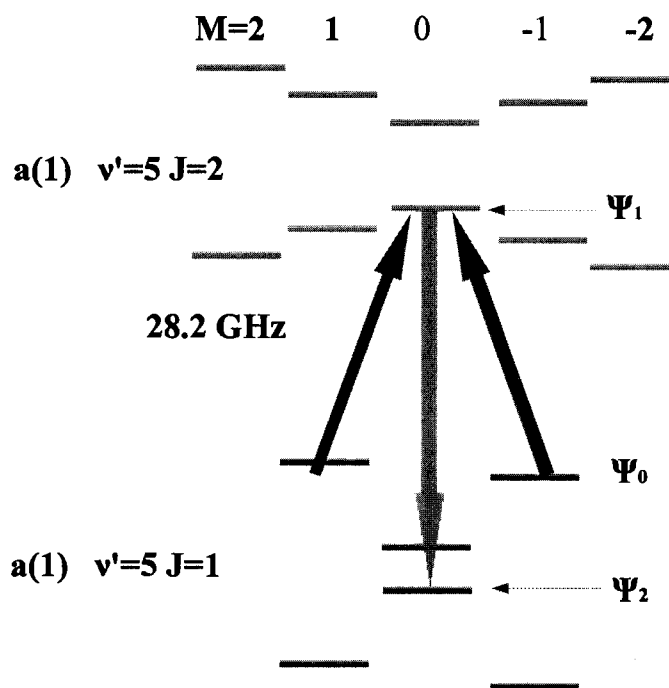


Figure 6.4: Level Scheme for Absorption of Vertically Polarized Microwave. $|J = 1, M = \pm 1, \tilde{e}\rangle$, $|J = 2, M = 0, f, |\Omega| = 1\rangle$, $|J = 1, M = 0, f, |\Omega| = 1\rangle$ are denoted as $|\Psi_0\rangle$, $|\Psi_1\rangle$, and $|\Psi_2\rangle$ respectively.

6.2.3 Signal to Noise

The statistical sensitivity to an EDM will be limited by the signal-to-noise ratio. In the microwave absorption scheme, the absorption signal will be collected by a microwave horn, amplified by a microwave amplifier and detected by a square-law detector. The microwave amplifier noise, treated as thermal noise at the input to the amplifier, will mix with the microwave signal carrying the absorption signal, and be boosted by the square law detector to limit the signal-to-noise ratio of the system.

Here we denote the gain of the amplifier G , the thermal noise amplitude of the amplifier V_T , and the microwave signal amplitude V_μ . The input amplitude to the amplifier, V_{in} is the sum of both: $V_{\text{in}} = V_\mu + V_T$. The output amplitude of the amplifier is $V_{\text{amp}} = GV_{\text{in}}$, and it is fed into the square-law detector. The output voltage of the detector will be proportional to the square of V_{amp} :

$$\begin{aligned} V_{\text{out}} &\propto G^2 (V_\mu + V_T)^2 \propto V_\mu^2 + 2V_\mu V_T + V_T^2 \\ &\propto P_\mu + 2\sqrt{P_\mu P_T} + P_T \\ &\approx P_\mu + 2\sqrt{P_\mu P_T}, \end{aligned}$$

where P_μ is the microwave power of the absorption beam, P_T is the thermal noise power, and the assumption $P_T \ll P_\mu$ is applied in the last approximation. It is easy to see that the thermal noise power P_T is boosted by the signal power P_μ , by the factor $2\sqrt{P_\mu/P_T}$, which is large by the assumption $P_T \ll P_\mu$. The thermal noise level of the microwave amplifier is characterized by the noise figure N , as $P_T = kT_{\text{eff}}B = k(N-1)T_0B$, where $T_0 = 293$ K and $B \approx 3$ kHz is the bandwidth (determined by the beat effective lifetime τ with $1/2\pi\tau \approx 3$ kHz). A typical value for N is 2.8 dB for available low-noise amplifiers. P_μ can be estimated based on the output power of microwave source P_s ($\sim 50 \mu\text{W}$ in Eq. 6.2) and transmission loss L before hitting the detector (10 dB in current setup), $P_\mu = P_s/L$.

The signal to noise ratio will be

$$\begin{aligned} \text{SNR} &\approx \frac{dP_\mu}{2\sqrt{P_\mu P_T}} = \frac{dP_s/L}{2\sqrt{k(N-1)T_0BP_s/L}} = \frac{d}{2} \sqrt{\frac{P_s}{Lk(N-1)T_0B}} \\ &= \frac{fn\sigma l}{2} \sqrt{\frac{P_s}{Lk(N-1)T_0B}}. \end{aligned} \quad (6.3)$$

Substitution of parameters for the current vapor cell setup yields $\text{SNR} \approx 20/\sqrt{\text{Hz}}$ at laser repetition rate 100 Hz. The shot-noise limited frequency resolution is given by

$$\delta\nu = \frac{1}{2\pi\tau\sqrt{T} \cdot \text{SNR}}.$$

where τ is the a(1) state lifetime $\sim 80 \mu\text{s}$, and T is the integration time. Hence, the frequency resolution using the current setup is $\sim 150\text{Hz}/\sqrt{\text{Hz}}$. To compare, the accumulated frequency resolution for 10 days collection with 30% duty cycle is $\sim 0.3 \text{ Hz}$. To reach the current best limit of $1.6 \times 10^{-27} \text{ e} \cdot \text{cm}$, it would take 10^4 days with 30% duty cycle of data collecting which is impossible to achieve.

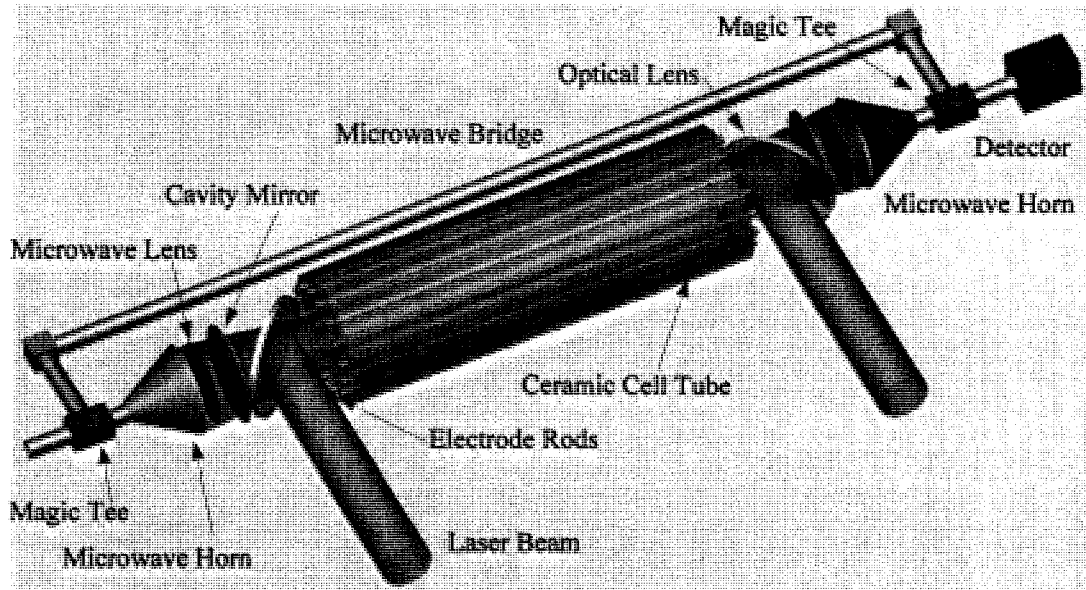


Figure 6.5: MW Absorption Setup. The new vapor cell for the microwave absorption is a cylindrical cell, about 50 cm long, with 16 rods going through the length of the cell.

However, the calculation shown above is just for the current vapor cell. For the new proposed setup, the new vapor cell for the microwave absorption (Fig. 6.5) will be a cylindrical cell, about 50 cm long, with 16 rods going through the length of the cell. These rods are distributed in a circle with equal spacing, supported by the sapphire windows on the ends of the cell. Cosine-distributed voltages will be applied on the corresponding rods to create a homogeneous transverse electric field. Any leakage currents will only flow through the end windows and have little effect on the main cell volume. The heating elements for this cell can be tantalum or tungsten wires, which are believed to be much easier to construct and maintain compared to current oven. The microwave beam is emitted from the microwave horn with some angular spread and will diverge further as it propagates. Microwave lenses are used to collimate and focus the microwave beam. A microwave cavity is used to increase the absorption path length dramatically, by a factor proportional to the cavity finesse. All these microwave optics will help to maintain the TEM₀₀ mode of the microwaves, hence maintaining the microwave polarization and the Gaussian beam profile. The microwave beam will have small beam width to avoid the perturbation from the metallic surface of the electrodes. A homodyne interferometer consists of a magic Tee, bridge, phase delay, and the square-law detector. This setup will diminish the noise due to amplitude fluctuations of the microwave source.

Many improvements can be carried out to increase the signal to noise ratio of microwave absorption detection. A long vapor cell will increase the absorption depth proportional to the transmission length as shown in Eq. 6.1. A 50 cm absorption length will increase the absorption by a factor of 10. Generating the static electric field by conducting rods with cosine voltage distribution will improve the electric field homogeneity by the factor of ~ 10 compared to current cell, which will reduce the inhomogeneous broadening to be comparable to the Doppler broadening. Better electric field homogeneity will increase the absorption cross section by 10, but to avoid saturation P_s will need to be turned down by 10, and based on Eq. 6.3, this will improve SNR by a factor of $\sqrt{10}$. A microwave cavity with finesse F (1,000 feasible) will increase the absorption path length by F , but, similar to

electric field homogeneity case, P_s will need to be reduced by $1/F$, giving an improvement on SNR by $\sqrt{1,000} \sim 32$. Further improvements include broadening the cavity modes of the dye laser, using a low-noise cryogenic microwave amplifier, and etc, which could contribute the improvement by another factor of 100 on the signal to noise.

In conclusion, the ultimate limit to SNR for the microwave absorption scheme is $\sim 3 \times 10^6 / \sqrt{\text{Hz}}$ per shot, yielding the frequency resolution $0.7 \text{ Hz}/\sqrt{\text{Hz}}$, or a sensitivity of $2 \times 10^{-31} e \cdot \text{cm}$ for 10 days of data collecting with 30% duty-cycle at a repetition rate of 100 Hz.

6.3 Future Direction II: Beam EDM

Recently a survey aimed to investigate candidate molecules suitable for a cold beam EDM experiment was carried out by Amar Vutha [81]. ThO and HfO appear promising for use in a future cold beam eEDM experiment.

6.3.1 Cold Beam Experiment

Polar molecular systems can provide great enhancement on the EDM sensitivity as the effective internal electric field the electrons experience can be five or more orders of magnitude higher than the maximal field achievable in the laboratory. Motivated by improvements in the cold molecule flux from He buffer-gas cells, cold molecular beam experiments for EDM measurement show great promise.

In a molecular beam frequency measurement, the obtainable frequency resolution is

$$\delta\nu = \frac{\bar{v}/L}{\sqrt{\eta_e \eta_d N_0 \frac{\mathcal{A}}{\Omega L^2}}}, \quad (6.4)$$

where \bar{v} is the longitudinal velocity of the beam, L is the interaction length, η_e , η_d are the efficiencies for excitation and fluorescence detection respectively, N_0 is the molecule flux from the beam source, Ω is the beam divergence solid angle and \mathcal{A} is the downstream

detection area. Here the dominant noise source is assumed to be Poissonian fluctuations in the beam flux. In order to take advantage of a molecular beam setup, a coherence time is required to be at least a few ms. The natural lifetime of PbO a(1) state is only $82\mu\text{s}$. Therefore we need to search for new candidates for a cold molecular beam EDM experiment.

6.3.2 Candidates for Cold Molecular Beam EDM Experiment

Candidates for a cold molecular beam EDM experiment should possess the following features. First, hetero-nuclear molecules with one atom substantially heavy will take advantage of the fact that the EDM enhancement is proportional to Z^3 . Furthermore, the larger mass will lead to lower velocity beams from thermalization with the buffer gas. Secondly, a small Ω -doublet splitting is desirable to facilitate the molecular polarization under the external electric field and to provide an excellent mechanism of systematic effect suppression. Molecules with total symmetry Σ have been preferred in current molecular EDM experiments: X $^2\Sigma_{1/2}^+$ of YbF and a(1) $^3\Sigma_1^+$ of PbO. The unpaired electron in the molecular orbital of σ symmetry has no orbital angular momentum about the molecular axis, and thus can penetrate close to the nucleus of heavy atom, and spend time near the nucleus, yielding a significant EDM enhancement factor.

Some molecule candidates with nonzero angular momentum about the intra-molecular axis have been studied in the survey. Molecules of interests will have two valence electrons, preferably in the $\sigma\delta$ molecular orbital configuration. The electron in the σ orbital gives an enhanced EDM signal as discussed before. The electron in the δ orbital allows the molecule to possess small Ω -doublet splitting. Hence molecules of interest have $(\sigma\delta)^3\Delta_\Omega$ symmetry overall. Further, the $\Omega = 1$ sub-state, $^3\Delta_1$, has a very small magnetic moment, suppressing spurious frequency shifts from ambient magnetic fields. Only the molecule TiO ($Z=22$) has a $^3\Delta$ ground state, but is too light to be favored for an EDM experiment. TiO-type molecules, ScF ($Z=21$), YF ($Z=39$), ZrO ($Z=40$), LaF ($Z=57$), HfO ($Z=72$), ThO ($Z=90$), all have very low lying $^3\Delta$ states arising from the same $\sigma\delta$ configuration as the $^3\Delta$ state in

TiO.

The heavier molecules LaF, HfO and ThO are considered. The internal effective electric field that the valence electrons experience, as well as the EDM enhancement, will depend mainly on the heavy atom in the molecule. So, although the detailed calculations of eEDM enhancement factors for these molecules haven't been carried out yet, the internal electric fields in HfO $^3\Delta$ state are expected to be not much different from the HfF⁺ calculated value $\mathcal{E}_{eff} = 5.8 \times 10^{24} \text{Hz/e} \cdot \text{cm}$ [82]. As for LaF and ThO $^3\Delta$ states, the effective electric field might be assumed to scale by the factor Z^3 respectively. The frequency resolution and eEDM sensitivities in molecular beam experiment for these molecules are listed in Table 6.2.

Parameter		Worst case	Best case
Beam flux/shot		5×10^{10}	10^{12}
Beam divergence	Ω (srad)	0.9π	$\pi \left(\frac{T[\text{k}]}{M[\text{u}]} \right)_{beam}$
Detection area A	(cm ²)	1	28
Ground state population	$\frac{B_e}{(2I+1)kT}$	0.0013 (LaF)	0.14 (HfO)
		0.12 (ThO)	
Excitation efficiency		10%	100%
Detection efficiency		0.10%	10%
Ablation laser rep. rate	(Hz)	10	100
Resolution $\delta\nu(\text{Hz}/\sqrt{\text{sec}})$	LaF	86	6.1×10^{-3}
	HfO	8.3	5.3×10^{-4}
	ThO	8.9	5.1×10^{-4}
EDM Sensitivity d_e ($10^{-29} \text{e} \cdot \text{cm}/\sqrt{\text{sec}}$)	LaF	1.49×10^6	106
	HfO	7.12×10^4	4.5
	ThO	3.93×10^4	2.2

Table 6.2: Frequency Resolution and eEDM Sensitivities for the Molecules Considered in Molecular Beam Experiment. This table is cited from Ref. [81].

Electronic states, excitation and detection schemes of HfO and ThO are shown in Fig. 6.6. The EDM state $a^3\Delta_1$ in HfO lies at 9230.7cm^{-1} above the ground $X^1\Sigma$ state. Excitation schemes exists from the ground state to the $a^3\Delta_1$ state with the intermediate $b^3\Pi_{0+}$ state. The transition from the ground state to $b^3\Pi_{0+}$ $v''=0$ is at 614 nm. This state decays back into the ground state and into $a^3\Delta_1$. Detection might be on the $a^3\Delta_1 \rightarrow$

$b^3\Pi_{0+}$ (1416 nm) or $a^3\Delta_1 \rightarrow c^3\Phi_2$ (508 nm) transitions. ThO has been spectroscopically studied and is a Hund's case (c) molecule. The analogue of the $^3\Delta_1$ state is the H state, located 5317cm^{-1} above the ground state. The EDM state H is populated via the A state. Detection can either be via E or C states.

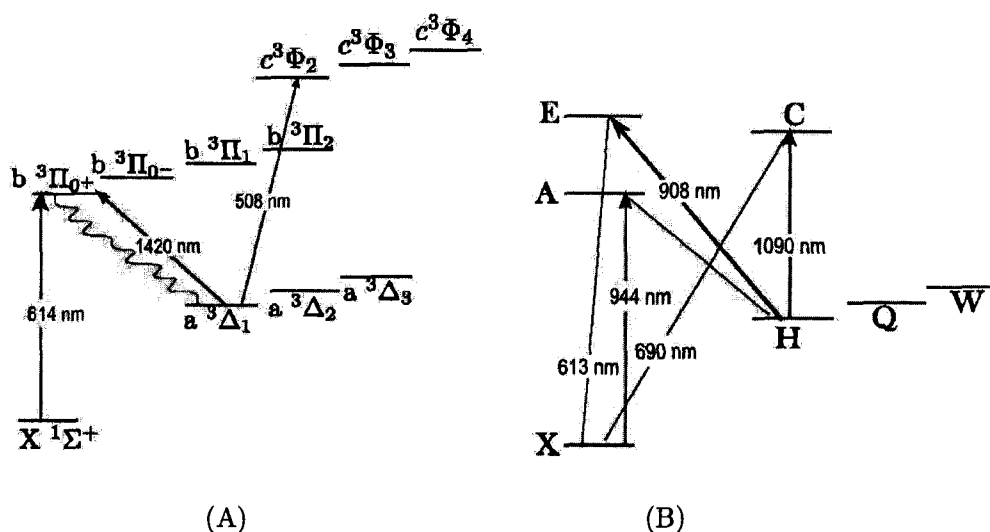


Figure 6.6: Electronic States in HfO and ThO. Excitation schemes are shown in red, detection schemes in blue. (A) For HfO, excitation from the ground state to the $a^3\Delta_1$ state is via $b^3\Pi_{0+}$ state; Detection might be on the $a^3\Delta_1 \rightarrow b^3\Pi_{0+}$ or $a^3\Delta_1 \rightarrow c^3\Phi_2$ transitions. (B) For ThO, the EDM state H is populated via the A state; Detection can either be via E or C states.

The feasibility and future direction of a beam eEDM measurement will rely on the measurement of the lifetime of the metastable state in these molecules. Crude estimates, yet to be confirmed by experimental results, show ThO and HfO appear promising for use in a future cold beam eEDM experiment.

Bibliography

- [1] J. H. Christenson, J. W. Cronin, V. L. Fitch, and R. Turlay. Evidence for the 2π decay of the K_2^0 meson. *Physical Review Letters*, 13(4):138–140, Jul 1964.
- [2] B. Aubert, D. Boutigny, J.-M. Gaillard, A. Hicheur, Y. Karyotakis, J. P. Lees, P. Robbe, V. Tisserand, A. Palano, G. P. Chen, J. C. Chen, N. D. Qi, G. Rong, P. Wang, Y. S. Zhu, G. Eigen, P. L. Reinertsen, B. Stugu, B. Abbott, G. S. Abrams, A. W. Borgland, A. B. Breon, D. N. Brown, J. Button-Shafer, R. N. Cahn, A. R. Clark, and M. S. Gill. Observation of CP violation in the B^0 meson system. *Physical Review Letters*, 87(9):091801, Aug 2001.
- [3] K. Abe, K. Abe, R. Abe, I. Adachi, Byoung Sup Ahn, H. Aihara, M. Akatsu, G. Alimonti, K. Asai, M. Asai, Y. Asano, T. Aso, V. Aulchenko, T. Aushev, A. M. Bakich, E. Banas, S. Behari, P. K. Behera, D. Beilene, A. Bondar, A. Bozek, T. E. Browder, B. C. K. Casey, P. Chang, Y. Chao, K.-F. Chen, and B. G. Cheon. Observation of large CP violation in the neutral B meson system. *Physical Review Letters*, 87(9):091802, Aug 2001.
- [4] M. E. Pospelov and I. B. Khriplovich. Electric-dipole moment of the W-boson and the electron in the Kobayashi-Maskawa Model. *Soviet Journal of Nuclear Physics-USSR*, 53:638–640, 1991.
- [5] A. D. Sakharov. Violation of cp invariance, c asymmetry, and baryon asymmetry of the universe. *Soviet Journal of Experimental and Theoretical Physics Letters*, 5:24,

jan 1967.

- [6] B. C. Regan, E. D. Commins, C. J. Schmidt, and D. DeMille. New limit on the electron electric dipole moment. *Physical Review Letters*, 88:071805, 2002.
- [7] D. F. Nelson, A. A. Schupp, R. W. Pidd, and H. R. Crane. Search for an electric dipole moment of the electron. *Physical Review Letters*, 2(12):492–495, Jun 1959.
- [8] S. Rosendorff. Upper limit for the intrinsic electric dipole moment of the proton and the neutrino. *Nuovo Cimento*, 27:251, 1960.
- [9] J. Bailey, K. Borer, F. Combleyg, H. Drummil, , W. Flegel, P.M. Hattersley, F.J.M. Farley, J.H. Field, F. Krienen, F. Langell, E. Picasso, and W. von Rudenil. New limits on the electric dipole moment of positive and negative muons. *Journal of Physics G*, 4:345–352, 1978.
- [10] L. Pondrom, R. Handler, M. Sheaff, P.T. Cox, J. Dworkin, O.E. Overseth, T. Devlin, L. Schachinger, and K. Heller. New limit on the electric dipole moment of the Λ^0 hyperon. *Physical Review D*, 23:814–816, 1981.
- [11] R. Escribano and E. Massó. New bounds on the magnetic and electric moments of the τ lepton. *Physical Review D*, 301:419–422, 1993.
- [12] E. M. Purcell and N. F. Ramsey. On the possibility of electric dipole moments for elementary particles and nuclei. *Physical Review*, 78(6):807, Jun 1950.
- [13] C. A. Baker, D. D. Doyle, P. Geltenbort, K. Green, M. G. D. van der Grinten, P. G. Harris, P. Iaydjiev, S. N. Ivanov, D. J. R. May, J. M. Pendlebury, J. D. Richardson, D. Shiers, and K. F. Smith. Improved experimental limit on the electric dipole moment of the neutron. *Physical Review Letters*, 97(13):131801, Sep 2006.
- [14] T. M. Ito and the n EDM Collaboration. Plans for a neutron EDM experiment at SNS. *Journal of Physics Conference Series*, 69:2037, May 2007.

- [15] S. K. Lamoreaux. Relativity - testing times in space. *Nature*, 416:803–804, 2002.
- [16] B. J. Heidenreich, O. T. Elliott, N. D. Charney, K. A. Virgien, A. W. Bridges, M. A. McKeon, S. K. Peck, D. Krause, J. E. Gordon, L. R. Hunter, and S. K. Lamoreaux. Limit on the electron electric dipole moment in gadolinium-iron garnet. *Physical Review Letters*, 95:253004, 2005.
- [17] Edward A. Hinds and P. G. H. Sandars. Experiment to search for P- and T- violating interactions in the hyperfine structure of thallium fluoride. *Physical Review A*, 21:480–487, 1980.
- [18] M. V. Romalis, W. C. Griffith, J. P. Jacobs, and E. N. Fortson. New limit on the permanent electric dipole moment of Hg-199. *Physical Review Letters*, 86:2505–2508, 2001.
- [19] Eugene D. Commins and David P. DeMille. Lepton dipole moments, chapter the electric dipole moment of the electron. *to be published*, in 2008.
- [20] D. DeMille, F. Bay, S. Bickman, D. Kawall, D. Krause, S. E. Maxwell, and L. R. Hunter. Investigation of PbO as a system for measuring the electric dipole moment of the electron. *Physical Review A*, 61:05250, 2000.
- [21] A. Derevianko and M. G. Kozlov. Molecular CP-violating magnetic moment. *Physical Review A*, 72:040101, 2005.
- [22] L. I. Schiff. Measurability of nuclear electric dipole moments. *Physical Review*, 1:2194, 1963.
- [23] P. G. H. Sandars. Electric dipole moment of an atom. *Physics Letters*, 14:194, 1965.
- [24] Eugene D. Commins, J. David Jackson, and David P. DeMille. The electric dipole moment of the electron: An intuitive explanation for the evasion of Schiff's theorem. *American Journal of Physics*, 75(6):532–536, 2007.

- [25] W. R. Johnson, D. S. Guo, M. Idrees, and J. Sapirstein. Weak-interaction effects in heavy atomic systems II. *Physical Review A*, 34(2):1043–1057, Aug 1986.
- [26] J. J. Hudson, B. E. Sauer, M. R. Tarbutt, and E. A. Hinds. Measurement of the electron electric dipole moment using YbF molecules. *Physical Review Letters*, 89(2):023003, Jun 2002.
- [27] M. G. Kozlov. Semiempirical calculations of P-odd and P,T-odd effects in diatomic molecule-radicals. *Zhurnal Eksperimentalnoi I Teoreticheskoi Fiziki*, 89:1933–1940, 1985.
- [28] M. G. Kozlov. Enhancement of the electric dipole moment of the electron in the YbF molecule. *Journal of Physics B-Atomic Molecular and Optical Physics*, 30:L607–L612, 1997.
- [29] N S Mosyagin, M G Kozlov, and A V Titov. Electric dipole moment of the electron in the YbF molecule. *Journal of Physics B: Atomic, Molecular and Optical Physics*, 31(19):L763–L767, 1998.
- [30] Y. Y. Dmitriev, Y. G. Khait, M. G. Kozlov, L. N. Labzovsky, A. O. Mitrushenkov, A. V. Shtoff, and A. V. Titov. Calculation of the spin-rotational hamiltonian including P-odd and P, T-odd weak interaction terms for HgF and PbF molecules. *Physics Letters A*, 167:280–286, 1992.
- [31] A. N. Petrov, A. V. Titov, T. A. Isaev, N. S. Mosyagin, and D. DeMille. Configuration-interaction calculation of hyperfine and P,T-odd constants on ^{207}PbO excited states for electron electric-dipole-moment experiments. *Physical Review A*, 72:022505, 2005.
- [32] T. A. Isaev, A. N. Petrov, N. S. Mosyagin, and A. V. Titov. In search of the electron electric dipole moment: Relativistic correlation calculations of the P,T-violating effect in the ground state of HI^+ . *Physical Review Letters*, 95(16):163004, 2005.

- [33] E. R. Meyer, J. L. Bohn, and M. P. Deskevich. Candidate molecular ions for an electron electric dipole moment experiment. *Physical Review A*, 73:062108, 2006.
- [34] R. C. Oldenberg, C. R. Dickson, and R. N. Zare. A new electronic band system of PbO. *Journal of Molecular Spectroscopy*, 58:283–300, 1975.
- [35] M. G. Kozlov and D. DeMille. Enhancement of the electric dipole moment of the electron in PbO. *Physical Review Letters*, 89:133001, 2002.
- [36] W. H. Beattie, M. A. Revelli, and J. M. Brom. Radiative lifetime of PbO a(1). *Journal of Molecular Spectroscopy*, 70:163–164, 1978.
- [37] J. M. Brown, J. T. Hougen, K.-P. Huber, J. W. C. Johns, I. Kopp, H. Lefebvre-Brion, A. J. Merer, D. A. Ramsay, J. Rostas, and R. N. Zare. The labeling of parity doublet levels in linear molecules. *Journal of Molecular Spectroscopy*, 55:500–503, Mar 1975.
- [38] F. Martin, R. Bacis, J. Verges, J. Bachar, and S. Rosenwaks. High-resolution Fourier-transform spectroscopy of the PbO molecule from investigation of the O[2]([1] Δ [g])-Pb reaction. *Spectrochimica Acta Part a-Molecular and Biomolecular Spectroscopy*, 44:889–897, 1988.
- [39] D. Kawall, F. Bay, S. Bickman, Y. Jiang, and D. DeMille. Precision Zeeman-Stark spectroscopy of the metastable a(1) [$^3\Sigma^+$] state of PbO. *Physical Review Letters*, 92:133007, 2004.
- [40] J. T. Hougen. The calculation of rotational energy levels and rotational line intensities in diatomic. *NBS Monograph 115*, 1970.
- [41] L. R. Hunter, S. E. Maxwell, K. A. Ulmer, N. D. Charney, S. K. Peck, D. Krause, S. Ter-Avetisyan, and D. DeMille. Detailed spectroscopy of the a(1) [$^3\Sigma^+$] state of PbO. *Physical Review A*, 65:030501, 2002.
- [42] S. Haroche. *High-Resolution Laser Spectroscopy, chapter: Quantum Beats and Time-Resolved Fluorescence Spectroscopy*. Springer-Verlag, 1976.

- [43] G. J. Gemmen and N. Rouze. Analysis of idealized Zeeman quantum beat experiments in the advanced laboratory. *American Journal of Physics*, 64:147–150, 1996.
- [44] Weng W. Chow, Marlan O. Scully, and John O. Stoner. Quantum-beat phenomena described by quantum electrodynamics and neoclassical theory. *Physical Review A*, 11(4):1380–1388, Apr 1975.
- [45] Fredrik Bay. *Construction of an Apparatus and Preliminary Measurements for a Search for the Electric Dipole Moment of the Electron using Lead Monoxide*. PhD thesis, Yale University, 2003.
- [46] William H. Press, Saul A. Teukolsky, William T. Vetterling, and Brian P. Flannery. *Numerical recipes in C++ : the art of scientific computing, Second Edition*. Cambridge Univeristy Press, 2002.
- [47] L. Duong and Muon g-2 Collaboration. Muon g-2 measurement: The Ratio Fit method. *Bulletin of the American Physical Society*, 46(2):C10.003, April 2001.
- [48] Jonathan M. Paley. *Measurement of the anomalous magnetic moment of the negative muon to 0.7 parts per million*. PhD thesis, Boston University, 2004.
- [49] E. D. Commins, S. B. Ross, D. DeMille, and B. C. Regan. Improved experimental limit on the electric-dipole moment of the electron. *Physical Review A*, 50:2960–2977, 1994.
- [50] Eugene D. Commins. Berry’s geometric phase and motional fields. *American Journal of Physics*, 59(12):1077–1080, 1991.
- [51] J. M. Pendlebury, W. Heil, Y. Sobolev, P. G. Harris, J. D. Richardson, R. J. Baskin, D. D. Doyle, P. Geltenbort, K. Green, M. G. D. van der Grinten, P. S. Iaydjiev, S. N. Ivanov, D. J. R. May, and K. F. Smith. Geometric-phase-induced false electric dipole moment signals for particles in traps. *Physical Review A*, 70:032102, 2004.

- [52] S. K. Lamoreaux and R. Golub. Detailed discussion of a linear electric field frequency shift induced in confined gases by a magnetic field gradient: Implications for neutron electric-dipole-moment experiments. *Physical Review A*, 71(3):032104, 2005.
- [53] D. S. Weiss, F. Fang, and J. Chen. Measuring the electric dipole moment of Cs and Rb in an optical lattice. *APS Meeting Abstracts*, page J1.008, Apr 2003.
- [54] C. DeMicco and C. M. Aldao. On the net radiation method for heat transfer. *European Journal of Physics*, 24:81–89, Jan 2003.
- [55] C. V. Dodd and W. E. Deeds. Analytical solutions to eddy-current probe-coil problems. *Journal of Applied Physics*, 39(6):2829–2838, 1968.
- [56] T. S. E. Thomas. Screening effect of a circular disk. *American Journal of Physics*, 29:37–39, Jan 1961.
- [57] Kent Davey and Larry Turner. The use of time space green’s functions in the computation of transient eddy current fields. *Journal of Applied Physics*, 64(11):6132–6137, 1988.
- [58] W. M. Saslow. Maxwell’s theory of eddy currents in thin conducting sheets, and applications to electromagnetic shielding and maglev. *American Journal of Physics*, 60:693–711, Aug 1992.
- [59] D. Schieber. Transient eddy currents in thin metal sheets. *IEEE Transactions on Magnetism*, MAG-8(4):775, 1972.
- [60] P. Horowitz and W. Hill. *The Art of Electronics*. Cambridge University Press, 2nd ed., 1989.
- [61] D. Shin and R. Magnusson. Diffraction by surface-relief gratings with conic cross-sectional grating shapes. *Journal of the Optical Society of America A*, 6:1249–1253, Sep 1989.

- [62] Tasso R. M. Sales. Structured microlens arrays for beam shaping. *Optical Engineering*, 42(11):3084–3085, 2003.
- [63] W.T. Welford and R. Winston. *The Optics of Nonimaging Concentrators*. Academic Press Inc, 1978.
- [64] Sarah Bickman. *Progress towards a Measurement of the Electric Dipole Moment of the Electron using PbO**. PhD thesis, Yale University, 2007.
- [65] Jr. J. M. Brom and W. H. Beattie. Laser excitation spectrum of PbO : Rotational analysis of the a(1)-x(0⁺) system. *Journal of Molecular Spectroscopy*, 81:445, 1980.
- [66] J. Bachar, R. Bacis, S. Churassy, F. Martin, S. Rosenwaks, G. Taieb, and J. Verges. PbO spectroscopy and studies of the interaction of singlet molecular-oxygen with lead atoms by laser-induced fluorescence and by high-resolution Fourier-transform spectroscopy. *Journal De Physique*, 48:381–383, 1987.
- [67] Clarence Zener. Non-adiabatic crossing of energy levels. *Proc. R. Soc. A*, 137:696, 1932.
- [68] I. S. Gradshteyn and I. M. Ryzhik. *Table of integrals, series and products*. Academic Press, 1994.
- [69] N. V. Vitanov and B. M. Garraway. Landau-Zener model: Effects of finite coupling duration. *Physical Review A*, 53(6):4288–4304, Jun 1996.
- [70] S. Thomas, S. Guérin, and H. R. Jauslin. State-selective chirped adiabatic passage on dynamically laser-aligned molecules. *Physics Review A*, 71(1):013402, 2005.
- [71] Wolfgang Petrich, Michael H. Anderson, Jason R. Ensher, and Eric A. Cornell. Stable, tightly confining magnetic trap for evaporative cooling of neutral atoms. *Physical Review Letters*, 74(17):3352–3355, Apr 1995.
- [72] Misha Lukin. . *private communication*, 2007.

- [73] David R. Lide and H.P.R. Frederikse. *CRC Handbook of chemistry and physics*. Chemical Rubber Publishing Company, 1995.
- [74] J. Drowart, R. Colin, and G. Exsteen. Mass-spectrometric study of the vaporization of lead monoxide*. *Transactions of the Faraday Society*, 61:1376–1383, 1965.
- [75] R.H. Lamoreaux and D.L. Hildenbrand. High temperature vaporization behavior of oxides II: Oxides of Be, Mg, Ca, Sr, Ba, B, Al, Ga, In, Tl, Si, Ge, Sn, Pb, Zn, Cd, and Hg. *Journal of Physical and Chemical Reference Data*, 16(3):419–443, 1987.
- [76] A. Popovič, A. Lesar, M. Guček, and L. Bencze. Mass spectrometric investigation of the evaporation properties of lead oxide. *Rapid Communications in Mass Spectrometry*, II:459–468, 1997.
- [77] S.I. Lopatin, I.Ya. Mittova, F.S. Gerasimov, S.M. Shugurov, V.F. Kostryukov, and S.M. Skorokhodova. Vaporization and thermodynamic properties of the PbO-V₂O₅ system. *Physicochemical Analysis of Inorganic Systems*, 51(10):1646–1652, 2005.
- [78] Richard G. Brewer and E. L. Hahn. Coherent raman beats. *Physical Review A*, 8(1):464–472, Jul 1973.
- [79] Richard G. Brewer and E. L. Hahn. Coherent two-photon processes: Transient and steady-state cases. *Physical Review A*, 11(5):1641–1649, May 1975.
- [80] Derek F. Kimball Dmitry Budker and David P. DeMille. *Atomic physics An Exploration Through Problems and Solutions*. Oxford University Press, 2004.
- [81] Amar Vutha. Molecules for a cold beam EDM experiment. *private communication*, 2007.
- [82] A. N. Petrov, N. S. Mosyagin, T. A. Isaev, and A. V. Titov. Towards the electron EDM search: Theoretical study of HfF⁺. *ArXiv:physics/0611254*, 2006.